DOE-ER-0313/34
Distribution
Categories
UC-423, -424

FUSION MATERIALS
SEMIANNUAL PROGRESS REPORT
FOR THE PERIOD ENDING
June 30, 2003

Prepared for
DOE Office of Fusion Energy Sciences
(AT 60 20 10 0)

DATE PUBLISHED: SEPTEMBER 2003

Prepared for
OAK RIDGE NATIONAL LABORATORY
Oak Ridge, Tennessee 37831
Managed by
U.T.-Battelle, LLC
For the
U.S. DEPARTMENT OF ENERGY

FOREWORD

This is the thirty-fourth in a series of semiannual technical progress reports on fusion materials science activities supported by the Fusion Energy Sciences Program of the U.S. Department of Energy. This report focuses on research addressing the effects on materials properties and performance from exposure to the neutronic, thermal, and chemical environments anticipated in the chambers of fusion experiments and energy systems. This research is a major element of the national effort to establish the materials knowledge base of an economically and environmentally attractive fusion energy source. Research activities on issues related to the interaction of materials with plasmas are reported separately.

The results reported are the product of a national effort involving a number of national laboratories and universities. A large fraction of this work, particularly in relation to fission reactor irradiations, is carried out collaboratively with partners in Japan, Russia, and the European Union. The purpose of this series of reports is to provide a working technical record for the use of program participants, and to provide a means of communicating the efforts of fusion materials scientists to the broader fusion community, both nationally and worldwide.

This report has been compiled and edited under the guidance of Ron Klueh and Renetta Godfrey, Oak Ridge National Laboratory. Their efforts, and the efforts of the many persons who made technical contributions, are gratefully acknowledged.

S. E. Berk
Facilities and Enabling Technologies Division
Office of Fusion Energy Sciences

TABLE OF CONTENTS

1.0 VANADIUM ALLOYS **1**

1.1 ELECTRICAL RESISTIVITY DATA OF VANADIUM ALLOYS IN THE RB-17J EXPERIMENT • M. Li, D. T. Hoelzer and S. J. Zinkle (Oak Ridge National Laboratory) **2**

The room temperature electrical resistivity was measured for tensile specimens of vanadium alloys containing 4-15% Cr and 0.2-15% Ti, V-4Cr-0.38Zr, V-4Cr-0.57Ti-0.1C, and V-4Cr-4Ti weld material. The influence of 100ppm boron on the resistivity of unalloyed vanadium and V-4Cr-4Ti alloy with different thermal-mechanical treatment (TMT) was also examined. It was found that Ti has the strongest effect on the resistivity of vanadium alloys among solute species of Ti, Cr and Zr. Carbon significantly increases the resistivity of the alloys. The resistivity of unalloyed vanadium increases with the addition of 100ppm boron, but the influence of the same amount of boron on the resistivity of vanadium alloys is minimal. The resistivity of vanadium alloys also depends on the final annealing temperature.

1.2 FABRICATION OF CREEP TUBING FROM THE US AND NIFS HEATS OF V-4Cr-4Ti A.F. Rowcliffe, D. T. Hoelzer (Oak Ridge National Laboratory), W. R. Johnson (RSME Services, San Diego), C. Young (Century Tubes Inc, San Diego). **6**

The first batch of commercially-fabricated creep tubing from the US program heat of V-4Cr-4Ti has been used for the on-going program of creep measurements in vacuum and Li environments and also for irradiation creep measurements both in ATR and in HFIR. This tubing (Batch A) had a fairly high frequency of surface cracking both at the ID and OD surfaces and both carbon and oxygen concentrations increased significantly during tube processing. Recently a second tubing campaign was undertaken (Batch B) to produce sufficient tubing to continue creep studies within both the US and Japanese programs. To overcome the shortcomings of Batch A tubing, modifications were made to the procedure including changes to the drawing schedule to reduce drawing stresses and changes to the cleaning procedures to reduce carbon pick-up. During the processing of Batch A, intermediate anneals at 000ºC were carried out under vacuum conditions in the 10^{-4} torr range. For Batch B, vacuum conditions of $< 2 \times 10^{-5}$ torr were specified and a different vendor selected.

1.3 PROCESSING AND FABRICATION OF EXPERIMENTAL VANADIUM ALLOYS FOR HFIR RB-17J EXPERIMENT - D. T. Hoelzer, A. F. Rowcliffe, and L. T. Gibson (ORNL) **22**

A proposed plan was formulated to make 12 experimental heats of vanadium alloys (HR1-HR12) to investigate the effects of composition, precipitation, and the presence of He on the microstructure and mechanical properties of vanadium during neutron irradiation in the HFIR RB-17J experiment. The main objectives for controlling the substitutional and interstitial solute concentrations in the alloys were achieved in this study. All of the alloys except the high N alloy (HR9) were successfully rolled into plates, which were suitable for machining flat sheet tensile (SS-J1 and SS-J2), TEM disks, and pre-cracked bend bars (PCBB) specimens. The alloys were processed with two (three for HR11) thermo-mechanical processes (TMP) in order to develop microstructures containing different precipitate and grain structures for the unirradiated annealing and neutron irradiation experiments.

1.4 **CHARACTERIZATION OF REACTION PRODUCTS AFTER OXIDATION OF V-4Cr-4Ti AT LOW PRESSURES** - B. A. Pint and H. M. Meyer (Oak Ridge National Laboratory) 27

There was a significant change in oxidation kinetics between 10^{-4}atm He and 10^{-3}atm He. The higher pressure results were similar to those observed in 1atm He where a surface oxide was observed. Using Auger electron spectroscopy (AES), a thicker (30-40nm) oxide was observed after 100h at 700°C in the higher He pressure whereas a thinner oxide (10-20nm) formed at the lower pressure.

1.5 **STRONGLY NON-ARRHENIUS INTERSTITIAL DIFFUSION IN VANADIUM**-- L. A. Zepeda-Ruiz (Lawrence Livermore National Laboratory), S. Han (Princeton University), G. J. Ackland (University of Edinburgh), R. Car (Princeton University), and D. J. Srolovitz (Princeton University) 30

The creation and evolution of point defects play an important role in determining the structural properties of materials. The two elementary point defects in elemental metals are vacancies and self-interstitial atoms (SIA). The creation and migration of SIA are critical for microstructural evolution of materials in high-energy radiation environments and in ion implantation. SIAs are usually very mobile (i.e., the migration barriers for SIAs are relatively small) and, hence, play an important role in controlling the rates of several types of microstructural processes in such applications.

1.6 **ON THE CHARACTER OF SELF-INTERSTITIAL LOOPS IN VANADIUM** - L. A. Zepeda-Ruiz (Lawrence Livermore National Laboratory), J. Marian (Lawrence Livermore National Laboratory), B. D. Wirth (University of California Berkeley), and D. J. Srolovitz (Princeton University) 31

Isolated self-interstitial atoms (SIA) and SIA clusters produced during collision cascades are key components of the microstructure observed when metals are irradiated with high-energy particles. The evolution of these defects may cause undesirable changes in the mechanical properties of the material under irradiation. Therefore, knowledge of the properties, formation and diffusion mechanisms of SIA is essential for understanding and predicting the effects of radiation damage.

1.7 **MOLECULAR DYNAMICS STUDY OF THE THRESHOLD DISPLACEMENT ENERGY IN VANADIUM** - L. A. Zepeda-Ruiz (Princeton University and Lawrence Livermore National Laboratory), S. Han (Princeton University), D. J. Srolovitz (Princeton University), R. Car (Princeton University) and B. D. Wirth (University of California, Berkeley) 32

One of the most important physical parameters for describing radiation damage is the threshold displacement energy (TDE). The TDE is the minimum kinetic energy transferred to an atom in the lattice from an impinging particle necessary to permanently displace an atom from its lattice site, thus generating stable defect, such as a Frenkel pair. In the case of high kinetic energy particle impingement (such as 14 MeV neutrons in a fusion reactor environment), the initial cascade gives rise to a series of subcascades which stop when the highest energy particle has kinetic energy smaller than the TDE. Hence, threshold displacement energies are critical parameters for both low and high energy irradiation conditions. The TDE provides a lower limit on particle kinetic energies that must be considered in molecular dynamics (MD) simulations of radiation damage and, hence, is a key parameter for enabling MD simulations of displacement cascades.

2.0 CERAMIC COMPOSITE MATERIALS 33

2.1 CHARACTERIZATION OF A 2D-SIC$_F$/SIC COMPOSITE MADE BY ICVI WITH HI-NICALON™ TYPE S FABRIC – G. E. Youngblood and R. H. Jones (Pacific Northwest National Laboratory) 34

In this report, the mechanical and thermal properties of a 2D-SiC$_f$/SiC composite made by the CVI process with the Hi-Nicalon™ type S fabric are assessed in detail with respect to meeting fusion design requirements. Minimum strength and stiffness structural requirements likely can be met by CVI processed SiCf/SiC composites when made with advanced SiC fibers. Unfortunately, it appears unlikely that the minimum thermal conduction goals can be met for CVI-processed material. Even for an optimized 2D SiCf/SiC system, the margin of improvement required is just too large for only minor improvements potentially possible through CVI-processing upgrades or other structural or architectural methods.

2.2 THERMAL DIFFUSIVITY/CONDUCTIVITY OF IRRADIATED HI-NICALON™ 2D-SIC$_F$/SIC COMPOSITE- G. E. Youngblood, D. J. Senor and R. H. Jones (Pacific Northwest National Laboratory) 41

NOTE: This report was inadvertently left out of the previous FMSPR (DOE/ER-0313/33). Two companion papers did appear in the previous FMSPR, "Thermal diffusivity/conductivity of irradiated Sylramic™ 2D-SiC$_f$/SiC composite" and "Thermal diffusivity/conductivity of irradiated monolithic CVDSiC." For continuity, these reports should be read in sequence since the details for all three experiments and the description of the H2L model are given in this report.

The primary objective of this task is to assess the thermal conduction properties of SiC$_f$/SiC composites made from SiC fibers (with various SiC-type matrices, fiber coatings and architectures) before and after neutron irradiation, and to develop analytic models that describe the transverse and in-plane thermal conductivity of these composites as a function of constituent properties and geometry as well as temperature and radiation dose.

3.0 FERRITIC MARTENSITIC STEELS 48

3.1 FRACTURE TOUGHNESS VARIABILITY IN F82H - D. S. Gelles (Pacific Northwest National Laboratory) and Mikhail A. Sokolov (Oak Ridge National Laboratory) 49

The fracture toughness database for F82H displays some anomalous behavior. Metallographic examination reveals banding in the center of 25 mm thick F82H plate, which is more evident in transverse section. The banding is shown to arise because some grains are etched on a very fine scale whereas the remainder is etched more strongly and better delineates the martensite lath structure. However, the banding found does not provide explanation for the anomalous fracture toughness behavior.

3.2 **FURTHER EXAMINATION OF CRACK TIP MICROSTRUCTURES IN F82H ON THE LOWER SHELF** - D. S. Gelles (Pacific Northwest National Laboratory), G. R. Odette (University of California at Santa Barbara) and P. Spätig (École Polytechnique Fédérale de Lausanne, – Centre de Recherches en Physique des Plasma, Villigen PSI, Switzerland) **56**

Dislocation microstructures have been further examined near the crack tip of a compact tension specimen of unirradiated F82H loaded to 25.6 MPa $m^{1/2}$ at –196°C after fatigue precracking. A specimen was prepared by sectioning, dimple grinding and ion milling to produce electron transparency just ahead of the crack tip. Further ion milling has allowed improved examination of the microstructure immediately ahead of the crack tip. It is found that subgrain structure is relatively unaffected near the crack tip whereas 3 μm from the crack tip, dislocation loop structure was identified.

3.3 **IRRADIATION EFFECTS ON IMPACT TOUGHNESS OF LOW-CHROMIUM BAINITIC STEELS** • R. L. Klueh and M. A. Sokolov (Oak Ridge National Laboratory) **63**

Charpy specimens of five bainitic steels were irradiated at 378-404ºC in the Experimental Breeder Reactor (EBR-II) to 26-33 dpa. The steels were experimental reduced-activation 3Cr-WV steels with additions tantalum, boron, and nickel. The steels were normalized, and specimens of the normalized steel were given two tempering treatments: 1 hr at 700ºC and 1 h at 750ºC. The Charpy tests demonstrated only minor effects of 1% W, 0.05% Ta, and 0.005 %B in the steels in the unirradiated condition. Tungsten and tantalum had a favorable effect on the irradiated properties. Nickel, on the other hand, had a favorable effect on the impact toughness of the steel before and after irradiation.

3.4 **IRRADIATION CREEP AND SWELLING OF RUSSIAN FERRITIC-MARTENSITIC STEELS IRRADIATED TO VERY HIGH EXPOSURES IN THE BN-350 FAST REACTOR AT 305-335°C** – Y. V. Konobeev, A. M. Dvoriashin, S. I. Porollo, and S. V. Shulepin. (Institute of Physics and Power Engineering, Russia), N. I. Budylkin, and E. G. Mironova (Research Institute of Inorganic Materials, Russia) F. A. Garner and M. B. Toloczko (Pacific Northwest National Laboratory) **70**

Russian ferritic/martensitic (F/M) steels EP-450, EP-852 and EP-823 were irradiated in the BN-350 fast reactor in the form of gas-pressurized creep tubes. The first steel is used in Russia for hexagonal wrappers in fast reactors. The other steels were developed for compatibility with Pb-Bi coolants and serve to enhance our understanding of the general behavior of this class of steels. In an earlier paper we published data on irradiation creep of EP-450 and EP-823 at temperatures between 390 and 520°C, with dpa levels ranging from 20 to 60 dpa. In the current paper new data on the irradiation creep and swelling of EP-450 and EP- 852 at temperatures between 305 and 335°C and doses ranging from 61 to 89 dpa are presented. Where comparisons are possible, it appears that these steels exhibit behavior that is very consistent with that of Western steels. Swelling is relatively low at high neutron exposure and confined to temperatures <420°C, but may be camouflaged somewhat by precipitation-related densification. These irradiation creep studies confirm that the creep compliance of F/M steels is about one-half that of austenitic steels.

4.0 COPPER ALLOYS **78**

4.1 STATUS OF IN-REACTOR TENSILE STRAINING OF PURE COPPER AT A CONSTANT STRAIN RATE - D. J. Edwards (Pacific Northwest National Laboratory), B. N. Singh (Risø National Laboratory, Denmark), S. Tähtinen, P. Moilanen (VTT Industrial Systems, Finland), P. Jacquet and J. Dèkeyser (Reactor Technology Department, SCK·CEN, Belgium) **79**

Annealed tensile samples of pure copper were irradiated in the fission reactor BR-2 in Mol, Belgium at 90°C with a damage rate of 6 x 10^{-8} dpa/sec. The tensile specimens were a sheet-type specimen with a 3-mm gage width and a gage length of 7 mm. The first experiment involved two specimens, one of which was irradiated with no load to provide a comparative specimen to the other specimen, which was loaded at a constant strain rate of 1.3 x 10^{-7} s^{-1}. The uniaxial tensile load was applied 4 hrs after the irradiation rig was inserted into the reactor core. This corresponded to a total displacement damage of 8.6 x 10^{-4} dpa accumulated before the tensile test was started. The tensile test was considered complete once the load began rapidly falling and reached 100 MPa, at which level the test was stopped and the load quickly reduced to zero to leave the specimen intact. For these test conditions the specimen reached a total plastic strain of ~13% when the test was stopped, considerably less than that of unirradiated pure copper tested under the same strain rate, which was on the order of 50% total elongation. The second experiment involved two samples irradiated under identical irradiation and test conditions, but in this case the tensile load was not applied until a total dose of 1 x 10-2 dpa (~50 hours after insertion into the reactor core) was reached. Once the load was applied, the stress immediately climbed to ~150 MPa with little plastic strain, followed by a small yield drop and work hardening up to a maximum stress of ~200 MPa. As in the first experiment, the tensile test was stopped when the load began decreasing and reached a level of 100 MPa.

4.2 THE EFFECT OF POST-IRRADATION ANNEALING ON STACKING FAULT TETRAHEDRA IN NEUTRON-IRRADIATED OFHC COPPER - D. J. Edwards (Pacific Northwest National Laboratory), B. N. Singh and M. Eldrup (Risø National Laboratory, Denmark) **85**

Two irradiation experiments have been completed wherein two sets of tensile specimens of OFHC copper were irradiated with fission neutrons, one set at 200°C and the other at 250°C. Post-irradiation annealing in vacuum was then used to evaluate the change in the defect microstructure, including vacancy-type SFT, voids, and dislocation loops. Individual samples within each set were given one annealing exposure at 300, 350, 400, 450, 500, or 550°C for 2 hours. The fine-scale defect microstructure was characterized by transmission electron microscopy (TEM) to compare the defect size and spatial distribution at each annealing temperature and reference the results to that measured in the as-irradiated condition. Based on the change in the SFT size distributions, post-irradiation annealing led to a preferential removal of the smaller sized SFT, but did not lead to a general coarsening as might be expected from an Oswald ripening scenario. The issue of whether the SFT produced during irradiation are all structurally perfect is still being investigated at the time of this report, however, the images of the SFT appeared more perfect after annealing at 300°C and higher. Further analysis is being performed to determine whether intermediate stages of SFT formation exist in the as-irradiated condition.

No contributions

No contributions

In order to determine the high temperature resistivity and Li compatibility of several candidate materials, bulk specimens were fabricated for testing. Results for Y_2O_3 showed sufficiently low resistivity up to 800°C. Combined with the Li compatibility results, Y_2O_3 meets the metrics for bulk materials and should be tested as a coating. Initial characterization of the electron beam physical vapor deposited (EB-PVD) Y_2O_3 coatings shows significant deterioration after exposure to Li at 700° or 800°C.

No Contributions.

The effects of irradiation on the mechanical behavior of face-centered cubic (FCC) and body centered cubic (BCC) metals are briefly reviewed, including dislocation channeling, cleavage fracture, and irradiation creep at low irradiation temperatures and helium grain boundary embrittlement at high temperatures. Particular emphasis is placed on the microstructural mechanisms responsible for the changes in mechanical behavior. Four different material systems are examined as typical examples of behavior in FCC (dispersion strengthened and precipitation strengthened copper, Type 316 austenitic stainless steel) and BCC (V-Cr-Ti alloys, 8-9 Cr ferritic/martensitic steel) metals. Similarities and differences in the mechanical behavior of irradiated FCC and BCC metals are highlighted. The stress and temperature regimes where various deformation mechanisms predominate before and after irradiation are displayed in terms of Ashby deformation maps. Tensile tests can often provide a misleading indication of the fracture toughness behavior due to the lack of stress concentrators in un-notched specimens.

9.2 **ATOMIC-LEVEL INTERACTION OF AN EDGE DISLOCATION WITH LOCALIZED OBSTACLES IN FCC AND BCC METALS -** Yu. N. Osetsky (Oak Ridge National Laboratory) and D. J. Bacon (Department of Engineering, The University of Liverpool, UK) **126**

Interaction between a moving dislocation and localized obstacles determines microstructure-induced hardening. The mechanisms and parameters of such interactions are necessary inputs to large scale dislocation dynamics modelling. We have developed a model to investigate these characteristics at the atomic level for dislocation-obstacle interactions under both static (T=0K) and dynamic (T>0K) conditions. We present results on hardening due to pinning of edge dislocations at obstacles such as voids, coherent precipitates and stacking fault tetrahedra in bcc-iron and fcc-copper at temperatures from 0 to 600K. It is demonstrated that atomic-scale simulation is required to determine the effects of stress, strain rate and temperature and that such effects cannot always be rationalized within continuum theory.

9.3 **A KINETIC MONTE CARLO MODEL FOR HELIUM DIFFUSION AND CLUSTERING IN FUSION ENVIRONMENTS** -- B. D. Wirth (University of California, Berkeley) and E. M. Bringa (Lawrence Livermore National Laboratory) **133**

Structural materials in fusion reactors will operate in harsh radiation conditions including high displacement rates from 14 MeV neutrons with accompanying high levels of hydrogen and helium production and will experience severe property degradation. Predicting their in-service performance requires a detailed understanding of the mechanisms of defect accumulation and microstructure evolution. Here, we describe a kinetic Monte Carlo (KMC) model to simulate the migration and clustering of transmutant helium gas atoms and ultimately determine the role of He in mediating the long term aging of primary defects (vacancies, self-interstitial atoms and their clusters) produced in displacement cascades.

9.4 **SUPPRESSION OF HELIUM BUBBLE GROWTH IN FRICTION STIR WELDING OF IRRADIATED MATERIALS** – Zhili Feng and Stan A. David (Oak Ridge National Laboratory) **134**

Computational simulations were conducted to investigate the helium bubble growth during friction stir welding of irradiated stainless steel. The helium bubble evolution model by Kawano et al was incorporated into the finite element based welding temperature and stress computational model to obtain the temporal and spatial distribution of the helium bubbles in the heat-affected zone of a weld. The predicted maximum helium bubble location in a gas tungsten arc weld correlated very well with the actual helium induced cracking site. The compressive thermal stress, coupled with the lower temperature, of the friction stir welding process inhibits the helium bubble growth. The calculations show that, even without fine-tuning the FSW process parameters, the maximum helium bubble size in a friction stir weld is only about 27% of a gas tungsten arc weld of comparable size. This preliminary study suggests that friction stir welding is advantageous in circumventing the helium induced cracking for welding of irradiated materials.

10.0 **DOSIMETRY, DAMAGE PARAMETERS, AND ACTIVATION CALCULATIONS** **139**

No contributions

The experimental matrix for JP-26 was finalized and final design of the irradiation vehicle was completed. Components needed to build the irradiation vehicle are being machined and will be delivered to ORNL by late August. Most of the necessary specimens have been fabricated and final delivery to ORNL is expected by late August. Assembly of the experiment is expected to take place in early September so that the irradiation can begin by mid September.

1.0 VANADIUM ALLOYS

ELECTRICAL RESISTIVITY DATA OF VANADIUM ALLOYS IN THE RB-17J EXPERIMENT

— M. Li, D.T. Hoelzer and S.J. Zinkle (Oak Ridge National Laboratory)

OBJECTIVE

The objective of this report is to summarize the room temperature electrical resistivity measurements on several vanadium alloys, which will be included in the RB-17J neutron irradiation experiment.

SUMMARY

The room temperature electrical resistivity was measured for tensile specimens of vanadium alloys containing 4-15% Cr and 0.2-15% Ti, V-4Cr-0.38Zr, V-4Cr-0.57Ti-0.1C, and V-4Cr-4Ti weld material. The influence of 100ppm boron on the resistivity of unalloyed vanadium and V-4Cr-4Ti alloy with different thermal-mechanical treatment (TMT) was also examined. It was found that Ti has the strongest effect on the resistivity of vanadium alloys among solute species of Ti, Cr and Zr. Carbon significantly increases the resistivity of the alloys. The resistivity of unalloyed vanadium increases with the addition of 100ppm boron, but the influence of the same amount of boron on the resistivity of vanadium alloys is minimal. The resistivity of vanadium alloys also depends on the final annealing temperature.

PROGRESS AND STATUS

Experimental Procedure

The electrical resistivity was measured on several vanadium alloys including V-4Cr-4Ti (U.S. 832665 heat and Japanese NIFS-2 heat) and a series of model alloys (designated HR heats) of V-10Cr-4Ti, V-15Cr-4Ti, V-4Cr-0.2Ti, V-4Cr-0.5Ti, V-4Cr-10Ti, V-4Cr-15Ti, V + 100ppmB, V-4Cr-4Ti +100ppmB, V-4Cr-0.38Zr, and V-4Cr-0.57Ti-0.1C. The electrical resistivity measurements were also carried out on V-4Cr-4Ti weld (Heat GTA25). All materials received a final annealing treatment for 2 hours between 950 and 1300°C. The GTA25 V-4Cr-4Ti weld was further annealed at 400°C for 2 hours to remove the hydrogen contamination. The electrical resistivity measurements were performed on types SS-J1 and SS-J2 sheet tensile specimens. The SS-J1 specimens had nominal gauge dimensions of 0.25×1.2×5 mm and total length of 16 mm, and the SS-J2 specimens had nominal gauge dimensions of 0.5×1.2×5 mm and total length of 16 mm. Table 1 lists alloy classes, heat number and final heat treatment of the materials examined in this study, and specimen identification and specimen type.

A four-point probe technique was used for electrical resistivity measurements following the guidelines in ASTM Standard Test Method for Resistivity of Electrical Conductor Materials, ASTM B 193-87 (reapproved 1992). A constant electrical current of 100 mA was supplied by a Keithley 237 High Voltage Source Measure Unit through electrical contacts located in the grip region of the tensile specimens. The voltage drop in the gauge section was measured using a Keithley 182 Sensitive Digital Voltmeter. The distance between the spring-loaded voltage contacts was 4.42 mm. Thermal emf offset potentials were subtracted using the "relative reading" offset function of the Keithley 182 voltmeter. Multiple specimens (between 6 and 19 specimens) were measured for each material and heat treatment condition. Five electrical measurements were made on each specimen and were averaged. The specimen thickness and width were measured to an accuracy of 1 μm using a Mitutoyo digital micrometer. The resistance data were converted to resistivity values with the measured specimen dimensions. The temperature was recorded at the beginning and end of the measurement period. The temperatures were between 26 and 27°C. Further details on the alloy processing and measured chemical composition will be reported separately.

Table 1. Alloy classes, annealing condition and specimen identification and type.

Alloy	Heat	Final Anneal (ºC)	Specimen I.D. (Start)	Specimen I.D. (End)	Specimen Type
V-4Cr-4Ti	832665	1000ºC/2h	UB30	UB48	SS-J1
V-4Cr-4Ti	GTA25	1000ºC/2h + 400ºC/2h	UW00	UW05	SS-J1
V-4Cr-4Ti	HR-1	1000ºC/2h	UE00	UE11	SS-J1
V-10Cr-4Ti	HR-2	1000ºC/2h	UF00	UF11	SS-J1
V-15Cr-4Ti	HR-3	1000ºC/2h	UV00	UV14	SS-J2
V-15Cr-4Ti	HR-3	1300ºC/2h	UV15	UV29	SS-J2
V-4Cr-10Ti	HR-4	1000ºC/2h	UH00	UH11	SS-J1
V-4Cr-15Ti	HR-5	1000ºC/2h	UM00	UM11	SS-J1
V-4Cr-4Ti + 100ppmB	HR-11	950ºC/2h	UP00	UP11	SS-J1
V-4Cr-4Ti + 100ppmB	HR-11	1000ºC/2h	UP12	UP23	SS-J1
V-4Cr-4Ti + 100ppmB	HR-11	1300ºC/2h	UP24	UP35	SS-J1
V + 100 ppm B	HR-12	1000ºC/2h	UR00	UR11	SS-J1
V + 100 ppm B	HR-12	1300ºC/2h	UR12	UR23	SS-J1
V-4Cr-4Ti	NIFS-2	1000ºC/2h	UN00	UN18	SS-J2
V-4Cr-0.20Ti	HR-6	1000ºC/2h	US00	US14	SS-J2
V-4Cr-0.20Ti	HR-6	1300ºC/2h	US15	US29	SS-J2
V-4Cr-0.38Zr	HR-7	1000ºC/2h	UT00	UT14	SS-J2
V-4Cr-0.38Zr	HR-7	1300ºC/2h	UT15	UT29	SS-J2
V-4Cr-0.57Ti-0.1C	HR-8	1000ºC/2h	UG00	UG11	SS-J1
V-4Cr-0.50Ti	HR-10	1000ºC/2h	UY00	UY14	SS-J2
V-4Cr-0.50Ti	HR-10	1300ºC/2h	UY15	UY29	SS-J2

Results and Discussion

Table 2 summarizes the results of the electrical resistivity measurements on annealed vanadium alloys and the weld. The resistivity data were corrected to a reference temperature of 20°C using the V-Cr-Ti temperature coefficient for resistivity of $d\rho/dT = 0.75$ nΩ-m/K [1]. The values of electrical resistivity in table 2 are the averages for multiple specimens of each material and heat treatment condition. The standard error of the mean ranged from ±0.6 nΩ-m to ±2.4 nΩ-m for the SS-J1 tensile specimens and ranged from ±0.3 to ±0.9 nΩ-m for the SS-J2 tensile specimens. A large portion of the experimental error in the resistivity measurements was caused by the uncertainties in the gauge section thickness of tensile specimens [1]. It is noted that the standard error of the mean is generally smaller for the SS-J2 specimens than for the SS-J1 specimens. Since the thickness of the SS-J1 specimens is half the thickness of the SS-J2 specimens, the uncertainties in the specimen dimensions in the tensile gauge section of the SS-J1 specimens gave a larger error in the resistivity measurements for the SS-J1 specimens than for the SS-J2 specimens.

Figure 1 compares the electrical resistivity at 20°C for the various classes of vanadium alloys and the weld in annealed condition. The experimental results showed that the resistivity of vanadium alloys increases with increasing Ti solute content. Ti showed a strong effect on the resistivity. In contrast, a nonmonotonic effect was observed for the influence of Cr solute content on the resistivity of vanadium.

Table 2. Results of electrical resistivity measurements.

Alloy	Heat	Final Anneal (ºC)	Electrical Resistivity at 26-27°C (nΩ-m)	Corrected Electrical Resistivity at 20°C (nΩ-m)	No. of Specimens
V-4Cr-4Ti	832665	1000ºC/2h	312.3 ± 1.5	307.1	19
V-4Cr-4Ti	GTA25	1000ºC/2h	314.7 ± 1.6	310.2	6
V-4Cr-4Ti	GTA25	1000ºC/2h +400ºC/2h	307.8 ± 1.7	302.6	6
V-4Cr-4Ti	HR-1	1000ºC/2h	293.5 ± 1.7	289.0	12
V-10Cr-4Ti	HR-2	1000ºC/2h	303.7 ± 1.0	298.5	12
V-15Cr-4Ti	HR-3	1000ºC/2h	298.0 ± 0.4	292.8	15
V-15Cr-4Ti	HR-3	1300ºC/2h	304.9 ± 0.4	299.7	15
V-4Cr-10Ti	HR-4	1000ºC/2h	378.6 ± 1.8	373.4	12
V-4Cr-15Ti	HR-5	1000ºC/2h	443.3 ± 1.7	438.1	12
V-4Cr-4Ti + 100ppmB	HR-11	950ºC/2h	297.7 ± 1.7	293.2	12
V-4Cr-4Ti + 100ppmB	HR-11	1000ºC/2h	296.7 ± 1.4	292.2	12
V-4Cr-4Ti + 100ppmB	HR-11	1300ºC/2h	304.3 ± 2.1	299.8	12
V + 100 ppm B	HR-12	1000ºC/2h	239.3 ± 1.1	234.8	12
V + 100 ppm B	HR-12	1300ºC/2h	252.2 ± 2.4	247.0	12
V-4Cr-4Ti	NIFS-2	1000ºC/2h	297.0 ± 0.9	292.5	18
V-4Cr-0.20Ti	HR-6	1000ºC/2h	239.7 ± 0.6	234.5	15
V-4Cr-0.20Ti	HR-6	1300ºC/2h	243.0 ± 0.3	237.8	15
V-4Cr-0.38Zr	HR-7	1000ºC/2h	228.1 ± 0.4	222.9	15
V-4Cr-0.38Zr	HR-7	1300ºC/2h	232.9 ± 0.4	227.7	15
V-4Cr-0.57Ti-0.1C	HR-8	1000ºC/2h	251.5 ± 0.6	246.3	12
V-4Cr-0.50Ti	HR-10	1000ºC/2h	241.8 ± 0.5	236.6	15
V-4Cr-0.50Ti	HR-10	1300ºC/2h	248.2 ± 0.4	243.0	15

According to the literature [2,3], the specific resistivity (resistivity per atomic percent, nΩ-m/at%) of Ti solute atoms is $\geq$15.5 nΩ-m/at%, and the specific resistivity of Cr solute atoms is 4.0 nΩ-m/at%. Based on Matthiessen's rule, a larger contribution to the resistivity for Ti than for Cr is expected on an atomic percent basis. Zr solute atoms were observed to have a smaller influence on the resistivity compared with Ti. The weld material (GTA25) showed higher resistivity compared to the base V-4Cr-4Ti alloy, as expected. The further annealing treatment at 400ºC for 2 hours on the GTA25 V-4Cr-4Ti decreased its electrical resistivity due to the elimination of hydrogen contamination.

The addition of 100 ppm boron significantly increased the resistivity of unalloyed vanadium (the resistivity of pure vanadium is 196 nΩ-m [1]), but the influence on resistivity of the same amount of boron in V-4Cr-4Ti alloy is trivial. The addition of carbon increased the resistivity of a vanadium alloy. The resistivity of V-4Cr-0.57Ti-0.1C is 10 nΩ-m higher than the resistivity of V-4Cr-0.5Ti. The increase in resistivity due to carbon solute atoms is lower than the reported specific resistivity of 90 nΩ-m/at% [4]. It implies that the matrix concentration of free carbon interstitial solutes is low due to precipitation.

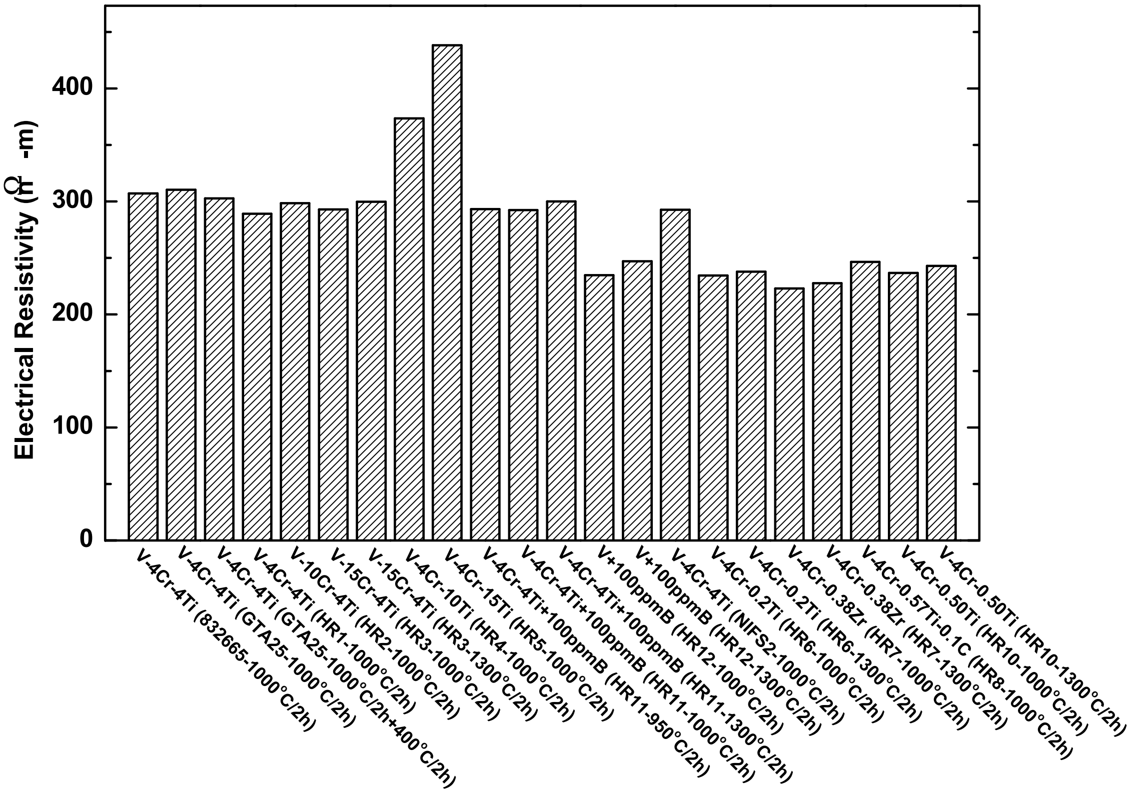

Figure 1. Comparison of the electrical resistivity of various classes of vanadium alloys.

The electrical resistivity results showed a small dependence on the final annealing temperature in the model HR6-8, and HR10-12 alloys. A slight increase of electrical resistivity was observed in all of the specimens annealed at 1300°C for 2 hours compared with the resistivity of the specimens annealed at 1000°C for 2 hours. This is likely attributed to interstitials dissolving back into the matrix during the annealing of the specimens at 1300°C. For V-4Cr-4Ti +100ppmB alloy, the resistivity of the specimens annealed at 950°C is the same as those annealed at 1000°C. The annealing temperature has a stronger effect on the resistivity of unalloyed vanadium (HR12) with 100ppmB. It is interesting to note that the measured resistivity in the V-4Cr-4Ti specimens (heat 832665) was somewhat higher than that measured on the same heat of material in a previous study [1]. The cause of this difference in electrical resistivity is uncertain.

Rererences

[1] S.J. Zinkle, A.N. Gubbi and W.S. Eatherly, Fusion Materials Semiannual Progress Report for Period Ending December 31, 1996, DOE/ER-0313/21, p.15.
[2] E.W. Collings, Phys. Rev. B9 (1970), p.3989.
[3] A. Giannuzzi, H. Tomaschke and K. Schroeder, Philos. Mag., 21(1970), p.479.
[4] J.T. Stanley, J.M. Williams, W.E. Brundage and M.S. Wechsler, Acta Metall., 20(1972), p.191.

Fabrication of Creep Tubing from the US and NIFS Heats of V-4Cr-4Ti

A.F. Rowcliffe, D.T. Hoelzer (Oak Ridge National Laboratory), W.R. Johnson (RSME Services, San Diego), C.Young (Century Tubes Inc, San Diego).

OBJECTIVE

Utilize commercial-scale processing to fabricate small-diameter ,thin-wall tubing from plate stock of V-4Cr-4Ti for both the US program heat no. 832665 and the NIFS-HEAT-2 and produce sufficient tubing to meet programmatic needs for investigating creep behavior in both lithium and vacuum environments and for carrying out irradiation creep measurements.

SUMMARY

The first batch of commercially-fabricated creep tubing from the US program heat of V-4Cr-4Ti has been used for the on-going program of creep measurements in vacuum and Li environments and also for irradiation creep measurements both in ATR and in HFIR. This tubing (Batch A) had a fairly high frequency of surface cracking both at the ID and OD surfaces and both carbon and oxygen concentrations increased significantly during tube processing. Recently a second tubing campaign was undertaken (Batch B) to produce sufficient tubing to continue creep studies within both the US and Japanese programs. To overcome the shortcomings of Batch A tubing, modifications were made to the procedure including changes to the drawing schedule to reduce drawing stresses and changes to the cleaning procedures to reduce carbon pick-up. During the processing of Batch A, intermediate anneals at 1000ºC were carried out under vacuum conditions in the 10^{-4} torr range. For Batch B, vacuum conditions of < $2x10^{-5}$ torr were specified and a different vendor selected.

In spite of these improvements, the rate of oxygen pick-up was higher during Batch B processing by a factor of 3-4. Because of the dependence of oxygen concentration on the surface area; volume ratio, the oxygen content of the tubing doubled during the final 2 anneals to reach 1745 wppm for the US heat and 1645 wppm for the NIFS heat. To reduce oxygen concentrations to more acceptable levels, a double heat treatment in liquid Li at 800ºC and 1000ºC was devised which lowered oxygen levels to below 750 wppm and simultaneously produced a uniform grain size distribution with 12-15 grains across the tubing wall for both heats. A sufficient number of creep tubes were prepared in this way for the RB-17J irradiation experiment in HFIR. Further experiments were carried out to determine the origins of the enhanced pick-up of oxygen in Batch B. Processing variables investigated included a) differences in furnace geometry, leak rate and vacuum measurement between the two vendors, b) differences in gettering procedure and c) differences in the rate of attack during the acid cleaning procedure.

Our preliminary conclusions are that although the above processing variables have some significance, the primary cause of the enhanced rate of oxygen pick-up is related to changes in the mechanism of oxidation of the V-4Cr-4Ti alloy with changes in the partial pressure of oxygen during the annealing treatment. The evidence suggests that under poor vacuum conditions (Batch A) the uptake of oxygen is slowed by the formation of a temporarily protective oxide film. Under improved vacuum conditions (Batch B) the protective oxide film does not form and the oxygen concentration increase more rapidly. It is probable that during Batch A processing conditions, a major fraction of the oxygen in the form of a visible oxide film, was removed each time the tubing was acid cleaned. Further investigation of these factors is proceeding with the object of defining a set of conditions under which a further batch of tubing could be fabricated with minimal oxygen pick-up.

PROGRESS AND STATUS

Introduction

The pressurized tube creep specimen measures 25.4mm long with a 4.57mm outside diameter and a wall thickness of 0.25mm. In 1995, Argonne National Laboratory coordinated a campaign to fabricate ~6 meters of tubing from the US program heat No.832665 with Century Tubes Inc. of San Diego as the primary sub-contractor [1]. This effort met with mixed success with a large fraction of the tubing developing cracks on both the inside and outside surfaces. These cracks were frequently linked together through the wall thickness via a band of severe macroscopic deformation. Since they were long enough to be visible to the naked eye, it was possible to select relatively sound segments of tubing to prepare a sufficient number of creep specimens to meet short term needs. This tubing was used for an initial series of testing both in vacuum and in lithium environments [2] and was also used to develop irradiation creep data in experiments conducted in the ATR [1] and in the HFIR [3]. However it was not possible to eliminate all defects by visual inspection, and it has been suggested that defects in the tube wall could be responsible for inconsistencies in the measured strains to failure. Thus an important goal for this tubing campaign was the elimination of surface cracking. In addition to the cracking problems it was also found that the levels of interstitials increased significantly during processing with carbon increasing from 80 to 300 wppm, oxygen increasing from 310 to 700 wppm and nitrogen increasing slightly from 85 to 95 wppm. The increase in oxygen was of particular concern since creep rate is sensitive to oxygen concentrations in this range and in general the analysis of creep behavior is complicated by the removal of oxygen during testing in Li and the pick–up of oxygen during ultra-high vacuum creep testing. The goal adopted for the new creep tube fabrication campaign was to maintain oxygen levels in the 300-400 wppm range so that at least the initial oxygen level would be similar to that for the other mechanical property specimens fabricated from plate-stock of V-4Cr-4Ti.

Two small heats of V-4Cr-4Ti with low levels of interstitials have been produced in Japan under the direction of the National Institute for Fusion Sciences (NIFS).A small quantity of creep tuning was prepared from the NIFS-HEAT-2 material using a three-directional rolling process [4]. Less severe problems were encountered with interstitial pick-up and the development of surface defects. Based upon the experience gained from processing the US heat into tubing (Batch A) and the experience gained from processing the NIFS heat, a new procedure was developed which was designed to minimize interstitial pick-up, improve initial surface quality and reduce the probability of surface cracking by lowering stress levels in the final drawing stages. These changes and the rationale behind them were detailed in the previous semi-annual progress report [5] which also described the status of the Batch B, US and NIFS tubing after 7 drawing and 8 annealing cycles. The present report documents the remaining steps to the completion of the campaign and describes the results of intermittent interstitial analyses and metallographic examination and an assessment of the quality of the final creep tubing.

BATCH B REVISED PROCEDURE

The complete drawing and annealing schedule for the Batch B tubing from both the US and NIFS heats is shown in Table 1; the drawing schedule for the earlier Batch A tubing from the US heat is shown in Table 2. To overcome the problems of surface cracking encountered with Batch A and to minimize oxygen pick-up, a number of changes were made to the Batch A procedure [4], which may be summarized as follows;

a) The intermediate heat treatments for Batch A were carried out by a commercial vendor (Certified Metalcraft) using a tube furnace with a reported vacuum in the 10^{-4} torr. range. For Batch B a minimum vacuum of 2x 10^{-5} torr was specified and the heat treatments carried out by a different vendor (Bodycote) using a large volume oven furnace capable of operating in the 10^{-6} torr range.

b) It was conjectured that the cracking problems encountered in Batch A resulted from a combination of high surface oxygen levels picked up during the annealing cycle and high stresses imposed by the large reductions in area, (> 40% per cycle), specified in the drawing schedule. For Batch B therefore it was specified that the reduction in area (R/A) per cycle should not exceed ~30%. for the last 6 drawing cycles.

c) A more rigorous cleaning operation involving successive treatments in Alconox, acetone and alcohol was introduced as a more effective mean of removing die lubricant prior to annealing. A less aggressive acid cleaning procedure was introduced consisting of a 30sec treatment with 20% HNO_3+10% HF +70%H_20 compared with the Batch A treatment of 5min with 20% HNO_3 +20%HF +60%H_20.

The twin requirements of reducing drawing stresses and reducing the rate of oxygen pick-up are somewhat in conflict since reducing the reductions per draw means an increase in the number of draw cycles and hence an increase in the number of anneals. Thus in Batch A the final size was achieved with a total of 10 anneals at 1000ºC for 1 hour whereas the modified procedure for Batch B necessitated a total of 13 anneals .However it was reasoned that the additional 3 hours at temperature would not result in higher oxygen levels since the specified vacuum was an order of magnitude better than that used during the processing of Batch A.

Table 1. Drawing schedule for Batch B tubing of US and NIFS heats.

Cycle No.	**OD (ins)**	**ID (ins)**	**Wall (ins)**	**RA/Cycle %**	**Anneal No.**
Tube blank	1.010	0.626	0.192		**1**
1	0.940	0.600	0.170	17.3	2
2	0.818	0.542	0.138	30.4	3
3	0.723	0.499	0.112	31.3	4
4	0.588	0.420	0.084	44.4	5
5	0.495	0.375	0.060	44.7	6
6	0.395	0.299	0.048	42.5	7
7	0.318	0.240	0.039	39.0	8
8	0.288	0.224	0.032	29.2	9
9	0.262	0.212	0.025	29.0	10
10	0.246	0.208	0.019	30.2	11
11	0.229	0.199	0.015	31.0	12
12	0.203	0.179	0.012	32.0	13
13	0.188	0.168	0.010	21.0	
Sizing	0.180	0.160	0.010	5.5	
				Final 26.5%	

Table 2. Drawing schedule for Batch A tubing of US heat.

Cycle No.	**OD (ins)**	**ID (ins)**	**Wall (ins)**	**RA/Cycle %**	**Anneal No.**
Tube blank	1.100	0.770	0.165		1
1	0.981	0.750	0.177	40.6	2
2	0.920	0.750	0.085	33.3	3
3	0.863	0.750	0.057	41.1	4
4	0.830	0.750	0.040	34.4	5
5	0.755	0.700	0.029	37.6	6
6	0.688	0.650	0.020	41.5	7
7	0.606	0.580	0.015	41.1	8
8	0.520	0.500	0.010	45.9	9
9	0.288	0.264	0.012	40.0	10
10	0.178	0.157	0.011	45.4	

CHARACTERIZATION OF BATCH B TUBING

INTERSTITIAL PICK-UP

Archive samples for chemical analysis and metallography were removed after each draw and after each vacuum anneal. During this study several anomalously high values for both oxygen and carbon were encountered and it was shown that these were due to contamination during sectioning and cleaning to prepare the analysis sample. Using careful cutting and cleaning procedures and multiple samples it was determined that the overall uncertainty in determining oxygen was of the order of +/- 15%. The interstitial analysis data for both heats is shown in Table 3.

Table 3. Chemical analysis (wppm) for Batch B tubing

Anneal No.	**Wall (mm)**	**U.S. Heat**			**NIFS Heat**		
		C	**O**	**N**	**C**	**O**	**N**
BLANK	4.87	119	331	88	59	130	156
1	4.87	134	346	93	63	152	132
2	4.32						
3	3.50						
4	2.85						
5	2.13	169	403	92	85	219	140
6	1.52	119	511	94			
7	1.22	155	494	101	90	378	148
8	0.99	179	637				
9	0.81						
10	0.64				223	741	210
11	0.48	264	994	133	253	879	206
12	0.38						
13	0.31	457	1745	170	390	1675	211

In the previous semi-annual report [4], data were available up to the eighth anneal for the US heat and the seventh anneal for the NIFS heat. At this stage the oxygen content had approximately doubled for both heats and with 5-6 more stages to be completed, these increases in oxygen were of concern. Accordingly, one half of the tubing from both heats was put on hold following the eighth anneal. After carefully checking the cleaning and Ta tenting procedures and ensuring that the vacuum was maintained at better than $2x10^{-5}$ torr while at temperature, processing to final size was completed on the other half of both heats.

In spite of these precautions, the rate of pick-up of oxygen accelerated rapidly in the final cycles. During the final two anneals, the oxygen content of both heats approximately doubled to reach 1745 wppm for the US heat and 1675 wppm for the NIFS heat. Significant increases also occurred in both the nitrogen and carbon concentrations of both heats. Thus in spite of the efforts to improve the fabrication procedures, the final oxygen content of the Batch B tubing was more than double that of the earlier Batch A tubing; carbon and nitrogen levels were also elevated above those for Batch A (C- 300wppm; N-95wppm) but not as dramatically.

For a given set of vacuum conditions, exposure time and temperature, the quantity of oxygen adsorbed depends on specimen geometry and is proportional to the surface area:volume ratio. The surface area:volume ratio (SAV) of the tubing is plotted for each annealing cycle in Figs.1and 2.(For a cylindrical tube the SAV is equal to 2/t where t is the wall thickness). The oxygen analysis data is also plotted for each stage. A curve having approximately the same shape as the SAV curve has been drawn through the oxygen analysis data. The rapid acceleration in the oxygen concentration reflects the rapid increase in SAV during the final 4-5 stages of the drawing schedule.

SURFACE DEFECTS

At the end of the fifth drawing cycle several longitudinal surface defects were observed on the OD of the US heat tubing which at this stage had a wall thickness of 1.5mm. The original plate material was characterized by a banded microstructure with arrays of Ti(CON) particles associated with regions of finer

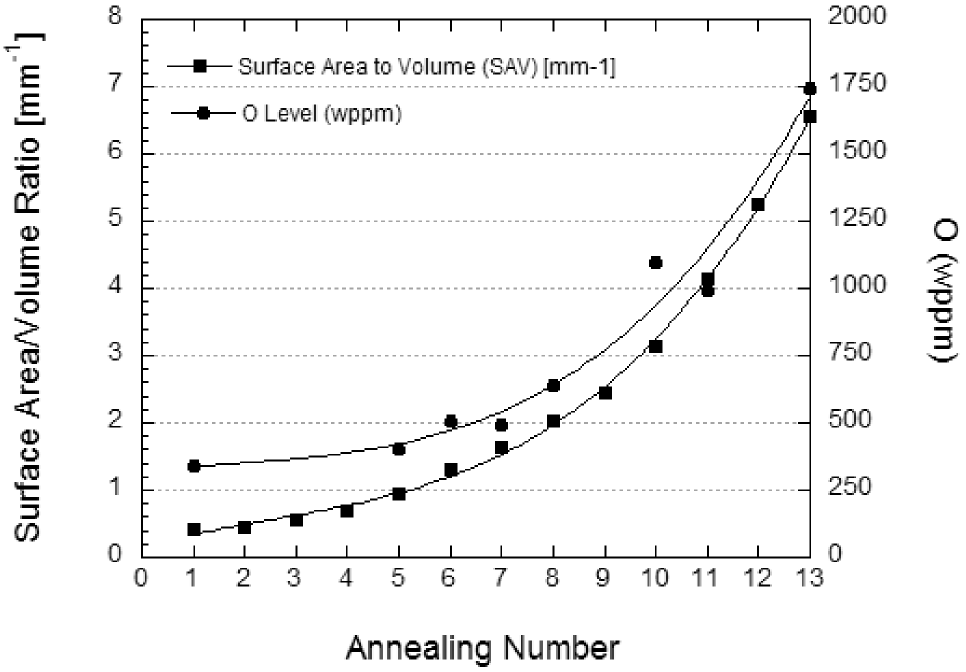

Figure 1. SAV ratio and O concentration versus annealing cycle for Batch B (U.S. Heat).

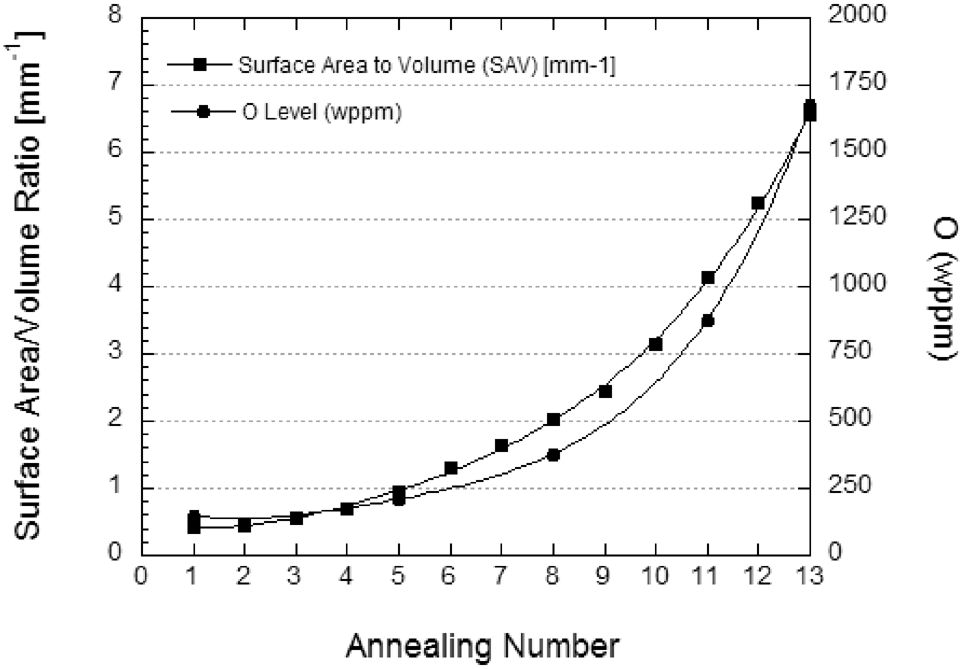

Figure 2. SAV ratio and O concentration versus annealing cycle for Batch B tubing (NIFS Heat).

gains where grain growth was impeded by the particles.[5]. At the outset it was recognized that the development of the cracks which penetrated from both surfaces in the Batch A tubing [4] was possibly related to regions of severe microstructural inhomogeneity in the original plate. A mechanism based on the rotation of bands of particles and their intersection with the surface during successive drawing stages has been suggested to explain the cracking observed in the NIFS tubing prepared in Japan [6]. Accordingly, during the processing of Batch B one of the LT surfaces of the original plate was designated as the top surface (zero degrees) and the corresponding position was tracked during tube drawing so that the appearance of surface defects could be related to the orientation of the bands in the original plate.

At the end of the fifth drawing cycle several longitudinal surface defects were detected visually on the OD of the tubing from the US heat . The defects occurred parallel to the drawing direction at a location of 90 degrees to the original top surface of the plate. Each defect appeared to be a shallow region approximately 1-2 mm long which had separated from the tube surface. Following the sixth draw cycle the tube from the US heat was cut into 2 sections with the region containing the defects confined to a localized region of one tube (Tube A, 177 cm long) while the other tube (TubeA1, 127 cm long) appeared to be defect-free. The development of these defects at a stage where very little oxygen pick-up had occurred (total oxygen 403wppm), and their localization in one section of the tubing strongly suggests that they are related to a macroscopic inhomogeneity in the original cold–rolled plate rather than developing from a loss of near–surface ductility due to oxygen pick-up. Defects of this type were not observed in the NIFS heat tubing at this stage of the drawing.

As noted above, one half of the tubing was put on hold because of concerns regarding the extent of oxygen pick-up. Tube A1 was held back and processing continued with Tube A, a portion of which contained the visible defects. After the eighth draw cycle tube A was again cut into two sections and the section containing the visible defects was designated Tube A2. After further sub-division into sections, A2 and A4, section A2 which contained multiple visible defects developed extensive longitudinal cracks during the eleventh draw cycle and processing was discontinued. The remaining sections continued through to the final draw to 4.57 mm OD and 0.254 mm wall thickness. For the US heat, three of the final tubes (A, AA, and A3, total length ~385 cm), contained very few visible surface defects. The fourth tube (A4, total length ~200 cm) contained approximately 30 visible defects irregularly spaced along one side of the tube.

Thus Batch B at this stage, delivered sufficient length of sound tubing for ~150 creep tubes with a further 200 cm (Tube A4) which could be used by judiciously avoiding regions containing visible defects. Similarly with the NIFS heat, ~100 cm of tubing (Tube B1) was put on hold after the eighth anneal because of concerns with oxygen pick-up. The other half of the tubing (Tube B) was processed satisfactorily without any signs of surface defects until during the final draw (No.13) when one section (B2, 138 cm long), developed longitudinal cracks which linked together and produced significant splitting; processing of this section was discontinued. A total length of ~370 cm of final tubing virtually free from visible defects was produced from the NIFS heat during Batch B processing.

MICROSTRUCTURE

During the early stages of processing the recrystallized microstructures were uniform across the wall thickness and consisted of well-developed equi-axed grains; Fig. 3 shows the microstructure following the fifth anneal. The microstructure of the NIFS heat was uniform with an average grain size of ~50 microns. The US heat contained a much higher fraction of small grains (5- 10 microns) with an overall average grain size of ~ 28 microns. These grain size differences are probably related to the differences in oxygen concentration, which at this stage is 400 wppm for the US heat and 220 wppm for the NIFS heat, and also differences in the number density and distribution of Ti (CON) particles in the starting plate materials. As noted previously [4], there was clear evidence at this stage that the original bands of Ti(CON) particles become strongly curved, particularly near the OD wall, as the grains rotate to accommodate the deformation as the material is drawn through the die.

As the drawing schedule progressed, the recrystallized microstructures reflected the increasing concentration of interstitials, particularly oxygen. A near surface zone developed which etched very differently and was characterized by very fine irregularly shaped grains. After the tenth anneal the oxygen concentrations had increased to ~950 and ~741 wppm in the US and NIFS heats respectively and the

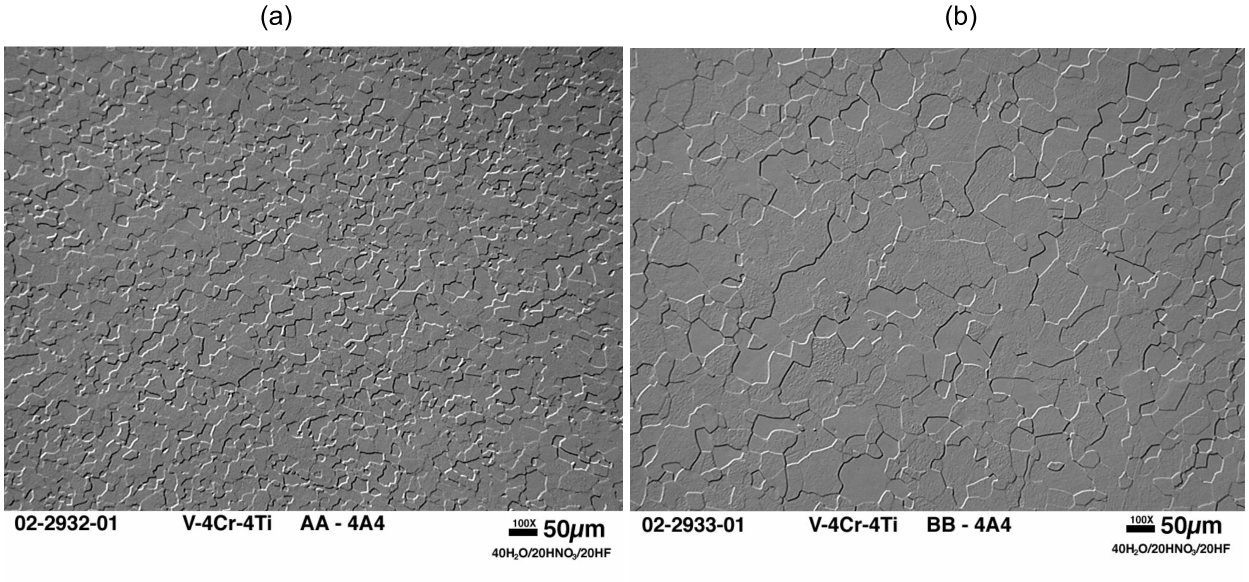

Figure 3. Optical micrographs of the Batch B tubes of the (a) US Heat and (b) NIFS Heat after the fifth anneal.

surface zones were 40-50 microns in depth Fig. 4. In some areas, primarily in the US heat, small cracks penetrated from the surface and were arrested at the edge of the zone. At this stage the average grain sizes in the central areas of the wall were ~62 and ~29 microns for the US and NIFS heats respectively. During the eleventh anneal the oxygen concentrations increase to ~1150 wppm (US) and ~880 wppm (NIFS) and the surface–affected layers increased to 60-80 microns deep at the OD surface and 40-50microns deep at the ID. The interior microstructures however were still similar to the microstructures after the fifth anneal, with the NIFS heat still having a factor of ~2 larger grain size. After the thirteenth anneal at Bodycote, the tubes were given a draw of 25.6% R/A to reach final size. During the thirteenth anneal, oxygen concentrations increased to 1770 wppm and 1675 wppm in the US and NIFS heats respectively. The microstructures resulting from a subsequent anneal at ORNL of 2 hours at 1000ºC in a vacuum of 10^{-6} torr are shown in Fig. 5. The tubing from both heats are similar with very irregular inhomogeneous grain structures suggesting extensive grain boundary pinning during recrystallization, and surface zones characterized by very fine grains extending 60-70 microns in from the OD surface and about 30-40 microns in from the ID. In spite of the very high oxygen concentrations, there was no generalized surface cracking.

To obtain more detailed information on the nature of the oxidation process and in particular the partitioning of oxygen between the matrix and the Ti(CON) particles, tubing cross-sections were examined using a Scanning-Auger system (PHI 680). Details of the surface zone in the US heat tubing following the tenth anneal (950 wppm oxygen) are shown in the scanning images of Fig. 6. Within the zone, grain growth is severely limited by the high number density of Ti(CON) particles with sizes in the range 0.1-0.5 microns. A detailed analysis of the composition of the particles, the partitioning of oxygen between the matrix and the particles and a discussion of the mechanisms of oxidation and will be reported later. However the preliminary findings indicate that a process of internal oxidation occurs with oxygen combining with Ti to form new particles of the globular form of Ti(CON) with possibly growth of the pre-existing Ti(CON)s also occurring. The number density of particles increases towards the surfaces, with most of the oxygen being associated with the Ti(CON) particles. There are no significant difference between the oxygen concentration in the matrix regions located near the center of the tube wall and the matrix regions near the surfaces.

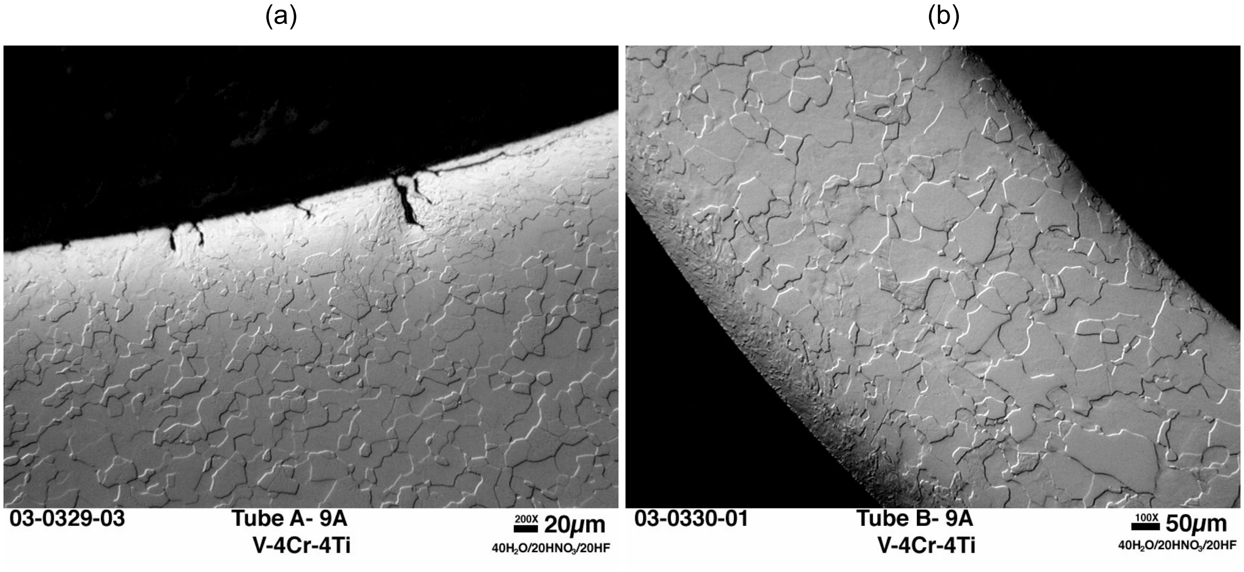
(a)

(b)

Figure 4. Optical micrographs of the Batch B tubes of the (a) US Heat and (b) NIFS Heat after the tenth anneal.

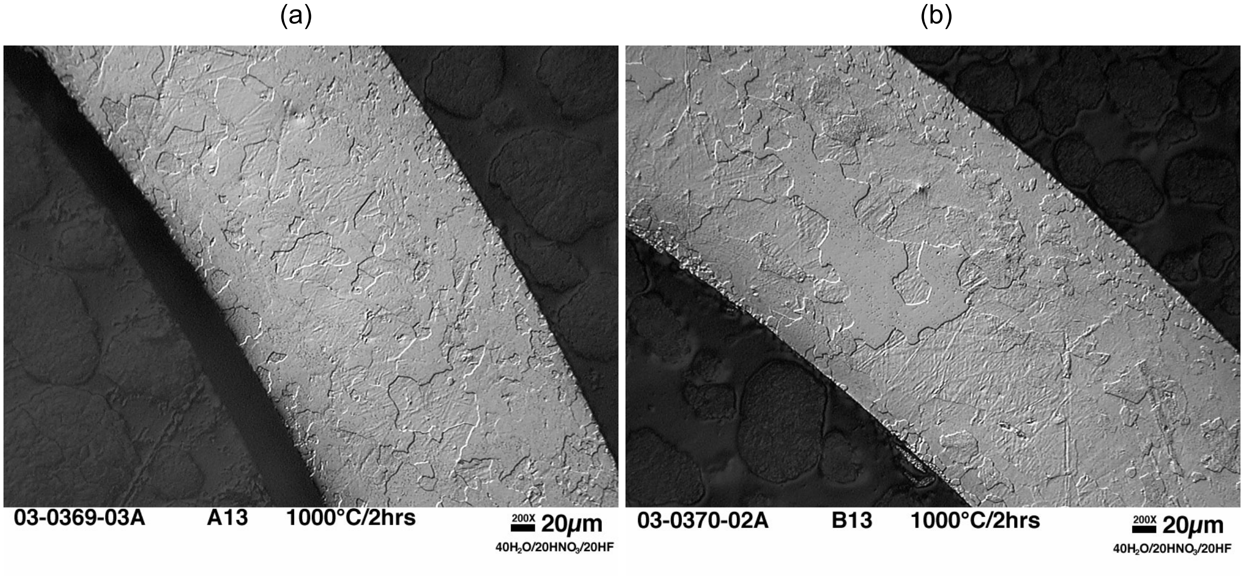
(a)

(b)

Figure 5. Optical micrographs of the Batch B tubes of the (a) US Heat and (b) NIFS Heat after annealing in vacuum for 2 hr at 1000ºC.

OXYGEN REMOVAL

The high overall oxygen content and inhomogeneous grain structure of the finished tubing made it unacceptable for the fabrication of irradiation creep specimens and it was decided to reduce the oxygen content by exposing non-pressurized creep specimens to Li, at 800ºC -1000°C, in a closed retort system. Previous experience with creep testing the Batch A tubing in molten Li at 800ºC had shown that the kinetics of oxygen transport were sufficiently high to make this a viable approach to lowering the oxygen levels of the Batch B tubing down to the 700 wppm level of the Batch A tubing. A series of different heat

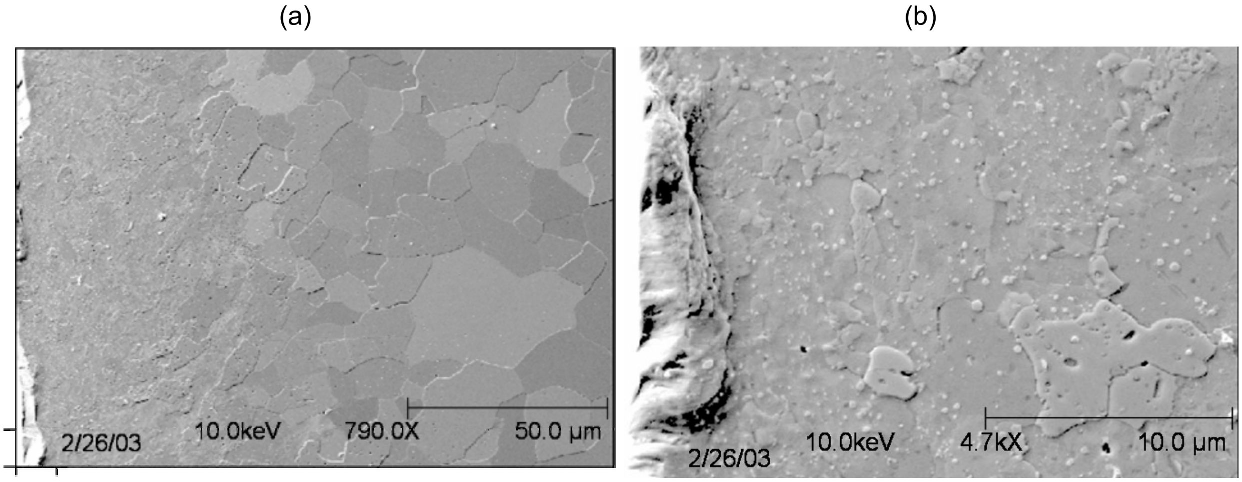

Figure 6. SEM micrographs showing (a) the changes in grain size from surface to the interior of the tube wall and (b) the increase in number density of TiCON particles near the surgace region of the Batch B tube (US Heat) after the tenth anneal.

treatments were carried out to accomplish the twin goals of lowering the oxygen concentration and developing a homogeneous recrystallized microstructure with a minimum of 10-12 grains across the tube wall. A summary of the interstitial concentrations following various heat treatments is shown in Fig. 7.

During the initial treatment of one week in Li at 800ºC, the oxygen concentration of the US heat tubing was reduced from 1745 wppm to 1060 wppm, confirming the viability of this approach to achieving acceptable oxygen levels. At this temperature, recrystallization does not occur and recovery may be strongly impeded by the high density of particles and elevated matrix oxygen levels, Fig. 8. The hardness decreased from the as-drawn value of 213 DPH down to 164 DPH, substantially higher than a fully recrystallized value of ~ 140 DPH.

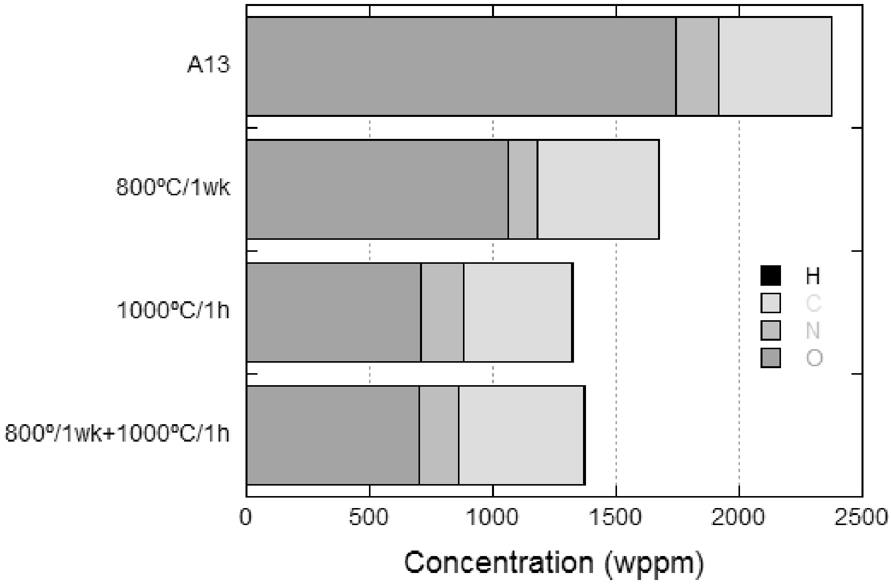

Figure 7. Interstitial concentrations measured in the Batch B tube (US Heat) following various conditions of exposure to molten Li.

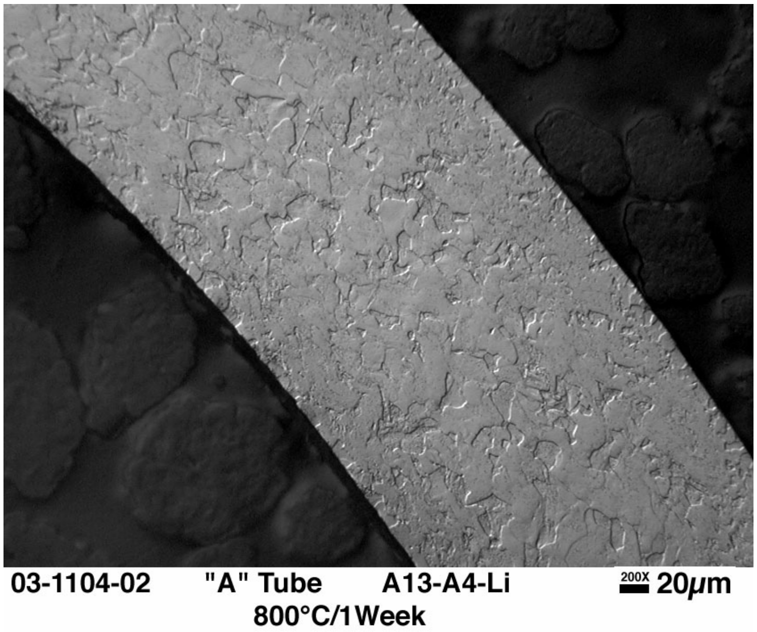

Figure 8. Optical micrograph of the Batch B tube(US Heat) after exposing in molten Li for 1 week at 800ºC.

The Li temperature was increased to 1000ºC to induce full recrystallization and it was found that a one hour treatment at 1000ºC reduced oxygen to acceptable levels for both heats, (710 wppm for the US heat and 572 wppm for the NIFS heat). Although recrystallization did occur, the grain size distribution was not uniform across the tube wall, Fig. 9. In the US heat, a zone of smaller grains extended some 50-60 microns in from the OD surface and 15-25 microns in from the ID surface. A possible explanation for this microstructure is that the nucleation and growth of new grains is strongly influenced by the size and

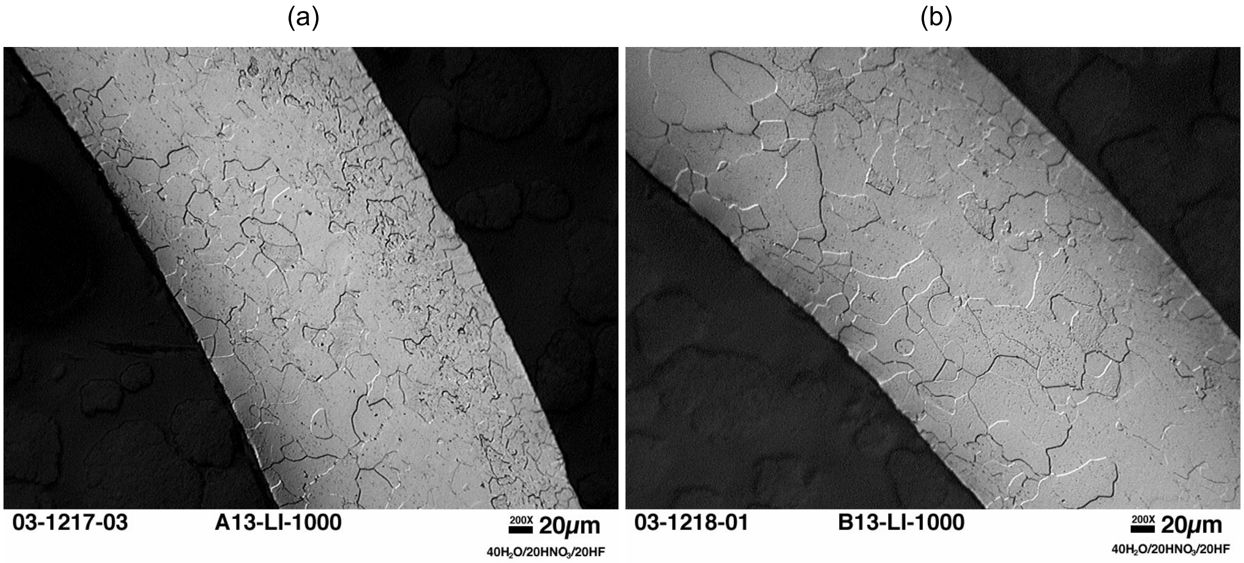
(a) (b)

Figure 9. Optical micrographs of the Batch B tubes of the (a) US Heat and (b) NIFS Heat after exposing in molten Li for 1 hr at 1000ºC.

number density of Ti(CON)s and that nucleation of new grains occurred rapidly before significant dissolution of the Ti(CON)s had take place. Based on these observations it was decided to combine the two Li exposure treatments and to allow Ti(CON) dissolution and oxygen transfer to the Li to occur at 800ºC before raising the temperature and recrystallizing at 1000ºC.

The double heat treatment of one week at 800ºC followed by one hour at 1000ºC lowered the oxygen concentrations to 700 wppm for the US heat, (analysis for the NIFS heat was not available at the time of writing but is expected to be of the same order). The levels of carbon and nitrogen were virtually unchanged by the exposures to Li. For both heats the double Li treatment resulted in a fully recrystallized microstructure with a fairly uniform grain distribution and approximately 12-15 grains across the tube wall. Apparently a sufficiently high level of stored energy is retained during the 800ºC exposure to drive recrystallization in the subsequent treatment at 1000ºC. The dissolution of the Ti(CON) particles occurs to such an extent that grain growth is fairly uniform across the tube wall and the surface zone of fine grains is eliminated, Fig. 10. A detailed description of the final preparation of pressurized creep tubes including final dimensions, fill pressures, and profilometry measurements will be reported later.

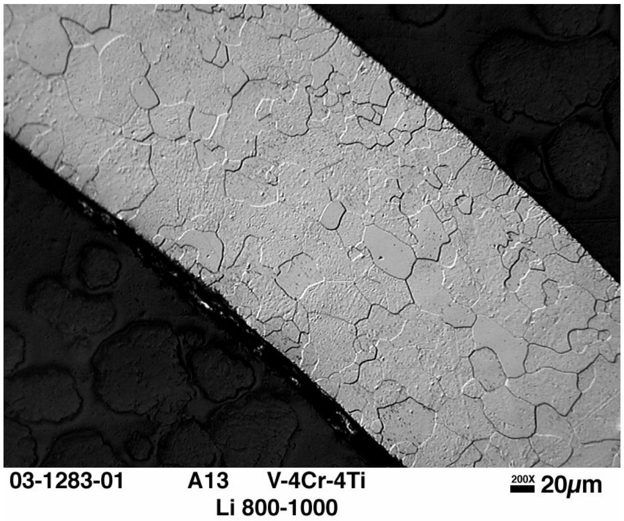

Figure 10. Optical micrograph of the Batch B tube (US Heat) after exposing to molten Li for 1 week at 800ºC followed by 1 hr at 1000ºC.

DISCUSSION OF OXIDATION BEHAVIOR

During the Batch B fabrication campaign, both the US and the NIFS heat tubing experienced increases in total oxygen concentration that far exceeded the increase that occurred during the fabrication of the Batch A tubing from the US heat (Table 4). The magnitude of the oxygen increase was totally unexpected since examination of the processing records from Certified Metalcraft (CM) for Batch A revealed that the intermediate anneals had been carried out with reported vacuum levels in the 10^{-4} torr range. For Batch B the vacuum specification was raised to >2 x 10^{-5} torr and the records from Bodycote (BC) show that the measured vacuum levels ranged from 1.2 x 10^{-6} to 2.0 x 10^{-5} torr.

Table 4. Increase in interstitial concentrations (wppm)

Campaign	**C**	**O**	**N**
US BATCH A	220	390	10
US BATCH B	338	1414	82
NIFS BATCH B	331	1545	55
NIFS (JAPAN)	70	208	24

The increase in oxygen concentration during each one hour anneal at 1000ºC is directly proportional to the impingement rate of oxygen atoms at the tube surface and to the SAV ratio of the tubing. The oxidation behavior of the two batches may be conveniently compared by plotting the incremental oxygen increase versus the SAV ratio for each anneal cycle. Although chemical analyses have not been completed on every archive sample taken, the increase in oxygen concentration for each stage can be estimated for Batch B from the smooth curve drawn through the chemical analysis data shown in Figs. 1 and 2. The oxygen increase data are tabulated in Table 5 together with the vacuum conditions reported by the vendor and plotted in Fig. 11. Deviations from proportionality occur because the vacuum conditions and hence the impingement rate of oxygen atoms vary from one anneal to the next; the error bars reflect the uncertainty in oxygen analysis.

Table 5: Estimated oxygen pick-up data for Batch B

Anneal No.	**Wall (mm)**	**SAV (mm^{-1})**	**O Content (wppm)**	**O Increase (wppm)**	**Vacuum (10^{-6} torr)**
4	2.85	0.70	375	20	5.1
5	2.13	0.94	400	25	4.0
6	1.52	1.3	450	50	2.6
7	1.22	1.6	525	75	2.8
8	0.99	2.0	625	100	1.2
9	0.81	2.5	760	135	3.8
10	0.64	3.2	950	190	7.2
11	0.48	4.1	1170	220	10.1
12	0.38	5.3	1425	255	12.1
13	0.31	6.6	1745	320	10.3

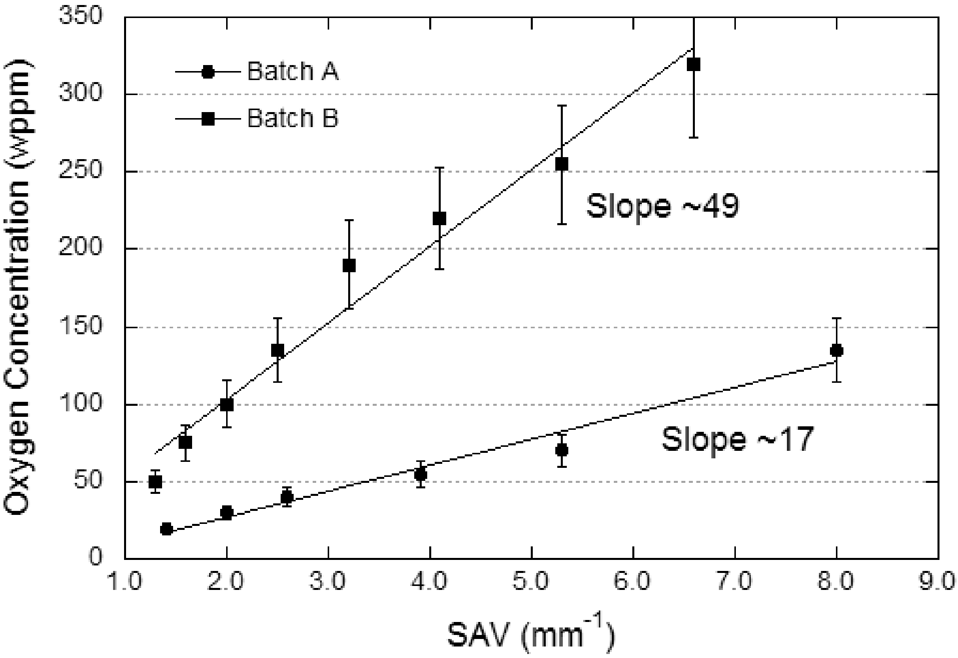

Figure 11. Linear curve fit to data. Error bars are 15% of the calculated value.

The only oxygen data available for Batch A are the initial and final analyses. The SAV ratios for the 10 cycles are plotted in Fig. 12 (The SAV ratio decreased during draw 9 which was a sinking operation to increase the final wall thickness). Superimposing the initial and final oxygen concentrations on a curve

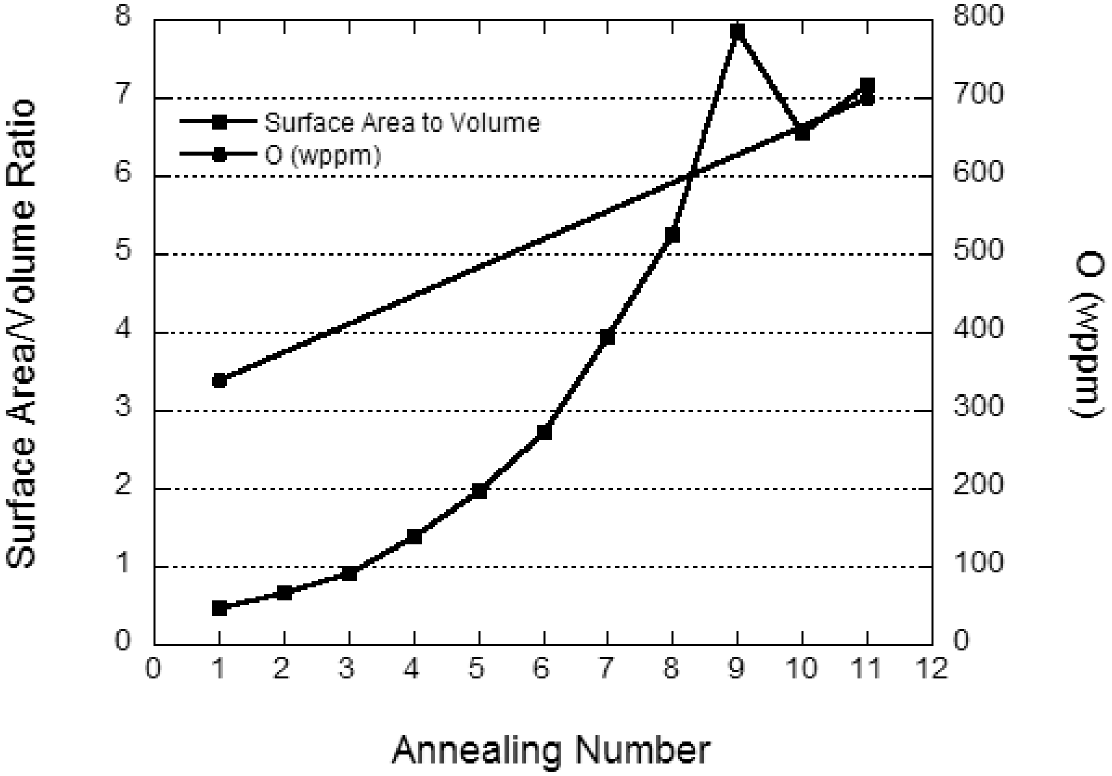

Figure 12. SAV ratio and O concentration versus annealing cycle for Batch A tubing (US Heat).

with the same shape as the SAV ratio curve allows us to estimate the incremental oxygen increase for each anneal; these incremental values are shown on Table 6 and plotted versus SAV ratio in Fig. 10. A comparison of the slopes of the two lines in Fig. 10 indicates that the increase in oxygen concentration for a given SAV ratio was a factor of 3-4 lower during the processing of Batch A than it was during the processing of Batch B.

Table 6 : Estimated oxygen pick-up data for Batch A

Anneal No.	Wall (mm)	SAV (mm^{-1})	O Content (wppm)	O Increase (wppm)
3	2.16	0.93	330	
4	1.45	1.4	350	20
5	1.02	2.0	380	30
6	0.77	2.6	420	40
7	0.51	3.9	475	55
8	0.38	5.3	545	70
9	0.25	8.0	680	135

The procedures followed together with the recorded heat treatment data from the two vendors were examined in an attempt to identify the origins of the factor of 3-4 difference in oxygen pick-up between the two batches. At least experimental 3 factors could be contributing the higher oxygen pick-up rates for Batch B, namely, a) differences in furnace geometry, vacuum measurement techniques and furnace leak rates, b) differences in gettering methods and c) differences in the rate of attack and removal of surface layers during chemical cleaning.

The intermediate heat treatments for Batch A were carried out in a horizontal tube furnace ~60 cm in diameter with a volume of ~170 liters. On the other hand the Batch B heat treatments were carried out in a furnace measuring ~150 cm in diameter with a volume of ~2760 liters. The internal surface area of the BC furnace is a factor of x50 greater than that of the CM furnace. The large volume and surface area of the BC furnace coupled with a high pumping rate and a high leak rate could possibly result in higher partial pressures of oxygen and water vapor than indicated by the ion gauge readings. However information on leak rates is not available from either of the vendors. For the Batch B processing, Ta foil was substituted for the Ti wrap used during Batch A processing because of problems associated with the diffusion bonding of the Ti foil to the tube surface. Although Ti is somewhat more effective getter than Ta, it was considered that the difference was not sufficiently great to off-set the order-of–magnitude better vacuum measured in the BC furnace. During the Batch A processing the same Ti tent was used throughout whereas for Batch B, fresh Ta foil was used for each anneal.

For the Batch A processing, the acid cleaning stage immediately prior to vacuum heat treatment consisted of 5 minutes in a $30HNO_3$-$10HF$-$60H_2O$ solution; the original solution was used unchanged for the complete processing. For Batch B, because of concerns regarding pitting or grain boundary attack, the acid cleaning time was reduced to 30 seconds and the solution changed to $30HNO_3$-$20HF$-$50H_2O$: again, the same solution was unchanged for all the cleaning stages. Because of the longer exposure time it is likely that surface layer removal by chemical etching after each draw cycle was greater during Batch A. However it is difficult to assess whether the rate of dissolution was aggressive enough to remove a sufficient depth of oxidized material to explain the measured differences in oxygen pick-up for the two batches. Tests carried out at ORNL with the latter solution indicate that a 3 minute immersion removes ~0.0005 in.

MODIFIED FABRICATION PROCEDURE; BATCH C

In an effort to produce a batch of tubing with a lower final oxygen concentration, the procedure used for Batch B was modified in several respects with the objective of lowering the oxygen pick-up rate by a factor of (3-4). Tube A1, which had been held back following anneal No. 8 was used as the starting material with the tube dimensions being 8.08mm OD with a 0.99mm wall and the oxygen concentration at 637wppm. Following a draw cycle of ~30% R/A, the tube was put through a sanding process to remove approximately 0.025 mm from the outside surface followed by the normal de-greasing operation and an extended chemical cleaning in the HNO_3/HF solution for 5 minutes. This resulted in a wall thickness of 0.71 mm (0.028 in) Chemical analysis at this stage showed that these surface treatments were effective in reducing the overall oxygen concentration from 637 wppm to 497 wppm. This tubing was then tented with an inner layer of fresh Ta foil and an outer layer of fresh Ti foil and annealed in the BTH furnace. The time at temperature was reduced from 1 hour to 30 minutes. To provide an additional measurement of the oxidation rate, a sample of the US heat in the form of a 0.5 mm thick sheet (S40) with an initial oxygen content of 366 wppm was also placed inside the Ta/Ti tent. The chemical analysis data from these operations are shown in Table 7.

Table7: Chemical analysis data for Batch C

Condition	I.D.	C (wppm)	O (wppm)	N (wppm)	O Change
Annealed Tube	A1	179	637	101	
30% RA; Sand/acid clean	C1	171	497	98	(140)
1000ºC 30 min	C1-A	175	594	150	97
30%CW sheet	S40	135	366	97	
1000ºC 30 min	S40-1	140	450	186	84

To assess the effectiveness of reducing the anneal time and introducing Ti in addition to the Ta wrap, the changes in oxygen content must be compared at the same thickness (SAV ratio). The increases in oxygen that occurred during the processing of Batch A and Batch B at the same SAV ratio as the Tube C1 sample were obtained from Figs. (q) and (s) and summarized in Table 8.

Table 8: Comparison of O pick-up for Batches B and C

I.D.	**Thickness (mm)**	**SAV (mm$^{-1)}$**	**O Increase (wppm)**	**Anneal Time (min)**	**Getter**
C1-A	0.71	2.8	97	30	Ta + Ti
Batch B	0.71	2.8	145	60	Ta
Batch A	0.71	2.8	42	60	Ti

The combination of reduced time at temperature and adding Ti as a getter reduced the oxygen pick-up at a tube wall thickness of 0.71 mm from 145 to 97 wppm.. The experimental uncertainty in measuring change in oxygen concentration is approximately +/- 25 wppm. This magnitude of change in oxygen pick-up could be entirely accounted for by the factor of two reduction in annealing time and it is evident that the addition of a Ti getter has a minimal effect under the conditions pertaining to the BHT furnace. It is concluded that the use of the Ti getter during Batch A processing was not responsible for the observed lower oxygen pick-up rates. This experiment therefore indicated that the lower oxygen pick-up rates experienced during Batch A processing (60 min. anneals) are related to more favorable vacuum furnace geometry and leak rate conditions at CM in spite of the fact that the vacuum gauge readings were an order of magnitude higher than in the BHT furnace. To assess this possibility, a second experiment was carried out to compare directly, the oxygen pick-up in the two furnace systems.

The Tube C1-A was given a further draw cycle of 28.4% R/A, and then given the surface sanding treatment followed by the 5 min acid cleaning procedure. This resulted in a tube with a 6.42 mm OD and a wall thickness of 0.533 mm Two 55 cm long sections of this tubing were wrapped in both Ta and Ti and heat treated at the two vendors for 30 minutes at 1000ºC with a request to maintain a vacuum of $>2 \times 10^{-5}$ torr. The furnace used at CM was the same furnace that was used for the processing of Batch A. The preliminary results of this comparison were surprising, but instructive. The tube that was annealed at CM was covered with a brownish oxide film whereas for the BC tube, the surface appearance was unchanged by the anneal at 1000ºC. A coupon of the US heat sheet material (S40) was included and this also developed a surface oxide during the anneal at CM. Chemical analysis of these materials is not available at this time but the preliminary conclusion can be drawn that the vacuum gauge readings reported by the vendors (CM $\sim 10^{-4}$ torr; BC $< 2 \times 10^{-5}$ torr) are a reasonable indication of the different vacuum conditions at the tubing and that the partial pressure of oxygen is indeed much higher in the CM furnace used in the processing of Batch A tubing. It is concluded that the differences in furnace volume and surface area, leak rate etc. are not responsible for the higher oxygen pick-up rates in the Batch B annealing treatments carried out at BC.

It now seems highly probable that the differences in behavior between the two batches of tubing are related to differences in the mechanisms of oxidation of V-4Cr-4Ti when exposed to different partial pressures of oxygen at 1000ºC. A possible explanation of the observed behavior may be found in the work of Pint and DiStefano [6] who studied the kinetics of oxidation of the US heat of V-4Cr-4Ti at 600-700ºC under partial pressures of oxygen in the range 10^{-3}-10^{-6} Pa. It was found that at very low oxygen partial pressures, oxidation is limited by a surface reaction such as oxygen absorption and the oxidation kinetics are linear. However at higher oxygen partial pressures a surface oxide may form and oxygen uptake is limited by diffusion through the surface oxide and under these conditions the kinetics take a linear-parabolic form. The observation of a visible oxide film during the 1000ºC anneal in the CM furnace and not in the BC furnace indicates that we are in two different oxidation regimes due to the differences in oxygen partial pressure. A possible scenario is that during the Batch A annealing at CM, oxygen pick-up in the bulk of the tubing was limited by the formation of a temporarily protective oxide layer. This oxide layer remained on the tubing during the next draw cycle and could possibly have contributed to the fairly high incidence of surface cracking on the OD and ID of the Batch A tubing. The subsequent 5 minute acid cleaning could well have been sufficient to remove the oxide layer and therefore a major fraction of the oxygen picked-up during the anneal. On the other hand, during the annealing treatments in the better vacuum conditions prevailing in the BC furnace, no protective layer was formed and the oxygen up-take was correspondingly much higher. Very little of the oxygen was removed during the acid cleaning because a) the oxygen was not concentrated in a surface oxide and b) the acid cleaning time was only 30 seconds duration.

FUTURE WORK

Further investigation of tubing samples taken from these experiments is in progress including the effectiveness of the acid cleaning process in lowering overall oxygen concentration. Oxidation rates will be estimated based on the weight gains calculated from the oxygen analyses and compared with empirical oxidation model [6]. Once the reasons for the high oxygen pick-up rates during the Batch B processing are understood, it should be possible to develop a procedure that limits oxygen pick-up during processing and proceed to the preparation of a new batch of creep tubing for both heats utilizing the 8.08mm OD tubing that was held back following the eighth annealing cycle.

REFERENCES

1. H. Tsai, M.C. Billone, R.V. Strain, and D.I. Smith; Fusion Materials Semi-annual Progress Report, DOE/ER-0313/23, December 1997, p.149.
2. M.L. Grossbeck, R.J. Kurtz, L.T. Gibson, and M.J. Gardner; Fusion Semi-annual Progress Report, DOE/ER-0313/32, June 2002, p. 6.
3. H. Tsai, M.C. Billone, T.S. Bray and D.L. Smith; Fusion Semi-annual Progress Report, DOE/ER-0313/27, December 1999, p. 65.
4. T. Nagasaka, T. Muroga, T. Likbo, “Development of Tubing Technique for High–Purity Low Activation Vanadium Alloys,” ANS Winter Meeting, Washington DC, Nov. 2002, (to be published).
5. A.F. Rowcliffe, W.R. Johnson and D.T. Hoelzer; Fusion Materials Semi-annual Progress Report, DOE/ER-0313/33 , December 2002, p. 7.
6. B.A. Pint and J.R. DiStefano, “Oxygen Embrittlement of Vanadium Alloys With and Without Surface Oxide Formation,” J. Nuclear Materials, 307-311, 2002, p. 560.

Processing and Fabrication of Experimental Vanadium Alloys for HFIR RB-17J Experiment

D.T. Hoelzer, A.F. Rowcliffe, and L.T. Gibson

OBJECTIVE

Process 12 experimental heats of vanadium alloys and fabricate into small plates to investigate the effects of composition, precipitation, and the presence of He on the microstructure during neutron irradiation in the HFIR RB-17J experiment.

SUMMARY

A proposed plan was formulated to make 12 experimental heats of vanadium alloys (HR1-HR12) to investigate the effects of composition, precipitation, and the presence of He on the microstructure and mechanical properties of vanadium during neutron irradiation in the HFIR RB-17J experiment. The main objectives for controlling the substitutional and interstitial solute concentrations in the alloys were achieved in this study. All of the alloys except the high N alloy (HR9) were successfully rolled into plates, which were suitable for machining flat sheet tensile (SS-J1 and SS-J2), TEM disks, and pre-cracked bend bars (PCBB) specimens. The alloys were processed with two (three for HR11) thermo-mechanical processes (TMP) in order to develop microstructures containing different precipitate and grain structures for the unirradiated annealing and neutron irradiation experiments.

PROGRESS AND STATUS

Experimental Procedure

In November 2002, participants of the Fusion Energy Program from ORNL, PNNL, and UCSB initiated weekly conference calls to finalize the specimen matrix and to coordinate activities for capsule assembly and insertion in the HFIR RB17J irradiation experiment. Early discussions addressed the finalization of the specimen matrix, which led to a conclusion that a series of small heats (~300g) of vanadium alloys were needed to investigate the effects of precipitate structure, grain size, He generation, and composition on the fracture and mechanical properties of vanadium alloys. A proposed plan was then formulated for making 12 small experimental heats of vanadium alloys, which are designated HR1 to HR12. Each processed alloy was fabricated into a small plate following one or two (three in the case of HR11) thermo-mechanical processing (TMP) procedures. Depending on the research objectives, specimens were then machined from the plates for investigation of microstructural changes and tensile and fracture properties resulting from exposure to the neutron irradiation conditions.

The Proposed Alloys

The compositions of the 12 vanadium-based alloys that were proposed based on research and processing objectives are listed in Table 1. The objective for making HR1-5 was to investigate higher Cr and Ti solute concentrations while keeping the interstitial C, N, and O concentrations the same in each alloy and close to the levels usually contained in the 832665 heat of V-4Cr-4Ti. HR1 is the reference alloy for the HR2-5 and HR11 alloys. For HR6-9, a 1:1 stoichiometric ratio between Ti, or Zr in HR7, and the interstitial C, N, and O atoms was the primary goal. However, it was also important to keep the C, N, and O concentrations the same in these alloys with the exception of the higher C level in HR8 and N level in HR9. HR10 is the reference alloy for HR8 and HR9 since it contains nearly the same Ti content but does not have the high C or N levels. The primary goal for HR11 and HR12 was to add 100 wppm B to V-4Cr-4Ti (HR11) and unalloyed V (HR12).

The primary goal for preparing HR1-HR5 was to explore higher substitutional Cr and Ti solute regimes as a basis for improving creep resistance while maintaining acceptable fracture behavior at 450ºC. This investigation will also address radiation phase stability, particularly the issue of two phase regime with higher Ti. In parallel with the irradiation experiment, these alloys will also form the basis of studies on thermal creep and phase stability. The objective for processing these alloys was to vary the Ti and Cr concentration while maintaining a constant interstitial concentration and a nearly constant grain size. The thermo-mechanical processing (TMP) of these alloys consists of a solutionizing treatment at 1300ºC and a final anneal at 1000ºC to produce a random dispersion of coarse globular-shaped TiCON particles in the BCC matrix. The specimens prepared from these alloys include TEM, SS-J1 tensile, and fracture toughness specimens. There will be TEM and SS-J1 specimens at all three irradiation temperatures. However, fracture toughness specimens will only be included at 450ºC since this pertains to the upper temperature range for irradiation hardening in V-Cr-Ti alloys.

An alternative approach to development of creep resistant microstructures and control of helium based on uniformly dispersed TiCON particles and control of grain boundary structure was proposed for preparing HR6-HR10. The investigation of these alloys includes the effects of interstitial concentration on the development of damage structure, radiation hardening and deformation behavior including dynamic strain aging (DSA) investigation of the effect of varying Ti: interstitial ratios on interstitial partitioning between matrix and precipitated phases; investigation of C, O and N solubilities; determination of regimes of phase stability (globular and plate morphologies); and investigation of relative effectiveness of Ti and Zr as interstitial getters. The objective for processing these alloys was to produce two different starting microstructures for the irradiation experiment. The TMP steps include a solutionizing treatment at 1300ºC and final annealing treatments to produce (a) randomly distributed globular-shaped TiCON particles and a 20-30 μm grain size in the matrix and (b) uniformly distributed nano-size plate-shaped TiCON particles and a large matrix grain size. Thermal aging and phase stability studies will be carried out in parallel with the irradiation experiments with the goal of eventually developing multi-phase microstructures with improved thermal creep resistance. The specimens consist of thicker SS-J2 tensile specimens for DSA measurements and TEM specimens for microstructural analysis.

An investigation of helium mobility and trapping in V-4Cr-4Ti and pure V was the primary goal for preparing HR11 and HR12, respectively. The investigation includes using boron doping to produce 100 appm helium and will be coupled with post–irradiation annealing with and without applied stress. The V-4Cr-4Ti (HR11) alloy will be processed to develop a range of microstructures to provide information on the effectiveness of various microstructural constituents as helium traps. Following the homogenization at 1300ºC, cold rolling and annealing at 1000ºC. Several TMT steps will be used to produce

Table 1. Heat designation and specified nominal compositions.

Alloy Number	V (wt.%)	Cr (wt.%)	Ti (wt.%)	Zr (wt.%)	C (wppm)	O (wppm)	N (wppm)	Comment
HR1	Bal.	4	4		140	350	85	Re-melt V-4Cr-4Ti
HR2	Bal.	10	4		140	350	85	Add Cr to V-4Cr-4Ti
HR3	Bal.	15	4		140	350	85	Add Cr to V-4Cr-4Ti
HR4	Bal.	4	10		140	350	85	Add Ti to V-4Cr-4Ti
HR5	Bal.	4	15		140	350	85	Add Ti to V-4Cr-4Ti
HR6	Bal.	4	0.195	-	70	330	200	Add Ti, Cr to V
HR7	Bal.	4	-	0.375	70	330	200	Add Zr, Cr to V
HR8	Bal.	4	0.57	-	1000	330	200	Add Ti, Cr, TiC to V
HR9	Bal.	4	0.48	-	70	330	1000	Add Ti, Cr, TiN to V
HR10	Bal.	4	0.50	-	70	330	200	Add Ti, Cr to V
HR11	Bal.	4	4	-	140	350	85	Add B to V-4Cr-4Ti
HR12	Bal.	-	-	-	25	210	150	Add B to V

microstructures containing, (a) uniformly dispersed globular TiCONs, (b) dispersion of plate morphology TiCON (~950ºC), and c) uniformly dispersed nano–size TiCON plates. Pure V will be processed to produce fine and coarse grain size microstructures.

Processing of the HR Alloys

The approach for making the HR alloys consisted of arc melting material from either the V-4Cr-4Ti plate (832665 heat) or unalloyed V ingot (820645 heat) with additional material to obtain the proposed alloy composition. HR1 consisted of material from the 1 in thick V-4Cr-4Ti plate (832665 heat) that was simply arc melted. HR2 and HR3 were made by arc melting material from the V-4Cr-4Ti plate with 99.999% pure Cr, in the form of -4/+7 mesh granules. HR4 and HR5 were made in a similar manner with 99.995% pure Ti, in the form of 0.125 in diameter x 0.25 in long slug. HR6, HR7, and HR10 were made by arc melting material from the V ingot with 99.999% pure Cr granules and either 99.995% pure Ti slug (HR6 and HR10) or 99.5% pure Zr slug (HR7). HR8 and HR9 were made in a similar manner as HR6 except that an additional amount of 99.5% pure TiC powder and 99.8% pure TiN powder was also arc melted to obtain the 1000 wppm C level in HR8 and 1000 wppm N level in HR9, respectively. The equivalent of 100 wppm natural B was arc melted with material from the V-4Cr-4Ti plate to make HR11 and with the V ingot to make HR12. All of the alloy samples were arc melted four times and then drop-cast into ~300 gram rectangular-shaped billets with dimensions of 1 in wide x 0.5 in thick x 5 in long.

The results of the chemical analyses of the HR alloys are shown in Table 2. Most of the processing objectives were achieved in making the alloys. Table 3 shows the average and total interstitial C, N, and

Table 2. Chemical analyses of V-4Cr-4Ti (832665), unalloyed V (820645), and HR alloys. The concentration for all elements are in wppm except for Ti, V, and Cr, which are in weight percent.

Element	V-4Cr-4Ti (832665)*	Pure V (820645)*	HR1	HR2	HR3	HR4	HR5	HR6	HR7	HR8	HR9	HR10	HR11	HR12
B	<7	<5	9	-	-	-	-	-	-	-	-	-	80	70
C	79	24	110	110	150	120	100	30	30	980	60	60	140	60
N	85	113	100	90	130	80	110	170	190	780	1210	180	90	180
O	310	313	380	360	380	350	370	290	290	530	320	330	360	290
Al	158	243	210	200	210	230	190	170	200	230	200	200	210	150
Si	783	173	570	620	660	570	530	20	30	<20	20	30	650	170
P	<30	<30	130	<20	<20	<20	<20	40	60	<20	<20	<20	110	<20
S	<10	<10	10	10	20	20	10	20	20	20	20	20	20	20
Cl	<2	-	<10	10	10	10	<10	<10	20	<10	<10	<10	<10	10
Ca	<10	<5	<20	10	40	<10	<10	<20	<20	30	<20	<20	<20	<20
Ti (%)	3.91	-	3.58	3.75	3.67	9.77	14.73	2100	30	5700	5000	5100	4.01	-
V (%)	Bal.	Bal.	92.87	86.33	81.47	86.47	81.66	95.56	95.38	95.05	95.11	95.26	92.00	99.88
Cr (%)	3.77	-	3.35	9.71	14.65	3.56	3.43	4.10	4.14	4.09	4.19	4.12	3.78	-
Fe	223	147	20	140	70	60	40	60	50	40	30	40	30	60
Ni	-	-	<20	20	20	70	30	20	<20	<20	<20	<20	<20	<20
As	-	-	<20	30	<20	<20	<20	100	<20	110	20	100	<20	40
Zr	-	-	<20	20	20	20	<20	<20	3700	<20	<20	<20	20	<20
Nb	<60	40	50	100	<20	100	30	180	20	40	<20	<20	<20	30
Mo	320	<50	280	300	290	290	270	50	50	70	60	60	310	50

* average of 3 positions.

O solute concentrations that were measured in HR1 to HR5. The results indicate that the total interstitial concentration did not change significantly for these alloys and was 588 ± 43 wppm. In addition, the individual C, N, and O concentrations were also nearly constant. Therefore, this series of alloys met the primary goal of changing only the substitutional Cr or Ti levels while maintaining a constant interstitial concentration. Maintaining an exact stoichiometric ration between Ti or Zr and the total interstitial C, N, and O concentration in the HR6 to HR10 alloys was more difficult in achieving. Table 4 shows the measured levels of Ti to interstitial C, N, and O solutes and the Ti:OCN ratio for HR6-HR10. Most of the alloys show a Ti:OCN ratio close to 1 or slightly larger, i.e. HR6 and HR7. However, HR8 showed a Ti:OCN ratio <1, which was due to a larger pick up of O and N than was observed in the other alloys. This may be attributed to a greater amount of impurities present in the TiC powder that was used to make the HR8 alloy. HR10 had a Ti:OCN ratio of 2.77. This alloy was designed to have a similar Ti level as in HR8 and HR9 and the lower total interstitial O, C, and N level observed in HR6. In the HR11 and HR12 alloys, the measured B level was slightly lower than the desired level of ~100 wppm.

Table 3. Average interstitial C, N, and O concentrations in the HR1-HR5.

Element	Average (wppm)
C	$\bar{x}$ = 118 ± 19
N	$\bar{x}$ = 102 ± 19
O	$\bar{x}$ = 368 ± 13
C, N, O (Total)	$\bar{x}$ = 588 ± 43

Table 4. Stoichiometric ratio between Ti or Zr and interstitial C, N, and O in HR6-HR10.

Heat	Ti:OCN (appm)	Ti/OCN Ratio
HR6	2232:1668	1.34
HR7	2068:1743	1.19
HR8	6025:8628	0.70
HR9	5298:5653	0.94
HR10	5418:1958	2.77

Fabrication of the HR alloys

The fabrication histories of the HR alloys are shown in Table 5. Each cast billet was cut into two sections. One section from each alloy was then rolled from ~0.50 to ~0.25 in thickness (50% reduction) at room temperature. All of the alloys were rolled without any evidence of cracking except for HR2, HR3, HR8, and HR9. This was not too surprising since these alloys were expected to have high strength properties resulting from the high Cr levels in HR2 and HR3 and high C and N levels in HR8 and HR9, respectively. The samples that were successfully cold rolled (CR) to 50% were cut into two sections that were to be used for different thermo-mechanical processing (TMP) conditions, i.e. TMP1 and TMP2 (plus a TMP3 for HR11) designations. For the HR2, HR3, HR8, and HR9 alloys, the remaining second section cut from the billet was cut into two sections and each section was then warm rolled (WR) at 400ºC from ~0.50 to ~0.25 in thickness (50% reduction). Only HR9, which contained the high N level, experienced cracking using this WR condition. Therefore, further work with HR9 was stopped in order to proceed with the fabrication of the remaining 11 HR alloys.

After the first rolling step, all of the samples were annealed in vacuum. The TMP1 and TMP3 samples were exposed to a solutionizing treatment by annealing at 1300ºC for 1h followed by removing the samples from the hot zone in the vacuum furnace. This treatment has been found to dissolve the globular Ti(CON) precipitate in the V-4Cr-4Ti alloy and then precipitate upon cooling a high number density of nano-size Ti(CON) plates in the matrix [1]. However, this heat treatment also produces a large grain size of several hundred microns. The TMP2 samples were annealed using the typical recrystallization treatment at 1000ºC for 2h followed by furnace cooling. This heat treatment has been shown to produce a grain size of typically 20-30μm and a low number density of sub-micron size globular Ti(CON) precipitates.

All of the samples were rolled a second time followed by a final heat treatment. A reduction in thickness of ~0.25 in to ~0.125 in (50%) was used for CR the HR1, HR4-HR7, and HR10-HR12 alloys and ~0.25 in to ~0.165 in (30%) for WR the HR2, HR3, and HR8 alloys. Only HR3 developed some cracks during the second rolling operation. A final annealing was performed on all the samples, which consisted of annealing the TMP1 and TMP3 samples at 1000ºC for 2h followed by furnace cooling and the TMP2 samples at 1300ºC for 1h followed removing the samples from the hot zone in the furnace.

Table 5. Fabrication history of the HR alloys.

Alloy	TMP	1st Rolling Operation	1st HT	2nd Rolling Operation	Final HT
HR1	1	52% CR	1300ºC/1h	50% CR	1000ºC/2h
	2	52% CR	1000ºC/2h	50% CR	1300ºC/2h
HR2	1	50% WR (at 400ºC)	1300ºC/1h	30% WR (at 400ºC)	1000ºC/2h
	2	50% WR (at 400ºC)	1000ºC/2h	30% WR (at 400ºC)	1300ºC/2h
HR3	1	50% WR (at 400ºC)	1300ºC/1h	30% WR (at 400ºC)	1000ºC/2h
	2	50% WR (at 400ºC)	1000ºC/2h	30% WR (at 400ºC)	1300ºC/2h
HR4	1	50% CR	1300ºC/1h	50% CR	1000ºC/2h
	2	50% CR	1000ºC/2h	50% CR	1300ºC/2h
HR5	1	50% CR	1300ºC/1h	50% CR	1000ºC/2h
	2	50% CR	1000ºC/2h	50% CR	1300ºC/2h
HR6	1	50% CR	1300ºC/1h	50% CR	1000ºC/2h
	2	50% CR	1000ºC/2h	50% CR	1300ºC/2h
HR7	1	50% CR	1300ºC/1h	50% CR	1000ºC/2h
	2	50% CR	1000ºC/2h	50% CR	1300ºC/2h
HR8	1	50% WR (at 400ºC)	1300ºC/1h	30% WR (at 400ºC)	1000ºC/2h
	2	50% WR (at 400ºC)	1300ºC/1h	30% WR (at 400ºC)	1300ºC/2h
HR9	1	Cracking occurred during 400ºC WR			
	2				
HR10	1	50% CR	1300ºC/1h	50% CR	1000ºC/2h
	2	50% CR	1000ºC/2h	50% CR	1300ºC/2h
HR11	1	50% CR	1300ºC/1h	50% CR	1000ºC/2h
	2	50% CR	1000ºC/1h	50% CR	1300ºC/2h
	3	50% CR	1300ºC/2h	50% CR	950ºC/2h
HR12	1	50% CR	1300ºC/1h	50% CR	1000ºC/2h
	2	50% CR	1000ºC/2h	50% CR	1300ºC/2h

Specimen Machining

A number of tensile (SS-J1 and SS-J2), TEM disks, and pre-cracked bend bar (PCBB) specimens were machined from the fabricated plates of the HR alloys and engraved with I.D. codes. These specimens will be used in the HFIR RB-17J experiment and a complete list of them will be published in the next semiannual. However, an unfortunate development that occurred during the fabrication of the alloys was that HR3 and HR8 samples were swapped during the first rolling operation. This was discovered during the resistivity measurements of the tensile specimens [2] and was confirmed by EDS on the XL30 SEM. This only affected the tensile and TEM specimens of these two alloys. Further details will be provided in the future semiannual which will describe the final specimen matrix for RB-17J.

References

[1] D.T. Hoelzer and J. Bentley, to be published in ICFRM-11, (2003).

[2] M. Li, D.T. Hoelzer and S.J. Zinkle, Electrical Resistivity Data of Vanadium Alloys in the RB-17J Experiment. This semiannual.

CHARACTERIZATION OF REACTION PRODUCTS AFTER OXIDATION OF V-4Cr-4Ti AT LOW PRESSURES -- B. A. Pint and H. M. Meyer (Oak Ridge National Laboratory)

OBJECTIVE

The objective of this task is to assess the high temperature oxidation behavior of V-4Cr-4Ti in low oxygen pressure environments and any related effect on mechanical properties. Several reactor designs involve vanadium alloys in high temperature environments such as vacuum or helium which will contain some level of oxygen and hydrogen impurities. Testing is being conducted in vacuum with low oxygen pressures, 10^{-3}-10^{-6}Pa (10^{-5}-10^{-8}Torr), and in high-purity helium and argon at 400-700°C. Recent emphasis has been on determining oxidation kinetics in low pressures of He to simulate higher purity He than is commercially available.

SUMMARY

There was a significant change in oxidation kinetics between 10^{-4}atm He and 10^{-3}atm He. The higher pressure results were similar to those observed in 1atm He where a surface oxide was observed. Using Auger electron spectroscopy (AES), a thicker (30-40nm) oxide was observed after 100h at 700°C in the higher He pressure whereas a thinner oxide (10-20nm) formed at the lower pressure.

PROGRESS AND STATUS

Introduction

Specimens of V-4Cr-4Ti have been exposed to He environments from 1atm down to 10^{-4}atm in order to determine oxidation kinetics and effects on mechanical properties. At 10^{-4}atm He, the reaction kinetics were nearly linear at 700°C. However, at 10^{-3}atm He, the specimen mass gains were lower and followed a sub-parabolic rate, very similar to the behavior observed in 1atm of He, Figure 1. These results suggest that an external oxide layer may be forming at the higher pressures. During exposures in 1atm He, specimens form a visible external oxide layer and retain some tensile ductility after exposure.[1] To determine if oxide layers had formed after exposures to 10^{-3} and 10^{-4}atm He, selected specimens were examined using Auger.

Experimental Procedure

All of the experiments were conducted on V-4Cr-4Ti (Heat#832665). Prior to exposure, the specimens were annealed at 1050°C to produce a uniform grain size. Specimens were 0.76mm thick tensile specimens. Low pressure exposures were conducted in an ultra high vacuum system in which a base vacuum of 10^{-7}Pa (10^{-9}Torr) could be achieved. A micrometering valve was used to achieve He partial pressures of either 10^{-3} or 10^{-4}atm. Oxygen content of the samples was determined by weighing before and after exposure.

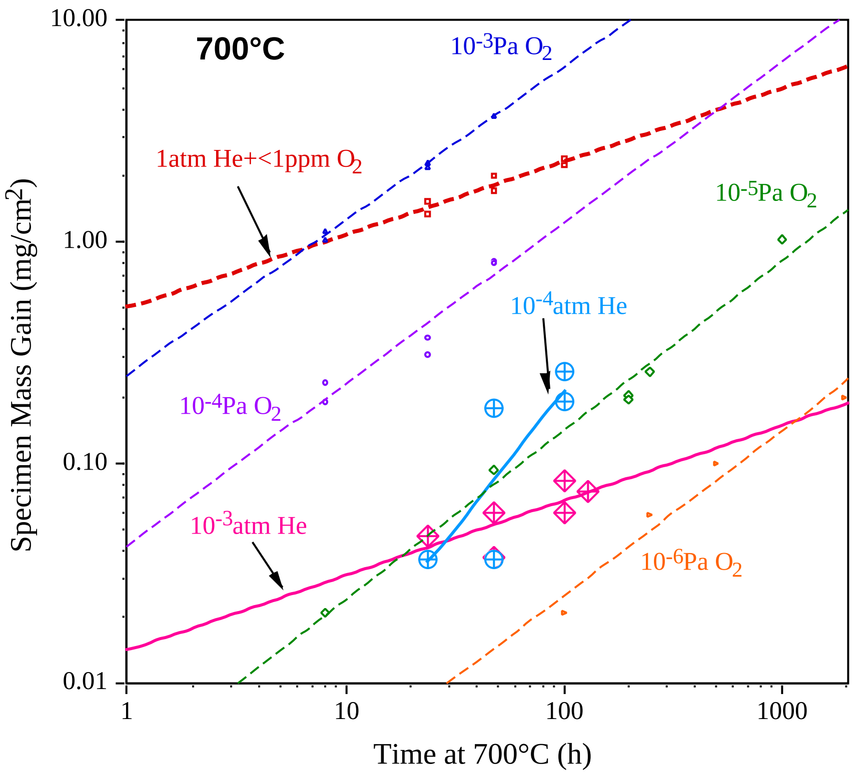

Figure 1. Log-log plot of the mass gains observed in this work at 700°C in low pressures of high purity (<1ppm O) He (solid lines). At 10^{-4}atm He, the mass gains were similar to that observed in 10^{-5}Pa O_2. At 10^{-3}atm He, the mass gains were lower and the reaction kinetics were similar to that observed in 1 atm He.

Results and Discussion

Two specimens of V-4Cr-4Ti were examined by AES. Both were exposed for 100h at 700°C, one at 10^{-3}atm He and the other at 10^{-4}atm He. Both surfaces had a similar appearance with some rough and smooth areas, Figure 2. There were significant difficulties in determining the surface composition because of peak overlaps between Ti and N as well as V and O. Also, Ti, V and Cr are all difficult to differentiate because of overlap. A slow (170Å/min) sputter rate was used because of the thin surface oxide. However, a high concentration of carbon in the form of a carbide was observed on both specimens to a depth of over 200nm. There was a clear change between the graphitic carbon peak observed on the specimen surface and the carbide peak observed within the specimen. Further characterization will be required to determine the nature of this carbon enrichment near the specimen surface.

Figure 3 shows the sputter depth profiles for each specimen. For the specimen exposed at 10^{-3}atm He, the O signal became negligible at ≈35nm, Figure 3a. For the specimen exposed at 10^{-4}atm He, the O signal disappeared at ≈15nm. Therefore, a thicker oxide layer was formed in the higher He pressure. However, whether this layer was responsible for the inhibition in the rate of oxygen uptake is not certain. Further work is needed to study this mechanism. Experiments are underway for longer times at these pressures and at higher and lower He pressures. As a final

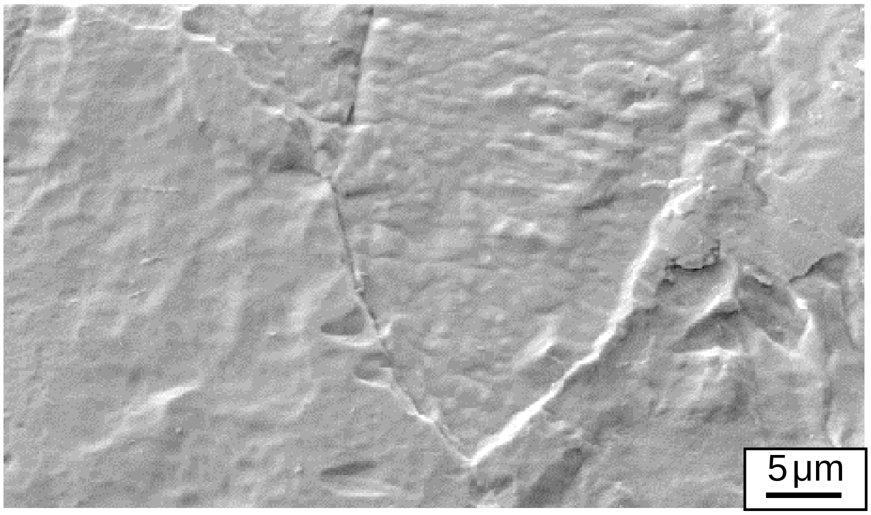

Figure 2. Secondary electron image of the specimen surface after 100h at 700°C in 10^{-3}atm He. There were smooth raised areas and rough areas observed on both specimens.

note, the formation of a surface oxide on a vanadium alloy cannot be considered a protective layer. Previous work[1] has shown that a surface oxide is not stable with vanadium and is actually a source for oxygen, which diffuses into the substrate and causes embrittlement.

REFERENCES

1. B. A. Pint and J. R. DiStefano, J. Nucl. Mater. 307-311 (2002) 560.

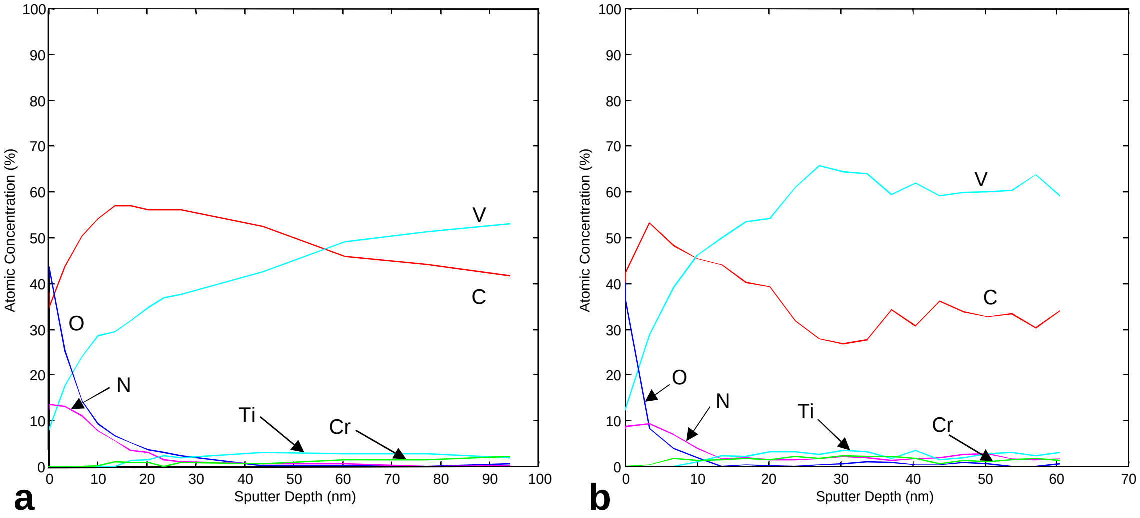

Figure 3. AES sputter depth profiles of V-4Cr-4Ti specimens exposed for 100h at 700°C in (a) 10^{-3}atm He and (b) 10^{-4}atm He.

STRONGLY NON-ARRHENIUS INTERSTITIAL DIFFUSION IN VANADIUM--L. A. Zepeda-Ruiz (Lawrence Livermore National Laboratory), S. Han (Princeton University), G. J. Ackland (University of Edinburgh), R. Car (Princeton University), and D. J. Srolovitz (Princeton University),

ABSTRACT

The creation and evolution of point defects play an important role in determining the structural properties of materials. The two elementary point defects in elemental metals are vacancies and self-interstitial atoms (SIA). The creation and migration of SIA are critical for microstructural evolution of materials in high-energy radiation environments and in ion implantation. SIAs are usually very mobile (i.e., the migration barriers for SIAs are relatively small) and, hence, play an important role in controlling the rates of several types of microstructural processes in such applications.

In this study, we examined the fundamental behavior of SIAs in vanadium through a series of molecular dynamics (MD) simulations based on an interatomic potential that is consistent with first principles calculations of point defects in V. We found that the stable SIA structure in V is a <111>-oriented dumbbell, rather than the <110>-oriented dumbbell found in Fe. Given this fundamental discrepancy, SIA migration in Fe and V must be fundamentally different and our current understanding of SIA diffusion in V is rather limited. In particular, we examined SIA diffusion as a function of temperature and determine the mechanisms that control it. We found that while SIA migration in V is similar to that in bcc Fe in many respects, several important differences exist and a range of interesting phenomena are observed.

Our MD results showed that <111>-oriented dumbells migrate quickly along <111> directions, even at very low temperatures. Rotation of the dumbbells and the migration path to other <111>-directions occurs with increasing frequency as the temperature is raised. The interstitial migration mechanism was found to be temperature dependent. For low and intermediate temperatures (100-600 K) the SIA executed an essentially one-dimensional (1D) random walk along a <111>-direction. Only 1D random walks were observed for temperatures from 100K to 600K. Upon increasing the temperature to T~700K, the SIA began to make infrequent rotations from one <111>- to another <111>-direction. This resulted in a 3D trajectory that consists of long 1D random walk segments with abrupt reorientations. As the temperature increased, the frequency of the rotation events increased and the lengths of the 1D segments of the trajectories decreased. At high temperatures, the rotation events became very frequent, such that the SIA is performing a truly 3D random walk. It was found that the apparent activation energy for diffusion increases with increasing temperature. This increase in apparent activation energy with increasing temperature occurs even at temperatures that are too low to be attributed to dumbbell rotation. Rather, we demonstrated that the intrinsic activation energy is not strongly temperature dependent, but rather the correlation factor is.

REFERENCE

Submitted for publication to Acta Materialia

ON THE CHARACTER OF SELF-INTERSTITIAL LOOPS IN VANADIUM--L. A. Zepeda-Ruiz (Lawrence Livermore National Laboratory), J. Marian (Lawrence Livermore National Laboratory), B. D. Wirth (University of California Berkeley), and D. J. Srolovitz (Princeton University)

ABSTRACT

Isolated self-interstitial atoms (SIA) and SIA clusters produced during collision cascades are key components of the microstructure observed when metals are irradiated with high-energy particles. The evolution of these defects may cause undesirable changes in the mechanical properties of the material under irradiation. Therefore, knowledge of the properties, formation and diffusion mechanisms of SIA is essential for understanding and predicting the effects of radiation damage.

In this study, we used molecular statics and molecular dynamics (MD) simulations based on a new Finnis-Sinclair potential, fit to first-principles calculations of point defect properties, to investigate the energy and structure of SIA dislocation loops in vanadium. We found that SIA dislocation loops with a/2<111> Burger's vector were the lowest energy configuration in vanadium, and migrated rapidly along their <111>-glide cylinder. Initial dislocation loop configurations with Burger's vector of a/2<110> or a<100> rotated into a/2<111> orientations at very low temperatures during the computational relaxation scheme used in this work and indicate that the formation energy of a/2<110> and a<100> loops is much higher than a/2<111> loops. Our results were compared to experimental observations and recent results in ferritic alloys which detail the formation mechanism responsible for the nucleation and growth mechanism of a<100> dislocation loops. Unlike in Fe, where a metastable a<100> loop is very close in energy to the ground-state a/2<111> orientation, constrained a<100> loops in V have considerably higher formation energies than a/2<111> loops, and the energy difference increases with size.

Finally, our MD simulations of the interaction between two mobile a/2<111> clusters, according to the reaction proposed for a<100>-loop formation in Fe, revealed the formation of a single resulting a/2<111> loop. The simulations indicated that while a junction reaction occurs (a <100>-junction does form), the junction has a low thermal stability and rotates into a a/2<111> orientation at temperatures of 600-800K. The simulations performed to date provide no indication that the smaller a<100> junctions will propagate across the loop, but instead will dissolve with low thermal stability.

Reference

Accepted for publication in Philosophical Magazine

MOLECULAR DYNAMICS STUDY OF THE THRESHOLD DISPLACEMENT ENERGY IN VANADIUM--

L. A. Zepeda-Ruiz (Princeton University and Lawrence Livermore National Laboratory), S. Han (Princeton University), D. J. Srolovitz (Princeton University), R. Car (Princeton University) and B. D. Wirth (University of California, Berkeley)

ABSTRACT

One of the most important physical parameters for describing radiation damage is the threshold displacement energy (TDE). The TDE is the minimum kinetic energy transferred to an atom in the lattice from an impinging particle necessary to permanently displace an atom from its lattice site, thus generating stable defect, such as a Frenkel pair. In the case of high kinetic energy particle impingement (such as 14 MeV neutrons in a fusion reactor environment), the initial cascade gives rise to a series of subcascades which stop when the highest energy particle has kinetic energy smaller than the TDE. Hence, threshold displacement energies are critical parameters for both low and high energy irradiation conditions. The TDE provides a lower limit on particle kinetic energies that must be considered in molecular dynamics (MD) simulations of radiation damage and, hence, is a key parameter for enabling MD simulations of displacement cascades.

Threshold displacement energies in V were calculated as a function of temperature (100 < T < 900 K) and orientation of the incident particle momentum by molecular dynamics simulation using a new parameterization of an embedded atom method/Finnis-Sinclair-type potential for V. A primary knock-on atom (PKA) was chosen near the center of the simulation cell and assigned a velocity along a particular direction, consistent with a chosen knock-on energy. The trajectories of all of the atoms in the system were traced for 10 ps following the knock-on event. The TDE was defined as the minimum kinetic energy transferred by the PKA to a lattice atom that resulted in the formation of a stable Frenkel pair.

It was found that the minimum TDE in V is approximately 13 eV. This corresponds to a displacement along the <100>-direction. The maximum TDE observed in the simulations was 51 eV, in a direction close to <101>. Since the simulations did not span all possible angles, it is likely that the true maximum TDE is even larger, especially when allowing for longer time recombination processes. A comparison of the TDE for V with experimental values for other body centered cubic metals (Fe and Mo) showed that the directional anisotropy is comparable in Mo but the TDE ordering in <110> and <111> orientations is different in Fe. In addition, it was found that the TDE in V is almost independent of temperature since the magnitude of the TDE is very much greater than thermal energies, even at temperatures approaching the melting point.

REFERENCE

Published in Physical Review B **67**, 134114 (2003)

2.0 CERAMIC COMPOSITE MATERIALS

CHARACTERIZATION OF A 2D-SIC$_F$/SIC COMPOSITE MADE BY ICVI WITH HI-NICALON™ TYPE S FABRIC – G. E. Youngblood and R. H. Jones (Pacific Northwest National Laboratory)*

OBJECTIVE

The objective of this task is to examine SiC fibers and SiC/SiC composites fabricated by various processing methods designed to improve the composite properties. Specifically, it is desired to optimize the thermal conductivity and the mechanical behavior of these composites to meet expected requirements for advanced fusion energy systems.

SUMMARY

In this report, the mechanical and thermal properties of a 2D-SiC$_f$/SiC composite made by the CVI-process with the Hi-Nicalon™ type S fabric are assessed in detail with respect to meeting fusion design requirements. Minimum strength and stiffness structural requirements likely can be met by CVI-processed SiC$_f$/SiC composites when made with advanced SiC fibers. Unfortunately, it appears unlikely that the minimum thermal conduction goals can be met for CVI-processed material. Even for an optimized 2D SiC$_f$/SiC system, the margin of improvement required is just too large for only minor improvements potentially possible through CVI-processing upgrades or other structural or architectural methods.

PROGRESS AND STATUS

Introduction

SiC/SiC composite has been proposed as a structural material for the first wall and blanket in several conceptual designs of a D-T fusion power reactor. The reactor concepts: TAURO in the European Union and the ARIES-AT in the United States utilize Pb-17Li self-cooled blankets, while DREAM in Japan utilizes 10 MPa helium cooling. In these designs, modules built from SiC$_f$/SiC composite would be from 0.5 to several meters high, and would operate under high-energy (14.1 MeV) neutron irradiation in a relatively high temperature range (600°C-1000°C). Important mechanical and thermal design criteria at this time are: elastic modulus > 200 GPa, tensile strength > 200 MPa, and through-thickness thermal conductivity (K_{eff}) at 1000°C > 15 W/mK [1]. With the use of crystalline, near-stoichiometric SiC fibers (e.g., Hi-Nicalon™ type S or Tyranno™ SA fibers), SiC$_f$/SiC composites made by the CVI-process exhibited little degradation of strength and stiffness after a 7.7 dpa irradiation dose at 800°C [2]. Thus, it appears likely that the fusion mechanical design criteria can be met by using SiC$_f$/SiC composites made with advanced SiC fibers. However, for a relatively low dose (typically less than a dpa in SiC) a steady-state concentration of point defects (vacancies and interstituals) will be induced in the SiC lattice during neutron irradiation. Such point defects efficiently scatter phonons, and depending upon the irradiation temperature will degrade the thermal conductivity by 50% or more [3]. To compensate for the inevitable thermal conductivity degradation and still attain the fusion energy K_{eff}-goal during operation, it is estimated that unirradiated SiC/SiC composite should have starting K_{eff}-values of at least 43 and 27 W/mK at 600 and 1000°C, respectively [4]. In this report, the mechanical and thermal properties of a 2D-SiC$_f$/SiC composite made by the CVI-process with the Hi-Nicalon™ type S fabric are assessed in detail with respect to meeting the listed fusion design criteria.

Experimental Procedure

Two SiC$_f$/SiC composite plates (15 x 23 cm^2) were purchased from GE Power Systems Composites

---

* Pacific Northwest National Laboratory (PNNL) is operated for the U.S. Department of Energy by Battelle Memorial Institute under contract DE-AC06-76RLO-1830.

(formerly DuPont Lanxide). One plate was made with eight plies, the other with six plies of 5HS-weave Hi-Nicalon™ type S fabric (18 epi, 500 filaments/yarn, lot number SCS0102, manufactured by Nippon Carbon Co in December, 2001). The properties given by Nippon for the type S fiber were: density 3.0 g/cc, tensile strength 2.8 GPa, tensile modulus 380 GPa, and oxygen content 0.7 wt%. A pyrocarbon (PyC) fiber coating (nominally 150 nm thick) was applied by CVD to each fabric lay-up prior to SiC matrix infiltration by the isothermal CVI-process (ICVI). The nominal bulk density of the plates was 2.69 g/cc after ICVI-SiC infiltration and the nominal overall fiber content was 40%.

Laser flash thermal diffusivity measurements were performed on several representative disc samples (1.79 mm x 9.00 mm dia.) cut from the as-received six-ply plate. Individual diffusivity sample bulk density values ranged from 2.60 to 2.74 g/cc. The samples were mounted four at a time in a sliding sample tray so that diffusivity measurements could be made in air on each sample for 50°C temperature steps from RT to about 400°C. Laser pulses and infrared temperature detector readings were made on the composite sample as-received surfaces. Further experimental details were presented previously [5]. Using previously measured fiber thermal conductivity values (K_f) and measured $K_{eff}(T)$-values, the constituent matrix and fiber coating thermal conductivity values were estimated using the H2L thermal conductivity model developed at PNNL [6].

Four-point bend flexure tests were performed on six ICVI-SiC/SiC composite bars cut from the six-ply plate of the Hi-Nicalon™ type S material (nominal bar dimensions 5.95 x 30.0 x 1.85 mm^3). The outer tensile and compressive bar surfaces were not machined. Bar dimensions were measured at several locations along each bar with a vernier caliper. Side views of the bars by SEM indicated that each surface profile had a roughness variation of about ±0.16 mm. Since the thickness was measured peak-to-peak with the caliper, the average bar thickness was obtained by subtracting an average 0.16-mm profile correction factor from the actual measured thickness values. Bar samples were mounted in a fully articulated inconel fixture in an Instron load frame. The four contact roller pins were made from sintered Hexalloy™ SA SiC and had an outer/inner pin spacing of 20/10 mm. A load deflection rate of 8.5×10^{-4} mm/s was used. Three bars each were tested at ambient (RT) and three at 800°C. The bend tests at 800°C were performed in flowing, dry argon. Linear elastic beam theory (LEBT) was used to calculate the maximum stress and strain expected at the outer tensile surface of the bar samples from measured bar midpoint displacement and load data, even though LEBT generally is not valid in the non-linear region of the stress-strain curves for fiber reinforced ceramic composites. The stress-strain data were corrected for machine compliance by testing two CVD-SiC bars of the same dimensions at RT and assuming that the elastic modulus for the monolithic CVD material was 460 GPa. The flexural modulus of the composite samples was then estimated from the corrected slope of the linear portion of the “pseudo-plastic” stress-strain curves. For comparison, similar 4-pt bend tests were performed on several bar samples of SiC_f/SiC composite, also made by ICVI (by DuPont Lanxide) with plain weave (PW) Hi-Nicalon™ fabric and a thin (0.110 μm) PyC fiber coating. Polished cross-sections of representative samples and several fracture surfaces of bars broken in the 4-pt bend tests were examined by SEM.

Results

In Figures 1(a-b), typical low and high magnification SEM micrographs of polished cross-sections of the 2D Hi-Nicalon™ type S composite are presented. From several views of this type, the following structural parameters were determined and used in the analysis of the thermal conductivity with the H2L model. The average fiber coating thickness was 0.188±0.036 μm; the average fabric- and matrix-layer volume fractions were 0.827±0.070 and 0.173±0.070, respectively; the average fiber packing and the microporosity volume fractions within the fabric layers were 0.502±0.060 and 0.065±0.007, respectively; and the interlayer macroporosity eccentricity factor was 0.17±0.05 (the average interlaminar macropore height-to-breadth ratio) [4]. Importantly, for the Hi-Nicalon™ type S composite the bulk density and fabric-layer volume fractions were higher, and the fiber packing and microporosity volume fractions were lower compared to those same values determined for the similarly fabricated 2D Hi-Nicalon™ composite [6].

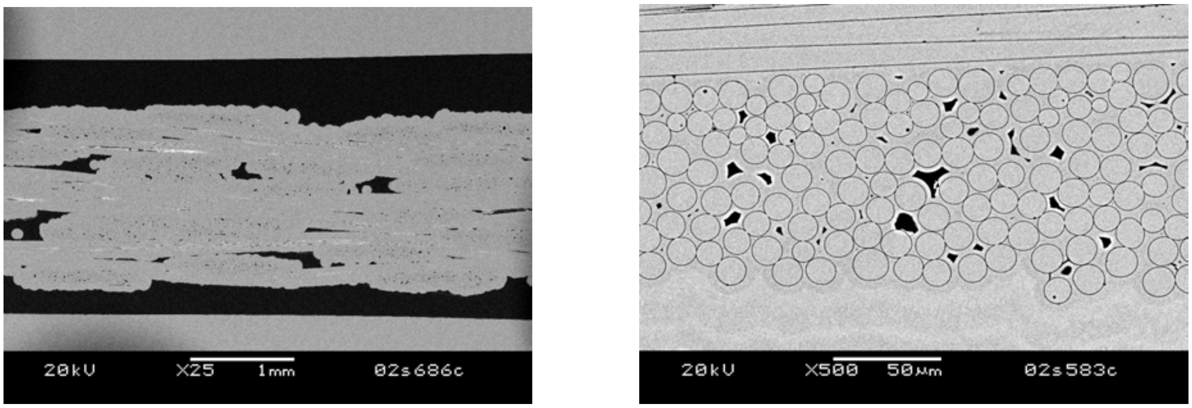

Figures 1(a-b). SEM micrographs (backscatter electron mode) of polished cross-sections depicting (a) the typical fiber bundle geometry and macroporosity content, shape and orientation, and (b) the excellent matrix infiltration of the individual fiber bundles for the 2D Hi-Nicalon™ type S SiC_f/SiC composite.

In Figure 2, the effective through-thickness thermal conductivity (K_{eff}) determined as a function of temperature for the type S composite is compared to K_{eff}-values similarly determined for the 2D Hi-Nicalon and a 2D Tyranno™ SA composite [4]. The K_{eff}-values for the type S composite decreased continuously from a 28 W/mK maximum at 100°C down to 14 W/mK at 1000°C. Also, the K_{eff}-values for the type S composite were greater than the K_{eff}-values for either the Tyranno™ SA or the Hi-Nicalon™ composites. H2L model analysis of the temperature dependent K_{eff}-curve for the type S composite led to the predictions that (a) the thermal conductivity of the PyC fiber coating constituent increased from 28 W/mK at RT up to a maximum 34 W/mK at 300°C then decreased gradually to 28 W/mK at 1000°C, and (b) the thermal conductivity of the "intrinsic" ICVI-matrix constituent decreased continuously from a maximum value of about 40 W/mK at RT down to a value of 18 W/mK at 1000°C [4].

In Figure 3, the 4-pt bend stress-strain behavior for the 2D Hi-Nicalon™ type S composite bars tested at RT in air and 800°C in argon is illustrated. Also presented are data for similarly fabricated 2D Hi-Nicalon™ composite bars tested at 800°C. For clarity, the strain data has been offset by 0.2% for each group of data. All the stress-strain curves exhibit "graceful" failure, which is characteristic of a toughened

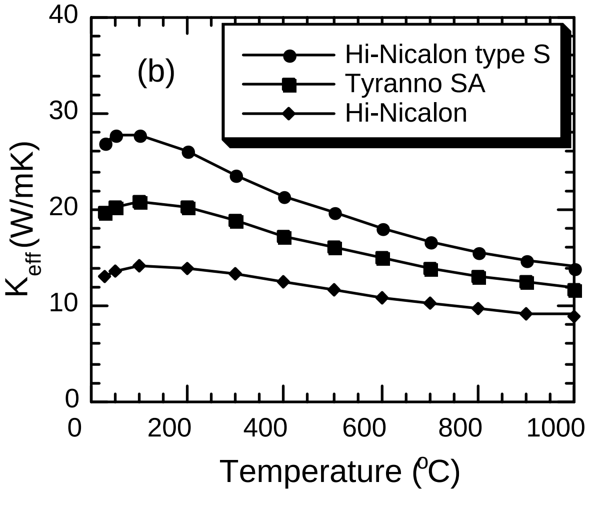

Figure 2. Average K_{eff}-values for 2D SiC_f/SiC composites made by ICVI with either Hi-Nicalon™ type S, Tyranno™ SA or Hi-Nicalon™ woven fabrics [4].

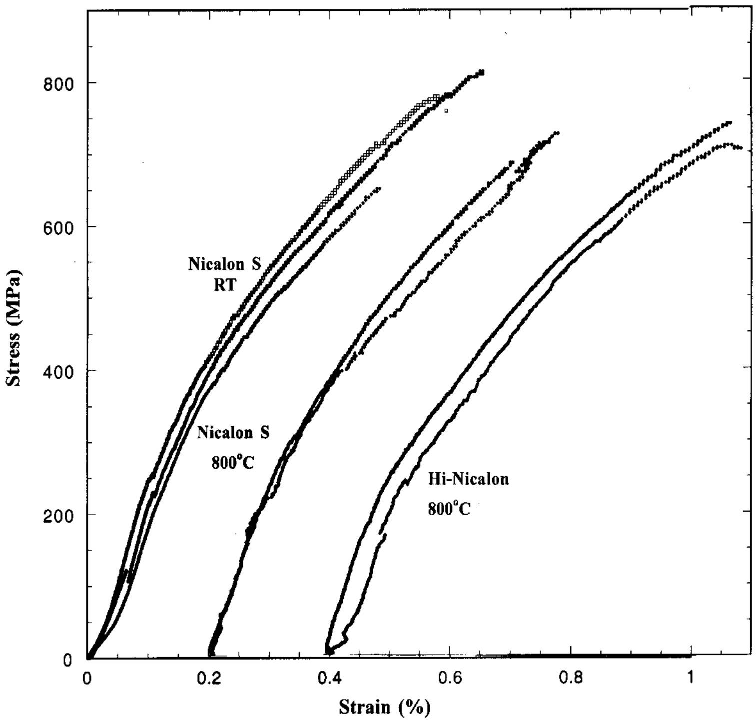

Figure 3. Stress-Strain curves for similarly CVI-fabricated SiC$_f$/SiC composite made with either Hi-Nicalon™ type S or Hi-Nicalon™ 2D woven fabric.

pseudo-plastic SiC$_f$/SiC composite. In Table 1, the average values of the ultimate stress and strain, the elastic modulus of the linear portion of the stress-strain curves, and the proportional limit stress determined from the stress-strain curves illustrated in Figure 3 are listed in bold print. For comparison, values for similarly tested 2D SiC$_f$/SiC composites made by FCVI with either PW type S or PW Hi-Nicalon™ fabric (by ORNL) and reported by Hinoki, et al [2] are given in standard print.

Table 1. Average values of ultimate stress and strain, elastic modulus and proportional limit stress determined from stress-strain curves for Hi-Nicalon™ type S and Hi-Nicalon™ SiC/SiC composites made by the CVI-process and tested in 4-pt bend configuration.

Material	Test Temp (°C)	Ult. Stress (MPa)	Ult. Strain (%)	Modulus (GPa)	Prop. Stress (MPa)
Nic S, 5HS	**RT**	**749 (66)***	**0.55 (0.08)**	**284 (16)**	**240 (20)**
Nic S, 5HS	**800**	**720 (8)**	**0.56 (0.01)**	**243 (12)**	**225 (25)**
Nic S, PW [4]	RT	425	1.42#	32#	280
Hi-Nic, PW	**RT**	**650 (60)**	**0.83 (0.10)**	**239**	**160**
Hi-Nic, PW	**800**	**724 (15)**	**0.66 (0.02)**	**255 (12)**	**180 (20)**
Hi-Nic, PW [4]	RT	450	1.40#	42#	200

* maximum variation from average values given in parentheses.

#Apparently the machine compliance was not correctly applied to this data as the ultimate strain values obviously are too high and the modulus values too low for SiC$_f$/SiC composite.

At least 6-8 bar samples should be tested for each condition to achieve statistically reliable average strength values. Since only a limited number of samples (6 total) were available at the time of testing, the results are expected to indicate trends, not statistically reproducible values. Also, in Table 1 the proportional limit stress was taken as the first occurrence of non-linearity in the stress-strain curve. For fiber reinforced composites, the PLS has importance primarily as an indication of the first matrix cracking stress, thus can be useful as a fabrication parameter.

Discussion

The as-received 2D Hi-Nicalon™ type S composite made by ICVI-processing had extremely good fiber bundle infiltration that produced well-bonded fiber/matrix interfaces with a high interfacial conductance of about 3 x 10^4 W/cm^{2}K (estimated using the H2L model) [7]. This material also had a relatively low microporosity within the fiber bundles and low interlaminar macroporosity content and shape factor for CVI-processed material (see Figure 1). For these reasons, the thermal conductivity and bend strength values also were considerably improved over corresponding values for either the Hi-Nicalon™ or the Tyranno™ SA composites similarly fabricated. The approximate factor of two improvement of K_{eff}-values for the type S over that of the Hi-Nicalon™ material was not unexpected since the Nicalon™ type S fiber thermal conductivity (K_f) values are ≈x4 higher than K_f-values for the Hi-Nicalon™ fiber [8]. However, the Tyranno™ SA composite was expected to have the highest K_{eff}-values because of its high K_f-values, larger than a factor x2 that of the Nicalon™ type S fiber [8]. Instead, K_{eff}-values for a similarly fabricated Tyranno™ SA system were 20-30% lower than values for the type S system (see Figure 2). According to the H2L model, the relatively high macroporosity content and shape factor for the SA system offset thermal conductivity gains expected from using the high conductivity SA fiber. Furthermore, the H2L model predicted that the intrinsic matrix constituent thermal conductivity resulting from the ICVI-process was about 25% higher than that resulting from the FCVI-process [4]. The ICVI-matrix was formed over a period of about a month, while the FCVI-matrix infiltration was completed in a few days. Apparently, subtle substructural differences between the slowly formed matrix of the ICVI- and the more rapidly formed FCVI-matrix components were responsible for the H2L-model predicted differences in matrix constituent conductivities, although this explanation needs further examination.

Further evidence for obtaining a “better” composite when using the ICVI- rather than the FCVI-process is revealed by examining the bend strengths for similarly tested type S or Hi-Nicalon™ composites (see Table 1). The ultimate bend strengths for the ICVI-processed type S and Hi-Nicalon™ composites were quite high (749 and 650 MPa at RT and 720 and 724 MPa at 800°C, respectively). The ultimate bend strengths for both the FCVI-processed type S and Hi-Nicalon composites were considerably lower (425 and 450 MPa at RT, respectively).

Interestingly, the RT bend strength of the Hi-Nicalon™ composite was about 75 MPa lower than its bend strength at 800°C, while little difference in strengths at RT and 800°C was observed for the type S composite. Subtle differences in the residual radial clamping stress likely are the reason for this temperature dependence. Since the thermal expansion coefficient for Hi-Nicalon™ fiber is less than that for CVI-SiC matrix, a clamping stress is expected to slightly decrease the strength for the Hi-Nicalon™ material, more so for the RT case. In contrast, the stoichiometric type S SiC fiber likely has similar thermal expansion characteristics as the CVI-SiC matrix constituent, and residual stresses due to thermal expansion mismatch are not expected in the as-received type S composite. Moreover, irradiation induced swelling is expected to be similar in these type S composite constituents, which likely is the major reason little strength degradation was observed for this material by Hinoki, et al when it was irradiated [2].

The bend stress-strain curves for the type S composite tested at either RT or 800°C (see Figure 3) exhibit similar behavior, i.e., besides high bend strengths (>720 MPa), the curves indicate a high ultimate strain (>0.55 %), bend modulus (>243 GPa) and proportional limit stress (>225 MPa). Furthermore, these stress-strain curves indicate a slow transition from linear to pseudo-plastic behavior with a rather small

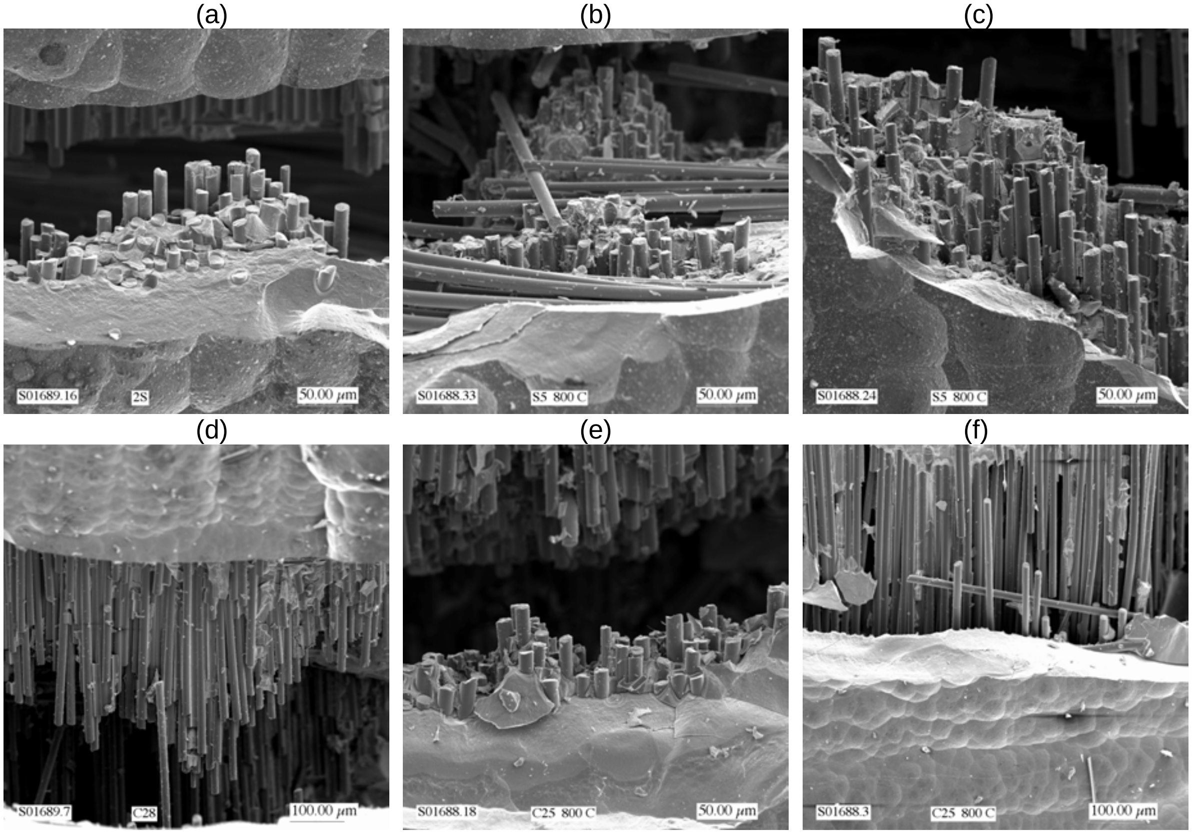

Figures 4(a-f). SEM micrographs showing characteristic fiber pull-out at tensile surface of bend bars tested at RT or 800°C: type S at (a) RT, (b) 800°C and (c) 800°C, respectively; and Hi-Nicalon at (d) RT, (e) 800°C and (f) 800°C, respectively.

decrease in the non-linear slopes. Several typical SEM views of fracture surfaces for the 2D type S and Hi-Nicalon™ composites taken at the tensile surface of the broken bend bars are compared in Figures 4(a-c) and 4(d-f), respectively. For the type S material tested at either RT or 800°C, Figures 4(a-c) reveal relatively short (10-50 μm), but random fiber pull-out lengths within a fiber bundle. Such observations were typical of views taken at many other locations. For the Hi-Nicalon™ material, some views revealed similar short, random pull-out length distributions (Figure 4e), but others revealed noticeably longer, and a not so random distribution of pull-out lengths (Figures 4d at RT and 4f at 800°C). The short, but random distribution of fiber pull-out lengths exhibited by the type S material are characteristic of a composite with relatively high fiber-matrix interfacial shear stresses as well as with uniformly high individual fiber strengths within the fiber bundles. Such stochastic fracture behavior leads to a desirable, relatively high proportional limit stress and also a gradual transitioning from linear to non-linear stress-strain, as observed. Although the mechanical properties of the Hi-Nicalon™ composite were quite good, the occurrence of some fiber bundles with longer and less randomly distributed fiber pull-out lengths suggests somewhat poorer fiber bundle infiltration for this material. This characteristic then leads to a slightly diminished proportional limit stress (160 and 180 MPa at RT and 800°C, respectively) compared to the type S material and a more abrupt transitioning from linear to non-linear stress-strain, also as observed.

For either 2D composite, the minimum fusion design strength and stiffness requirements can be met by ICVI-processing. Unfortunately, it does not appear likely that minimum fusion K_{eff}-goals can be obtained even for an optimized 2D SiC_f/SiC composite system when using the CVI process for matrix infiltration. The margin of improvement required to meet fusion design K_{eff}-goals is just too large for only minor improvements potentially possible through CVI-processing upgrades or structural or architectural methods. Other strategies to obtain fusion K_{eff}-goals are recommended.

Future Work

Slow crack growth tests currently are being performed on compact tension samples cut from the eight-ply Hi-Nicalon™ type S plate. Additional bars and discs of the six-ply material are available for testing by others.

Acknowledgments

This research was supported by the U.S. DOE Office of Fusion Energy. Ken Cartwright performed the thermal diffusivity measurements, and John Keaveney performed the 4-pt. bend tests.

References

[1] L. Giancarli, "SiC/SiC Designs and Main Resulting Issues," p. 1 in the 5th IEA workshop on SiC/SiC ceramic matrix composites for fusion structural applications, Eds. R.H. Jones, B. Riccardi and A. Kohyama, April 12-13, 2002, San Diego, CA.

[2] T. Hinoki, et al., "The effect of high dose/high temperature irradiation on high purity fibers and their silicon carbide composites," J. of Nuclear Materials, 307-311 (2002) 1157-1162.

[3] D. J. Senor, G. E. Youngblood, C. E. Moore, D. J. Trimble, G. A. Newsome and J. J. Woods, "Effects of neutron irradiation on thermal conductivity of SiC-based composites and monolithic ceramics," Fusion Technology 30(3) 943-955 (1996).

[4] G. E. Youngblood, D. J. Senor and R. H. Jones, "Modeling the transverse thermal conductivity of 2D-SiC_f/SiC composites made with woven fabric: Results for composites made with Hi-Nicalon, Tyranno SA and Hi-Nicalon type S fabrics," presented at the 2002 ANS Winter Meeting, Washington D.C., November 17-21, 2002.

[5] D. J. Senor, G. E. Youngblood, D. V. Archer and C. E. Chamberlin, "Recent progress in thermal diffusivity testing of SiC-based materials for fusion reactor applications," p. 102 in the 3rd IEA workshop on SiC/SiC ceramic matrix composites for fusion structural applications, Eds. R. H. Jones and A. Kohyama, January 29-30, 1999, Cocoa Beach, Florida.

[6] G. E. Youngblood, D. J. Senor and R. H. Jones, "Modeling the transverse thermal conductivity of 2D-SiC_f/SiC composites," p. 57 in the Fusion Materials Semiannual Progress Report for Period Ending December 31, 2001. (DOE/ER-0313/31)

[7] G. E. Youngblood, D. J. Senor, R. H. Jones and Witold Kowbel, "Optimizing the transverse thermal conductivity of 2D-SiCf/SiC composites, II. Experimental," J of Nuclear Materials, 307-311 (2002) 1120-1125.

[8] G. E. Youngblood, R. H. Jones, W. Kowbel, Reiji Yamada, Paul deHeij, Toshihiro Ishikawa and Akira Kohyama, "The 'KFIB' fiber thermal conductivity experiment," p. 175 in the 4th IEA workshop on SiC/SiC ceramic matrix composites for fusion structural applications, Eds. B. Riccardi, R. H. Jones and A. Kohyama, October 12-13, 2000, Frascati, Italy.

THERMAL DIFFUSIVITY/CONDUCTIVITY OF IRRADIATED HI-NICALON™ 2D-SIC$_F$/SIC COMPOSITE-

G. E. Youngblood, D. J. Senor and R. H. Jones (Pacific Northwest National Laboratory)*

NOTE: This report was inadvertently left out of the previous FMSPR (DOE/ER-0313/33). Two companion papers did appear in the previous FMSPR, "Thermal diffusivity/conductivity of irradiated Sylramic™ 2D-SiCf/SiC composite" and "Thermal diffusivity/conductivity of irradiated monolithic CVD-SiC." For continuity, these reports should be read in sequence since the details for all three experiments and the description of the H2L model are given in this report.

OBJECTIVE

The primary objective of this task is to assess the thermal conduction properties of SiC$_f$/SiC composites made from SiC fibers (with various SiC-type matrices, fiber coatings and architectures) before and after neutron irradiation, and to develop analytic models that describe the transverse and in-plane thermal conductivity of these composites as a function of constituent properties and geometry as well as temperature and radiation dose.

SUMMARY

The H2L model was used to critically assess degradation within the individual fiber, fiber coating and matrix components for irradiated 2D-SiC$_f$/SiC composite made with an ICVI-SiC matrix and Hi-Nicalon™ fabric. The composites were made with either a 1.044-μm ("thick") or a 0.110-μm ("thin") PyC fiber coating and were irradiated in the HFIR reactor as part of the JUPITER 12J (355°C, 7.1 dpa-SiC) or 14J (330 and 800°C, 5.8 and 7.2 dpa-SiC, respectively) series. Laser flash diffusivity measurements were made on representative samples before and after irradiation and after various annealing treatments.

The ratio of the transverse thermal conductivity after to before irradiation (K_{irr}/K_o) determined at the irradiation temperatures and predicted by the H2L model were: 0.18, 0.23 and 0.29 for the 330, 355 and 800°C irradiations, respectively. Thermal diffusivity measurements in air, argon, helium and vacuum indicated that physical separation of the fiber/matrix interface was minimal after the irradiations, but was significant after annealing irradiated composites to 1200°C. These results suggest that during irradiation to 6 dpa or more radial swelling of the PyC interface would compensate for the radial shrinkage of the Hi-Nicalon™ fiber and the SiC matrix swelling. The fiber shrinkage is due to irradiation-induced grain-growth and recrystallization and the matrix swelling is due to accumulation of irradiation-induced point defects. However, when the irradiation induced swelling in the matrix and fiber coating components was removed by recombination of point defects during high temperature annealing there was significant fiber/matrix separation.

PROGRESS AND STATUS

Introduction

To predict the overall thermal conductivity (K_{eff}) for a SiC$_f$/SiC composite made with stacked, woven fabric layers, the hierarchical two-layer (H2L) model was developed [1]. In this H2L model, the composite architecture is represented by alternating SiC fabric layers in series with SiC matrix layers that usually contain considerable amounts of porosity. The H2L model describes K_{eff} in terms of the composite constituent (fiber, fiber coating and matrix) properties as well as the fiber/matrix (f/m) interfacial effects and the porosity amount, distribution, shape and orientation. In this report, the H2L model is used to critically assess degradation within the individual constituents for irradiated SiC$_f$/SiC composites made

---

* Pacific Northwest National Laboratory (PNNL) is operated for the U.S. Department of Energy by Battelle Memorial Institute under contract DE-AC06-76RLO-1830.

with an ICVI-SiC matrix and Hi-Nicalon™ fabric. The model equations and definitions were presented in a previous semi-annual report and at the recent 5th IEA SiC/SiC workshop where they were applied to the unirradiated 2D-SiC$_f$/CVI-SiC systems made with either Hi-Nicalon™ or Tyranno™ SA fabrics [1,2].

Composite Samples

The Hi-Nicalon™ composite was made by DuPont with either a "thin" (0.110 μm) or a "thick" (1.044 μm) pyrolytic carbon (PyC) fiber coating applied by CVD prior to matrix infiltration. The Hi-Nicalon™ fabric was plain-weave (PW) in a 0-90 layup for both cases. Four thermal diffusivity samples of each type (9.3 mm dia. X 2.3 mm thick) were diamond-cored from plates. The bulk density values, determined by simple weighing and measuring of the disc dimensions, were in the range 2.50-2.60 g/cc. Several flexural bars of each type composite also were cut from the plates. Example SEM views of the typical two-layer fabric/matrix macroscopic structures for these composites were given in a previous report [1].

Irradiation and Test Conditions

The thermal diffusivity of the unirradiated discs was measured in air as a function of temperature up to about 400°C by the laser flash method described elsewhere [3]. The sample discs with "thick" and "thin" interfaces were irradiated in the HFIR reactor at ORNL as part of the JUPITER 12J and 14J test series, respectively. Only two discs with "thick" interface (D1 and D2) were recovered after irradiation at 355 ± 35 °C to an equivalent dose of 7.1 dpa-SiC in 12J. Three discs were recovered after irradiation in 14J (JD2 at 330 ± 20°C, 5.8 dpa-SiC and JD3 and JD4 at 800 ± 5°C, 7.2 dpa-SiC).

Two separate laser flash diffusivity systems, a "low" and a "high" temperature one, were used to make the thermal diffusivity measurements after irradiation. Measurements in the low temperature system were made in air from RT up to about 400°C. The high temperature system was contained inside a steel bell jar so that diffusivity measurements could be made in vacuum or in different inert atmospheres (argon or helium). Measurements in the high temperature system were made from about 200°C up to the irradiation temperature. In addition, in situ post-irradiation annealing treatments in argon up to the irradiation temperature and beyond to 1200°C also were made in the high temperature system. Finally, four other unirradiated disc samples (two with each fiber coating thickness) were heated in air for 15 hours at 700°C to remove the PyC fiber coating by oxidation. The coating "burn-out" temperature was about 100°C below that where significant SiO_2 formation begins, so the PyC coatings were removed without sealing off the interface layers. Later, weight change measurements confirmed that this likely was the case. In an attempt to determine the composite matrix contribution to the thermal conductivity alone, the thermal diffusivity was then remeasured for each pair of samples, now with the fibers physically separated from the matrix. Other diffusivity measurements were made sequentially on specific samples before and after irradiation (and during and after annealing treatments) and in different atmospheres.

Results and Discussion

In Figures 1(a-b), the thermal diffusivity values as a function of temperature for the Hi-Nicalon™ ICVI-SiC composites with (a) "thick" and (b) "thin" PyC interfaces for various conditions are presented. The conditions in sequence of performance were: [1] average diffusivity values for four as-received samples (heavy solid line) and [2] average values for two unirradiated samples with PyC interface removed by oxidation (light solid line). Then for two specific irradiated samples in sequence of performance ("thick" = D1 and D2, irradiated at 355°C, 7.1 dpa and "thin" = JD2 irradiated at 330°C, 5.8 dpa-SiC and JD3 at 800°C, 7.2 dpa-SiC) and with open or filled data points separating the pairs of samples: [3] values in air (dashed lines), [4] values in vacuum (short dashed lines), [5] values in argon during in situ annealing from about 200°C up to 1200°C (2-hr hold time) and after as the temperature was decreased back to 200°C (diamond data points with dashed-dot lines), [6] values in vacuum from 200-400°C (short dashed lines), [7] values in helium from 200-400°C (long dashed lines), and finally [8] values in air again from RT up to

400°C (dashed lines).

Previously reported H2L-model results for the as-received Hi-Nicalon™ composites indicated that the matrix porosity content and shape factors had a large impact on K_{eff}. The relevant measured and calculated data from reference [1] are reviewed in Table 1.

Table 1. Measured and calculated data for Hi-Nicalon™ composites with different interface thickness.

Type	t (μm)	ρ_b (g/cc)	f_M	f_p	P_{avg}	P_M	β	K_{eff} 200C (W/mK)	K_{eff} 1000C (W/mK)
"thick"	1.044	2.63	0.31	0.65	0.073	0.062	1.3	15	10
"thin"	0.110	2.60	0.29	0.67	0.126	0.107	1.3	15	8.5

In Table 1: t is the PyC interface thickness; ρ_b is the composite bulk density; f_M, f_p and P_M (measured from several SEM views) are the fractional matrix layer, fabric layer fiber packing and matrix layer macroporosity contents, respectively; P_{avg} is the calculated overall composite porosity content; β is the matrix layer macroporosity shape and orientation factor; and K_{eff} is the measured composite thermal conductivity at 200°C and 1000°C, respectively. Both composite types, made by the same isothermal-CVI process with similar Hi-Nicalon™ fabric layups, had similar values of ρ_b, f_M, f_p and β. However, the composite with the "thin" interface had noticeably higher porosity contents (P_{avg} and P_M) compared to the composite with the "thick" interface, which likely is somewhat responsible for the slightly lower K_{eff}-values observed for the "thin" interface composite.

Assuming that the temperature dependent equivalent fiber coating and the "intrinsic" matrix thermal conductivity values ($K_c(T)$ and $K_m(T)$, respectively) each were the same for each composite type (which primarily differed only in the thickness of their PyC interface), the H2L-model predicted that values of K_c and K_m ranged from maximum values of 34 and 40 W/mK (at 200°C) down to 28 and 18-20 W/mK (at 1000°C), respectively. Apparently K_c had more impact on K_{eff} for the composite with the thick interface where conduction along the interface begins to become important. For this reason, the somewhat shallow temperature dependence predicted for $K_c(T)$ was responsible for the separation between the K_{eff}-values observed for the "thick" and "thin" composites, particularly as temperatures were increased.

When the PyC interfaces were removed by oxidation, the thermal diffusivity values for each composite dramatically decreased about 60% of their as-received values (Figures 1(a-b)). If it is assumed that only the individual fiber filaments were thermally separated by the oxidation treatment (i.e., equivalent to treating the fiber content simply as an additional porosity content), the H2L model would predict that the decrease in values should have been about 40% rather than the observed 60%. Apparently entire fiber bundles (and the included continuous matrix within the bundles) were thermally separated by the treatment. In fact, if about 85% of the fiber bundles were assumed thermally separated from the matrix in their entirety, the H2L model predictions would match the observed results.

Detailed SEM cross-section views near the edge of a fiber bundle in the composite with a "thick" interface before and after the oxidation treatment are shown in Figures 2(a-b), respectively. In Figure 2a, generally good infiltration of the ICVI-SiC matrix with pore-free bonding to the individual filaments is observed. A few needle-like pores (axis parallel to the fiber lengths) are observed at interstices between the matrix radial growth patterns. A significant amount of fiber coating interconnectivity also is observed. As shown in Figure 2b, when the interconnected PyC fiber coating was removed large sections of the matrix within the fiber bundle also became separated from the remaining matrix. The thermal diffusivity of the samples with their interface removed by oxidation also was measured in vacuum and in helium atmospheres. Compared to the values measured in air, the thermal diffusivity increased by 15-30% when measured in

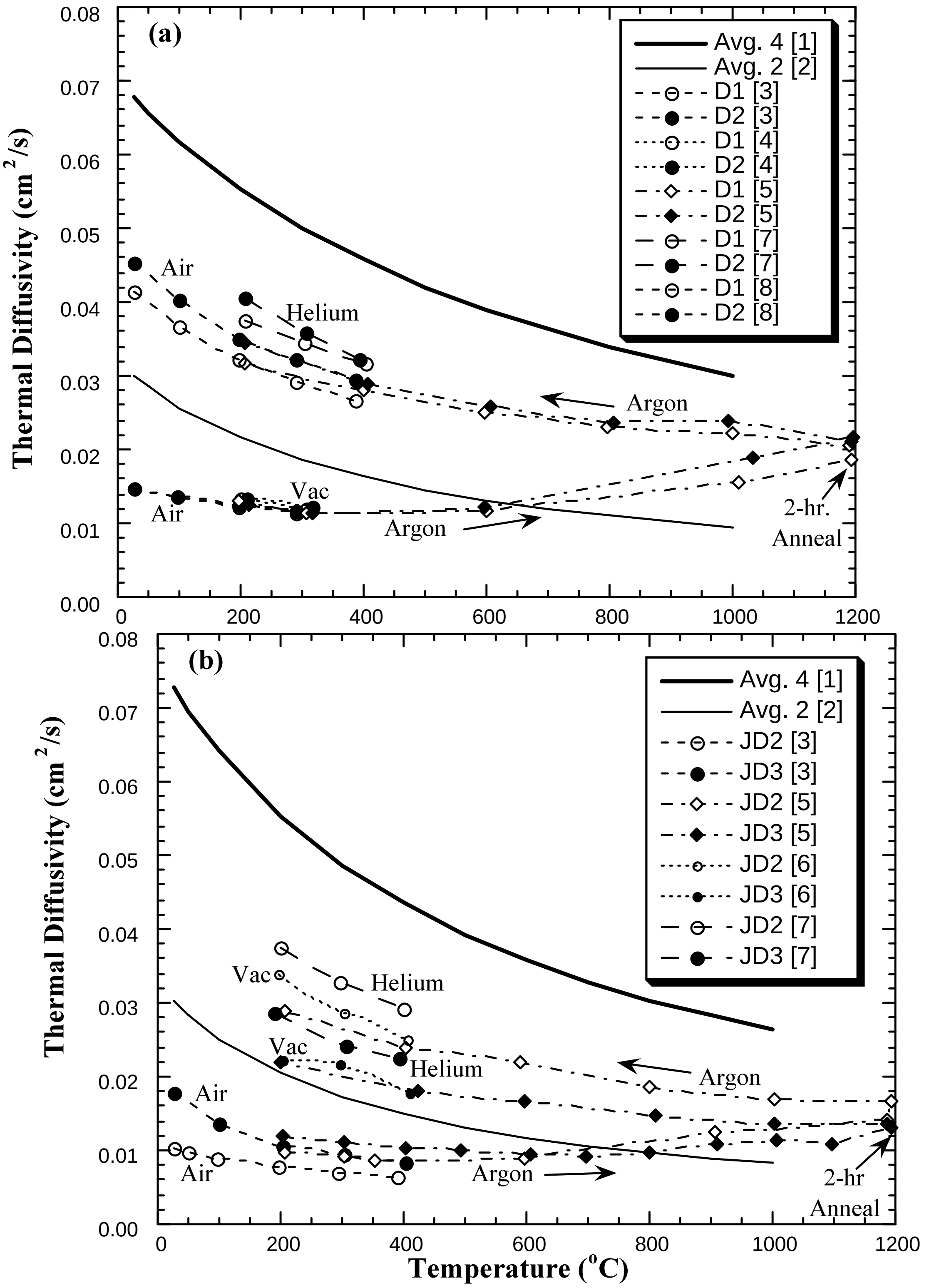

Figure 1(a-b). Thermal diffusivity of 2D Hi-Nicalon™/ICVI-SiC composites with (a) “thick” and (b) “thin” PyC interface for various unirradiated and irradiated conditions. See text for key.

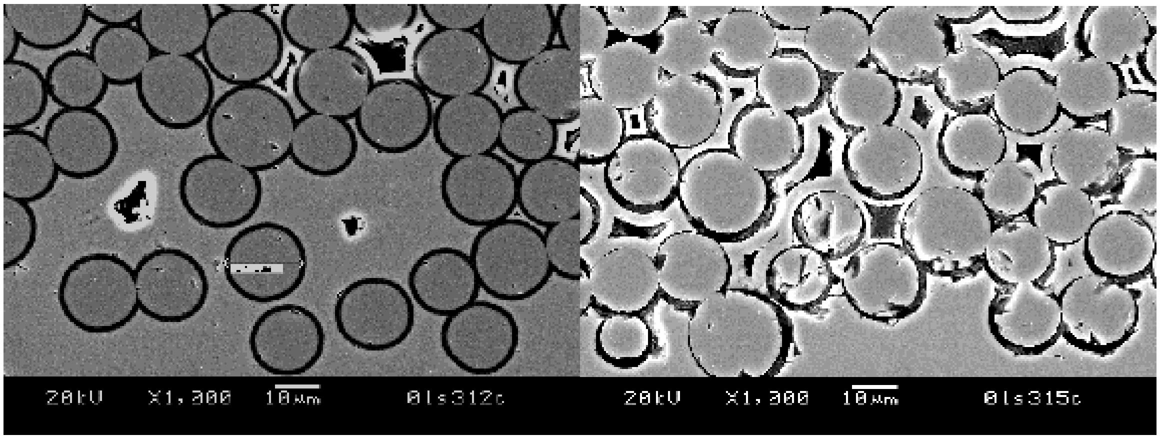

(a) (b)

Figure 2(a-b). Cross-section SEM views of a region near the edge of a fiber bundle in the Hi-Nicalon™ composite with a "thick" interface (a) before and (b) after removal of the interface by oxidation in air at 700°C for 15 hours.

helium, and it decreased by 20-40% when measured in vacuum (data not shown in Figure 1). Such effects are expected for composites with physical gaps formed at numerous fiber/matrix interfaces where the interfacial conductance depends upon the thermal conduction of the atmosphere within these gaps [6].

After irradiation, the thermal diffusivity of each composite was severely degraded. The degradation was significantly larger for the irradiations at 330 and 355°C compared to those at 800°C. The actual thermal diffusivity values before and after irradiation determined from Figures 1(a-b) at three different irradiation temperatures are listed in Table 2. If it is assumed that the density and heat capacity values weren't significantly affected by the irradiation, then the ratio of the thermal diffusivity values after to before irradiation is approximately equal to the ratio of the thermal conductivity after to before irradiation, K_{effi}/K_{effo}. This ratio also is listed in Table 2.

Table 2. Comparison of thermal diffusivity values for the Hi-Nicalon™ composites with "thick" and "thin" PyC interfaces determined at their irradiation temperature.

Quantity	"Thick," 355°C	"Thin," 330°C	"Thin," 800°C
T Diff (before irrad.), cm^2/s	0.047	0.049	0.031
T Diff (after irrad.), cm^2/s	0.0108	0.0090	0.0088
K_{effi}/K_{effo} (after/before)	0.23	0.18	0.29
H2L-model T Diff predict after irradiation,* cm^2/s	0.0113	0.0088	0.0086

* Assumed constituent values $K_{fi} = 0.5K_{fo}$, $K_{ci} = 0.5K_{co}$ and $K_{mi} = 0.1K_{mo}$ after irradiation.

The relative degradation ratios are slightly lower than similar ratios determined previously for 2D-SiC_f/SiC composite made with Nicalon™ CG fabric with a "thin" PyC interface and irradiated to doses in excess of 25 dpa-SiC (0.27 at 500°C, 0.40 at 800°C and 0.50 at 1000°C) [5]. However, the general trend that this ratio tends to gradually increase with increasing irradiation temperature is consistent. Note that all the thermal diffusivity values measured for irradiated samples represent saturated conditions, i.e., all the irradiation doses were well above saturation doses for SiC.

After measuring the thermal diffusivity in air up to about 400°C in the low temperature system, the samples were remounted in the high temperature system and measurements continued in argon up to 1200°C. Excellent agreement of the thermal diffusivity values occurred for the 200-400°C overlap region for the composite with "thick" interface, while the agreement was within 20% for the composite with "thin" interface when measured in the different laser systems in air or argon. Agreement within 20% is considered barely within uncertainty limits for such measurements; nevertheless continuity of the thermal diffusivity values through the temperature overlap region was assumed.

Once the annealing temperature exceeded the irradiation temperature, the thermal diffusivity was observed to increase with further increase in temperature in three steps up to 1200°C, where the samples were held for two hours to complete the anneal of the irradiation induced point defects. After the 2-hr anneal at 1200°C, the thermal diffusivity values at 1200°C for each composite returned to about 70-80% of expected unirradiated values at that temperature. Further thermal diffusivity measurements were made in argon as the temperature was then decreased in several steps from 1200°C down to 200°C. Although sample JD3 irradiated at 800°C initially had higher thermal diffusivity than sample JD2 irradiated at 300°C, after annealing at 1200°C the reverse situation occurred, i.e., the thermal diffusivity of JD2 was significantly higher than that of JD3. This observation can be qualitatively explained if the thermal diffusivity degradation is considered primarily due to the accumulation and recombination of irradiation induced point defects in the matrix constituent. Since saturation in SiC occurs for a lower concentration of defects at higher irradiation temperatures (at least up to 800°C, or so), the thermal diffusivity degradation for the 800°C irradiation is expected to be less than for the 330-355°C irradiations, as observed. However, in SiC after an 800°C irradiation to saturation the relative amount of recovery is less than after a similar 330-355°C irradiation. In fact, after the annealing treatment and returning to 200°C the thermal diffusivity of the composite irradiated at 330°C is about 25% higher than that of the composite irradiated at 800°C. Similar trends have been observed in the recovery of volume swelling for irradiated and annealed monolithic SiC [7].

The thermal diffusivity of a fiber-reinforced SiC/SiC composite has been shown to be sensitive in some cases to the actual condition of the relatively thin fiber/matrix (f/m) interface [6]. In particular, if physical gaps are formed at composite f/m interfaces, e.g., due to removal of a PyC fiber coating by oxidation or due to differential f/m shrinkage-swelling caused by the different effects of the irradiation in each constituent, the thermal diffusivity becomes dependent on the gas atmosphere within the gaps. Interestingly, after the 355°C irradiation of the composite with a “thick” PyC interface, the thermal diffusivity measured in vacuum was almost identical to the values measured in air or argon in the 200-350°C overlap region. Apparently, at this point physical f/m gaps did not exist in the irradiated composites even though the matrix was expected to swell about 0.8% and the Hi-Nicalon™ fiber was expected to shrink about 1.7%. The radial swelling in the irradiated PyC fiber coating with its somewhat anisotropic microstructure is estimated to be larger than 2% (with a commensurate axial shrinkage of about 0.7%). At least it is plausible that the expected swelling at 6 dpa in the PyC interface compensated somewhat for the differential shrinkage-swelling in the f/m components, and significant f/m thermal decoupling in the composite no longer existed. However, radial tensile stresses generated at lower doses (1-2 dpa, i.e., low enough so that swelling in the PyC fiber coating were not yet substantial) likely were sufficient to cause serious f/m debonding and loss of composite strength.

After annealing and cooling the composites to the 200-400°C range, the thermal diffusivity was remeasured with different atmospheres (vacuum and helium) admitted into the bell-jar enclosure. Although some inconsistency occurred for the measurements made in vacuum, for the measurements made in helium the thermal diffusivity values were significantly greater than values measured in air, argon or vacuum for all three cases.

Apparently, the relative shrinkage-swelling situation changed when the irradiated and annealed composites were then cooled back to the 200-400°C temperature range. The shrinkage in the irradiated Hi-Nicalon fiber, caused by irreversible recrystallization and grain growth, was permanent. Meanwhile, the swelling and partial recovery in the irradiated and annealed SiC matrix, caused by accumulation and then recombination of point defects, was reversible. Therefore, the final situation appears to be a matrix with dimensions similar to the pre-irradiation conditions, while the fiber dimensions were significantly reduced. The shrinkage-swelling situation in the irradiated and annealed PyC interface is more complex, since irradiated PyC does not exhibit saturation effects, and the swelling (or shrinkage) is highly temperature and dose dependent. Nevertheless, significant physical f/m separation must have occurred in the irradiated, annealed and cooled composites to account for the noticeable dependence of their thermal diffusivity values on atmosphere.

Finally, the H2L model was used to predict the expected thermal diffusivity values from RT to 200°C for the Hi-Nicalon™ composites with complete thermal decoupling of the fiber constituent (i.e., let $K_c = 0$), but with no other changes in the matrix or porosity factors. For each composite, the predicted values closely matched the observed magnitudes and slopes of the measured thermal diffusivity values, at least in this narrow temperature range. Perhaps somewhat fortuitous, such agreement with model predictions nevertheless suggests that the described thermal and dimensional behavior of the irradiated and annealed Hi-Nicalon™ composites is consistent.

Future Work

Flexural stress-strain measurements will be made on bar samples of the Hi-Nicalon™ composites with “thick” and “thin” PyC interfaces, also irradiated in the 12J and 14J experiments. Results will be compared to a recently developed stress-strain model for such composites. The mechanical property results will be correlated with the thermal property results.

Acknowledgments

The U.S. DOE Nuclear Energy Research Initiative (NERI) funded the model development work.

References

[1] G. E. Youngblood, D. J. Senor and R. H. Jones, “Modeling the transverse thermal conductivity of 2D-SiC_f/SiC composites,” p. 57 in the Fusion Materials Semiannual Progress Report for Period Ending December 31, 2001. (DOE/ER-0313/31).

[2] G. E. Youngblood, D. J. Senor, R. H. Jones and Y. Katoh, “Modeling the thermal conductivity of 2D-SiC_f/SiC composites with woven architectures,” p. 36 in the Proceedings of the 5th IEA SiC/SiC Workshop April 12-13, 2002, San Diego, CA (PNN-SA-37623).

[3] D. J. Senor, G. E. Youngblood, D. V. Archer and C. E. Chamberlin, “Recent progress in thermal diffusivity testing of SiC-based materials for fusion reactor applications,” p. 102 in the Proceedings of the 3rd IEA SiC/SiC Workshop, January 29-30, 1999, Cocoa Beach, Florida.

[4] G. E. Youngblood, D. J. Senor, W. Kowbel, J. Webb and Akira Kohyama, “Thermal conductivity of SiC and C fibers,” p. 113 in Fusion Materials Semiannual Progress Report for period ending December 31, 1999 (DOE/ER-0313/27).

[5] D. J. Senor, G. E. Youngblood, C. E. Moore, D. J. Trimble, G. A. Newsome, and J. J. Woods, “Effects of neutron irradiation on thermal conductivity of SiC-based composites and monolithic ceramics,” Fusion Technology 30(3), 943-955, (1996).

[6] G. E. Youngblood and R. H. Jones, “The transverse thermal conductivity of 2D-SiC_f/SiC composites,” p. 190 in the Proceedings of the 4th IEA SiC/SiC Workshop, October 12-13, 2000, Frascati, Italy.

[7] R. J. Price, “Annealing behavior of neutron-irradiated SiC temperature monitors,” Nuclear Technology 16, 536-542 (1972).

3.0 FERRITIC/MARTENSITIC STEELS

FRACTURE TOUGHNESS VARIABILITY IN F82H - D. S. Gelles (Pacific Northwest National Laboratory)[*], and Mikhail A. Sokolov (Oak Ridge National Laboratory)

OBJECTIVE

The objective of this effort is to better understand the fracture toughness response of low activation ferritic steel F82H.

SUMMARY

The fracture toughness database for F82H displays some anomalous behavior. Metallographic examination reveals banding in the center of 25 mm thick F82H plate, which is more evident in transverse section. The banding is shown to arise because some grains are etched on a very fine scale whereas the remainder is etched more strongly and better delineates the martensite lath structure. However, the banding found does not provide explanation for the anomalous fracture toughness behavior.

PROGRESS AND STATUS

Introduction

Fracture toughness measurements of 25 mm F82H plate [1] are showing indications of non-uniform behavior as a function of thickness. The point was most clearly made by Wallin and colleagues [2] based on small specimen testing reported in the 4th ASTM symposium on Small Specimen Test Techniques. They found larger than normal scatter for master curve analysis of their F82H data, and because they had kept track of the plate location of each tested specimen, they were able to show degraded behavior for some of the specimens coming from a region 12-17 mm from the plate upper surface, (and less so for specimens adjacent to the upper surface.) Also, cleavage initiation site examination of compact tension specimens of full thickness geometries showed initiation had consistently occurred in the 12-17 mm layer. Therefore, a lower toughness zone was indicated for the mid thickness of the plate, and small specimens fabricated away from this central zone showed higher toughness. However, this behavior can be identified in ORNL and JAERI measurements as well, [3] as will be shown. The purpose of the present effort is to identify the microstructure features that may be responsible for this fracture toughness degradation.

Experimental Procedure

A piece of the grip area of a tested full thickness compact tension specimen was selected for optical metallography. Longitudinal- and cross-rolling directions were maintained. Sections parallel to the plate rolling direction (longitudinal) and perpendicular to the rolling direction (transverse) were prepared for metallographic analysis using standard procedures, and were then etched using Kellers etch (1% hydrofluoric acid, 1.5% hydrochloric acid, and 2.5% nitric acid in water) as a dip. Microscopy was performed using a JEM-840 Scanning Electron Microscope (SEM) operating at 20 KeV equipped with a backscatter detector. Images were stored digitally.

Results

<u>Metallography</u>

Both etched samples of the full plate thickness revealed a difference in microstructural contrast towards the center. Examples are given in Figures 1 and 2 showing a mosaic for the full thickness of the

---

[*] Pacific Northwest National Laboratory (PNNL) is operated for the U.S. Department of Energy by Battelle Memorial Institute under contract DE-AC06-76RLO-1830.

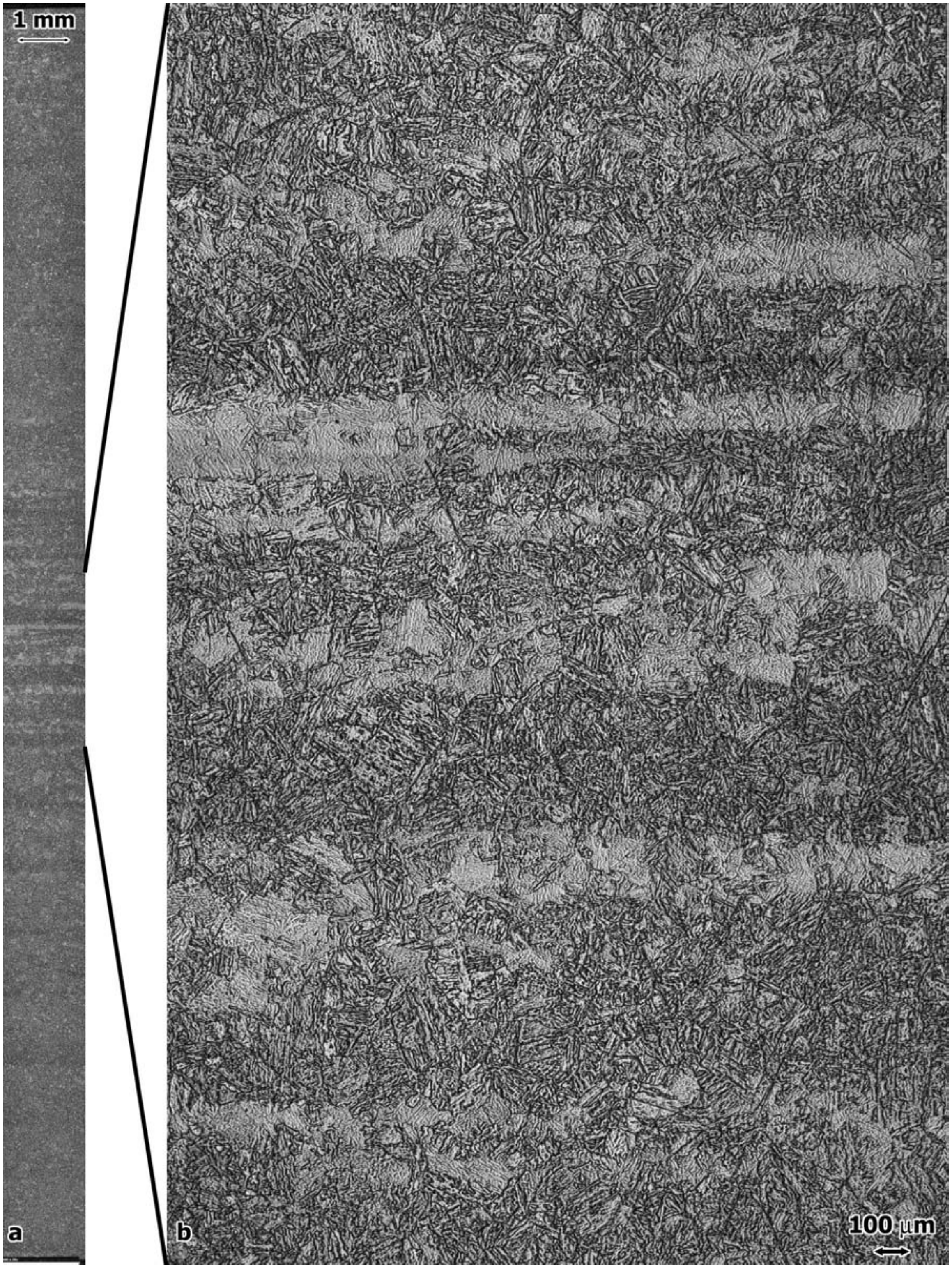

Figure 1. Transverse section etched microstructure of F82H plate showing in a) a mosaic of the microstructure across the full width of the 25 mm plate and in b) the central region at higher magnification.

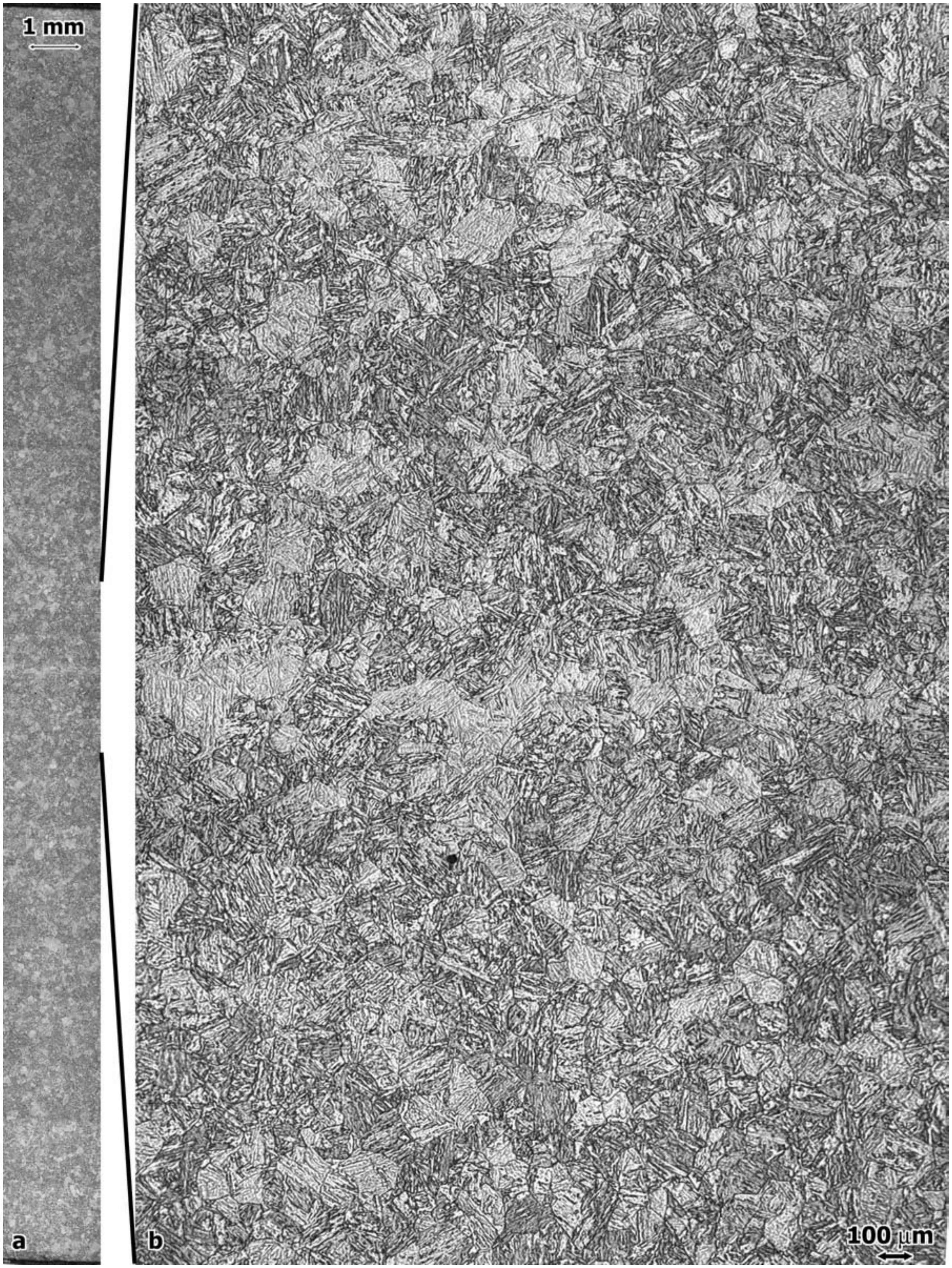

Figure 2. Longitudinal section etched microstructure of F82H plate showing in a) a mosaic of the microstructure across the full width of the 25 mm plate and in b) the central region at higher magnification.

transverse section in a) and the central region of the sample in b) for transverse and longitudinal sections, respectively. Bands can be identified that appear lighter and contain less structure. The difference in contrast appears to be due to the fact that these bands are less heavily etched than are neighboring bands or other regions away from the center. The distribution of grains showing less etching is different for the transverse and longitudinal section, indicating that the bands appear more often in the transverse direction and are concentrated at the center of the plate.

Scanning Electron Microscopy

SEM verified that the central bands showing less contrast were less affected by the etchant. Examples are provided in Figure 3, showing six views, the first four using a backscatter detector so that carbide particles show up brightly. Figure 3a) shows an area at low magnification containing both structures, with the area towards the upper left corresponding to the structure showing less etching. Note the two large carbide particles probably on prior-austenite grain boundaries at the upper left. Figure 3b) provides the central area at higher magnification, revealing evidence for lath structure within the less etched region. Figures 3c) and d) show comparison of the etch variations at higher magnification. The less etched region in Figure 3c) is found to contain very fine structure whereas the strongly etched region actually contains two types of features, one deeply etched and the second showing very little structure. The final two examples are similar, but at slightly lower magnification and without the backscatter detector. Therefore, the effect of etching is to produce bands of grains that are very finely etched within the remaining grains that etch non-uniformly, and better reveal the martensite lath structure.

Discussion

The variations in fracture toughness for 25 mm thick F82H plate obtained by Wallin and colleagues [2] at VTT Manufacturing Technology, Finland are best demonstrated in the figures reproduced from their work in Figure 4 showing behavior in 5 x 5 x 27 mm notched bend bars. Similar behavior can be identified in smaller 3 x 4 x 7 mm bend bars but the trends are not as clear. Figure 4a) shows master curve analysis of the data with many points clearly below the 95% confidence limits. Figure 4b) compares the results as a function of position in the 25 mm plate. It is clear that the solid triangles for samples prepared from the 12-17 mm layer are distributed into two groups, some within the master curve response but the remainder falling below the curve (and the remainder of the low points are for specimens taken from the 1.6-6.6 mm layer.) Therefore, it can be anticipated that there are features within the 12-17 mm layer that can reduce fracture toughness in the 25 mm F82H plate.

Similar behavior can be shown in results from ORNL and JAERI. Figure 5 provides a compilation of fracture toughness from these data bases [3]. It should be noted that JAERI testing was done at –40 and –60ºC, fitting the trend along with several other measurements below 100 MPa $m^{1/2}$ and above –100ºC. Therefore, fracture toughness behavior in the 25 mm thick plate of F82H can show response below expected master curve prediction and this behavior has been demonstrated worldwide.

It may be worth noting that unexpected response has been found both in Japan and Europe regarding fatigue crack propagation in F82H [4-5]. Fatigue generally results in transgranular crack propagation, but these tests on F82H showed intergranular cracking. The behavior was confirmed during recent studies of crack tip microstructures in F82H [6]. The cause is not yet understood.

Anomalous fracture toughness and fatigue cracking response can generally be attributed to either grain boundary weakening due to segregation or enhancement of sites promoting crack nucleation. As the most prominent crack nucleation sites are large carbides, and the largest carbides in martensitic steels such as F82H are generally on prior austenite grain boundaries, it is reasonable to expect that large carbides exist in the center of the F82H plate and are responsible. Note that fractography of the F82H specimens showing anomalously low toughness does not show intergranular fracture, and therefore grain boundary weakening due to segregation is unlikely to be relevant. Therefore, evidence of sites for

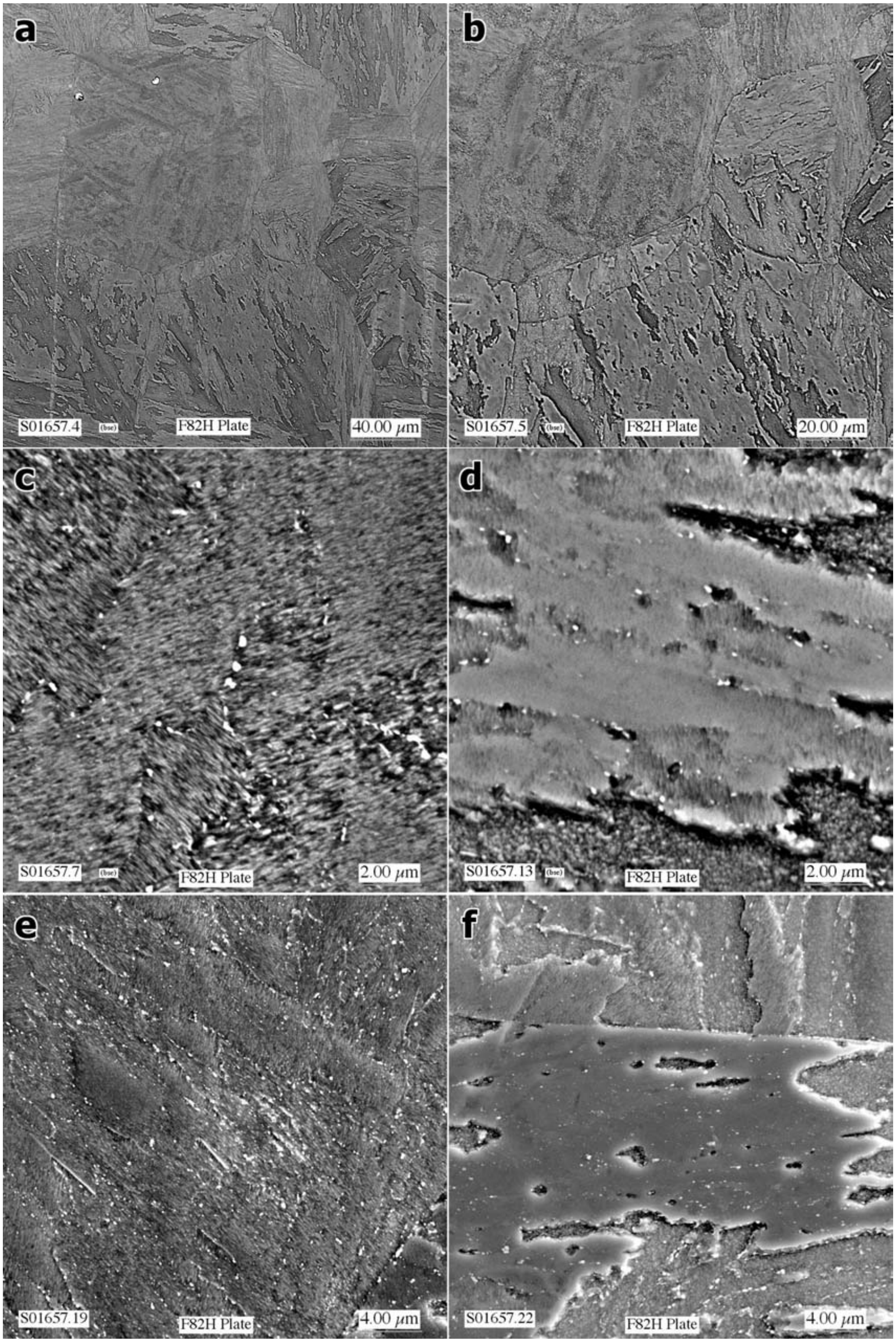

Figure 3. SEM images of the center of the transverse etched section.

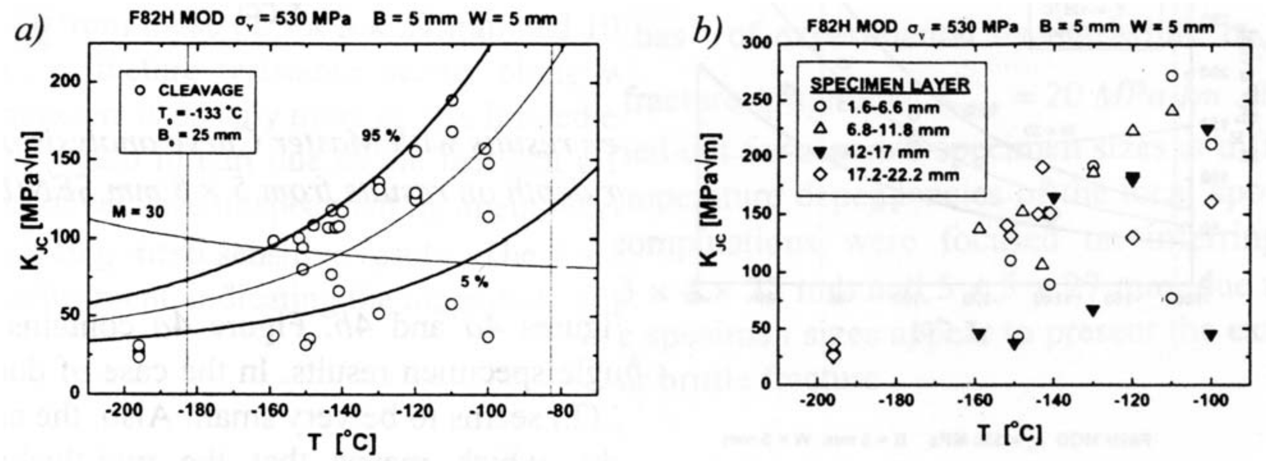

Figure 4. Fracture toughness of 5 x 5 x 27 mm bend bar specimens from reference [2].

enhanced crack nucleation in the plate center in the form of large carbide particles is most likely to explain the observed behavior.

It was noted that Figure 3a) contained two large carbide particles probably on prior austenite grain boundaries. Unfortunately, this evidence is insufficient to demonstrate the source of anomalous fracture toughness behavior because larger carbides do exist elsewhere in the plate, and a more complete statistical distribution of these large carbides is required. Also, the metallographic observation of bands in the center of the plate (shown in Figures 1 and 2) cannot be used to explain reduced toughness because no mechanism for enhanced fracture can be envisioned based on the structural differences of these bands. For example, the prior austenite grain size is similar not only for the lighter bands found metallographically and nearby darker grains, but also throughout the thickness. (A larger prior austenite grain size would enhance levels of carbide forming elements at boundaries and produce larger carbide particles.) Therefore, the present effort does not appear to provide sufficient information to explain anomalous fracture toughness response in F82H 25 mm plate.

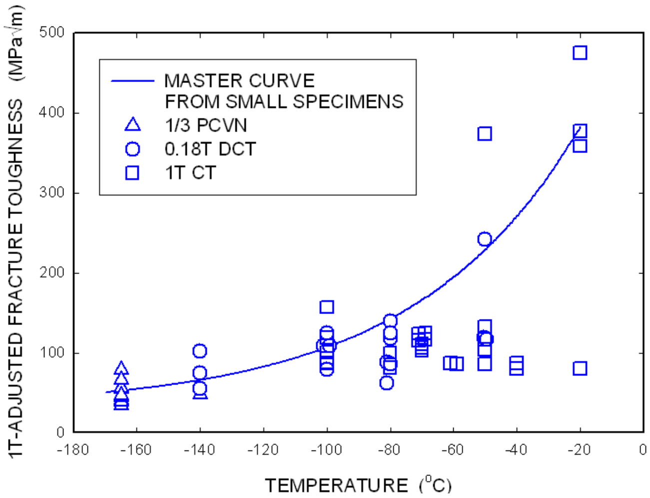

Figure 5. 1TCT fracture toughness data for 25 mm F82H plate from ORNL and JAERI.

It is likely that the problem is to envision a simple mechanism that creates larger carbides in the center of the plate and not elsewhere. Larger carbides may arise during casting because the center of the heat cools more slowly. The center is therefore the last to solidify and remains at higher temperatures longer, allowing more coarsening of particles that do not dissolve during heat treatment. After processing, the center of the billet would normally become the center of the plate. However, the 25 mm F82H plate was made from heat 9753 which was split into two parts to create 15 mm and 25 mm plate, and the 25 mm plate came from the ingot bottom [1]. The procedure whereby the plate was made from the bottom of the ingot is unclear, and so the center of the plate may not be directly traceable to the center of the ingot.

Conclusions

Fracture toughness measurements on 25 mm plate of F82H show anomalous response outside the Master Curve 95% confidence limits for specimens prepared from the center of the plate. Metallographic examination shows bands in the center of the plate that appear lighter and contain less structure. The difference in contrast appears to be due to the fact that these bands are less heavily etched than are neighboring bands or other regions away from the center. The distribution of grains showing less etching is different for the transverse and longitudinal section, indicating that the bands extend more often in the transverse direction and are concentrated at the center of the plate. SEM verified that the central bands showing less contrast were less affected by the etchant but the effect of etching is to produce bands of grains that are very finely etched within the remaining grains which are etched non-uniformly, and therefore better reveal the martensite lath structure. However, these results do not explain the anomalous toughness response.

Future Work

The effort will be continued as opportunities become available.

References

[1] Y. Takagi and A. Hishinuma in Proceedings of the IEA Working group Meeting on Ferritic/Martensitic Steels held February 1, 1995, ORNL/M-4230.

[2] K. Wallin, A. Laukkanen and S. Tähtinen in Small Specimen Test Techniques: Fourth Volume, ASTM STP 1418, M. A. Sokolov, J. D. Landes and G. E. Lucas, Eds., (ASTM International, West Conshohocken, PA, 2002) 33.

[3] M. A. Sokolov, this progress report

[4] H. Hanigawa, T. Hirose, M. Ando, S. Jitsukawa, Y. Katoh and A. Kohyama, J. Nucl. Mater., V. 307-311 (2002) 293.

[5] A. Möslang, and E. Doegele, reported at the 10th International Conference on Fusion Reactor Materials, 14-19 October 2001, Baden Baden, Germany.

[6] D. S. Gelles, G. R. Odette and P. Spätig in DOE/ER-0313/33 (2003) 79.

FURTHER EXAMINATION OF CRACK TIP MICROSTRUCTURES IN F82H ON THE LOWER SHELF -

D. S. Gelles (Pacific Northwest National Laboratory)*, G. R. Odette (University of California at Santa Barbara) and P. Spätig (École Polytechnique Fédérale de Lausanne, – Centre de Recherches en Physique des Plasma, Villigen PSI, Switzerland)

OBJECTIVE

The objective of this effort is to better understand deformation behavior in low activation ferritic steels with regard to fracture toughness testing.

SUMMARY

Dislocation microstructures have been further examined near the crack tip of a compact tension specimen of unirradiated F82H loaded to 25.6 MPa $m^{1/2}$ at –196°C after fatigue precracking. A specimen was prepared by sectioning, dimple grinding and ion milling to produce electron transparency just ahead of the crack tip. Further ion milling has allowed improved examination of the microstructure immediately ahead of the crack tip. It is found that subgrain structure is relatively unaffected near the crack tip whereas 3 µm from the crack tip, dislocation loop structure was identified.

PROGRESS AND STATUS

Introduction

In a previous report [1] procedures were described to allow observation of dislocation structures at the crack tip of a compact tension specimen. The specimen of F82H was fatigue precracked and then loaded to 25.6 MPa $m^{1/2}$ at –196ºC. It was then prepared for TEM by sectioning, dimple grinding and ion milling in order to produce electron transparency just behind the crack tip. The present effort is a continuation of that effort following further milling so that the structure ahead of the crack tip could be examined in greater detail.

Experimental Procedure

As described previously [1] a 0.4T compact tension specimen of F82H (0.35x0.84x0.89 $in.^3$) in the fully tempered precracked condition was loaded in order to produce crack tip deformation. The specimen, identified as P4-10, was fatigue precracked about half way through and then loaded to 25.6 MPa $m^{1/2}$ in a liquid nitrogen bath.

The specimen was then sectioned using a slow speed diamond-impregnated-bladed saw to provide a central longitudinal slice perpendicular to the crack surface and a 3 mm disk was cut with the crack tip located at the midpoint. One side was ground and polished to a high polish using 1-2 µm BN grinding compound and the other side was dimple ground to a thickness of ~10 µm with a similar final polish. Final thinning was performed on an ion mill using ultra high purity (99.999%) argon. Milling was centered just behind the crack tip with conditions for thinning 1 h at ±6º and 5 kV, and for final polishing 15 min at ±4º and 2 kV. The present effort included three further milling steps in order to allow improved examination of microstructure ahead of the crack tip.

Microscopy was performed using a Tecnai 30 Transmission Electron Microscope (TEM) operating at 300 KeV. All images were digitized from scanned negatives. Image processing included electronic dodging to compensate for negatives with very high contrast.

---

* Pacific Northwest National Laboratory (PNNL) is operated for the U.S. Department of Energy by Battelle Memorial Institute under contract DE-AC06-76RLO-1830.

Results

The thinned cross section sample of P4-10 was remilled and examined to determine the location of the region of electron transparency relative to the crack tip. After three attempts, only ~200 nm of the tip remained. The milling stages are shown in Figure 1, with the original transparent region reported previously labeled "1st", and subsequent milling stages labeled "2nd" through "4th". Following the 4th milling stage, the region that was electron transparent included more than 3 μm ahead of the crack tip.

The region in the vicinity of the crack tip was tilted repeatedly to provide g=200 dislocation contrast for most of the subgrain structure. The g=200 contrast will show all (a/2)<111> dislocations in the field of view. The images have been combined to provide the montage in Figure 2 intended to show as much

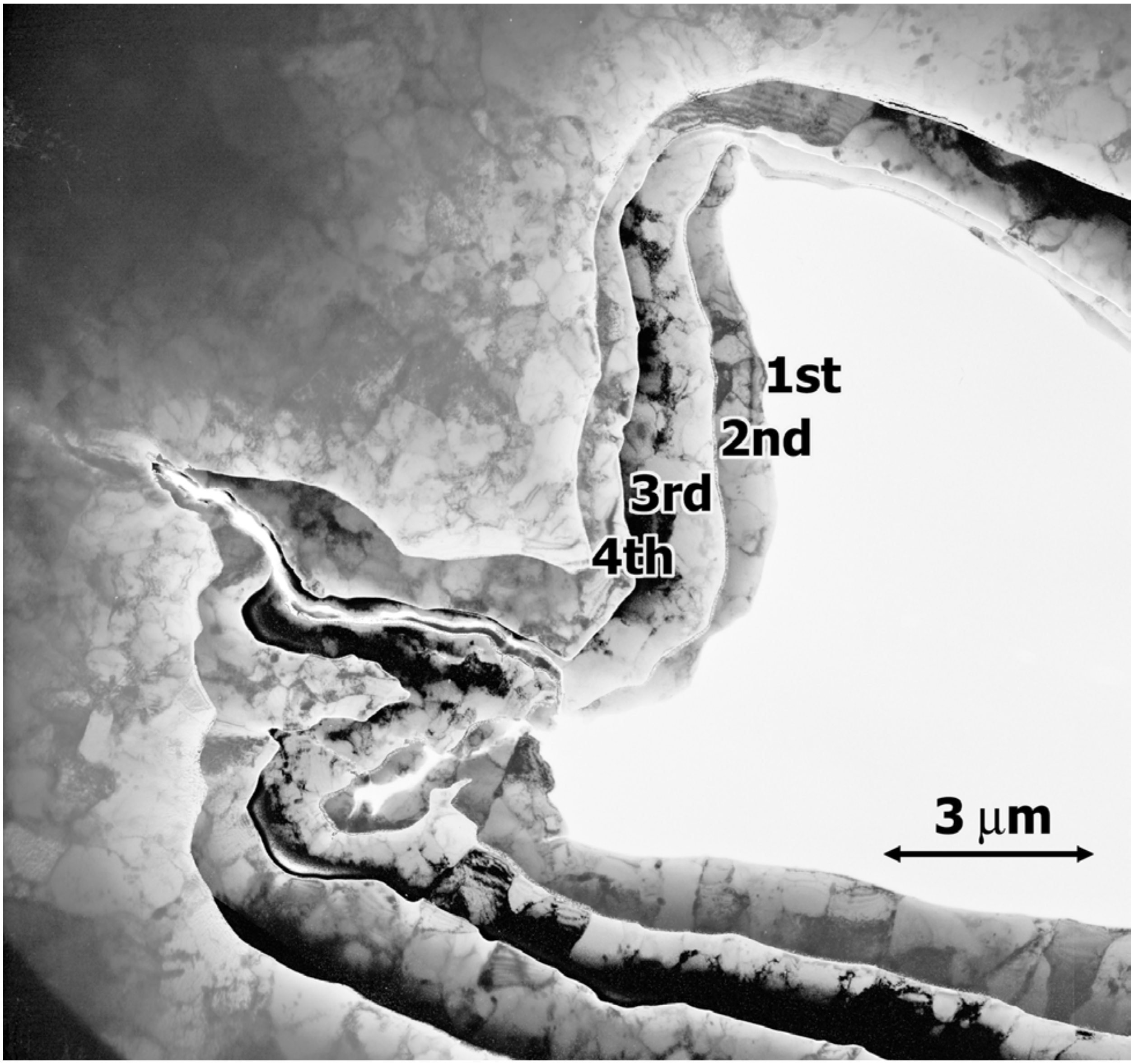

Figure 1. Montage showing the regions of electron transparency as initially prepared and after a further three remilling procedures.

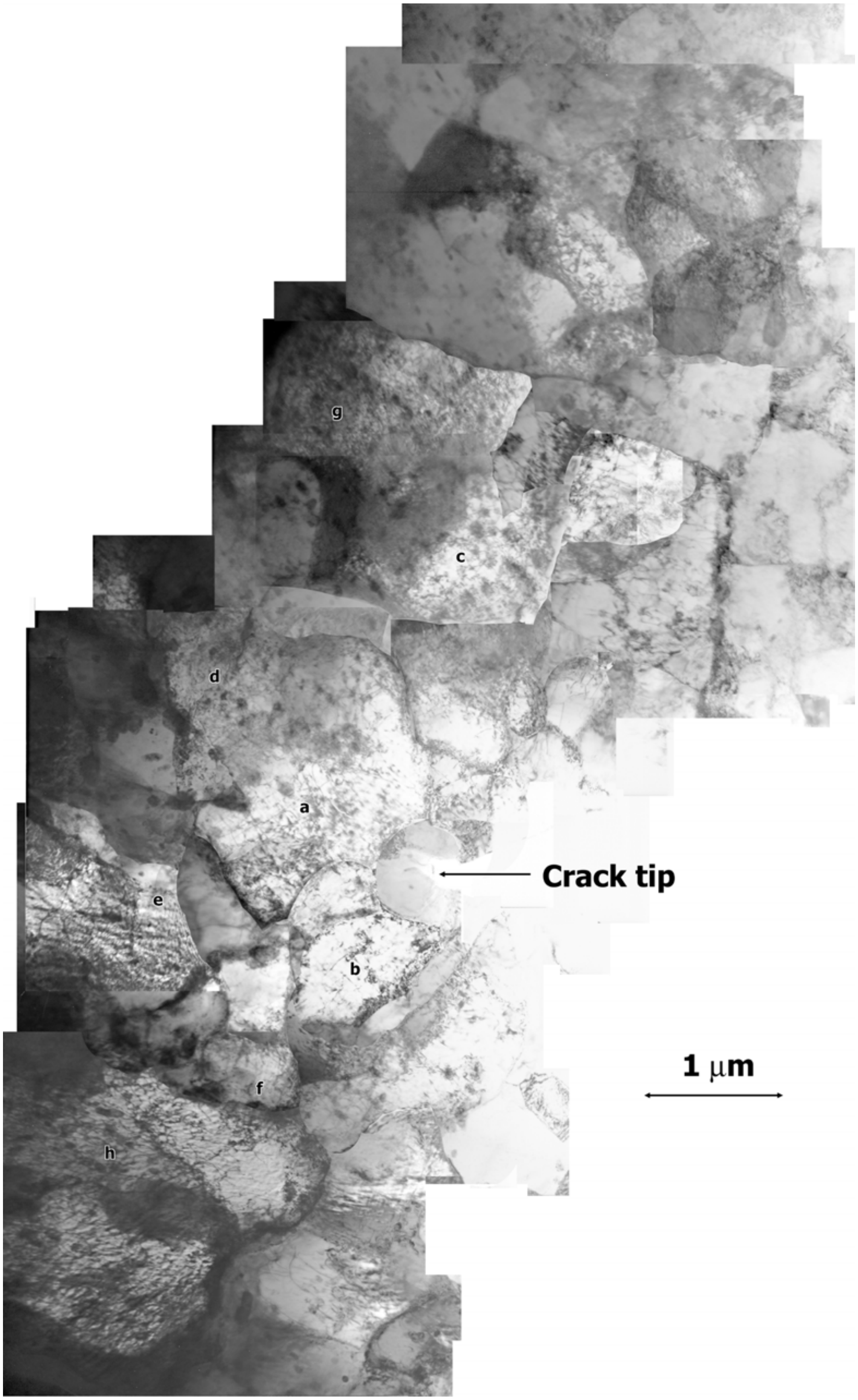

Figure 2. Montage showing dislocation structure ahead of the crack tip in g=200 contrast.

dislocation structure as possible in the region. Separation between images was generally chosen along subgrain boundaries, so that boundary configurations have not been conserved.

The microstructure in the vicinity of the crack tip consisted of intergranular carbides, carbides decorating martensite lath (sub-grain) boundaries, sub-grain boundary dislocation arrays and dislocations within the laths. The dislocation density within 1 µm of the crack tip was very low, consisting predominantly of subgrain boundary structure. (In fact, no attempt was made to image the dislocations within 0.5 µm of the crack tip.) Further from the crack tip, the dislocation spacing within subgrains decreased, but no attempt has been made to measure foil thickness and quantify the dislocation density.

Higher magnification images of dislocation structures 1, 2 and 3 µm from the crack tip are provided in Figure 3. Figure 3b) shows very few dislocations within a small 1 µm subgrain and Figure 3a) shows a larger subgrain with a crosshatched dislocation array at about half the spacing. Both regions are ~1 µm from the crack tip. Figures 3c) through 3f) show similar structures but containing tighter dislocation spacings for regions 2 µm from the crack tip. Figures 3g) and 3h) are for regions 3 µm from the crack tip, and the dislocation structures appear somewhat different, showing still tighter spacing, but no longer simply as crosshatch arrays. Instead, examples of elongated loop structures can be identified. These regions can be located on Figure 2 by the small letters a through h. Therefore, figures 3d) and 3e) are located almost directly ahead of the crack tip whereas the remainder tend to be above or below it.

Discussion

The results obtained for dislocation structures in the vicinity of a crack tip demonstrate the difficulty of such efforts in martensitic steels. The microstructure of undeformed fully heat treated F82H consists of subgrain structure as small as 1 µm in diameter, with well defined arrays of dislocations defining subgrain boundaries. Deformation can be expected to promote dislocation motion through the structure, enhancing dislocation densities. The difficulties arise when imaging the dislocations from one subgrain region to the next, and differentiating the deformation dislocations from dislocations present prior to deformation, including subgrain boundary structure. Further difficulties can be noted. After completing a large number of specimen tilts to record dislocation structures, it was found that the crack tip had advanced and the dislocation density at the tip had increased. Therefore, the electromagnetic forces on the thin foil were sufficient to cause further deformation. Apparently, crack tip specimens can have a limited lifetime for imaging experiments, and concern must also be given regarding dislocation rearrangements due to surface interactions, as well.

Several observations made are noteworthy. Dislocation densities ~1 µm from the crack tip tend to be quite low with the original subgrain boundary dislocation structure relatively intact. The process of dislocation generation at the tip (and returning to the tip upon unloading) is hard to envision. Such motion would be expected to destroy the subgrain boundary dislocation structure or at least put in steps, which did not appear to be the case. An example showing a subgrain in g=200 contrast very near the crack tip is given in Figure 4. Note that the subgrain boundaries are step-free at this magnification (so steps ~10 nm should be visible), and rearrangements of the dislocations in the subgrain boundary are similar to those reported by us previously well away from the crack tip and attributed to fatigue damage. In fact, no evidence for slip band formation was identified, either close to the crack tip or more than 3 µm away from it. Observations of dislocation loops within subgrains ~3 µm from the crack tip suggest that deformation is arising from small carbide particles distributed through the microstructure. The loops were found in regions containing carbide particles that were smaller than the loops. Away from the carbides, dislocations were more crosshatched in nature. Therefore, it can be suggested that dislocation nucleation may arise from interfacial dislocations breaking away from these small carbides. Larger carbides should be more greatly affected.

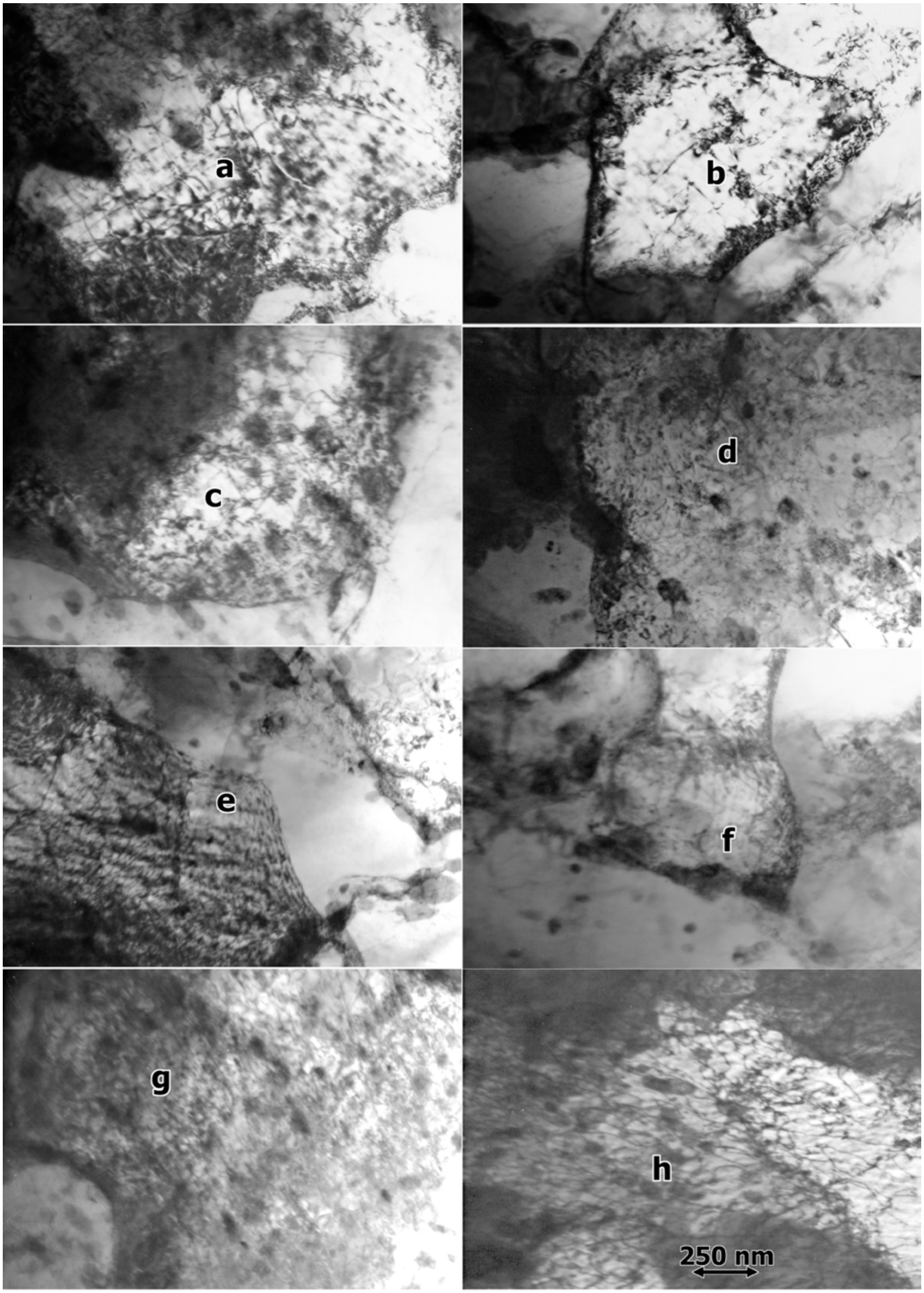

Figure 3. Selected regions of Figure 2 shown at higher magnification.

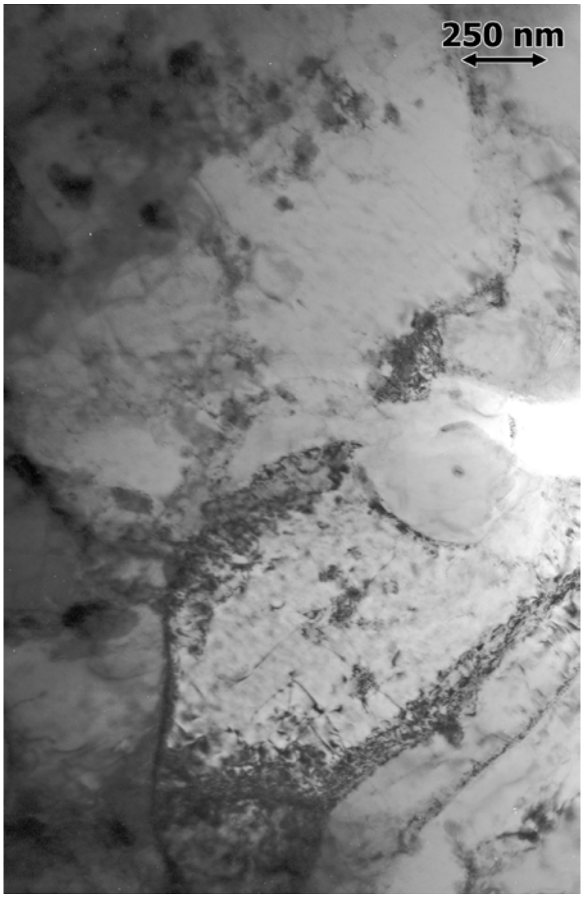

Figure 4. Dislocation microstructure near the crack tip.

It can also be noted that recently published work by Tanigawa and coworkers [2] is based on similar goals with similar results regarding fatigue precracking. They studied microstructures at crack tips associated with prior fatigue deformation in both unirradiated and irradiated F82H. Specimen preparation employed a focused ion beam microsampling system so that small thin specimens suitable for microscopy were cut by an ion milling process perpendicular to an available surface. They showed that fatigue crack propagation often followed prior austenite grain boundaries, similar to conclusions drawn in our previous report. Also, they noted a breakdown of the lath structure during cyclic fatigue but prior to crack propagation into more equiaxed subgrain structure. It can be argued that the structure found here is similarly controlled by the fatigue precracking. Further studies of crack tip microstructures in precracked specimens may be required.

Finally, it is worthwhile putting these results into perspective. The load of 25.6 MPa $m^{1/2}$ applied at –196°C to specimen P4-10 corresponds to approximately half the fracture toughness for F82H plate at that temperature as estimated by Master Curve analysis [3] but several fracture toughness data points exist at ~25 MPa $m^{1/2}$ [4]. Therefore, the load applied created plasticity at the crack tip, as demonstrated by a crack tip width of 200 nm, and could have exceeded K_{JC} if the microstructure had been appropriate. The stress distribution on the plane ahead of a blunting crack tip can be expected to exceed the tensile stress σ_0 by more than a factor of 3 at a distance ~ (J/σ_0) [5]. As $J=K_J^2/E$, with σ_0 ~ 1000 MPa [6] and E ~ 230 Gpa, [7] both estimated for -196°C, the distance ahead of the crack where the maximum stress is found is estimated to be 2.7 μm. Therefore, the scale of the experimental observations appears to make sense in terms of the expected fracture toughness parameters for F82H.

Conclusions

Dislocation microstructures have been examined ahead of the crack tip of a fatigue pre-cracked compact tension specimen of F82H loaded at -196°C to 25.6 MPa $m^{1/2}$. It is found that dislocation densities within subgrains are moderate in regions 1 to 2 μm from the crack tip, and slip band behavior is not observed either within subgrains or by its effect on subgrain boundary structure. In regions ~3 μm from the crack tip containing fine carbide particles, dislocation loops were found.

Future Work

The effort is expected to continue and eventually shift to examination of a specimen tested following irradiation in HFR, Petten.

References

[1] D. S. Gelles, G. R. Odette and P. Spätig, in DOE/ER-0313/33, July-December 2002, 79.

[2] H. Hanigawa, T. Hirose, M. Ando, S. Jitsukawa, Y. Katoh and A. Kohyama, J. Nucl. Mater., V. 307-311 (2002) 293.

[3] M. A. Sokolov, this progress report.

[4] K. Wallin, A. Laukkanen and S. Tähtinen in Small Specimen Test Techniques: Fourth Volume, ASTM STP 1418, M. A. Sokolov, J. D. Landes and G. E. Lucas, Eds., (ASTM International, West Conshohocken, PA, 2002) 33.

[5] R. M. McMeeking and D. M. Parks in Elastic-Plastic Fracture, ASTM STP 668, J. D. Landes, J. A. Bergley and G. A. Clarke, Eds., American Society for Testing and Materials, 1979, 175.

[6] P. S, G. E. Odette, G. E. Lucas and M. Victoria, DOE/ER-0313/26 (1999) 83.

[7] IEA Data Base for F82H.

IRRADIATION EFFECTS ON IMPACT TOUGHNESS OF LOW-CHROMIUM BAINITIC STEELS—

R. L. Klueh and M. A. Sokolov (Oak Ridge National Laboratory)

OBJECTIVE

The objective of this work is to develop an understanding of the effect of irradiation on fracture behavior the reduced-activation ferritic/martensitic steels that are of interest for fusion applications and to use that knowledge to develop steels with improved properties.

SUMMARY

Charpy specimens of five bainitic steels were irradiated at 378-404ºC in the Experimental Breeder Reactor (EBR-II) to 26-33 dpa. The steels were experimental reduced-activation 3Cr-WV steels with additions tantalum, boron, and nickel. The steels were normalized, and specimens of the normalized steel were given two tempering treatments: 1 hr at 700ºC and 1 h at 750ºC. The Charpy tests demonstrated only minor effects of 1% W, 0.05% Ta, and 0.005 %B in the steels in the unirradiated condition. Tungsten and tantalum had a favorable effect on the irradiated properties. Nickel, on the other hand, had a favorable effect on the impact toughness of the steel before and after irradiation.

PROGRESS AND STATUS

Introduction

The 9% Cr reduced-activation ferritic/martensitic steels are being considered favorably for applications as first wall and blanket structural materials for future fusion reactors. Oak Ridge National Laboratory (ORNL) has developed reduced-activation ferritic/martensitic steels, and a martensitic 9Cr-2WVTa (nominally Fe-9Cr-2W-0.25V-0.07Ta-0.1C; all compositions are in weight percent) steel has proved to have excellent high-temperature strength and exceptional irradiation resistance [1-3].

ORNL also developed a bainitic 2¼Cr-2WV (nominally Fe-2.25Cr-2W-0.25V-0.1C) steel that had excellent strength [1], but the toughness and irradiation resistance were inferior to those of 9Cr steels [2,3]. By modifying the 2.25 Cr steel with additional chromium and tungsten additions, the strength and toughness were improved [4,5].

When these types of steel are irradiated below ≈425ºC, displacement damage by neutron irradiation hardens the steel lattice, causing an increase in strength and a decrease in toughness. The effect on impact toughness is measured in a Charpy test as an increase in the ductile-brittle transition temperature (DBTT) and a decrease in the upper-shelf energy (USE).

The possible effect of helium on hardening and embrittlement is important because large amounts of transmutation helium will form in the ferritic/martensitic steel first wall of a fusion reactor. Nickel-doped 9 and 12 Cr steels have been irradiated in a mixed-spectrum reactor such as the High Flux Isotope Reactor (HFIR) to study the effect of helium on fracture [6]. Helium is formed in a mixed-spectrum reactor by a two-step transmutation reaction between ^{58}Ni and the thermal neutrons in the mixed-neutron spectrum. This technique allows for the simultaneous production of displacement damage and helium in the steel matrix, thus simulating what will happen in a first wall. Results from such irradiation experiments at 400ºC have been interpreted to indicate an effect of helium on embrittlement [6]. This conclusion was based on the comparison of the steels with and without nickel and on the differences between the behavior of the nickel-doped steels in a mixed-spectrum reactor, where considerable helium forms, and in a fast reactor, where very little helium forms [6].

More-recent irradiation experiments of nicked-doped 9Cr reduced-activation steels have indicated that the nickel-doped steels hardened more than steels without the nickel addition [7,8]. A 9Cr-2W steel with and without 1% Ni was irradiated in the Japanese Materials Test Reactor (JMTR) to 0.15 dpa at 170ºC, and an increase in the room temperature yield stress of up to 350 MPa was observed for the nickel-containing steel, compared to a 120 MPa increase for the steel without nickel. However, no difference in the strength increases was observed for the steels irradiated at 220ºC [7]. Irradiation of these steels to 2.2 and 3.8 dpa at 270 and 348ºC, respectively, in the Advanced Test Reactor (ATR) indicated that the nickel-containing steel hardened about 20% more than the steel without nickel at 270ºC, but strengths were similar after the irradiation at 348ºC [8]. Likewise, there was a larger shift in DBTT for the nickel-containing steel than the one without nickel when irradiated at 270ºC, but not after irradiation at 348ºC. TEM analysis indicated that nickel refined the size of the defect clusters, which were more numerous in the nickel-containing steel [8].

Helium can also be generated in a steel that contains boron by an (n,α) reaction between a neutron and ^{10}B. This reaction will occur quite rapidly in both a mixed-spectrum reactor and a fast reactor.

In this report, Charpy properties are reported for a series of reduced-activation 3Cr-WV steels that contained different tungsten levels, and steels that contained small additions of tantalum, boron, and nickel after irradiation in the Experimental Breeder Reactor (EBR-II).

Experimental Procedure

Compositions and designations of the steels used in this experiment are given in Table 1. In the original Oak Ridge National Laboratory (ORNL) alloy development program for development of reduced-activation steels [1], 18-kg heats of electroslag-remelted steels ranging from 2.25 Cr to 12 Cr were prepared by Combustion Engineering Inc, Chattanooga, TN. Material from the 18-kg heat of 2.25Cr-2WV steel was used as the master alloy to prepare 450-g vacuum arc-melted button heats of 3Cr steels prepared for this work.

Table 1. Chemical composition of the steels tested

Element[a]	3Cr-2WV	3Cr-3WV	3Cr-3WV-2Ni	3Cr-3WVTa	3Cr-3WVTaB
C	0.087	0.091	0.089	0.089	0.088
Mn	0.31	0.30	0.29	0.30	0.30
Si	0.09	0.09	0.08	0.08	0.09
P	0.014	0.015	0.015	0.016	0.015
S	0.008	0.009	0.008	0.008	0.008
Cr	3.07	3.05	3.02	3.02	3.03
Mo	<0.01	<0.01	<0.01	<0.01	<0.01
W	2.10	3.01	2.86	3.25	2.95
Ni	0.02	0.02	2.01	0.02	0.02
V	0.25	0.24	0.23	0.24	0.24
Nb	<0.01	<0.01	<0.01	<0.01	<0.01
Ta	<0.01	<0.01	<0.01	0.05	0.05
N	0.014	0.015	0.013	0.015	0.013
B	<0.001	<0.001	<0.001	<0.001	0.005

[a] Balance iron

The small heats were cast as 25.4 mm x12.7mm x 152 mm ingots, after which they were rolled to 6.4-mm plate and 0.76-mm sheet. The steels were normalized by austenitizing for 0.5 h at 1050ºC in a helium atmosphere, and they were quickly cooled in flowing helium. Specimens were irradiated in two tempered conditions: 1 h at 700ºC and 1 h at 750ºC.

One-third-size Charpy specimens measuring 3.3 x 3.3 x 25.4 mm with a 0.51-mm-deep 30º V-notch and a 0.05- to 0.08-mm-root radius were machined from normalized-and-tempered 6.4-mm plates. Specimens were machined with the longitudinal axis along the rolling direction and the notch transverse to the rolling direction (L-T orientation). The absorbed energy vs. temperature values were fit with a hyperbolic tangent function to permit the USE and DBTT to be consistently evaluated. The DBTT was determined at an energy level midway between the upper- and lower-shelf energies. Details of the test procedure for the subsize Charpy specimens have been published [9-11].

Six Charpy specimens of each heat and each heat-treated condition were irradiated in the COBRA experiment in EBR-II at temperatures of 378 to 405ºC. Fluence was determined from flux monitors in the irradiation canisters. There was some variation in fluence for different specimens, depending on their position in the canisters, but the individual sets of specimens for a given steel and heat treatment were kept together in the canisters and experienced the same irradiation conditions. Specimens were irradiated to about 5.5×10^{26} to 6.9×10^{26} n/m^2 (E>0.1 MeV), which produced between 26 and 33 dpa. Helium concentrations were calculated to about 3 appm for the steels without nickel and boron, about 6 appm for the nickel-containing steel, and about 50 appm for the steel with boron.

Results

First, the properties of the normalized-and tempered properties will be discussed, followed by a discussion of the properties after irradiation.

Normalized-and-Tempered Properties

Optical microstructures for the normalized-and-tempered (1 h at 700ºC) steels indicate they are 100% bainite (Fig. 1). The major difference in the steels is the prior-austenite grain size (Table 2). For the

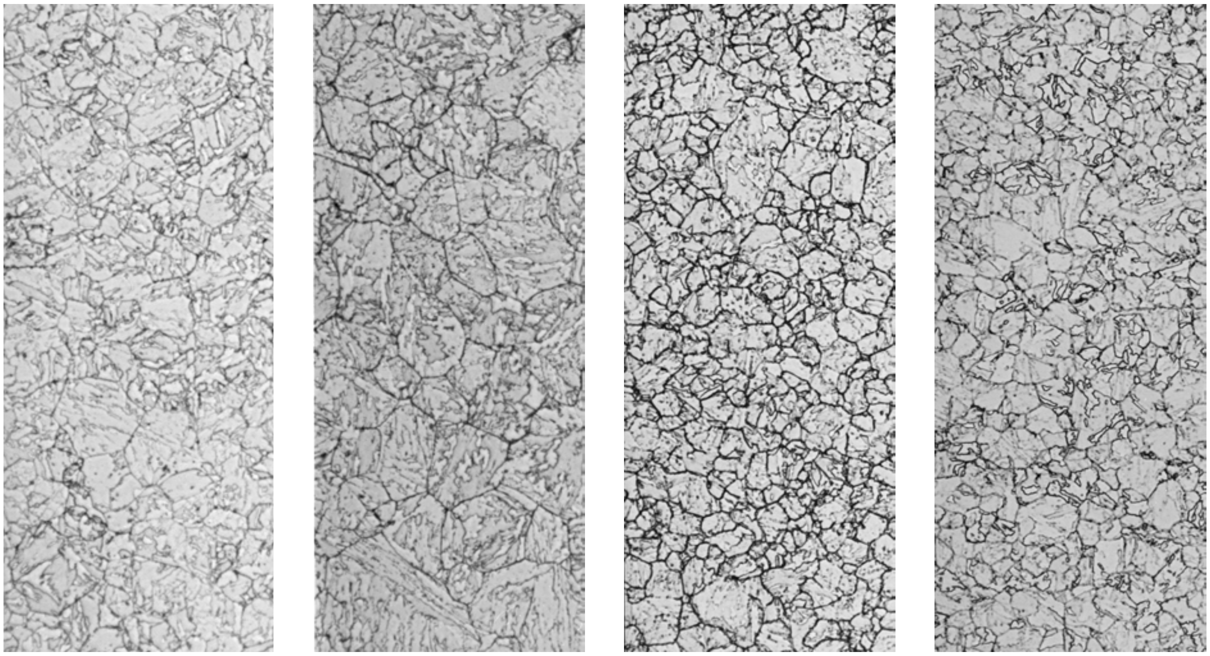

3Cr-2WV **3Cr-3WV** **3Cr-3WVTa** **3Cr-3WVTaB**

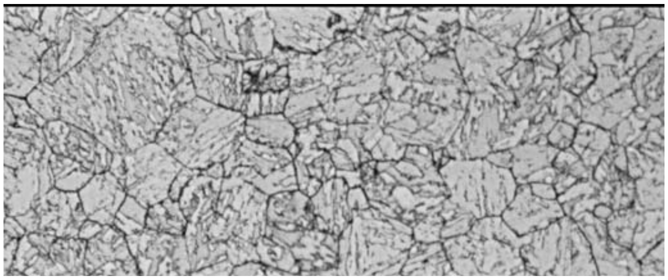

3Cr-3WV-2Ni

Figure 1. Bainitic microstructure of the 3Cr steels.

Table 2. Prior austenite grain size of steels

Steel	Prior-Austenite Grain Size (μm)
3Cr-2WV	20
3Cr-3WV	38
3Cr-3WVTa	31
3Cr-3WVTaB	16
3Cr-3WV-2Ni	15

steels without tantalum, the grain sizes of the 3Cr-3WV and 3Cr-3WV-2Ni are larger than those of the 3Cr-2WV, and the grain size of the steel containing the nickel is slightly smaller than for the steel without nickel. The addition of the tantalum refines the grain size, and the prior-austenite grain sizes of the 3Cr-3WVTa and 3Cr-3WVTaB, which are similar, are much smaller than for the steels without tantalum.

The Charpy data for the 3Cr steels are summarized in Table 3, and in Figs. 2-4, the ductile-brittle transition temperature (DBTT), shift in DBTT (ΔDBTT) and upper-shelf energy (USE) are compared for the five steels. The base composition for this discussion is the 3Cr-2WV steel, which was the first modification from the 2¼Cr-2WV steel [5].

Table 3. Charpy data for unirradiated and irradiated steels

Steel	Temper	Irrd Temp	Dose	Uirrd DBTT	Irrd DBTT	DBTT Shift	Uirrd USE	Irrd USE
3Cr-2WV	700ºC	378ºC	27 dpa	-92ºC	76ºC	168ºC	10.7 J	4.8 J
	750ºC	379ºC	26 dpa	-150ºC	51ºC	201ºC	11.4 J	7.0 J
3Cr-3WV	700ºC	378ºC	27 dpa	-73ºC	78ºC	151ºC	9.0 J	5.6 J
	750ºC	383ºC	31 dpa	-116ºC	9ºC	125ºC	10.4 J	7.5 J
3Cr-3WVTa	700ºC	392ºC	33 dpa	-66ºC	52ºC	118ºC	9.4 J	7.5 J
	750ºC	386ºC	32 dpa	-103ºC	-15ºC	88ºC	11.8 J	8.4 J
3Cr-3WVTaB	700ºC	404ºC	26 dpa	-74ºC	62ºC	123ºC	7.8 J	5.8 J
	750ºC	386ºC	32 dpa	-111ºC	12ºC	136ºC	10.4 J	6.0 J
3Cr-3WV-2Ni	700ºC	392ºC	33 dpa	-125ºC	-104ºC	21ºC	10.0 J	8.4 J
	750ºC	389ºC	33 dpa	-148ºC	-125ºC	23ºC	11.2 J	10.2 J

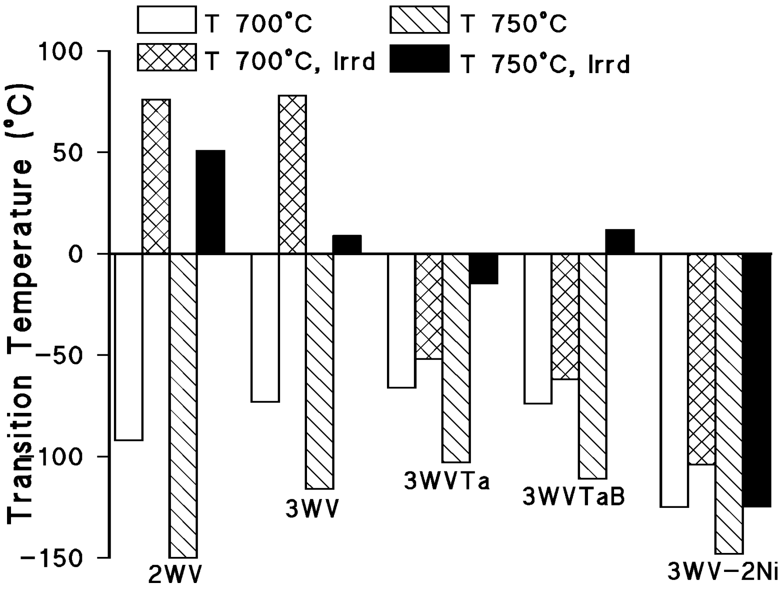

Figure 2. Ductile-brittle transition temperature for 3Cr steel before and after irradiation.

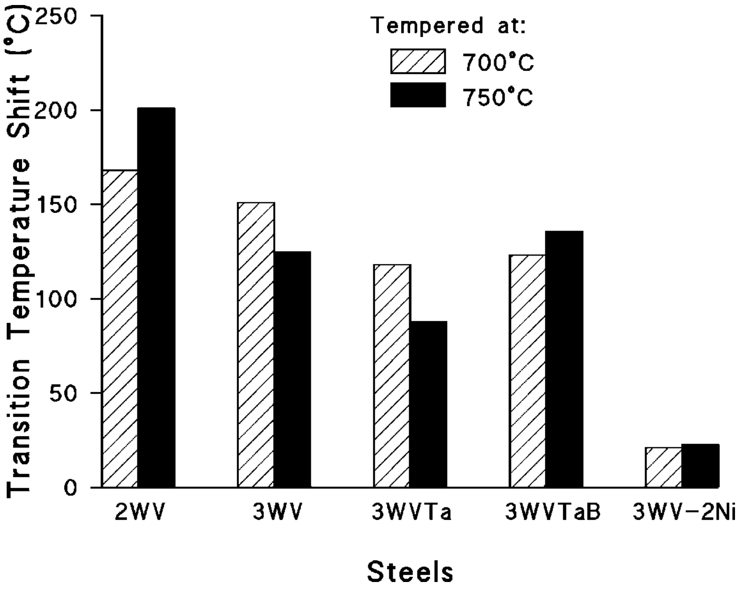

Figure 3. Shift in ductile-brittle transition temperature for irradiated 3Cr steels.

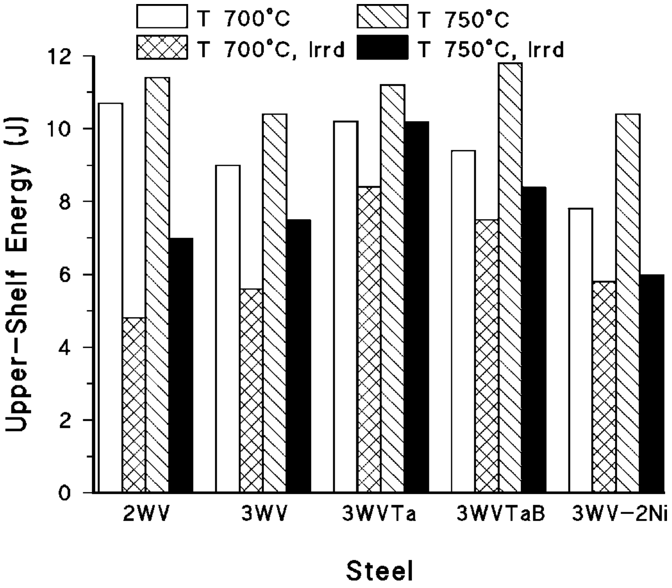

Figure 4. Upper-shelf energy for 3Cr steels before and after irradiation.

Before irradiation, the 3Cr-2WVsteel has excellent impact toughness—low transition temperature and high USE—after both tempering treatments (Figs. 2 and 3). The DBTT and USE for the steels given the 700°C temper were always higher and lower, respectively, than those for the steels tempered at 750°C. The addition of another 1% W to the 3Cr-2WV to produce the 3Cr-3WV caused a slight decrease in the DBTT and USE. The addition of 0.05 Ta to the 3Cr-3WV (3Cr-3WVTa) had essentially no effect on the properties relative to 3Cr-3WV. Likewise, the addition of 0.005B to the 3Cr-3WVTa (3Cr-3WVTaB) did not change the DBTT, although the USE of the 3Cr-3WVTaB appeared to be slightly less than that of the 3Cr-3WVTa. The addition of nickel to the steels had the largest effect on the impact properties relative to the properties of the 3Cr-3WV steel, especially after the 700°C temper. The 3Cr-3WV-2Ni had properties similar to those of the 3Cr-2WV.

Irradiated Properties

After irradiation, the DBTT of the steels tempered at 700ºC were higher than for those steels given the 750ºC temper (Table 3 and Fig. 2). This did not always translate into a larger ΔDBTT (Fig. 3) for the steel given the 700ºC temper. For the 3Cr-2WV, the DBTT after the 700ºC temper showed the largest difference for a 700ºC-tempered specimen. Although there was a slightly lower ΔDBTT for the 3Cr-3WVTaB and 3Cr-3WV-2Ni steels tempered at 700ºC than 750ºC, the differences were so small that the steels can be considered as having the same ΔDBTT for both tempering conditions.

With the exception of the 3Cr-3WV-2Ni, the results show fairly large DBTT values after irradiation for the 3Cr-2WV steel after both tempering conditions and the other steels after the 700ºC temper. After tempering at 750ºC, the DBTT values after irradiation indicated that adding 1% W to the 3Cr-2WV to get 3Cr-3WV and adding 0.05% Ta to 3Cr-3WV to get 3Cr-3WVTa were beneficial (DBTT values of -15 and 9ºC, respectively). The 3Cr-3WVTaB steel also had a fairly low DBTT (12ºC) after the 750ºC temper, although it was not as low as that of the steel without boron. It should be noted that the 3Cr-3WVTaB contained over 50 appm He generated from the ^{10}B, but there was no indication that this helium affected the Charpy properties.

By far, the steel displaying the best irradiation resistance was the 3Cr-3WV-2Ni. This steel had the lowest DBTT values before irradiation, and after irradiation, shifts of only 21 and 23ºC were observed for the specimens tempered at 700 and 750ºC, respectively. As a result of these small shifts, the measured DBTT values remained below -100ºC after irradiation for both tempering conditions.

Discussion

In the unirradiated condition, several observations can be made. First, the addition of 1% W to the 3Cr-2WV did not improve the impact properties. The properties of the 3Cr-3WV were slightly below those of the 3Cr-2WV, which may reflect the relative difference in prior-austenite grain size of the two steels. Adding 0.05% Ta to the 3Cr-3WV had little effect on the impact properties, even though there was a significant reduction in the prior-austenite grain size for the tantalum-containing steel, nor did the addition of 0.005% B to the 3Cr-3WVTa steel have any noticeable effect on the tantalum-containing steel.

Nickel has long been known to favorably affect the impact properties of steels, and the results for the unirradiated properties for the 3Cr steels show that the 2% Ni addition to the 3Cr-3WV composition resulted in a significant improvement of the impact properties over the steel without the nickel addition. For the steels tempered at 700ºC, the nickel-containing steel had a transition temperature that was better than that for all the steels but the 3Cr-2WV after the other steels were tempered either at 700 or 750ºC. After tempering the 3Cr-3WV-2Ni at 750ºC, the transition temperature was similar to that of the 3Cr-2WV steel and superior to the other steels. Likewise, the USE of the steel with nickel was always about as high or higher than for the other steels for the respective tempering conditions.

After irradiation, the effects of composition are somewhat different than in the unirradiated condition. For all five steels, the DBTT values for the steels irradiated at 750ºC were less than those for the respective steels tempered at 700ºC, although the shifts in DBTT were not always more for the steel with the 750ºC temper. If the steels tempered at 750ºC are compared, it appears that increasing the tungsten from 2 to 3% improves the irradiation resistance. Likewise, adding the 0.05% Ta to the 3Cr-3WV had a favorable effect. The boron addition did not appear to favorably affect the 3Cr-3WVTa composition.

By far the most impressive irradiation resistance was exhibited by the 3Cr-3WV-2Ni steel. In this case, the ΔDBTT for the steel tempered at 700 and 750ºC were similar and very low. The steel tempered at 750ºC had the lowest DBTT after irradiation because it had a considerably lower value prior to irradiation. However, the DBTT for the steel after both tempering conditions was <-100ºC. The other interesting observation was that the USE of the 3Cr-3WV-2Ni tempered at 700ºC was higher than that of any of the steels except the 3Cr-3WVTa after they were tempered at either 700 or 750ºC. It had the same USE as the 3Cr-3WVTa steel that was tempered at 750ºC. The DBTT and USE values for the 3Cr-3WV-2Ni after either temper were better than most steels for similar irradiation conditions, including the 9Cr-2WVTa [2] , which in the past has been shown to have excellent properties for most irradiation conditions.

Nickel was originally added to the steel in this experiment because the 3Cr-3WV and 3Cr-3WV-2Ni steels were to be irradiated in the HFIR, where an (n,α) reaction between ^{58}Ni and the thermal neutrons in the mixed-neutron spectrum of HFIR would produce helium, thus allowing for a determination of the effect of helium on impact properties. Irradiation of the steels in the fast-neutron spectrum of EBR-II, where very little helium forms, would thus provide a comparison of the properties of 3Cr-3WV-2Ni with and without the high helium concentration. Unfortunately, the HFIR experiments were cancelled. Nevertheless, the observations on the nickel-containing steel provide some insight into the effect of nickel on irradiation resistance.

As discussed in the Introduction, there have been some apparent contradictory observations on the effect of nickel [7,8] on irradiated steels. At temperatures below ≈300ºC, small irradiation doses were shown to cause excess hardening and an increase in DBTT of a 9Cr-2W steel that contained 1-2% Ni compared to the steel without the nickel addition [7], whereas at higher temperatures and higher doses, no indication of such hardening due to nickel in 9 and 12% Cr-Mo steels was observed [8,9]. However, in no instance in these latter studies was there any indication of an improvement in properties of the type displayed in the present experiment for the 3Cr-3WV-2Ni.

References

[1] R. L. Klueh and P. J. Maziasz, Met. Trans. 20A (1989) 373.
[2] R. L. Klueh and D. J. Alexander, in: Effects of Radiation on Materials: 18th International Symposium, ASTM STP 1325, eds. R. K. Nanstad, M. L. Hamilton, F. A Garner, and A. S. Kumar (American Society for Testing and Materials, Philadelphia, 1999) 911.
[3] R. L. Klueh and W. R. Corwin, J. Eng. Mater., 11 (1989) 169.
[4] R. L. Klueh, D. J. Alexander, and E. A. Kenik, J. Nucl. Mater., 227 (1995) 11.
[5] R. L. Klueh, D. J. Alexander, and P. J. Maziasz, Metall. and Matls. Trans., 28A (1997) 335.
[6] R. L. Klueh and D. J. Alexander, J. Nucl. Mater. 187 (1992) 60.
[7] R. L. Klueh and D. J. Alexander, J. Nucl. Mater. 187 (1992) 60.
[8] R. Kasada, A. Kimura, H. Matsui, and M. Narui, J. Nucl. Mater. 258-263 (1998) 1199.
[9] D. J. Alexander, R. K. Nanstad, W. R. Corwin, and J. T. Hutton, in: Applications of Automation Technology to Fatigue and Fracture Testing, ASTM STP 1092, Eds. A. A. Braun, N. E. Ashbaugh, and F. M. Smith (American Society for Testing and Materials, Philadelphia, 1990) p. 83.
[10] D. J. Alexander and R. L. Klueh, in: Charpy Impact Test: Factors and Variables, ASTM STP 1072, ed. J. M. Molt (American Society for Testing and Materials, Philadelphia, 1990) p. 179.
[11] M. A. Sokolov and R. K. Nanstad, in: Effects of Radiation on Materials: 17th International Symposium, ASTM STP 1270, eds. D. S. Gelles, R. K. Nanstad, A. S. Kumar, and E. A. Little (American Society for Testing and Materials, Philadelphia, 1996) p. 384.
[12] R. L. Klueh and M. A. Sokolov, R. L. Klueh and M. A. Sokolov, Fusion Materials Semi-Annual Progress Report for Period Ending December 31, 2002, DOE/ER-0313/33, p. 85.

IRRADIATION CREEP AND SWELLING OF RUSSIAN FERRITIC-MARTENSITIC STEELS IRRADIATED TO VERY HIGH EXPOSURES IN THE BN-350 FAST REACTOR AT 305-335°C – Y. V. Konobeev, A. M. Dvoriashin, S. I. Porollo, and S. V. Shulepin. (Institute of Physics and Power Engineering, Russia), N. I. Budylkin, and E. G. Mironova (Research Institute of Inorganic Materials, Russia) F. A. Garner and M. B. Toloczko (Pacific Northwest National Laboratory)*

OBJECTIVE

The objective of this effort is to provide data on the dimensional stability and mechanical properties of ferritic/martensitic steels after high fluence irradiation at temperatures below that obtainable in Western reactors.

SUMMARY

Russian ferritic/martensitic (F/M) steels EP-450, EP-852 and EP-823 were irradiated in the BN-350 fast reactor in the form of gas-pressurized creep tubes. The first steel is used in Russia for hexagonal wrappers in fast reactors. The other steels were developed for compatibility with Pb-Bi coolants and serve to enhance our understanding of the general behavior of this class of steels.

In an earlier paper we published data on irradiation creep of EP-450 and EP-823 at temperatures between 390 and 520°C, with dpa levels ranging from 20 to 60 dpa. In the current paper new data on the irradiation creep and swelling of EP-450 and EP- 852 at temperatures between 305 and 335°C and doses ranging from 61 to 89 dpa are presented. Where comparisons are possible, it appears that these steels exhibit behavior that is very consistent with that of Western steels. Swelling is relatively low at high neutron exposure and confined to temperatures <420°C, but may be camouflaged somewhat by precipitation-related densification. These irradiation creep studies confirm that the creep compliance of F/M steels is about one-half that of austenitic steels.

PROGESS AND STATUS

Introduction

Ferritic/martensitic (F/M) steels are widely used as structural materials in various types of reactor facilities. The main advantages of F/M steels are their high resistance to void swelling, low irradiation creep rates and a relatively low radioactivation after neutron irradiation. At the same time, the well-known disadvantages of these steels are their low long-term creep strength at high temperatures and their inclination to low-temperature irradiation embrittlement.

Earlier measurements of irradiation creep and short-term mechanical properties were performed as part of the current effort for two Russian F/M steels designated EP-450 (12Cr-1.3Mo-2V-Nb-B) and EP-823 (11Cr-1Mo-1Si-Nb, V, W) [1]. They were irradiated in the BN-350 fast reactor to doses of 20-60 dpa and have demonstrated that at irradiation temperatures below ~500°C the irradiation creep rate in the steels is rather low and consistent with measurements made on various Western F/M steels over the same temperature range.

Some results of this earlier study are shown in Figure 1 and demonstrate that not all strains measured in creep tests arise from irradiation creep alone. Note that at the irradiation temperature of 520°C an apparent increase of irradiation creep modulus is observed due to the onset of thermal creep and concurrent loss of strength. Note also that the creep modulus B appears to increase as swelling begins at lower temperatures. The data are also interpreted to show negative precipitation-related strains that lower the apparent creep modulus when the irradiation creep component is relatively small.

---

* Pacific Northwest National Laboratory (PNNL) is operated for the U.S. Department of Energy by Battelle Memorial Institute under contract DE-AC06-76RLO-1830.

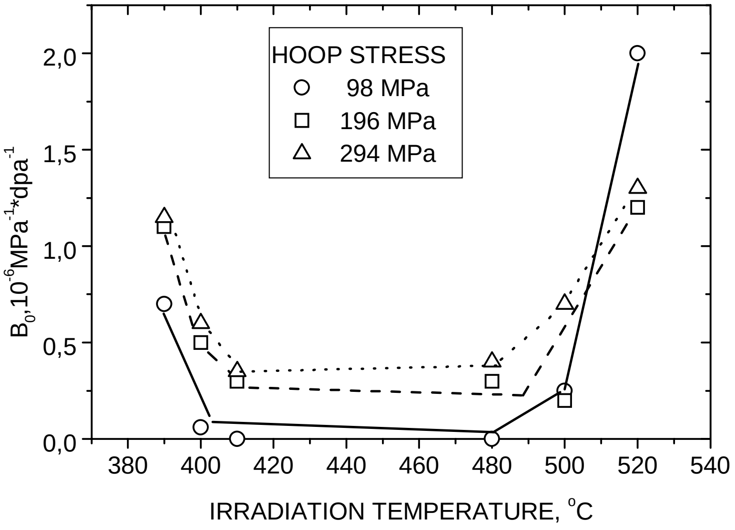

Figure 1. Average creep coefficients (B) derived for EP-450 in the range 390-520°C for three levels of hoop stress [1]. The data are interpreted to show the combined influence of swelling at low temperature, thermally assisted creep at higher temperature and precipitate-related densification over the entire temperature range. Similar behavior was observed in EP-823 at 390 and 480°C.

However, the most sought-after data for such steels are those at relatively low temperatures. Acquisition of such data require that the irradiation be performed in a reactor with a relatively low inlet coolant temperature, such as found in the BN-350 fast reactor in Kazakhstan but not available in Western reactors. In the present paper results are presented of further investigation of irradiation creep and swelling in EP-450 and EP-852 ferritic-martensitic steels. These steels were irradiated as pressurized creep tube cladding in the reactor BN-350 at temperatures in the range of 305-335°C to a maximum dose of 89 dpa.

Experimental Details

The measured chemical composition and final heat treatment of the creep tubes made of the EP-450 and EP-852 F/M steels are shown in Table 1. Creep tubes of 6.9 mm external diameter and 0.4 mm wall thickness (Figure 2) were used. To produce hoop stresses in the range 0 - 250 MPa at irradiation temperatures of 305-335°C, the tubes were filled with argon of 99.998% purity through a needle valve located in the large blank end flange. Note that one unusual feature of Russian tube fabrication is the use of annealing of tubes via electrical resistance for only seconds as shown in Table 1.

To reach high damage doses, the creep tubes were irradiated in the BN-350 reactor in special experimental subassemblies having extractable containers. These subassemblies are similar to regular driver subassemblies of the BN-350 reactor, but with 31 central pins replaced by an extractable cylindrical container of 32 mm in diameter. In each container, perforated cylindrical canisters were placed at different heights (Figure 3), with each of the canisters containing seven gas-filled tubes (one tube with zero gas pressure and six gas pressurized tubes, two tubes for each of three nominal hoop stress levels). The canisters were 97 mm in length, 26 mm in outer diameter and with 0.3 mm wall thickness. The required irradiation temperature for the creep tubes was ensured due to heating the container by surrounding pins. The calculated irradiation temperatures and doses for each container depend on the location of the canister with respect to the reactor core midplane. After irradiation in four consecutive

Table 1. The chemical composition of the EP-450 and EP-852 F/M steels.

Steel	Content, wt.%										
	C	Si	Mn	S	P	Cr	Ni	Mo	Nb	V	B
EP-450	0.14	0.20	0.31	0.009	0.017	12.95	0.20	1.54	0.47	0.22	0.004
	Solution treated 1050°C, 1 s + aged 850°C, 5 s.										
EP-852	0.13	1.91	0.31	0.009	0.017	13.15	0.27	1.69	-	-	-
	Solution treated 1050°C, 1 h + aged 720°C, 1 h.										

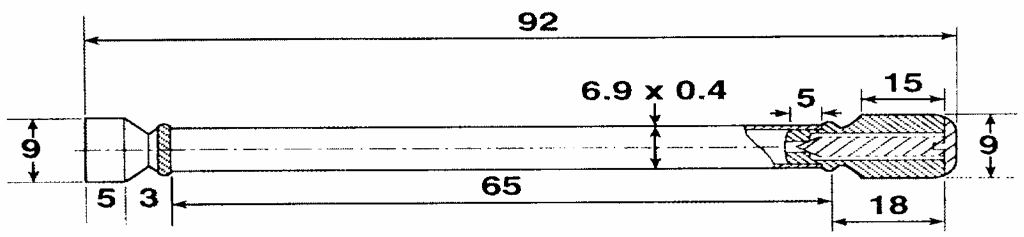

Figure 2. Irradiation creep tube (all sizes in mm.).

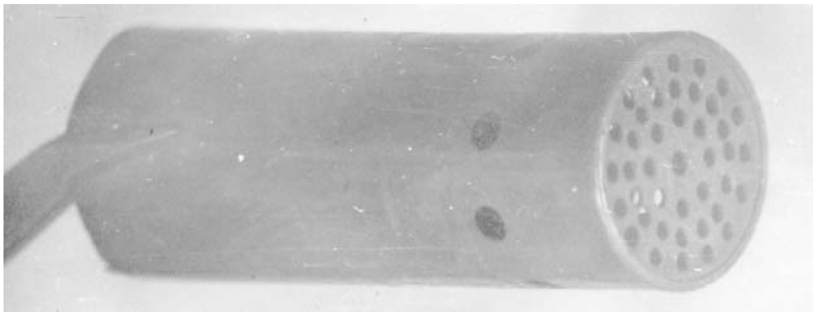

Figure 3. View of the canister for containing the creep tubes.

reactor runs the containers were extracted from the spent subassemblies and inserted in fresh subassemblies, which then were placed at the same positions in the core. Afterwards, the irradiation of the samples was continued for an additional four runs. The final calculated doses and irradiation temperatures for the steels investigated are shown in Tables 2 and 3.

The surfaces of the irradiated creep tubes were cleaned in 50% ethanol-water solution, and then the tube diameters were measured by a micrometer with an accuracy of 0.01 mm. For each tube the measurements were made at three cross sections: in the middle and at 15 mm apart from both tube ends, for two tube orientations that differ by rotation around the tube axis by 90°.

There were some gradients in dose and temperature along the tubes. For steels EP-852 (305°C/69 dpa), EP-450 (320°C/81 dpa) and EP-450 (335°C/89 dpa) the calculated gradient of dose was equal to 0.1 dpa/mm and the calculated gradient of temperature was 0.15°C/mm. For the distance of 50 mm between two cross sections at which tube diameters were measured, the difference of doses equals 5 dpa, and the difference of temperature was equal to 7.5°C. For EP-852 (310°C/61 dpa) and EP-450 (310°C/61 dpa) steels the calculated gradients of damage dose and of temperature were equal to 0.12 dpa/mm and 0.2°C/mm, respectively, so the doses and the temperatures vary by 6 dpa and 10°C, respectively.

For testing to ensure that the tube did not release its fill gas and for determining the actual hoop stresses, the tubes were punctured at room temperature in a remote installation of known volume and the pressure of the gas in that volume was measured. Hoop stresses at the end of irradiation were calculated from the following equation.

$$\sigma_\theta = P(T_0/T)(V/V_0)d_{\text{int}}/2t \qquad (1)$$

where T is the temperature of the gas released from a punctured creep tube, P is the pressure of the released gas at temperature T, V is the volume of the puncture facility, T_o is the irradiation temperature, V_0 is the internal volume of the creep tube at temperature T_o, $d_{int.}$ is the internal tube diameter, and t is the tube wall thickness. The total irradiation creep strain ε^{ic} was determined as the difference between the total diametral strain and strain due to swelling (the diametral strain of the stress-free tube).

The irradiation creep modulus was calculated from the following equation, where the stress is the hoop stress.

$$B = \varepsilon^{ic}/0.75\sigma_0 \times dpa \qquad (2)$$

Table 2. Irradiation creep characteristics of EP-450 F/M steel.

310°C/61 dpa				**320°C/81 dpa**				**335°C/89 dpa**			
σ_θ, MPa measured (nominal)	**$\Delta d/d$, %**	**ε^{ic}, %**	**B 10^{-6} (MPa×dpa)$^{-1}$**	**σ_θ, MPa measured (nominal)**	**$\Delta d/d$, %**	**ε^{ic}, %**	**B 10^{-6} (MPa×dpa)$^{-1}$**	**σ_θ, MPa measured (nominal)**	**$\Delta d/d$, %**	**ε^{ic}, %**	**B 10^{-6} (MPa×dpa)$^{-1}$**
0	0.1	0	0	0	0	0	0	0	0	0	0
59 (60)	0.3	0.2	0.74	49.8(50)	0.03	0.03	0.1	50.6(50)	0.19	0.19	0.56
59 (60)	0.3	0.2	0.74	50.1(50)	0.08	0.08	0.26	52.3(50)	0.25	0.25	0.72
0 (120)	0.1	0	0	94.6(100)	0.19	0.19	0.33	97.4(100)	0.45	0.45	0.69
69.5 (120)	0.6	0.5	1.57	94.4(100)	0.17	0.17	0.3	97.4(100)	0.40	0.40	0.61
130 (230)	1.1	1.0	1.68	190.8(200)	0.55	0.55	0.47	196.5(200)	0.97	0.97	0.74
141 (230)	1.2	1.1	1.7	190.5(200)	0.59	0.59	0.51	196.5(200)	0.97	0.97	0.74

Table 3. Irradiation creep characteristics of EP-852 F/M steel.

305°C/69 dpa					**310°C/61 dpa**				
σ_θ, MPa (nominal)	**σ_θ, MPa (measur.)**	**$\Delta d/d$, %**	**ε^{ic}, %**	**B, 10^{-6} (MPa×dpa)$^{-1}$**	**σ_θ, MPa (nominal)**	**σ_θ, MPa (measur.)**	**$\Delta d/d$, %**	**ε^{ic}, %**	**B, 10^{-6} (MPa×dpa)$^{-1}$**
0	0	0	0	0	0	0	0.1	0	0
50	38.5	0.05	0.05	0.25	60	56.0	0.15	0.05	0.19
50	38.2	0.03	0.03	0.15	60	58.0	0.3	0.2	0.75
100	100.5	0.1	0.1	0.19	120	0	0.35	0.25	-
100	99.5	0.1	0.1	0.19	120	77.0	0.45	0.35	0.99
200	143.8	0.25	0.25	0.33	230	0	0.45	0.35	-
200	143.0	0.25	0.25	0.33	230	35.0	0.35	0.25	1.56

Results

Upon removal of the tubes from the various canisters, a visual inspection of the creep tubes did not reveal any surface defects. All irradiated tubes retained their initial shape and appearance. As a result of mechanical loading, however, five creep tubes, namely, one tube of the EP-450 steel and four tubes of

EP-852 steel were destroyed while puncturing for gas release, with the large head sections breaking off. Two such brittle creep tubes are shown in Figure 4.

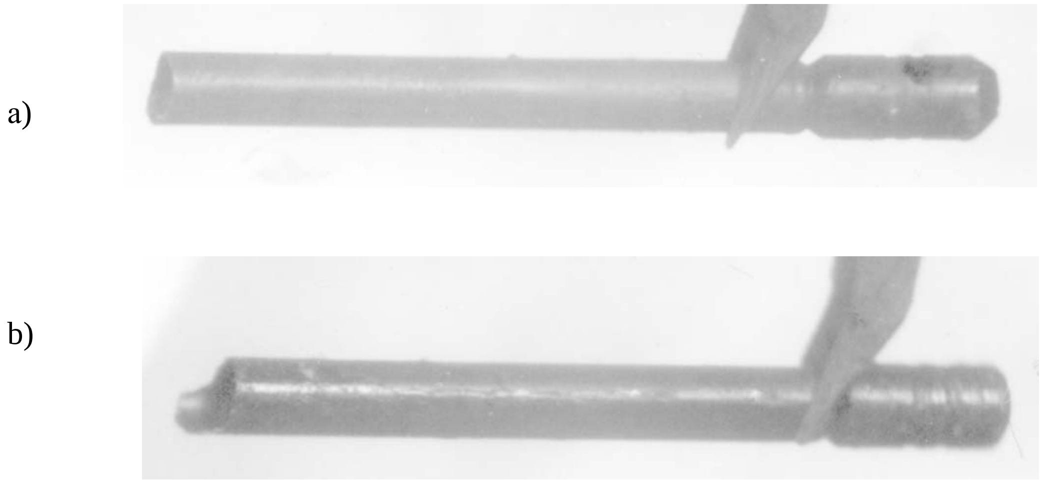

Figure 4. View of failed creep tubes of the EP-450 steel (a) and EP-852 steel (b), both irradiated at the temperature of 310°C to 61 dpa.

The gas volume measurement data expressed as applied hoop stresses are shown in Tables 2 and 3. As follows from these data, some creep tubes were found to have lost all or part of their fill gas before puncturing. This required some judgment to determine what stress level to use in the data analysis. Based on the measured strains some tubes obviously lost their pressure early and were treated as stress-free. Others were treated as having maintained their design nominal pressure until the final stages of their extraction from the reactor.

The results of measuring total creep tube diametral strains, irradiation creep strains and calculated magnitudes of the irradiation creep modulus in EP-450 and EP-852 steels are also shown in Tables 2 and 3. No systematic trend in the variation of tube diameter along the tube length was observed for EP-852 (310°C/61 dpa) and EP-450 (310°C/61dpa) steels. For EP-852 (305°C/69dpa) and EP-450 (320°C/81dpa, 335°C/89dpa) steels the tube diameter near the large plug (the top of the tube) was found to be slightly larger than near the small plug end, probably arising from dose and temperature variations along the length of the tubes.

From data on the diameter of stress-free tubes it follows, that the diameter change due to swelling is negligible in tubes of both steels. For stress-free creep tubes made of the EP-450 steel irradiated at 320°C and 335°C the diameter did not change under irradiation. For the tube of this steel irradiated at 310°C the diametral strain is equal to 0.1 %, but that does not exceed measurement errors. The same magnitude of the diametral strain (0.1 %) was measured for EP-852 steel irradiated at 310°C. Comparison with the results of the previous study [1], swelling of these steels appears to peak in the vicinity of 400°C.

Thus, as a first approximation it is reasonable to assume that the diametral strain of creep tubes investigated near 300°C is equal to the irradiation creep strain. The final conclusion concerning the balance of swelling, creep and densification strains will be made after TEM examination of the irradiated creep tubes.

One can see from the data shown in Table 2 that for the EP-450 steel the maximum irradiation creep strain is equal to 1.1% at the irradiation temperature of 310°C and at the dose of 61 dpa. At the hoop stress of 200 MPa the increase of both the irradiation temperature and dose does not result in an increase of the irradiation creep strain. The plot of the irradiation creep strain versus hoop stress is linear in EP-450 steel at all three irradiation temperatures investigated with some possible indication that precipitate-related strains may be included (see Figure 5).

The maximum irradiation creep strain of the EP-852 steel does not exceed 0.45 % and appears to be linear with stress. However, a full comparison between the two steels is somewhat impeded due to gas leakage or failure of several creep tubes with EP-852 steel cladding irradiated at 310°C to 61 dpa. At the irradiation temperature of 305°C and the dose of 69 dpa the irradiation creep strain of EP-852 steel is relatively small (see also Figure 5).

Discussion

At present, experimental data on irradiation creep characteristics of F/M steels are relatively scarce. In References 2 and 3 cladding creep tubes from the HT-9 F/M steel irradiated in the FFTF up to the high dose of 208 dpa have been investigated. French ferritic-martensitic steels EM-10 and EM-12 were irradiated to 77 dpa in PHENIX as creep tubes from typical cladding [4]. In the experiments mentioned above the minimum irradiation temperature was equal to 400°C. Lower irradiation temperatures are not available in the FFTF and PHENIX reactors because of their high inlet coolant temperatures. The inlet temperature of sodium in the BN-350 reactor is lower (~280°C) and allows irradiation of samples at much lower temperatures in comparison with those of other fast reactors.

From the data of the present work (see Table 2) one can see that for EP-450 steel the maximum value of the irradiation creep modulus *B* equals 0.74×10^{-6} $(\text{MPa}\times\text{dpa})^{-1}$ at irradiation temperatures in the 310-335°C range. Higher *B* values of $(1.6–1.7)\times10^{-6}$ $(\text{MPa}\times\text{dpa})^{-1}$ for several creep tubes should be ignored because the measured gas pressure in these tubes was found to be much lower than the initial pressure. If we assume that these tubes have lost part of the gas inventory after termination of the irradiation and that during irradiation the gas pressure in the tubes was equal to the nominal pressure, the values of *B* for these tubes will be equal to $(0.91\text{-}1.0)\times10^{-6}$ $(\text{MPa}\times\text{dpa})^{-1}$. For the EP-852 steel the nominal and measured hoop stresses differ insignificantly, and the calculated value of *B* does not exceed 0.75×10^{-6} $(\text{MPa}\times\text{dpa})^{-1}$.

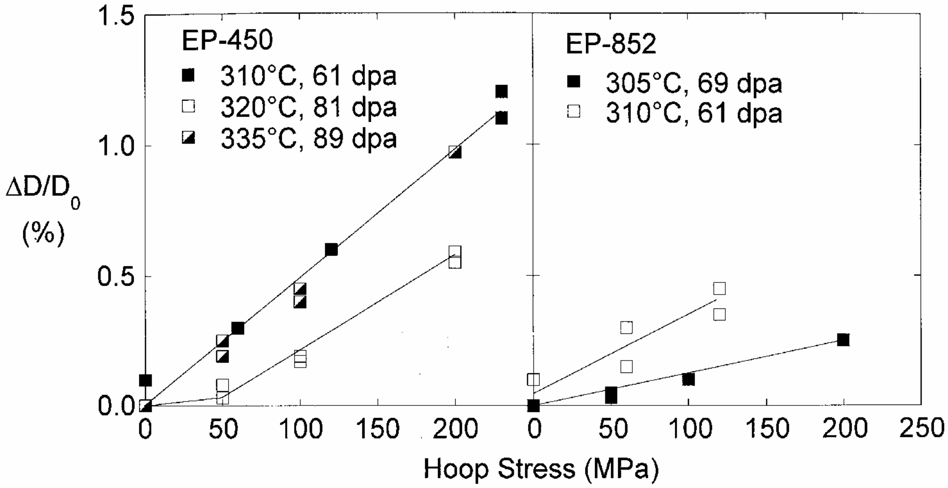

Figure 5. Irradiation creep strain versus nominal hoop stress for creep tubes made of EP-450 and EP-852 F/M steels irradiated in BN-350 fast reactor.

By comparing these values of irradiation creep moduli with the results of previous investigations [2-4] one can conclude that lowering the irradiation temperature from 400°C to 305-335°C does not lead to a significant change of irradiation creep rate in F/M steels.

The design of experimental subassemblies in the present experiment did not provide an opportunity to perform intermediate measurements of creep tube diameters during the course of irradiation. Therefore, it was not possible to determine the dependence of irradiation creep strain on dose for the EP-450 and EP-852 steels. As for the irradiation creep strain dependence on applied stress, this dependence is approximately linear in the EP-450 and EP-852 steels at all irradiation temperatures investigated (Figure 5). It was anticipated that there might be a deviation from linearity at higher stress levels, as sometimes observed at higher irradiation temperatures in other F/M steels.

For example, in HT-9 investigated in reference 2 the transition from linear behavior to a power law dependence with the exponent $n>1$ has been observed at ~400°C for hoop stresses in the range of 150-200 MPa. High values of n are typical following the onset of thermal creep, where the stress dependence of thermal creep rate can be described by a power law with exponent of 4 and higher [5, 6]. Thus, most likely, an increase of n from unity beginning from some critical hoop stress provides evidence of a change of irradiation creep mechanism [7]. In the present case, however, the thermal creep is negligible at irradiation temperatures of 305-335°C, as this fact was confirmed earlier in special thermal creep tests conducted on these tubes.

Conclusions

Measurements of stress-free swelling and irradiation creep strains in EP-450 and EP-852 F/M creep tubes irradiated in BN-350 at temperatures of 305-335°C to doses of 61-89 dpa allow us to draw the following conclusions.

1. Neutron irradiation at conditions mentioned above results in a strong degradation of ductility of the steels. While puncturing to release gas one of the gas creep tubes of EP-450 steel and four tubes of EP-852 irradiated at 310°C to 61 dpa failed in a very brittle mode.

2. Swelling and possibly precipitate-related densification of the EP-450 and EP-852 steels determined by measuring the stress-free creep tube diameter are very small in the vicinity of 300°C, falling within the measurement accuracy. Comparing with the results of the previous study, swelling of these steels appears to peak in the vicinity of 400°C.

3. The irradiation creep strain dependence on hoop stress of these steels is essentially linear at the irradiation conditions investigated.

4. At irradiation temperatures of 305-335°C and doses of 61-89 dpa the magnitude of irradiation creep modulus B for the EP-450 and EP-852 steels does not exceed 1.0×10^{-6} $(\mathrm{MPa} \times \mathrm{dpa})^{-1}$, confirming the relative resistance of F/M steels to irradiation creep at these low irradiation temperatures.

Acknowledgements

The Civilian Research and Development Foundation under Grant RE2-2224 sponsored the Russian portion of this effort. The Office of Fusion Energy, U.S. Department of Energy provided support for the U.S. portion of this research under Contract DE-AC06-76RLO 1830 with Battelle Memorial Institute.

References

[1] S. I. Porollo, Yu. V. Konobeev, A. M. Dvoriashin, N. I. Budylkin, E. G. Mironova, M. V. Leontyeva-Smirnova, A. G. Ioltukhovsky, and F. A. Garner, “Irradiation Creep and Mechanical Properties of Two Ferritic-Martensitic Steels Irradiated in the BN-350 Fast Reactor,” in Fusion Materials Semiannual Progress Report DOE/ER-0313/31, December 31, 2001, pp. 106-114; also submitted to Journal of Nuclear Materials.

[2] M. B. Toloczko, F. A Garner, and C. R. Eiholzer, “Irradiation Creep and Swelling of the US Fusion heats of HT9 and 9C-1Mo to 208 dpa at ~400°C,” Journal of Nuclear Materials, Vol. 212-215, 1994, pp. 604-607.

[3] M. B. Toloczko, and F. A Garner, “Variability of Irradiation Creep and Swelling of HT9 Irradiated to High Neutron Fluence at 400-600°C,” Effects of Radiation on Materials: 18th International Symposium, ASTM STP 1325, R. K. Nanstad, M. L. Hamilton, F. A. Garner, and A. S. Kumar, Eds., American Society for Testing and Materials, West Conshohocken, PA, 1997.

[4] J. L. Seran, V. Levy, P. Dubuisson, D. Gilbon, A. Maillard, A. Fissolo, H. Touron, R. Cauvin, A. Chalony, and E. Le Boulbin, “Behavior under Neutron Irradiation of the 15-15 Ti and EM10 Steels Used as Standard Materials of the Phenix Fuel Subassembly,” Effects of Radiation on Materials: 15th International Symposium, ASTM STP 1125, R. E. Stoller, A. S. Kumar, and D. S. Gelles, Eds., American Society for Testing and Materials, West Conshohocken, PA, 1992, pp. 1209-1233.

[5] D. G. Morris, “Creep in Type 316 Stainless Steel,” Acta Metallurgica, Vol. 26, 1978, pp. 1143-1151.

[6] B. A. Chin, “An Analysis of the Creep Properties of 12Cr-1Mo-W-V Steel”, Proceedings Conference on Ferritic Alloys for use in Nuclear Energy Technologies”, Snowbird, Utah, USA, 19-23 June 1983, TMS/AIME pp. 593-599, 1984.

[7] J. R. Mathews, and M. W Finnis, “Irradiation Creep Models-An Overview,” Journal of Nuclear Materials, Vol. 159, 1988, pp. 257-285.

4.0 COPPER ALLOYS

STATUS OF IN-REACTOR TENSILE STRAINING OF PURE COPPER AT A CONSTANT STRAIN RATE

RATE - D. J. Edwards (Pacific Northwest National Laboratory)*, B. N. Singh (RISØ NATIONAL LABORATORY, DENMARK), S. Tähtinen, P. Moilanen (VTT Industrial Systems, Finland), P. Jacquet and J. Dèkeyser (Reactor Technology Department, SCK·CEN, Belgium)

OBJECTIVE

The primary objective of this collaboration was to study the effect of in-reactor tensile straining on microstructural evolution and mechanical behavior in pure copper irradiated at 90°C in the BR-2 reactor in Mol, Belgium.

SUMMARY

Annealed tensile samples of pure copper were irradiated in the fission reactor BR-2 in Mol, Belgium at 90°C with a damage rate of 6×10^{-8} dpa/sec. The tensile specimens were a sheet-type specimen with a 3-mm gage width and a gage length of 7 mm. The first experiment involved two specimens, one of which was irradiated with no load to provide a comparative specimen to the other specimen, which was loaded at a constant strain rate of 1.3×10^{-7} s^{-1}. The uniaxial tensile load was applied 4 hrs after the irradiation rig was inserted into the reactor core. This corresponded to a total displacement damage of 8.6×10^{-4} dpa accumulated before the tensile test was started. The tensile test was considered complete once the load began rapidly falling and reached 100 MPa, at which level the test was stopped and the load quickly reduced to zero to leave the specimen intact. For these test conditions the specimen reached a total plastic strain of ~13% when the test was stopped, considerably less than that of unirradiated pure copper tested under the same strain rate, which was on the order of 50% total elongation. The second experiment involved two samples irradiated under identical irradiation and test conditions, but in this case the tensile load was not applied until a total dose of 1×10^{-2} dpa (~50 hours after insertion into the reactor core) was reached. Once the load was applied, the stress immediately climbed to ~150 MPa with little plastic strain, followed by a small yield drop and work hardening up to a maximum stress of ~200 MPa. As in the first experiment, the tensile test was stopped when the load began decreasing and reached a level of 100 MPa.

These samples were removed from the reactor and shipped to Risø, where mechanical tests were performed on the unloaded specimens and microstructural characterization performed on the all four individual conditions. The tensile specimens subjected to the in-reactor loading were found to have a necked region with a crack partially separating the two halves of the tensile specimen. Transmission electron microscopy (TEM) specimens were taken from areas as close to the cracked region as possible and also from regions further into the gage section away from the failed region. The TEM analysis revealed no evidence of substantial homogenous plastic flow in either of the loaded conditions, i.e. no cell wall formation and only minimal dislocation tangles due to forest hardening interactions. Dislocation channels were the predominant marker of plastic flow, however, these channels varied greatly from area to area in number density and width. The dislocation channels were relatively free of deformation-induced dislocations; however, a qualitative assessment indicated defects such as stacking fault tetrahedra were still present inside the channels, although at a much lower density than the surrounding regions outside the channels. These defects may have formed inside inoperative dislocation channels as the irradiation continued. This work demonstrated that the defects produced during irradiation begin to alter the deformation response of the material from very early stages even in the presence of deformation-induced dislocations, effectively inhibiting homogenous flow and the accumulation of dislocations. Future work will quantify the distribution of defects and dislocations in the microstructure.

---

* Pacific Northwest National Laboratory (PNNL) is operated for the U.S. Department of Energy by Battelle Memorial Institute under contract DE-AC06-76RLO-1830.

PROGRESS AND STATUS

Introduction

Post-irradiation tensile testing has been the primary investigative method for studying the effects of radiation hardening on metals and alloys. These experiments have typically involved irradiation of a particular material in an unstressed condition to a desired displacement level, followed by removal from reactor for testing and microstructural characterization. In effect the specimens are allowed to accumulate radiation damage in the absence of an applied stress and the deformation-induced dislocations. In-reactor pressurized tube creep tests have proven that applied stresses can produce a different microstructure than observed in post-irradiation testing and characterization of materials not loaded when in reactor, but these tests were usually not aimed at studying radiation hardening at low irradiation temperatures ($<0.3\text{-}0.4T_m$). While the post-irradiation tensile experiments have certainly provided unique insights into the behavior of irradiated materials, these experiments do not necessarily represent their in-service behavior.

The materials employed in the structural components of fission or fusion reactors are exposed simultaneously to external stresses and irradiation-induced defect populations produced continuously during neutron irradiation. Under these conditions both the magnitude and the spatial distribution of defect accumulation and hence the deformation behavior may be substantially different from that observed in the case of post-irradiation experiments. This raises the question of whether the results and conclusions of such post-irradiation testing can always be safely extrapolated to the behavior of structural materials in a nuclear reactor. To address this question, a series of in-reactor uniaxial tensile tests have been initiated in the BR-2 fission reactor in Mol, Belgium. The dynamic stress-strain curves have been measured for samples of pure copper loaded at a continuous strain rate while neutron irradiated at 90°C. The in-reactor tests have been completed and the samples returned to Risø, where the samples have recently been characterized by TEM. The preliminary results of microstructural characterization and their implications will be discussed in the following sections.

Experimental Procedure

A more thorough description of the experimental setup for the in-reactor tests have been described elsewhere by Singh et al. [1], so only a brief description will be provided here. The material used for this experiment was oxygen-free high conductivity (OFHC) copper containing 10 and 3 ppm of Ag and Si, respectively, and <1 ppm of Fe and Mg each. Tensile samples were fabricated from polycrystalline copper annealed for 550°C for 2 hrs to yield a well annealed microstructure with a dislocation density $<10^{12}$ m^{-2} and a grain size of ~30 μm. The specimens were loaded into a specially designed test assembly constructed to apply a continuous load at a constant strain rate inside the reactor core. Additional specimens were included near the loaded samples, but these specimens were not loaded during the experiment in order to provide a direct comparison.

The basic principle of the tensile test module inserted into the reactor core involved using a pneumatic bellow (pressurized by He gas) to apply the stress and a linear variable displacement transducer to measure the resulting displacement. The entire test assembly and specimens remained submerged in stagnant, demineralized water for the duration of the experiment. The temperature was monitored using three thermocouples located in the assembly near the specimen, and three dosimeters were placed in the assembly to measure the neutron flux. The test assembly was inserted into the core in open tube G60 of BR-2 during steady state operation of the reactor. The neutron flux at this position was 3×10^{17} n/m^2 (E>1 MeV) corresponding to a displacement damage rate of $\sim 6 \times 10^{-8}$ dpa/s. The water near the specimens reached 90°C in ~15 minutes, and the bellow was monitored constantly to ensure no load was applied to the specimen. The strain rate chosen for this experiment was 1.3×10^{-7} s^{-1} to ensure an appreciable displacement level was reached before the specimen failed. The tensile test was stopped once the stress decreased to 100 MPa, at which point the load was completely removed to preserve the specimen.

For the first set of experiments involving copper (other metals and alloys will be tested in future experiments), two test conditions were employed. The first condition involved loading the specimen at four hours after insertion of the test assembly into the reactor core. The total dose when the load was applied was ~8.6 x 10^{-4} dpa. The second condition allowed the specimen to sit in the reactor for 50 hours before the load was applied, letting the specimen accumulate a total dose of 1 x 10^{-2} dpa. The resulting load versus time curves for these two test conditions are compared in Figure 1. The 1st condition ended when the specimen began failing after ~300 hours (the total strain when the load was removed was ~13% elongation), whereas the second test condition began failing after roughly a 160 hours in reactor under load (load was removed at ~7.5% total elongation). These specimens were removed from the reactor and shipped to Risø. Optical metallography and SEM revealed a necked region in the gage section that had begun separating by cracking. TEM disks were punched from regions close to the cracked region and further away to characterize the microstructure that may have experienced different levels of strain than the crack region. A preliminary assessment of the microstructural results will be presented in the following section.

Results

The TEM characterization revealed that neither of the two samples tested in reactor exhibited cell walls or a significant dislocation network. Examples of the microstructures of the two tested conditions (13% elongation and 7.5% elongation) are shown in Figures 2 and 3, respectively. It was anticipated based on the tensile curves in Figure 1 that each of the two conditions would exhibit some dislocation networks and

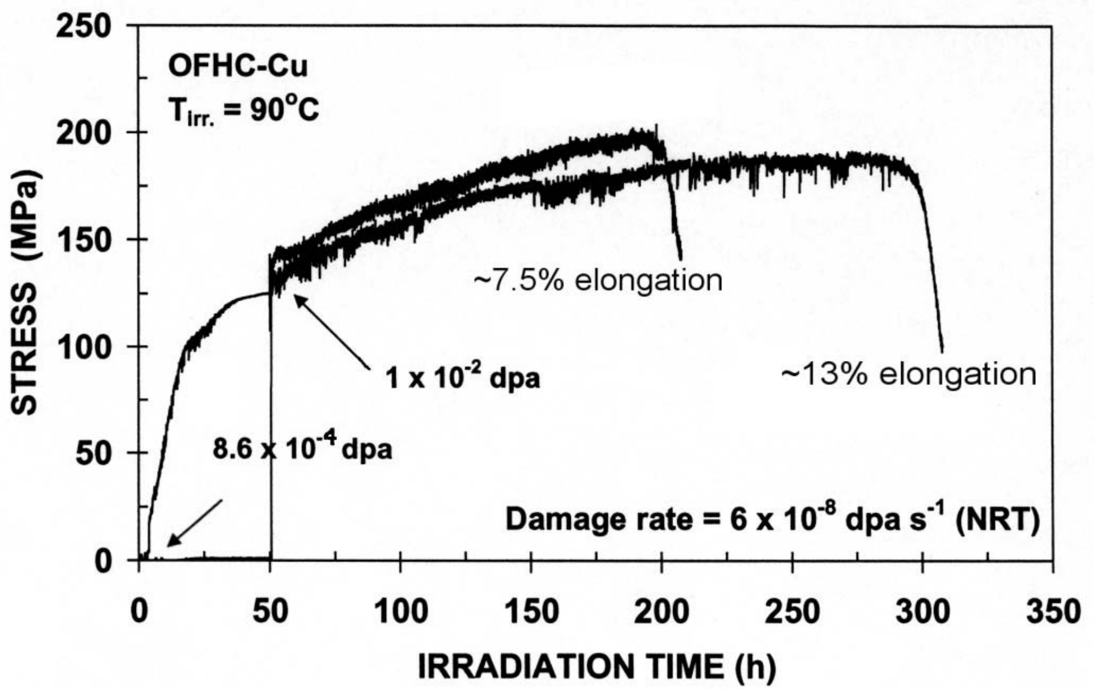

Figure 1. Uniaxial loading curves versus time are shown for the two different samples loaded while in reactor. The first sample loading was started 4 hours the test assembly was inserted into the reactor core, whereas in second experiment the test was started 50 hours after insertion. The first test was stopped at ~13% elongation, whereas the second test was stopped at ~7.5% elongation. The fluctuation in the tensile stress was determined to be noise in the electronics and test assembly.

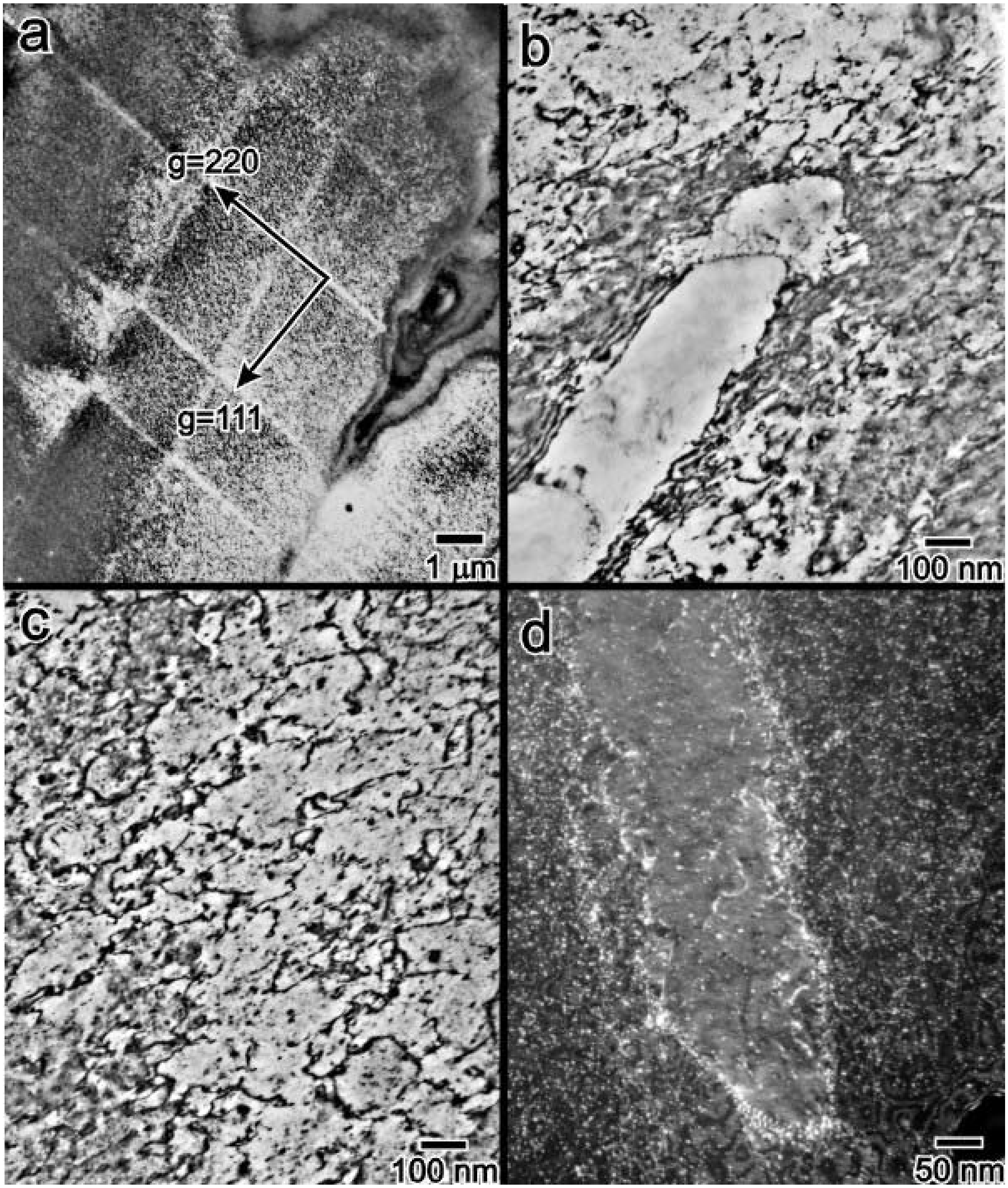

Figure 2. Dislocation channels in the sample that failed after 13% are shown in (a) oriented on a g=111 2-beam condition between a <112> and a <011> zone axis. A cleared channel similar to a shear band in heavily deformed, unirradiated copper is shown in Figure (b) and (d). The dislocation microstructure shown in (c) indicates some minor movement or “percolation” of the dislocations through the defects in the matrix, but in general no large scale clearing of the defects is visible.

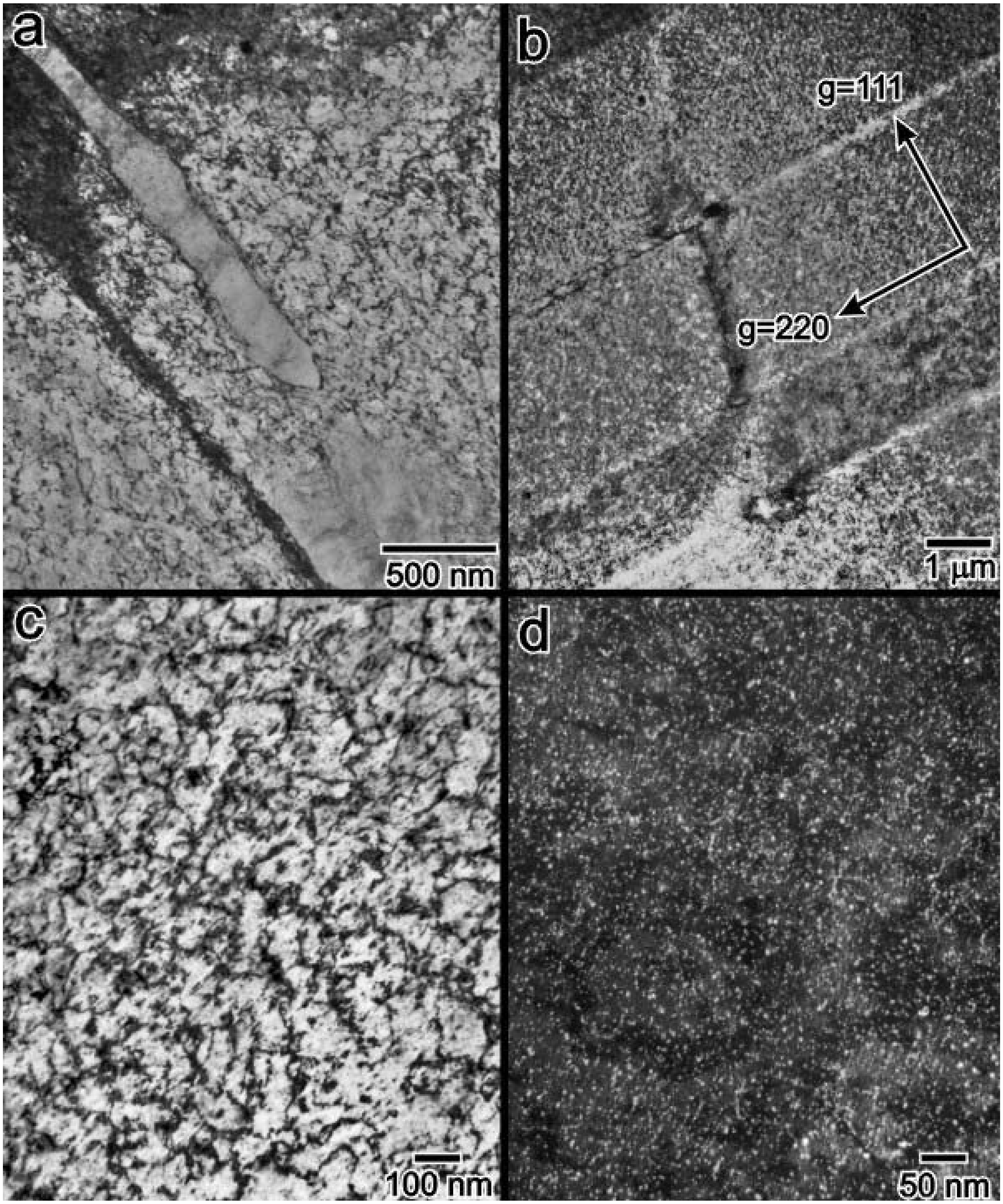

Figure 3. Examples of dislocation channels in the sample that began failing around 7.5% elongation. The channel in (a) resembles a shear band commonly observed in heavily cold rolled copper. The dislocation segments shown in (c) don't appear to have participated in the overall deformation, perhaps pinned by the high density of small defects shown in (d).

perhaps a cell wall structure given the large degree of plastic strain and work hardening observed. However, the most noticeable features of the deformed microstructures were the presence of dislocation channels and the lack of homogenous deformation, not unlike the situation observed in tensile samples irradiated and then tested out of reactor. The degree of channeling varied considerably from grain to grain, and the TEM samples taken closer to the failure region contained grains that exhibited a greater degree of channeling. Because of the variable microstructure and limited sampling volume it is difficult to make quantitative comparisons on channeling between the two different test conditions. Overall there does not appear to be a definitive difference between the two cases, but further analysis of the dislocation and defect densities is needed to confirm this statement. The defect densities in each sample are very high in the regions between the channels, and with few exceptions no general clearing of defects outside channeled regions occurred. Examples of grain and twin boundaries intersected by channels were quite common, and these examples often demonstrated that large strains had occurred judging from the shear offset along the boundaries.

The absence of cell wall formation and no visible reduction in defect density outside the channels (based strictly on qualitative estimates at this point), indicates that the defects produced during irradiation were very effective at hindering the motion of dislocations generated during the early stages of deformation. Further support for this can be extracted from the behavior of the sample tested in the second experiment where the load was not started until the sample had accumulated a dose of 10^{-2} dpa. The loading curve shown in Figure 1 indicates that not only did the extra dose result in a higher yield stress before plastic deformation began, but that a visible yield drop occurred. One explanation for the lower elongation in this case is that the extra dose accumulated forced the material into a more severe localized flow mode than the sample where the load was applied at a lower dose (8.6×10^{-4} dpa). The experimental data suggests that for this combination of strain rate and radiation damage rate, the defects produced during irradiation can strongly affect both the generation and mobility of the dislocations. A higher strain rate might prove more effective at removing the defects and prevent a buildup of high density, but further experimentation is needed. A higher strain rate would, of course, limit the dose accumulated before the sample failed, making direct comparisons very difficult.

Future Work

A more detailed analysis of microstructures for each of the different test conditions will be performed in the next two quarters. A comparison of defect and dislocation densities outside and inside the dislocation channels will be made, as well as comparisons made of the defect and dislocation distributions produced by the two loading conditions. These results will also be compared to the unloaded reference samples irradiated along side each of the in-reactor tested samples to provide a baseline for the microstructural characterizations. Additional comparisons will be made with the microstructures of unirradiated samples of pure copper tested under the same strain rate and test temperatures to further evaluate the effect of in-reactor loading. Future irradiation experiments are planned that will include in-reactor testing of CuCrZr, pure Fe and a ferritic steel.

Acknowledgements

The present work was partly funded by the European Fusion Technology Programme. D. J. Edwards would like to thank Risø National Laboratory for the support and assistance during his visit. His work was also partly supported by the U.S. Department of Energy under contract DE-AC06-76RLO 1830 with the Battelle Memorial Institute at the Pacific Northwest National Laboratory.

References

[1] B. N. Singh, S. Tähtinen, P. Moilanen, P. Jacquet and J. Dèkeyser, Journal of Nuclear Materials, **320**, 299-304 (2003).

THE EFFECT OF POST-IRRADATION ANNEALING ON STACKING FAULT TETRAHEDRA IN NEUTRON-IRRADIATED OFHC COPPER -

D. J. Edwards (Pacific Northwest National Laboratory)[*], B. N. Singh and M. Eldrup (RISØ NATIONAL LABORATORY, DENMARK)

OBJECTIVE

Evaluate the annealing behavior of stacking fault tetrahedra (SFT) formed during neutron irradiation in OHFC copper irradiated at 200 and 250°C.

SUMMARY

Two irradiation experiments have been completed wherein two sets of tensile specimens of OFHC copper were irradiated with fission neutrons, one set at 200°C and the other at 250°C. Post-irradiation annealing in vacuum was then used to evaluate the change in the defect microstructure, including vacancy-type SFT, voids, and dislocation loops. Individual samples within each set were given one annealing exposure at 300, 350, 400, 450, 500, or 550°C for 2 hours. The fine-scale defect microstructure was characterized by transmission electron microscopy (TEM) to compare the defect size and spatial distribution at each annealing temperature and reference the results to that measured in the as-irradiated condition.

Based on the change in the SFT size distributions, post-irradiation annealing led to a preferential removal of the smaller sized SFT, but did not lead to a general coarsening as might be expected from an Oswald ripening scenario. The issue of whether the SFT produced during irradiation are all structurally perfect is still being investigated at the time of this report, however, the images of the SFT appeared more perfect after annealing at 300°C and higher. Further analysis is being performed to determine whether intermediate stages of SFT formation exist in the as-irradiated condition.

PROGRESS AND STATUS

Introduction

Post-irradiation annealing is a useful tool to explore the stability of defect agglomerates in irradiated materials. One of the issues that has arisen recently is how do stacking fault tetrahedra interact with mobile dislocations generated during deformation. This issue arose during attempts to model the clearing of defects produced during irradiation when cleared channels form inside neutron irradiated copper deformed in tensile tests. Analysis of such interactions by Wirth et al. [1] and by Hiritani et al. [2] revealed that a mobile dislocation interacts differently with an SFT depending on whether the SFT is in a perfect configuration or is truncated. These efforts have pointed to the importance of understanding more about the nature of the SFT produced during irradiation.

By annealing neutron irradiated samples of pure copper, insight can be gained into the relative stability of SFT and how they interact with other defects within the irradiated material. An earlier post-irradiation experiment by the authors [3] revealed that the SFT were very stable, with a large fraction of the defects surviving after 50 hours of annealing at 300°C, a temperature well above recovery Stage V. Above recovery Stage V the vacancy-type defects become increasingly unstable and emit vacancies into the lattice. From this experiment it was observed that the images of the SFT became more easily discernible after annealing, partly in response to a slight reduction in density and increase in average size. However, an alternative, additive reason for this observation is that the more perfect triangular appearance of the SFT after annealing may have been aided by the preferential removal of SFT that were not structurally perfect or were partially dissociated loops. The release of vacancies from these defects may have been

---

[*] Pacific Northwest National Laboratory (PNNL) is operated for the U.S. Department of Energy by Battelle Memorial Institute under contract DE-AC06-76RLO-1830.

partially absorbed by surrounding, closely-spaced SFT. This question of whether non-perfect SFT exist in the as-irradiated material is an important issue for describing the annealing kinetics of SFT in irradiated copper as well as how the defects interact with mobile dislocations.

To further explore this issue, an annealing experiment has been performed on samples of OFHC copper that were neutron irradiated at two different temperatures, 200°C and 250°C, in the DR-3 reactor in Denmark. These two irradiation temperatures were chosen in order to compare the effect of having an additional high density of vacancy sources/sinks (a moderate density of voids form at 250°C) present in the microstructure along with the vacancy-type SFT. An earlier semi-annual report [4] briefly described this experiment and the results obtained after annealing the samples irradiated at 200°C. In the following report the results obtained from annealing both sets of samples irradiated at the two temperatures will be presented and compared.

Experimental Procedure

Irradiation experiments have been completed wherein two sets of tensile specimens of OFHC copper were irradiated with fission neutrons in the DR-3 reactor in Denmark, one set at 200°C and the other at 250°C, to a total dose of 0.3 dpa. The post-irradiation annealing was performed by taking individual samples from each set and annealing (in vacuum) each sample at either 300, 350, 400, 450, 500, or 550°C for 2 hours. Positron annihilation spectroscopy was conducted on each annealed sample as well as on the specimens in the as-irradiated conditions. Results of those experiments will be described in later reports. After the PAS was completed, 3-mm disks were punched from each condition and electropolished using a solution of 25% perchloric acid, 25% ethanol and 50% water at 11V for about 15s at ~20°C. The microstructure of each condition was characterized in a JEOL 2000FX transmission electron microscope. The SFT and void images were taken by imaging near a <011> zone axis oriented along the 200 direction in either weak beam dark field or bright field kinematical conditions for the SFT and voids, respectively. Dislocation and loop images were obtained from the same zone axis orientation, but imaged using the [111] reflection.

Results

The specimens irradiated at 200°C contained a high density of small SFT and small SIA (self interstitial atom) loops. Those specimens irradiated at 250°C contained an additional microstructural component in the form of voids with an average size of ~15 nm and a density of 3.5 x $10^{20}m^{-3}$. The SFT microstructure formed both at 200 and 250°C proved to be very stable, with a significant density of defects remaining up to 400°C, after which their density began to decrease rapidly. The measured size distributions for the SFT (and voids at 250°C) are plotted in Figures 1 through 3 to illustrate the changes that occurred due to annealing after irradiation. Images of the SFT are shown in Figures 4 and 5 comparing the effect of annealing to the SFT imaged in the as-irradiated samples.

For samples irradiated at 200°C, a gradual decrease in SFT density occurred up to ~400°C, after which the decrease was more pronounced (see Figure 1). Annealing at 550°C for 2 hours removed all of the defect clusters produced at 200°C, including the dislocation loops, and yielded a well-annealed microstructure with only a few line dislocations. The annealing response of the SFT formed at 200°C cannot be considered as Oswald ripening, but as a reduction in the total number of vacancies contained within the SFT with only a slight coarsening that did not exceed a maximum size. The samples irradiated at 250°C possessed a reasonable density of cavities (~5 x 10^{20} m^{-3}) that seemed rather immune to the effects of annealing up to 450°C (see Figure 3). The density of SFT after irradiation at 250°C was lower than that measured at 200°C. The annealing response for samples irradiated at 250°C (Figure 2) was somewhat different than observed for samples irradiated at 200°C in that the size distributions shifted to the larger sizes when annealed at 300 and 350°C, indicating a real growth of SFTs. On the other hand, when annealed at 400°C and above, the density began to decrease substantially with little change in the

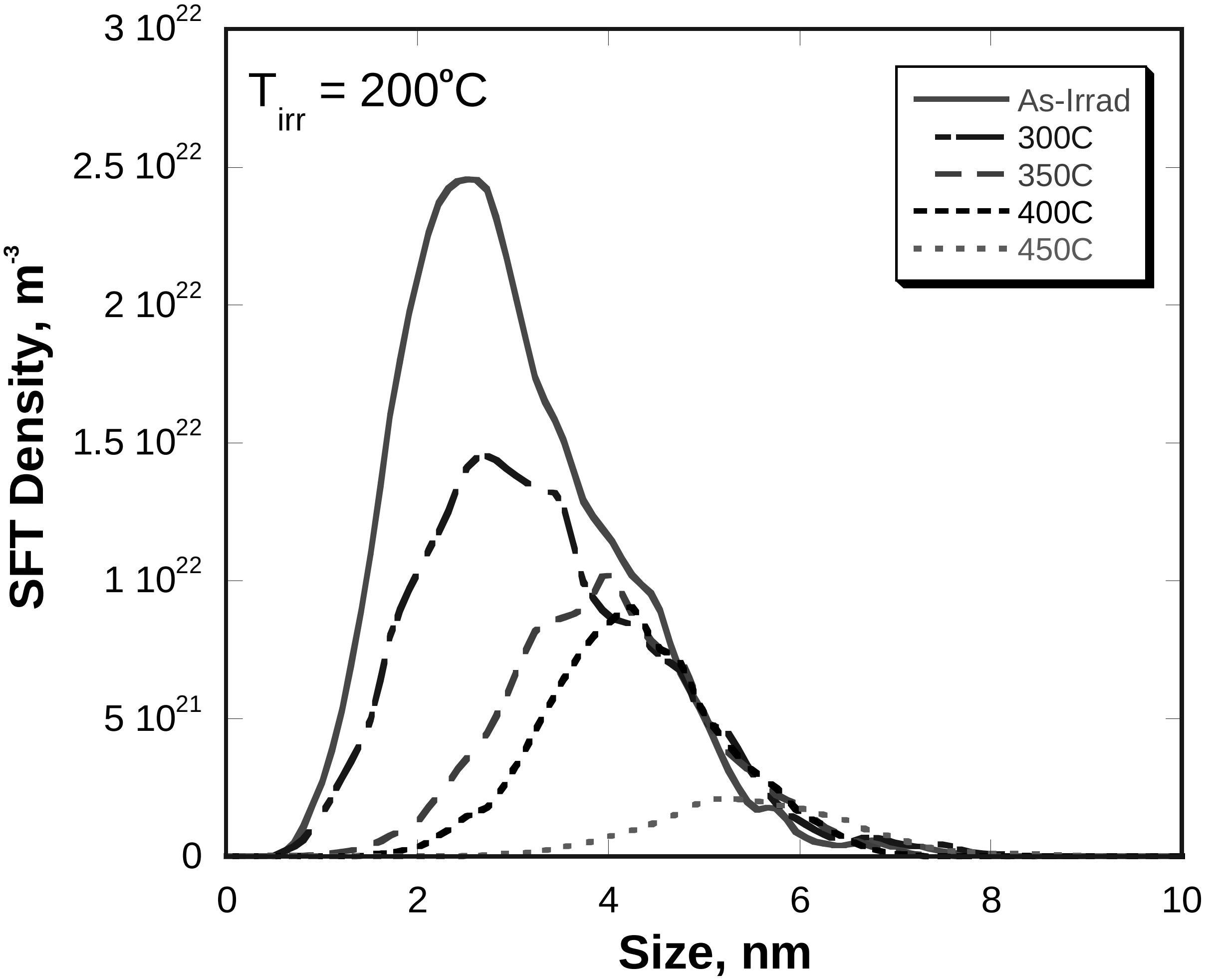

Figure 1. Size distributions for the SFT in OFHC copper irradiated at 200°C and exposed to different annealing temperatures for 2 hours. Note that the size distributions do not indicate a general coarsening such Oswald ripening, but rather the preferential removal of the smaller SFT.

peak of the size distribution. Annealing a 250°C irradiated sample at 500°C for 2 hours produced a very heterogeneous distribution of both SFT and voids, with some grains completely free of defects of either type. The role of the voids remains unclear, but their influence will have to be accounted for in the modeling of the annealing behavior of the SFT. It is interesting to note that the size of the smallest SFT survive during annealing increase with increasing annealing temperature. Furthermore, the mean size of the SFT surviving during annealing increases with increasing annealing temperature. Both of these observations are significant since in the as-irradiated condition neither the size of the smallest SFT nor the mean size measured after irradiation are affected in any substantial way by the irradiation temperature.

Unfortunately, the issue of whether the SFT are structurally perfect cannot be addressed adequately from the images obtained thus far. Higher magnification images are needed under better controlled imaging conditions to be able to reliably determine whether the small SFT are indeed perfect or not. Thickness fringes appearing in the stacking fault of the SFT complicate the images of the SFT, in some cases giving the appearance of small Frank loops with a triangular strain field when it may in fact just be a bright

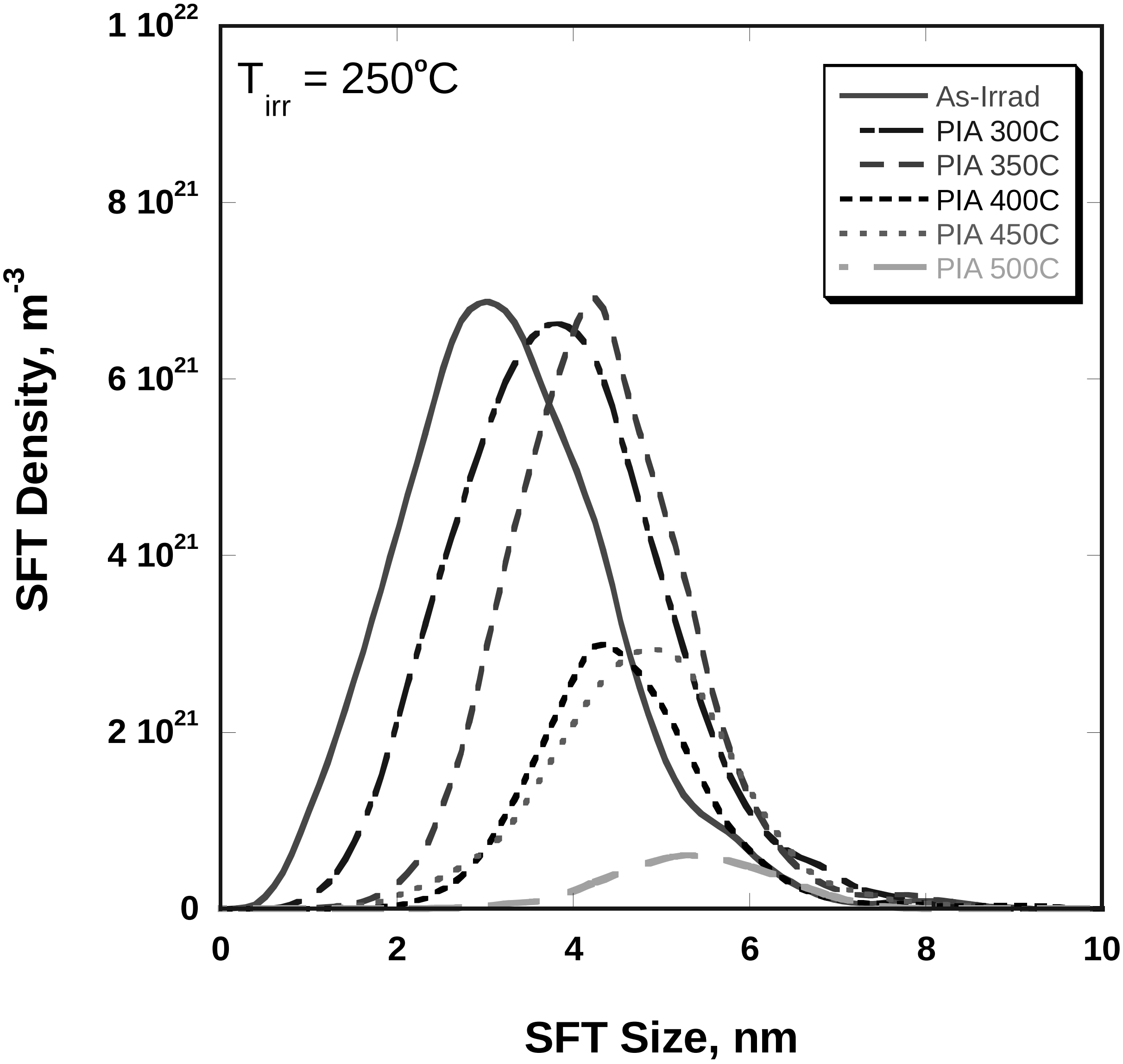

Figure 2. Size distributions for the SFT in OFHC copper irradiated at 250°C and exposed to different annealing temperatures for 2 hours. Compared to the annealing response shown in Figure 1, coarsening up to 350°C, then the smaller SFT begin to disappear at higher annealing temperatures.

thickness fringe. A more careful analysis of the SFT is needed to study this issue and find more suitable imaging conditions and criteria.

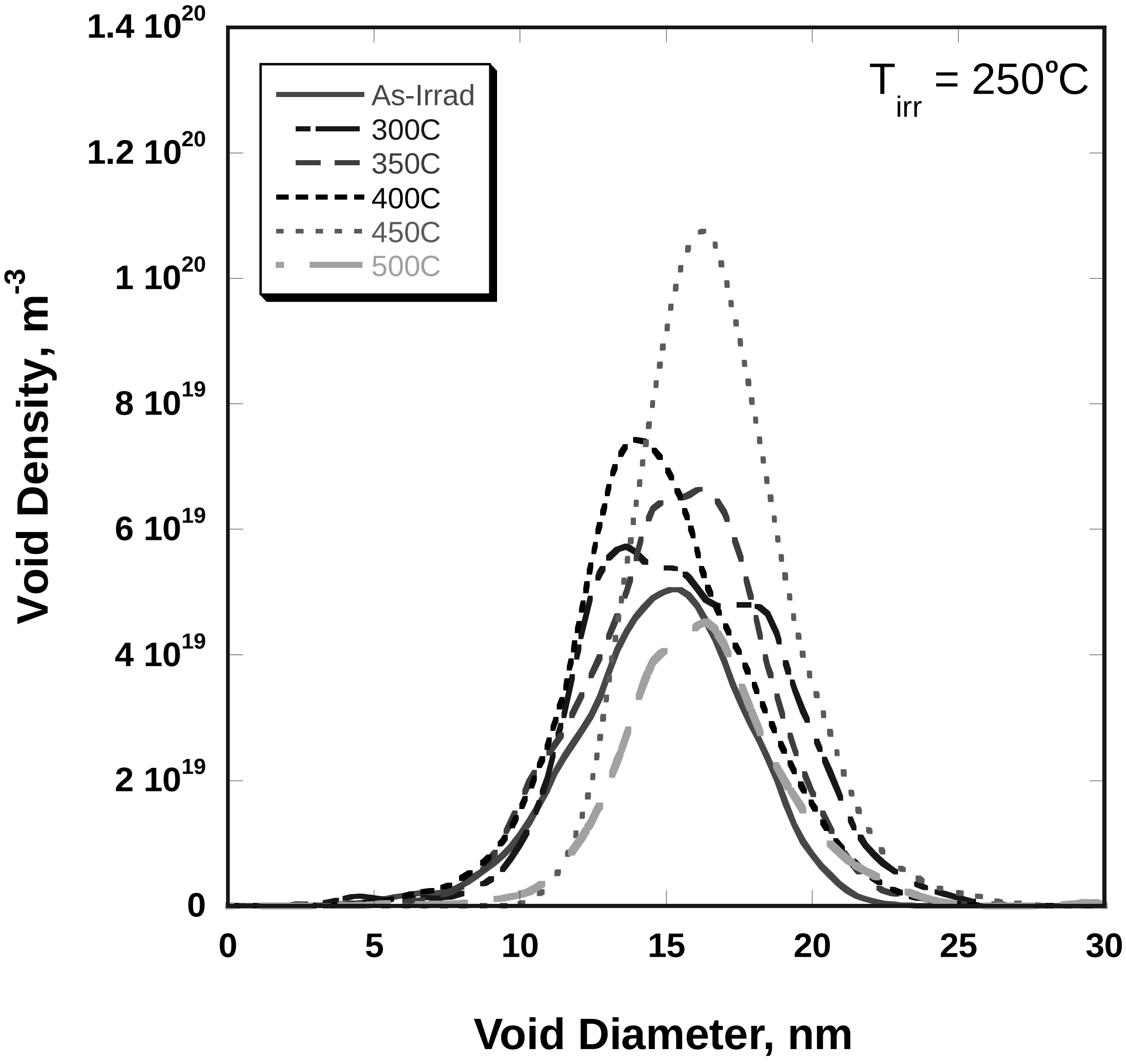

Figure 3. Size distributions for the cavities formed in OFHC copper after irradiation at 250°C and exposed to different annealing temperatures for 2 hours. The higher peak density after annealing at 450°C is being evaluated further to see if it is a real behavior or simply a scatter in the density measurements.

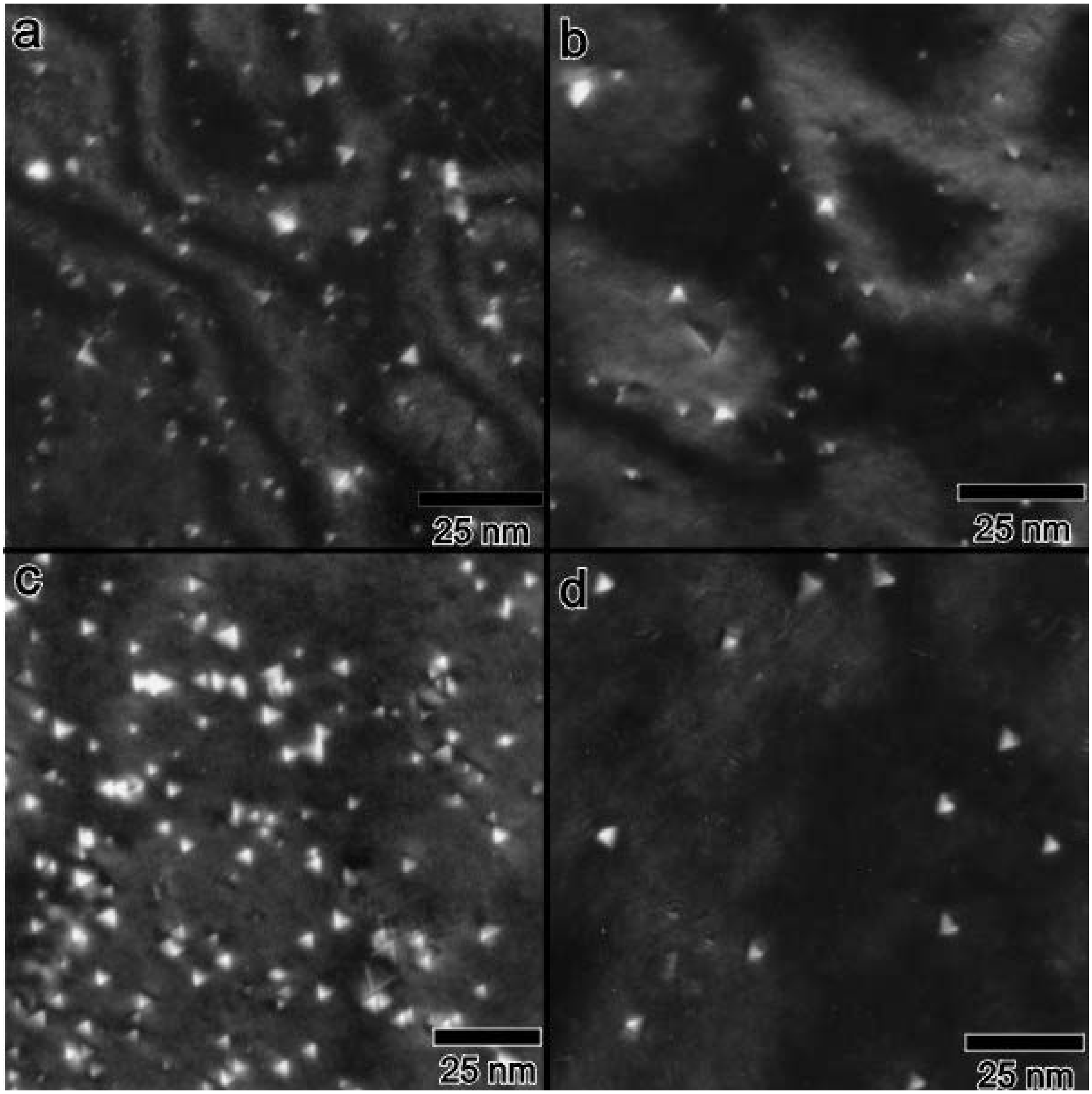

Figure 4. Images of the SFT formed in OFHC copper after irradiation at 200°C and exposed to different annealing temperatures for 2 hours. The image shown in (a) represents the as-irradiated condition, whereas the images provided in (b), (c) and (d) are from samples post-irradiation annealed at 300, 350 and 450°C, respectively. The area in (c) is thicker than the areas shown in the other images, hence the apparent higher density of SFT.

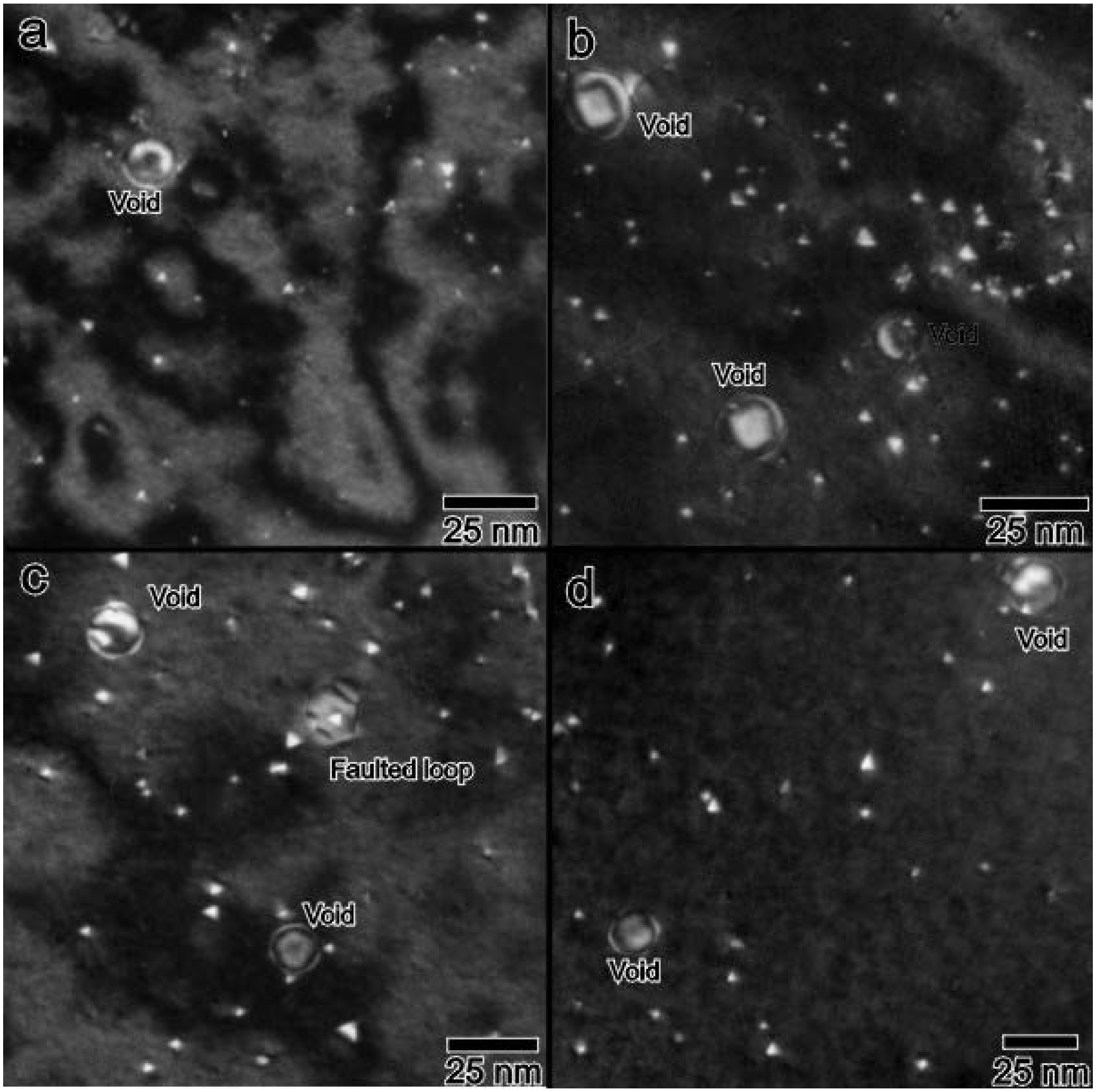

Figure 5. Images of the SFT formed in OFHC copper after irradiation at 250°C and exposed to different annealing temperatures for 2 hours. The image shown in (a) represents the as-irradiated condition, whereas the images provided in (b), (c) and (d) are from samples post-irradiation annealed at 300, 350 and 450°C, respectively. Voids and a large, faulted dislocation loop are indicated in the figure.

Future Work

Modeling of the annealing response of the SFT is in progress, and will have to address a number of issues to describe accurately the annealing response. These issues include the possibility that some fraction of the SFT are not perfect in the as-irradiated condition, that is, some of the SFT may be truncated. The presence of small vacancy-type Frank loops or intermediate defect configurations (partially-dissociated Frank loops) needs to be considered also. Another issue is that the relative structural perfection of the SFT may play a strong role on determining their annealing behavior. The spatial distribution is deemed an important factor since the relative close spacing of the defects produced at 200°C yields a small mean free path that may promote a simple exchange of vacancies between SFT for intermediate annealing temperatures and annealing times. The details of the microstructure will continue to be analyzed, including a measurement of the line dislocation and dislocation loop density. Other samples of OFHC irradiated at 200°C or less are going to be reevaluated to see if the images can provide any insight into the issue regarding the perfection of the SFT.

Acknowledgements

The present work was partly funded by the European Fusion Technology Programme. D. J. Edwards would like to thank Risø National Laboratory for the support and assistance during his visit. His work was also partly supported by the U.S. Department of Energy under contract DE-AC06-76RLO 1830 with the Battelle Memorial Institute at the Pacific Northwest National Laboratory.

References

[1] B. D. Wirth, V. V. Bulatov and T. Diaz de la Rubia, Journal of Engineering Materials and Technology, **124**, 329-334 (2002).

[2] M. Hiritani, H. M. Zbib and B. D. Wirth, Phil. Mag. A, **82**, No. 18, 2709-2735 (2002).

[3] B. N. Singh, D. J. Edwards and P. Toft, J. Nucl. Mater. **299** (2001) 205.

[4] D. J. Edwards and B. N. Singh, “Status Of Collaborative Research Program Between PNNL And Risø National Laboratory”, DOE/ER-0313/33, Fusion Semi-Annual Progress Report, for the period ending Dec. 31, 2002, 111-119.

5.0 REFRACTORY METALS AND ALLOYS

No contributions.

6.0 AUSTENITIC STAINLESS STEELS

No contributions.

7.0 MHD INSULATORS, INSULATING CERAMICS AND OPTICAL MATERIALS

STUDY OF THE LONG-TERM STABILITY OF MHD COATINGS FOR FUSION REACTOR APPLICATIONS -- B. A. Pint and L. D. Chitwood (Oak Ridge National Laboratory, USA) and A. Suzuki (NIFS, Japan)

OBJECTIVE

The objective of this task is to assess the long-term, high-temperature compatibility of high electrical resistance coatings with lithium at high temperatures. Electrically insulating coatings on the first wall of magnetic confinement reactors are essential to reduce the magnetohydrodynamic (MHD) force that would otherwise inhibit the flow of the lithium coolant. Experimental work is being conducted on bulk ceramics to determine resistivity, basic lithium compatibility and maximum-use temperatures of candidate ceramics such as Er_2O_3, Y_2O_3 and $YScO_3$. As the next step, coatings of Y_2O_3 are now being evaluated.

SUMMARY

In order to determine the high temperature resistivity and Li compatibility of several candidate materials, bulk specimens were fabricated for testing. Results for $YScO_3$ showed sufficiently low resistivity up to 800°C. Combined with the Li compatibility results, $YScO_3$ meets the metrics for bulk materials and should be tested as a coating. Initial characterization of the electron beam physical vapor deposited (EB-PVD) Y_2O_3 coatings shows significant deterioration after exposure to Li at 700° or 800°C.

PROGRESS AND STATUS

Introduction

Based on positive results for bulk, polycrystalline Y_2O_3 specimens, Y_2O_3 coatings were fabricated and tested.[1-3] However, coating delamination and/or reaction with Li was detected after static Li exposures at 700° and 800°C. Initial post-exposure characterization of the coatings is now being conducted. The problems with Y_2O_3 as well as previously reported problems with CaO dissolving with Li and lack of compatibility between AlN and V alloys indicates that none of these candidates are likely to meet the coating performance metrics[4] for a viable MHD coating material at 700°C. Thus, two new candidates are now being considered, Er_2O_3 and $YScO_3$. In bulk form, both have shown some compatibility to Li. However, no high temperature resistivity data has been found for $YScO_3$ to meet the bulk material performance metrics.[4] Current work is being conducted to fabricate and test high-purity dense specimens of these materials.

Experimental Procedure

The $YScO_3$ specimen was made by ball milling powders, cold-pressing and then hot-pressing in a graphite die. The Y_2O_3 coatings were deposited on V-4Cr-4Ti substrates by EB-PVD at Lawrence Livermore National Laboratory and have been described previously.[2-3] The experimental procedure for lithium exposures also has been outlined elsewhere.[1,5] After exposure, the coatings were cleaned by submerging them in methanol for 24h to dissolve the residual Li. The coatings were characterized using field emission gun, scanning electron microscopy (SEM) with energy dispersive x-ray analysis (EDX), auger electron spectroscopy

(AES) and x-ray diffraction (XRD) with 300kV Cu Kα radiation. The resistance of coated specimens and bulk specimens was measured from 25°-800°C in a test rig with a vacuum pressure of ≈10^{-6} Torr. The vacuum system was used to avoid oxidation of the coated V-4Cr-4Ti substrate. For bulk specimens (≈3mm thick by 12-15mm diameter), gold electrodes were deposited on opposite sides for the resistance measurement.

Results and Discussion

Figure 1 shows the measured resistivity results for several specimens compared to literature values for Y_2O_3.[6] As reported previously, the as-received, EB-PVD Y_2O_3 coatings showed lower resistivity than these literature values. However, recent measurements on bulk Y_2O_3 showed considerably higher results. Measurements for bulk $YScO_3$ were very encouraging, showing a restivity at 700°C several orders of magnitude higher than that required by the metrics (dashed lines in Figure 1).

Specimens with Y_2O_3 coatings were examined by SEM before and after exposure to Li. Figure 2a shows the as-deposited coating grain structure in plan-view. After 2000h at 700°C, only fragments of the coating remained on the V-4Cr-4Ti substrate, Figure 2b. The coatings were intact on the substrates after exposures for 100 and 1000h at 800°C but all of the coating was gone after a 2000h exposure at 800°C. Figure 3 shows the coating appearance in plan-view after the shorter exposures at 800°C. The original coating morphology is not apparent. Smooth patches (slightly darker) appeared after 100h, Figure 3a, and the entire surface appears covered by this morphology after 1000h, Figure 3b. Analysis by EDX showed significant Ti in or on the coating which may indicate a Ti-rich oxide phase is forming. Both the V alloy test capsule and substrate contain Ti that may have reacted to form a compound. However, a specific phase has not been identified by XRD. Subsequent characterization work will section the coatings for Auger and/or

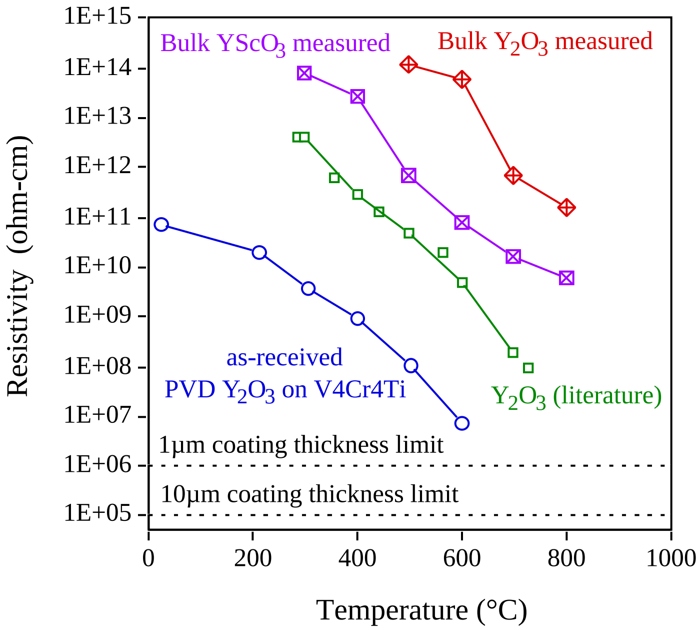

Figure 1. Resistivity as a function of temperature for bulk ceramic specimens of Y_2O_3 and $YScO_3$ and EB-PVD Y_2O_3 coatings compared to values cited in the literature.[5]

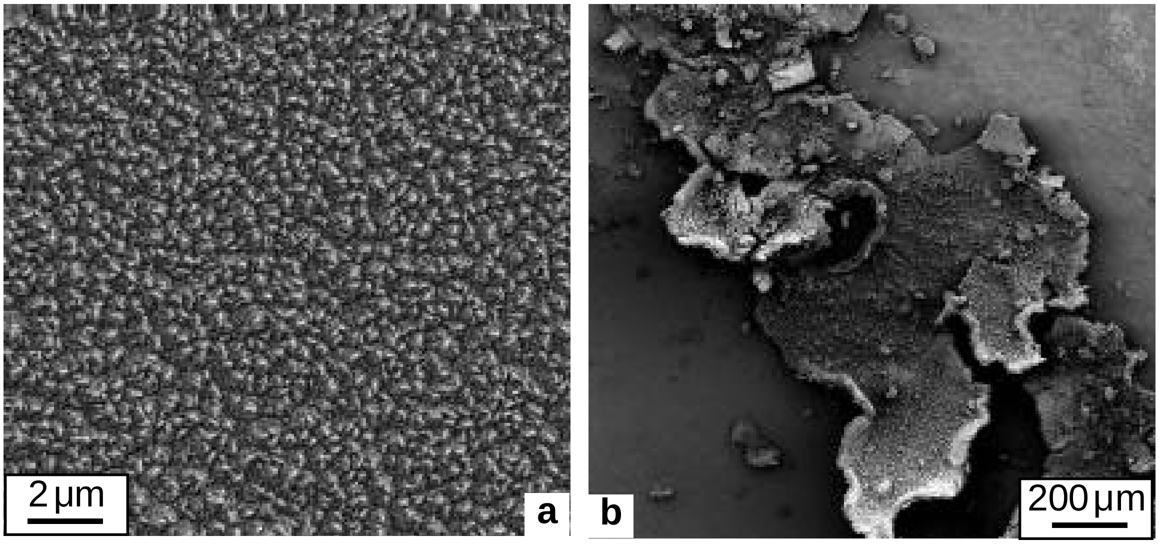

Figure 2. SEM secondary electron images of EB-PVD Y_2O_3 coatings (a) as-received and (b) after 2000h at 700°C in static Li.

TEM analysis.

REFERENCES

1. B. A. Pint, J. H. DeVan and J. R. DiStefano, J. Nucl. Mater. 307-311 (2002) 1344.
2. B. A. Pint and L.D. Chitwood, DOE/ER-0313/32 (2002) 101.
3. B. A. Pint and L. D. Chitwood, DOE-ER-0313/33 (2002) 129.
4. B. A. Pint and J. R. DiStefano, DOE/ER-0313/32 (2002) 87.
5. B. A. Pint, L. D. Chitwood and J. R. DiStefano, J. Nucl. Mater. 289 (2001) 52.
6. K. Natesan, C. B. Reed, M. Uz, J. H. Park and D. L. Smith, ANL/TD/TM00-10 (2000).

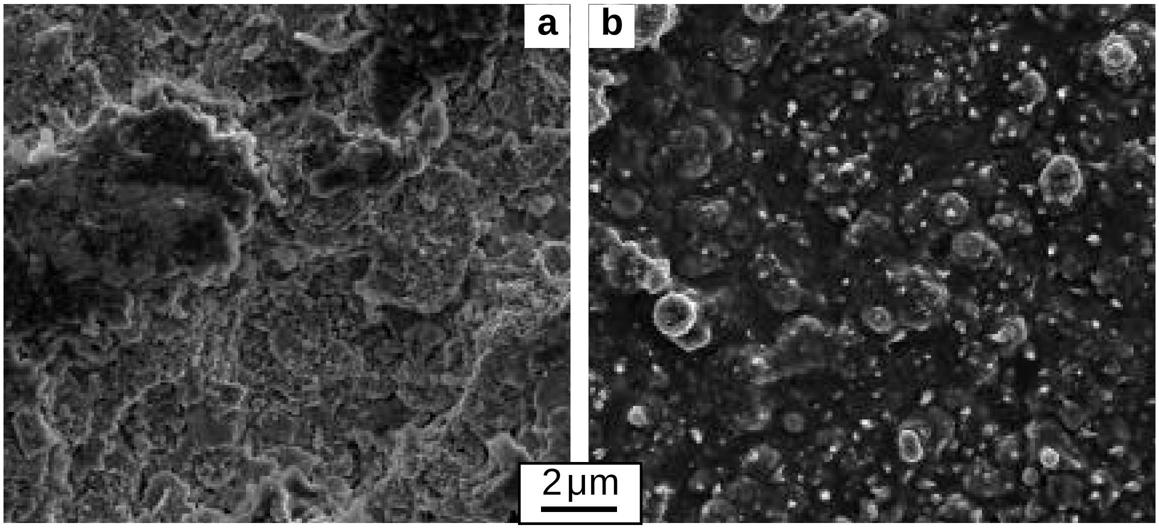

Figure 3. SEM secondary electron images of EB-PVD Y_2O_3 coatings after exposure to static Li for (a) 100h and (b) 1000h.

8.0 BREEDING MATERIALS

No contributions.

9.0 RADIATION EFFECTS, MECHANISTIC STUDIES, AND EXPERIMENTAL METHODS

DEFORMATION AND FRACTURE MECHANISMS IN IRRADIATED FCC AND BCC METALS

–S.J. Zinkle (Oak Ridge National Laboratory) and G.E. Lucas (University of California-Santa Barbara)

OBJECTIVE

The objective of this report is to assess deformation mechanisms in several irradiated alloy systems that are of interest for fusion energy applications.

SUMMARY

The effects of irradiation on the mechanical behavior of face-centered cubic (FCC) and body centered cubic (BCC) metals are briefly reviewed, including dislocation channeling, cleavage fracture, and irradiation creep at low irradiation temperatures and helium grain boundary embrittlement at high temperatures. Particular emphasis is placed on the microstructural mechanisms responsible for the changes in mechanical behavior. Four different material systems are examined as typical examples of behavior in FCC (dispersion strengthened and precipitation strengthened copper, Type 316 austenitic stainless steel) and BCC (V-Cr-Ti alloys, 8-9 Cr ferritic/martensitic steel) metals. Similarities and differences in the mechanical behavior of irradiated FCC and BCC metals are highlighted. The stress and temperature regimes where various deformation mechanisms predominate before and after irradiation are displayed in terms of Ashby deformation maps. Tensile tests can often provide a misleading indication of the fracture toughness behavior due to the lack of stress concentrators in un-notched specimens.

PROGRESS AND STATUS

1. Introduction

Irradiation can produce dramatic changes in the mechanical properties of metals [1-7]. For example, early studies on irradiated metals [3,4,8,9] clearly demonstrated that irradiation at low temperatures ($<0.3\ T_M$, where T_M is the melting temperature) produced pronounced hardening. The hardening is typically accompanied by a severe decrease in uniform plastic elongation as measured in a uniaxial tensile test [1-3]. Embrittlement as measured by decreases in fracture toughness and increases in the ductile to brittle transition temperature (DBTT) of BCC alloys are commonly observed consequences of low temperature irradiation hardening [10-13]. Irradiation creep [14,15] and high temperature He embrittlement of grain boundaries [16,17] are examples of additional mechanical property degradation processes that occur in irradiated metals at progressively higher temperatures.

The decrease in tensile ductility associated with low temperature neutron irradiation was the topic of numerous studies performed in the 1960s, and the phenomenon was commonly referred to as "low temperature radiation embrittlement". However, these early studies did not attempt to measure the fracture toughness of irradiated specimens. As will be discussed in section 4 of this paper, tensile "embrittlement" does not universally correlate with fracture toughness embrittlement and there are numerous examples now available where high dynamic and/or quasi-static toughness is maintained in irradiated metals that exhibit low uniform elongations. A more appropriate term for the low uniform elongation typically observed following low-temperature irradiation is “loss of strain hardening capacity” (which may or may not be associated with a reduction in fracture toughness).

The present paper will focus on the mechanical properties of four FCC and BCC alloy systems before and after irradiation. Copper alloys (GlidCop Al25 oxide dispersion strengthened copper, CuCrZr and CuNiBe) and Type 316 austenitic stainless steel were chosen as representative FCC metals. V-4%Cr-4%Ti and 8-9%Cr ferritic/martensitic steels have been chosen to demonstrate behavior observed in BCC metals. Ashby-type maps [18] have been constructed in order to assist in the identification of the various deformation processes that occur at different stresses and temperatures before and after irradiation.

2. Fundamentals of radiation hardening at low temperatures

Irrespective of the alloy type or crystal structure, a general feature associated with irradiation at low temperature (below ~0.3 T_M) is increased matrix hardness due to the presence of radiation-induced defects which act as obstacles to dislocation motion. Figure 1 shows the yield strength of copper as a function of damage level for irradiation near room temperature [19-26]. The yield strength increases with increasing dose up to ~0.1 displacements per atom (dpa), and then reaches an apparent "saturation hardening" regime where the yield strength remains nearly constant (~300 MPa) as the dose is increased. A similar low-dose rapid hardening regime followed by a slowly evolving hardening behavior at higher doses has been observed in several other FCC and BCC metals irradiated at low temperatures, although materials such as austenitic and ferritic-martensitic stainless steel maintain a slight positive slope in the "saturation hardening" regime [27-30].

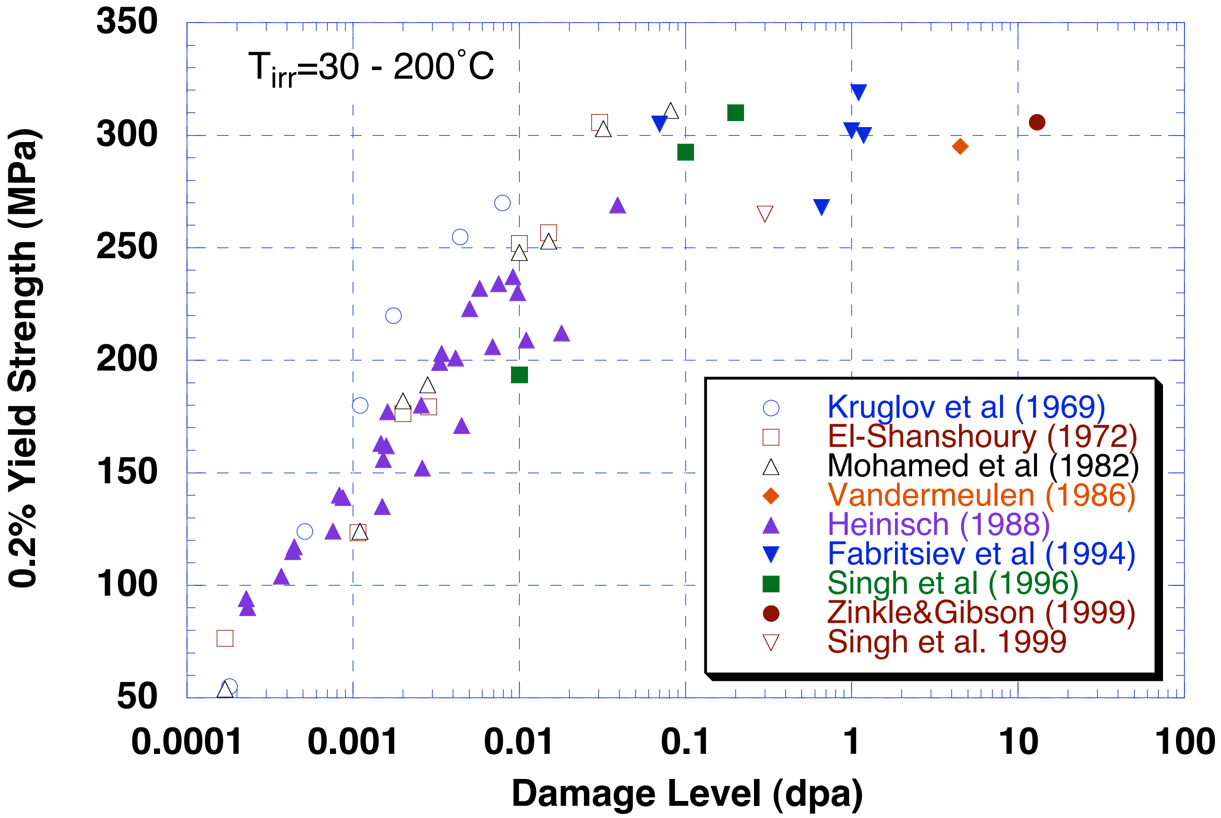

Fig. 1. Dose dependence of radiation hardening in pure copper irradiated with neutrons at 30-200˚C [19-26].

The increase in matrix hardness at low irradiation temperatures is due to the presence of small radiation-induced clusters of vacancies and self-interstitial atoms. From simple geometric considerations of a dislocation traversing a slip plane which intersects randomly distributed obstacles of diameter d and atomic density N, and using the approximation for dislocation line tension $T \sim 0.5\mu b^2$, the increase in the critical resolved shear stress ($\Delta\tau$) in a pure metal is given by the well-known dispersed barrier hardening equation [5,31,32]

$$\Delta\tau = \alpha\mu b(Nd)^{1/2} \qquad (1)$$

where μ is the shear modulus, b is the magnitude of the Burgers vector of the glide dislocation ($a_0/\sqrt{2}$ for FCC, $\sqrt{3}\, a_0/2$ for BCC, where a_0 is the lattice parameter), and α is average barrier strength of the radiation-induced defect clusters. Early experimental estimates of the barrier strength of defect clusters produced during low-temperature neuron irradiation were typically □~0.5. More recent experimental estimates (obtained on electron microscopes with improved resolution in order to detect small defect clusters) range from □~0.10-0.25 for copper [33,34], austenitic stainless steel [32,35], and V-4Cr-4Ti [36] irradiated at low temperatures. Since the mean defect cluster size changes very slowly at these low irradiation temperatures, the increase in strength (eqn. 1) is mainly due to an increase in the defect cluster density at low doses. Transmission electron microscopy studies of metals irradiated at low temperature [36,37] have observed that the defect cluster density typically reaches an apparent saturation value of ~$1x10^{24}$ to $1x10^{24}m^3$ at doses above ~0.1 dpa. Pure Fe is known to be an exception to this general trend; saturation in the visible black spot defect cluster density has not been observed in Fe following irradiation near room temperature to doses in excess of 0.3 dpa [38].

The appropriate dislocation barrier superposition rules need to be considered when analyzing radiation hardening in alloys. Depending on the relative barrier strength of the hardening agents in the alloy (solid solution hardening, precipitation hardening, etc.), the radiation hardening component may be given by a square root summation of the squares of the preirradiation and irradiation hardening components (or more complex superposition equations), rather than a simple linear superposition [4,39,40].

For polycrystalline specimens, the uniaxial tensile stress is related to the critical resolved shear stress by the Taylor factor (M):

$$\square = M\ \square \qquad (2)$$

where M equals 3.06 for equiaxed FCC and BCC metals [41]. It should be noted that several studies have found evidence that the rate of radiation hardening increases with decreasing grain size [3,9,42,43]. On the other hand, conflicting results on the effect of grain size have been obtained in BCC metals such as Fe [4,44,45]. Further work is needed to determine the quantitative significance (and possible physical mechanisms) of this effect [32]. If a radiation modified grain size effect exists, the value of □ determined from studies on polycrystalline specimens is an upper limit to the value appropriate for large-grained or single crystal specimens.

A characteristic feature that accompanies the pronounced hardening in metals irradiated at temperatures below electrical resistivity recovery stage V (~0.35 T_M) is loss of work hardening capacity. Early studies of radiation hardening produced competing models for the hardening mechanism, based on “dislocation source locking” and “lattice friction” concepts. Several researchers have proposed that both mechanisms operate, with source hardening responsible for the upper yield point and lattice hardening responsible for the lower yield stress observed in metals irradiated at low temperatures [38,46-48]. The loss of work hardening capacity produces sharp decreases in uniform elongation. Both effects have been shown to be generally due to dislocation channeling [2,36,38,49-55]. Dislocation channeling occurs because the radiation-induced defect clusters present at these low temperatures can be readily cut by gliding dislocations (□~0.1-0.25, as opposed to 0.8 for impenetrable Orowan obstacles). This produces a defect-free path for subsequent dislocations emitted from the operating source [2,38,50-54,56-66]. Dislocation channeling begins to occur above a critical dose/hardening level (corresponding to N>~$1x10^{24/}m^3$ for copper tested at room temperature [32]). At low doses, the presence of dislocation channeling may also depend on the amount of deformation [53] (channeling is present at low levels of deformation, whereas the deformation mode reverts to cell structure at high levels of deformation/stress). Twinning has also been observed to cause a pronounced loss in strain hardening capacity in austenitic stainless steel irradiated at 290˚C and tested near room temperature [66-68].

3. Brief overview of deformation behavior of irradiated metals

Several aspects of the deformation behavior of irradiated BCC and FCC metals are qualitatively similar. In particular, the physical phenomenon of dislocation channeling has been observed in numerous BCC, FCC, and hexagonal close-packed metals following neutron irradiation at temperatures below ~0.3 T_M [2,38,69,70]. The irradiation creep compliance of BCC and FCC steels at moderate temperatures are within a factor of two of each other [14,71,72]. Finally, high temperature He embrittlement of grain boundaries has been observed to occur in numerous BCC and FCC metals and alloys at irradiation temperatures above 0.5 T_M [16,17,73,74], although the threshold helium concentration for pronounced high temperature embrittlement has been observed to be significantly higher in ferritic/martensitic steels compared to austenitic stainless steels. For high levels of radiation hardening, cleavage fracture can be induced in BCC alloys due to the well-known Ludwig-Davidenkov relationship (due to the localized stress exceeding the cleavage stress) [10].

Radiation hardening is typically most pronounced in BCC and FCC metals following irradiation at low temperatures [13,29,75,76] (neutron irradiated stainless steel being a notable exception [28,77]). Figure 2 summarizes the yield strength vs. temperature for unirradiated and neutron irradiated GlidCop Al25 oxide dispersion strengthened copper [26,78,79]. The yield strength of GlidCop following neutron irradiation is significantly higher than the unirradiated yield strength for irradiation temperatures up to ~300˚C. At irradiation and test temperatures above ~300˚C, the yield strength of irradiated GlidCop is comparable to that of unirradiated specimens. The temperature-dependent increase in strength of the irradiated pure copper and copper alloy specimens can be directly correlated with the temperature-dependent defect cluster density produced by irradiation [32].

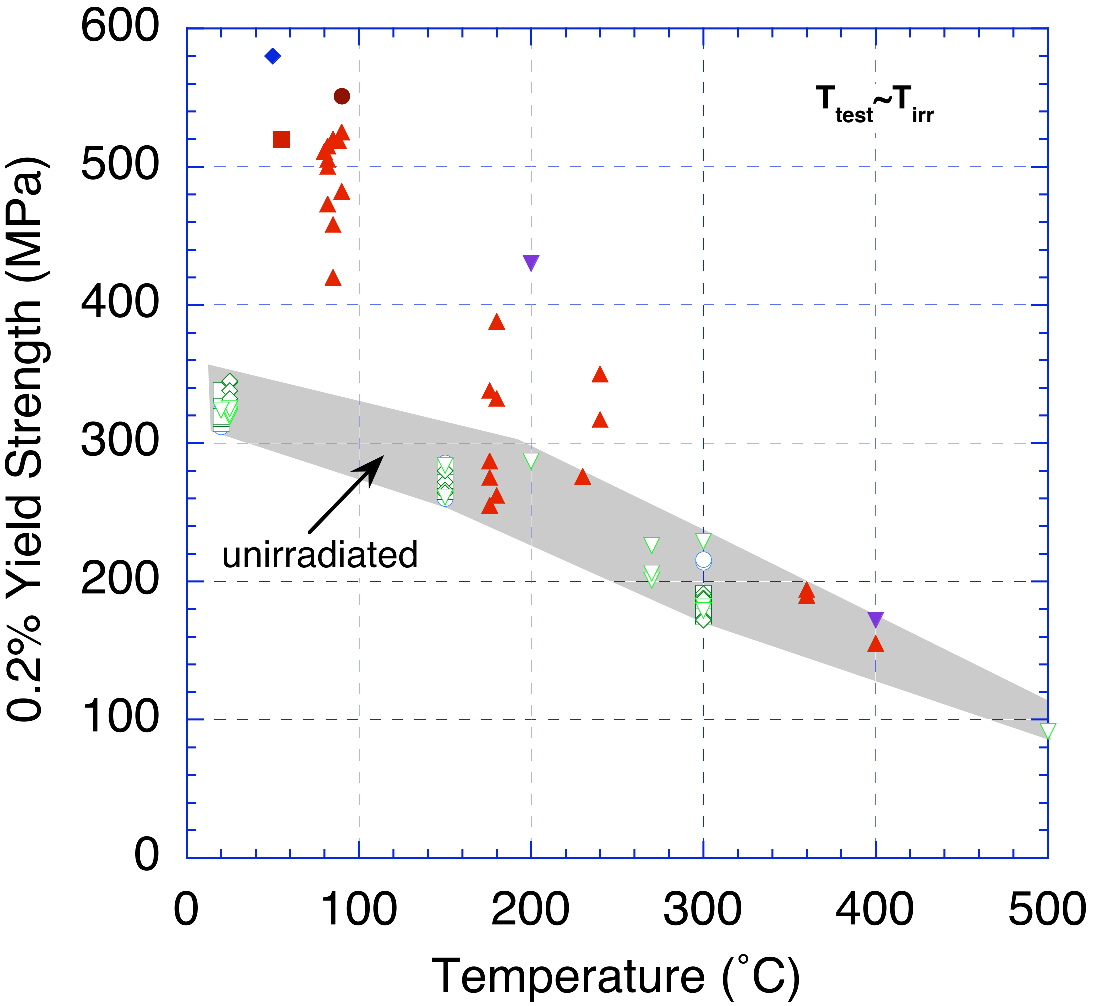

Fig. 2. Temperature dependence of yield strength in unirradiated and neutron irradiated GlidCop AL25 oxide dispersion strengthened copper [26,78,79].

metals above ~0.3 T_M. At these higher irradiation temperatures, rapid coarsening of the vacancy and interstitial defect cluster microstructure with increasing irradiation temperature is observed [32,36]. For FCC metals, the dominant defect clusters in the low-temperature radiation hardening regime are generally either vacancy-type stacking fault tetrahedra or a mixture of vacancy- and interstitial-type dislocation loops. For BCC metals, a significant hardening contribution is deduced to be associated with submicroscopic cavities; interstitial-type dislocation loops also make a significant contribution. The radiation hardening behavior of neutron-irradiated austenitic stainless steel is particularly noteworthy because it exhibits a nonmonotonic temperature dependence. The tensile strength of stainless steel irradiated to moderate damage levels (above ~3 dpa) exhibits a maximum value at irradiation temperatures near 300˚C [28,77,80-82]. The microstructure at these conditions consists of a mixture of faulted dislocation loops, “black spot” defect clusters, and nanometer-sized cavities [83].

It has been suggested that dislocation channeling may also induce grain boundary cracking in some irradiated BCC alloys [38]. At higher temperatures, channel fracture has been observed in the grain interiors of some irradiated and deformed metals containing a high concentration of voids [84].

4. Comparison between tensile behavior and fracture toughness

One major consequence of dislocation channeling is that the associated extreme localization in the deformation within the cleared channels produces a very low macroscopic value for the uniform elongation as measured in a uniaxial tensile test [2,51,54]. Uniform elongations below 1% are commonly observed in both BCC and FCC metals irradiated at low temperatures. Although low values of uniform elongation can impose significant impacts on structural design criteria, low tensile elongation (and/or low tensile toughness) is not universally associated with low fracture toughness. The term "low temperature radiation embrittlement" dates back to the 1950s, and was originally associated with the low uniform elongation commonly observed in tensile tests of irradiated metals. Fracture toughness tests were performed infrequently on irradiated materials during this time period. Therefore, accurate comparisons between tensile behavior and fracture toughness of irradiated metals were virtually nonexistent (although low temperature irradiation was known to often produce significant reductions in fracture toughness, particularly in BCC alloys). In many cases, the pronounced decrease in uniform elongation in metals irradiated at low temperatures is not accompanied by comparable dramatic reductions in total elongation or reduction in area. Unfortunately, there is widespread association of the term “low temperature radiation embrittlement” to describe the behavior of irradiated metals with low uniform elongation.

There are many examples where low temperature radiation causes a simultaneous reduction in the uniform elongation (and also the tensile toughness, defined as the integrated area under the stress vs. strain tensile curve) and fracture toughness. However, radiation-induced reductions in uniform elongation and tensile toughness cannot be universally correlated with changes in fracture toughness (due to the importance of stress concentrators and prompt crack propagation effects in fracture toughness measurements). As outlined below, there are several recent examples in BCC and FCC alloys where tensile toughness and uniform elongation behavior has been explicitly shown to not correlate with fracture toughness.

Figure 3 compares the tensile and fracture toughness behavior of CuCrZr before and after irradiation [85,86]. Large reductions in uniform elongation and tensile toughness occur after irradiation to 0.3 dpa at ~50 and 200˚C (irradiated $e_u \leq 1\%$), whereas there was no change in the fracture toughness ($K_J \sim 150$ MPa-$m^{1/2}$ before and after irradiation). Similarly, pronounced reductions in uniform elongation (irradiated $e_u \leq 1\%$) and tensile toughness have been observed in austenitic stainless steel irradiated to ~2 to 7 dpa at 225-330˚C [28,77,80-82]. However, high fracture toughness ($K_J > 150$ MPa-$m^{1/2}$) is maintained in several heats of irradiated austenitic stainless steel even when the uniform elongation is low [80,87].

Figure 4 summarizes the tensile and fracture toughness behavior for two ferritic-martensitic steels irradiated to 2-3 dpa at low temperatures [87,88]. The tensile curves for HT-9 show significantly *higher* uniform elongations and *higher* work hardening capacity than the corresponding curves for F82H. The tensile toughness for HT-9 irradiated at 250˚C is about a factor of two *higher* than that for irradiated F82H. In contrast, the fracture toughness of irradiated HT-9 is significantly *lower* than that of irradiated F82H. The highest tensile toughness was observed for HT-9 irradiated at 250˚C and tensile tested at 90˚C; this set of experimental conditions produced the lowest fracture toughness (lower shelf behavior) in the corresponding fracture toughness tests. Similar differences in the qualitative trends for tensile and fracture toughness have been observed in V-4Cr-4Ti alloys [12,13,89]. For example, the uniform elongation and tensile toughness of V-4Cr-4Ti irradiated to 4 dpa at 400˚C *increased* by more than a factor of two as the test temperature was decreased from 400˚C to room temperature, whereas the fracture toughness *decreased* by nearly an order of magnitude. Due to the lack of stress concentrators in the smooth tensile tests, it is clearly apparent that tensile toughness and/or uniform elongation is not a reliable quantitative or qualitative indicator of fracture toughness behavior.

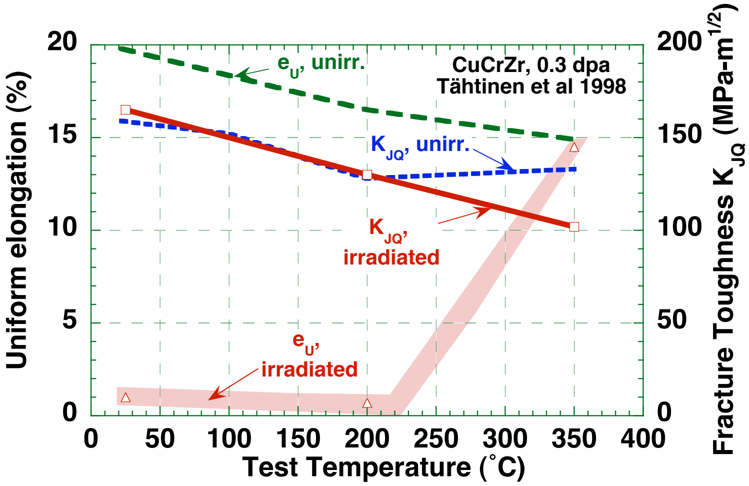

Fig. 3. Comparison of the uniform elongation and fracture toughness of CuCrZr before and after irradiation to 0.3 dpa, T_{test}~T_{irr} [85].

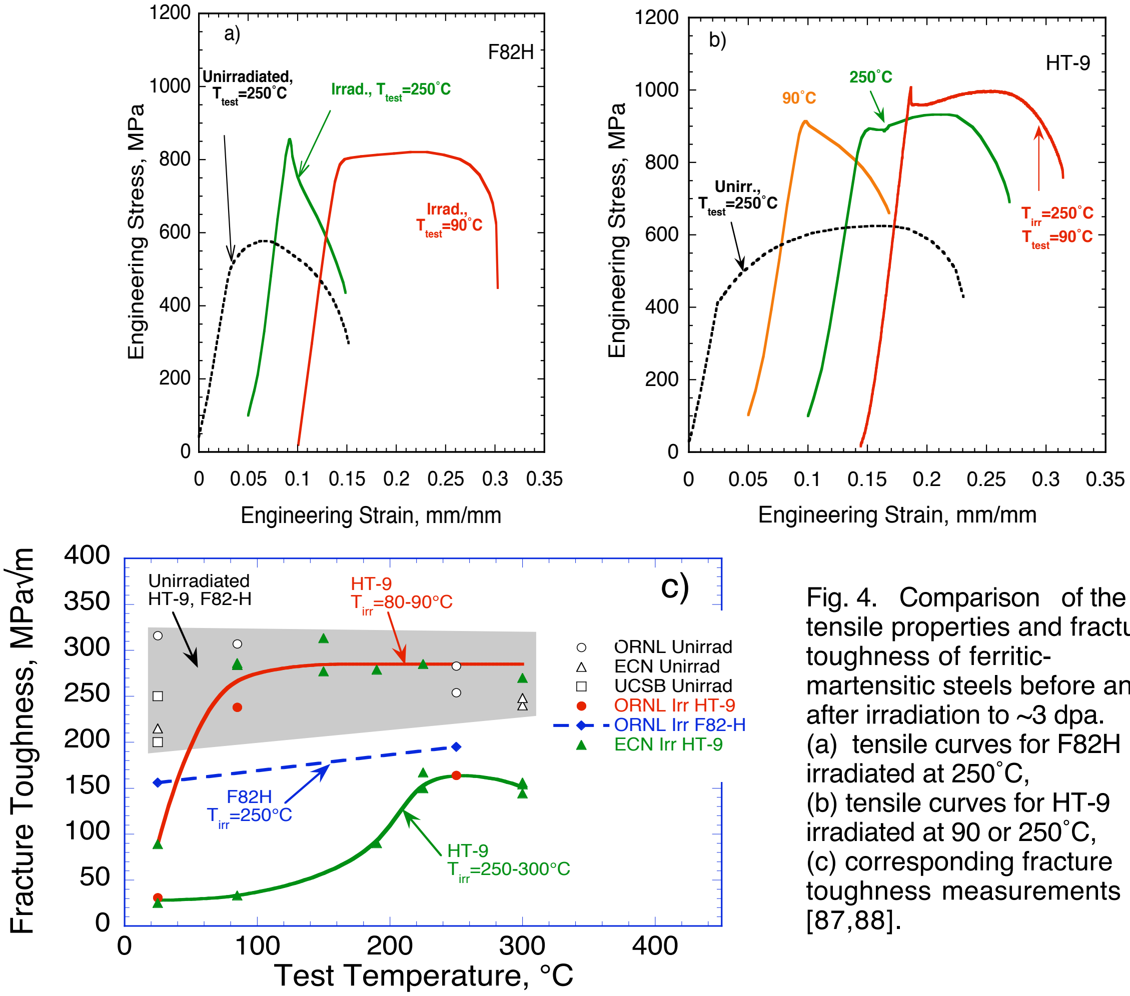

Fig. 4. Comparison of the tensile properties and fracture toughness of ferritic-martensitic steels before and after irradiation to ~3 dpa.
(a) tensile curves for F82H irradiated at 250˚C,
(b) tensile curves for HT-9 irradiated at 90 or 250˚C,
(c) corresponding fracture toughness measurements [87,88].

5. Deformation maps for unirradiated and irradiated metals

5.1. Unirradiated deformation maps.

As outlined by Ashby [18], at least six different deformation mechanisms can be distinguished which produce permanent plastic deformation in metals: 1. In the absence of any defects, plastic deformation is induced when the stress exceeds the *theoretical shear strength*, which has a value of ~0.04μ. 2. The presence of dislocations in metals enables deformation to occur at stresses well below the theoretical shear stress. The stress required to induce *dislocation glide* is dependent on the spacing and strength of the microstructural obstacles (precipitates, solute atoms, etc.), and occurs via a thermally activated process. 3. *Twinning* occurs predominantly at low temperatures and moderate stresses. 4. Diffusional creep of atoms along grain boundaries (*Coble creep*) is important at moderate stresses and temperatures, particularly in fine-grained materials. 5. Diffusional creep via vacancy self-diffusion in the grain interior (*Nabarro-Herring creep*) becomes significant at very high temperatures. 6. At elevated temperatures and stresses, *dislocation creep* (power law creep) occurs by a process of dislocation climb and glide that is dependent on the vacancy self-diffusion coefficient and has a superlinear stress dependence, resulting in a cellular deformation structure. As in Ashby's original paper on deformation maps [18], we have ignored several other creep deformation mechanisms (in particular diffusional creep via pipe diffusion and Harper-Dorn creep [90]) in the present analysis in order to maintain readability of the deformation maps.

The strain rates for these 6 different deformation mechanisms are given by the following constitutive equations.

Ultimate shear strength $\dot{\gamma}_1 = \quad ,\qquad \tau \geq 0.04\mu$ (3a)

$\dot{\gamma}_1 = 0,\qquad \tau < 0.04\mu$ (3b)

Dislocation glide $$\dot{\gamma}_2 = \dot{\gamma}_0 \exp - \frac{[H_0 - V(\tau - \tau_0)]}{kT} \qquad \tau > \tau_0 \tag{4a}$$

$\dot{\gamma}_2 = 0,\qquad \tau < \tau_0$ (4b)

where H_0 is the interaction enthalpy between glide dislocations and microstructural obstacles, b is the glide dislocation Burgers vector, k is Boltzmann's constant, T is the absolute temperature, and τ_0 is the athermal part of the flow stress [18,91,92]. The activation volume for dislocation glide is given by V~bdl, where l is the obstacle spacing on the glide plane and d is the obstacle size. The value for the pre-exponential constant for dislocation glide was assumed to be $\dot{\gamma}_0 = 10^6$ s^{-1} for all calculations. The key microstructural parameters for dislocation glide (H_0 and V) can be experimentally obtained from the temperature dependence of the flow stress at different strain rates. From equation 4, the dislocation glide flow stress is given by $\tau_0 + H_0/V$ at absolute zero, and it equals τ_0 (athermal flow stress) at high temperatures. For this report, τ_0 is assumed to be constant although it is recognized that a temperature-dependence similar to that for the shear modulus would be more appropriate.

For BCC metals such as vanadium and ferritic steel, the lattice resistance associated with directional bonding (Peierls forces) has a strong impact on the dislocation glide behavior at low temperatures. Since the Peierls barrier represents a strengthening contribution rather than a deformation mechanism, its impact on the dislocation glide regime is handled by superposition of stresses instead of strain rates [18]. A linear superposition of the obstacle and Peierls stresses was assumed for this report (by modifying the low temperature glide stress component, H_0/V). In general, the nature of the various dislocation glide obstacles must be considered in order to determine the appropriate superposition relation. For example, short range obstacles would be expected to contribute as the square root of the sum of the squares of the Peierls and solute hardening components (quadratic superposition), whereas linear superposition is appropriate for the superposition of long range obstacles (e.g., coherent precipitates) and Peierls hardening [4,6,40].

The constitutive equations for deformation twinning are not firmly established [93], although there is evidence that the critical stress for twinning decreases with increasing strain rate and increases slowly with test temperature (both of which suggest that twinning is not a thermally activated process). For the present study, we have adopted a simplified version of the Venables model, where the twinning stress (σ_{tw}) is constant for a given material (except for the slight temperature dependence of the stacking fault energy, γ_{SF}):

$$\sigma_{tw} = 2\frac{\gamma_{SF}}{b} \tag{5a}$$

The following simple constitutive equation for twinning was assumed for the purpose of constructing the deformation maps, where it was assumed C_0=1 s^{-1} and $\dot{\varepsilon}_3$=0 for $\sigma < \sigma_{tw}$.

$$\dot{\varepsilon}_3 = C_0\frac{\sigma - \sigma_{tw}}{\mu} \qquad \sigma > \sigma_{tw} \tag{5b}$$

The constitutive equation for diffusional creep is given by [90]

$$\dot{\varepsilon}_{4,5} = \frac{30\Omega\sigma}{kTL^2}\left[D_{SD} + \frac{2\pi D_B b(\sigma - \sigma_1)}{L\sigma} + C_1 D_P \rho_d b^2\right] \tag{6}$$

where Ω is the atomic volume ($a_0^3/4$ for FCC, $a_0^3/2$ for BCC) L is the grain diameter, D_{SD}, D_B and D_P are the diffusion coefficients associated with self-, grain boundary- and pipe dislocation-diffusion, respectively, ρ_d is the dislocation density, and C_1 is a constant of order unity. In this equation, the first term inside the brackets is associated with *Nabarro-Herring creep*, the second term is associated with *Coble creep*, and the third term (which is ignored for the present analysis) is associated with dislocation pipe diffusion [90]. Since the dislocation density in deformed specimens is proportional to the square of the applied stress [90,94], diffusional creep via pipe diffusion can be of particular importance at higher stress levels, and is responsible for a superlinear (cubic) dependence of diffusional creep on applied stress. Although diffusional creep via pipe diffusion was not included in the present analysis for sake of simplicity, it should be included in any detailed analysis of creep mechanisms. We have included a grain boundary friction stress (σ_1) in eqn. (6) to account for the minimum stress needed to unpin grain boundaries from particles during creep deformation. A more accurate representation would also involve computing the maximum velocity that particles can be dragged by grain boundaries [95]. Previous work [96] has reported that the grain boundary frictional stress can be described by the following functional dependence: $\sigma_1 = C_2(1-T/T_M)$, where C_2 is the frictional stress at zero kelvin.

The constitutive equation for diffusion-controlled dislocation creep (power law creep) is given by [90,94]

$$\dot{\varepsilon}_6 = \frac{A\mu b}{kT}\left[D_{SD} + 200 D_P\left(\frac{\sigma - \sigma_2}{\mu}\right)^2\right]\left(\frac{\sigma - \sigma_2}{\mu}\right)^n \qquad \sigma \geq \sigma_2 \tag{7a}$$

$$\dot{\varepsilon}_6 = 0, \qquad \sigma < \sigma_2 \tag{7b}$$

where the dimensionless constant A~10^9 and the power law exponent is n~5 [94] and σ_2 is the dislocation friction stress associated with solute or other dislocation obstacles (e.g., precipitates). Power law creep thereby gives rise to stress exponents of 5 to 7 depending on the relative importance of self-diffusion and dislocation pipe diffusion. Alternative expressions for creep of alloys containing dispersed precipitates have also been developed [90,97], but will not be considered in the present analysis for sake of simplicity.

The relevant materials data used for the deformation calculations on copper alloys, Type 316 austenitic stainless steel, V-4Cr-4Ti, and 8-12%Cr ferritic/martensitic steel are summarized in Table 1 [18,94,98-109]. Due to a lack of data, the stacking fault energy was assumed to be constant for all materials except 316 stainless steel, where experimental data suggest the temperature coefficient is 0.00003 J/m^2-K [107]. There is considerable variability in the literature regarding dislocation creep constitutive equations and associated creep constants. We have adopted the recommendations by Sherby and Miller [94] in our calculations as opposed to the values contained in the original Ashby map paper [18]. Following the method outlined by Ashby [18], the stress and temperature regimes where a particular deformation mechanism is dominant was determined from calculations of the deformation rates given by equations 3-7 over a wide range of stresses and temperatures. The boundary between two deformation fields corresponds to the stress-temperature conditions where both processes contribute equally to the plastic strain rate. In most of the figures to be presented, the boundary between elastic behavior and the various plastic deformation fields was drawn for an arbitrary plastic strain rate of 10^{-8} s^{-1}. The elastic-plastic boundary (and the boundaries between the plastic deformation fields) for other strain rates can be readily determined with equations 3-7. It should be noted that there is significant uncertainty in several of the materials parameters used for the deformation map calculations. For example, the variability in the reported grain boundary diffusion energy is nearly a factor of two for several material systems [99,110]. This causes a corresponding significant uncertainty in the quantitative values for the deformation maps. Detailed analyses of experimental thermal creep data are needed to determine these fundamental materials parameters, and to confirm the extent of the different thermal creep mechanism regimes.

Table 1. Summary of materials parameters used in the Ashby deformation map calculations [18,98-109]. A constant value of A=1x10^9 [94] was used for the dislocation creep constant (eqn. 7a) for all materials.

Alloy	Burgers vector (nm)	T_M (K)	Shear modulus at 300 K (GPa)	$1/\mu$ $d\mu/dT$ (10^{-4}/K)	Stacking fault energy at 300 K (J/m^2)	D_0 for bulk diffusion (10^{-4} m^2/s)	Bulk diffusion activation energy (kJ/mol)	D_0 for g.b. diffusion (10^{-4} m^2/s)	g.b. diffusion activation energy (kJ/mol)	D_0 for pipe diffusion (10^{-4} m^2/s)	Pipe diffusion activation energy (kJ/mol)
Cu-Al_2O_3 CuNiBe	0.256	1356	44.7 [98]	-3.8 [98]	0.055 [106]	0.6 [99]	200 [99,100]	0.1 [18]	100 [18,99]	0.04 [99]	148 [99]
316 SS	0.258	1650	77 [101]	-3.9 [101]	0.03 [106,107]	0.4 [100]	280 [100]	0.1 [18]	150	0.1	190
V-4Cr-4Ti	0.262	2175	46 [102]	-1.7 [103]	0.2 [108]	0.3 [100]	300 [100,104]	1.0 [18]	160	0.1	230
Fe-8Cr-2WVTa	0.248	1800	84 [105]	-2.3 [105]	0.2 [109]	1.0 [100]	260 [100,104]	1.0 [18]	150	0.1	210

Figures 5-11 show the calculated deformation maps for the four classes of unirradiated materials. The right hand axes show the uniaxial tensile stresses for equiaxed polycrystalline materials, which were obtained by multiplying the shear stress by the Taylor factor (3.06). Most of the deformation maps were calculated for a elastic-plastic boundary strain rate of 10^{-8} s^{-1}, which is a common deformation rate for experimental studies (equivalent to ~30%/year plastic deformation). One example of a higher strain rate deformation map is given to illustrate the strong effect of strain rate on the location and extent of the various deformation mode regimes. The internal boundaries for the deformation maps were calculated by determining the conditions for equal strain rate by competing mechanisms (corresponding strain rates are much higher than the elastic-plastic boundary strain rate). The dominant deformation mode at low temperatures and moderate stresses (greater than or equal to the yield stress) is dislocation glide. Twinning was not calculated to occur in any of the unirradiated materials except for Type 316 SS at very low temperatures. Diffusional creep (Coble creep, Nabarro-Herring creep) dominates at high temperatures and low stresses, particularly in fine-grained materials. Dislocation (power law) creep is dominant at moderate stresses (typically 20-100% of the yield stress) at temperatures above ~0.4 T_M.

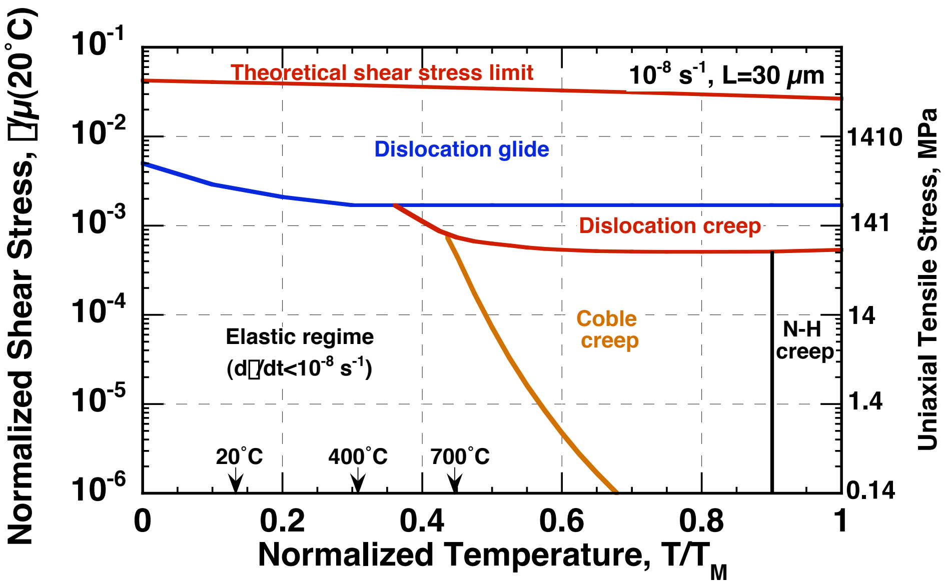

Fig. 5. Deformation map for V-4Cr-4Ti at a plastic strain rate of 10^{-8} s^{-1}. The map was constructed assuming □$_0$=90 MPa, H$_0$=1.5 eV, V=100 b^3, □$_1$=0 and □$_2$=15 MPa.

Figures 5 and 6 compare the calculated deformation maps for V-4Cr-4Ti at a strain rate of 10^{-8} and 10^{-4} s^{-1}, respectively. The grain size was taken to be 30 μm for the calculations; typical grain sizes in published V-4Cr-4Ti studies range from 18 to 35 μm. In both of these figures the assumed value for the grain boundary friction stress was □$_1$=0 and the value of the solute and precipitate friction stress was taken to be □$_2$=15 MPa (independent of temperature). The assumption of zero grain boundary friction stress causes the Coble creep regime to extend to unrealistically low stresses at temperatures above 800˚C; a more accurate calculation in this temperature range should use a nonzero value for □$_1$, although the quantitative magnitude of □$_1$ for V-4Cr-4Ti is uncertain. It is worth noting that twinning is not predicted to occur at any conditions for the values assumed in Table 1, whereas twinning has been experimentally observed in vanadium deformed at low temperature [111]. This implies that the stacking fault energy for the {112} slip plane may be less than 0.2 J/m^2. The calculated deformation map indicates that both Coble creep and dislocation creep will have significant contributions at 10^{-8} s^{-1} for temperatures of 700-800˚C and uniaxial

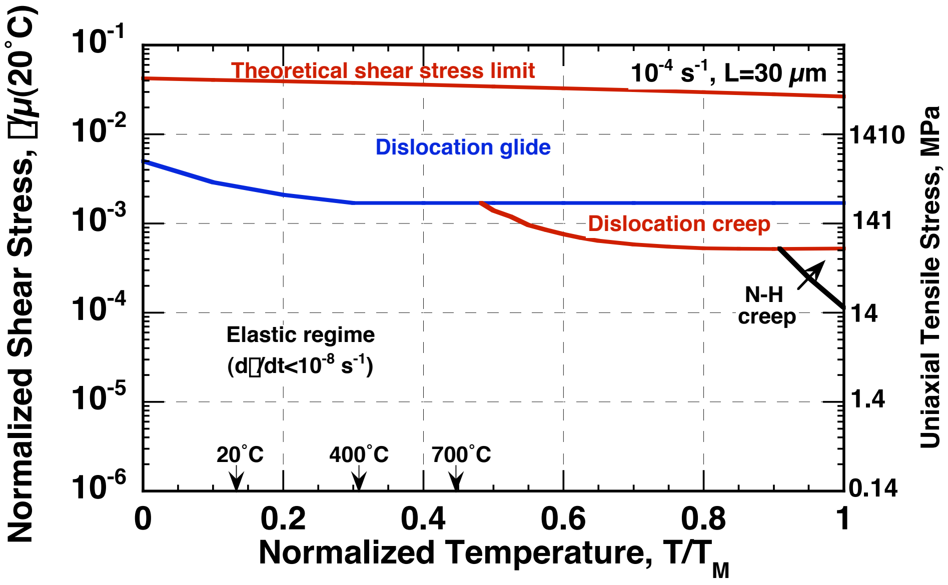

Fig. 6. Deformation map for V-4Cr-4Ti at a plastic strain rate of 10^{-4} s^{-1}. The map was constructed assuming □$_0$=90 MPa, H$_0$=1.5 eV, V=100 b^3, □$_1$=0 and □$_2$=15 MPa

.

tensile stresses of 50-120 MPa. Therefore, detailed analyses of the creep behavior at these conditions are necessary in order to separate the contributions associated with these two creep mechanisms (stress dependence and controlling activation energy). It is also apparent from the calculated V-4Cr-4Ti creep deformation map (Fig. 5) that the dominant creep deformation mode at moderate temperatures (~600˚C) will likely be different from the deformation mode at temperatures above 650˚C. Therefore, a simplistic application of Larson-Miller correlation plots should not be used to extrapolate thermal creep results to temperatures or strain rates (test times) significantly outside the experimental regime where data were acquired [18,90,91]. The main impact of increasing the strain rate from 10^{-8} to 10^{-4} s^{-1} is to shift the creep regime to higher temperatures and stresses. In addition, the Coble creep deformation regime does not exist in V-4Cr-4Ti for the higher strain rate condition. The calculations suggest that a straightforward experimental determination of the dislocation power law creep parameters for V-4Cr-4Ti may be obtained at strain rates of ~10^{-4} s^{-1} and temperatures of 700-900˚C, since Coble creep would not have a significant influence at any temperature or stress and Nabarro-Herring creep is insignificant for temperatures up to ~1500˚C. Recently, V-4Cr-4Ti thermal creep and tensile data at a wide range of strain rates have been acquired under uniaxial tensile conditions in vacuum [112-114] and under biaxial stress conditions in vacuum [115] and lithium [116]. The experimental data will be compared with the calculated deformation map results in a future contribution in order to confirm the values of several of the material variables used in the calculation.

Figure 7 shows the calculated deformation map for Fe-8Cr-2WVTa (F82H ferritic-martensitic steel) at a strain rate of 10^{-8} s^{-1}. The assumed value for the grain boundary friction stress was $\square_1$=0 and the value of the solute and precipitate friction stress was taken to be $\square_2$=20 MPa. The grain size of the original heat of F82H (22 *μ*m) was used for the calculation; larger grained heats of F82H and other reduced-activation ferritic-martensitic steels have also been fabricated. Since the martensitic phase is unstable at high temperatures, the parameters used for the ferritic-martensitic steel Ashby deformation map restricts the validity of the calculation to temperatures below ~0.6 T_M. The dislocation glide stress boundary decreases rapidly at temperatures above 0.5 T_M due to age-softening of the tempered martensitic structure; for the purposes of the deformation map calculation, it was assumed that the dislocation glide stress decreased by a factor of about three due to age-softening near 700˚C. The calculated deformation map for a plastic strain rate of 10^{-8} s^{-1} indicates that deformation of F82H is controlled by dislocation (power law) creep at temperatures above ~450˚C (~0.4 T_M), and by Coble creep at temperatures above ~0.5 T_M. The extent of the Coble creep regime to low stresses is somewhat exaggerated in Fig. 7 due to the assumption of a grain boundary friction stress of $\square_1$=0. Inclusion of a nonzero grain boundary friction stress would significantly reduce the extent of the Coble creep regime (see example for GlidCop dispersion strengthened copper presented in Figs. 8-9 later in this section). Coble creep is also calculated to be negligible for ferritic-martensitic steels with grain size >40 *μ*m. In the absence of Coble creep, Nabarro-Herring creep is predicted to become significant at 10^{-8} s^{-1} for temperatures above ~750˚C. It should be noted that dislocation creep can be suppressed by microstructural changes (which increase $\square_2$). This may be the basis for the impressive creep strengths of

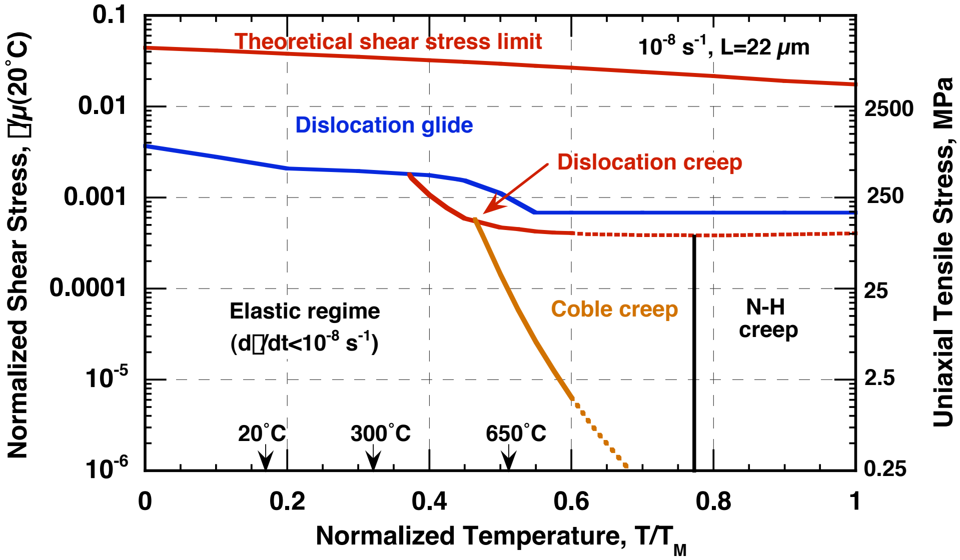

Fig. 7. Deformation map for Fe-8Cr-2WVTa at a plastic strain rate of 10^{-8} s^{-1}. The map was constructed assuming $\square_0$=170 MPa, H_0=1.5 eV, V=100 b^3, $\square_1$=0 and t_2=20 MPa. Dashed lines are used for temperatures above 0.6 T_M due to a phase change.

oxide dispersion strengthened (ODS) ferritic steels at temperatures above 550˚C [117,118]. For example, the reported 1000 h creep rupture strength for ODS Fe-12Cr steel [117] at 650˚C was about three times higher than that for F82H [105]. Deformation map calculations for ODS ferritic steel (not shown) using the F82H material parameters in Table 1 and a grain size of 50 μm suggest that the upper temperature limit for structural applications of ODS steel may be as high as ~850˚C (temperature limit determined by Nabarro-Herring creep). Recent thermal creep tests on nanocomposited ODS steels [118] have observed good creep strength for temperatures in excess of 800˚C, in agreement with this calculation.

Figures 8 and 9 compare the calculated deformation maps for oxide dispersion strengthened copper at a strain rate of 10^{-8} for a dispersoid friction stress of $\square_2$=15 MPa and a grain boundary friction stress of $\square_1$=0 and 10(1-T/T_M) MPa, respectively. The latter grain boundary friction stress value was reported for oxide dispersion strengthened copper [96]. The grain size was taken to be 5 μm, which is intermediate between the grain size in the short transverse (<1 μm) and longitudinal (~10 μm) directions for GlidCop Al25 oxide dispersion strengthened copper. The relatively small grain size in GlidCop Al25 causes the calculated Coble creep to become significant for temperatures as low as 200˚C (~0.35 T_M) at this strain rate. Since the oxide dispersion does not significantly influence the grain boundary sliding behavior, the potential high-temperature strength benefits associated with the oxide particles are not achieved in GlidCop Al25. The low strength of GlidCop Al25 (compared to larger-grained Cu alloys such as CuCrZr) is observable at elevated temperatures (400-600˚C) even for normal tensile test strain rates of ~10^{-3} s^{-1} [79,119-121]. The deformation map analysis suggests that significant improvement in the elevated temperature strength of GlidCop could be achieved if the manufacturing process could be altered to create a larger grain size.

The assumption of zero grain boundary friction stress ($\square_1$=0) in Fig. 8 produces high thermal creep at exceedingly small stresses (<1 MPa) at temperatures above 400˚C, in disagreement with the existing literature data. The inclusion of a frictional stress of $\square_1$ = 10(1-T/T_M) MPa in Fig. 9 produces fair agreement between the calculated and experimental [78,122] creep of dispersion strengthened copper at 300-600˚C. The dominant creep deformation mechanism is predicted in Fig. 9 to change from Coble to Nabarro-Herring creep at a temperature near 500˚C.

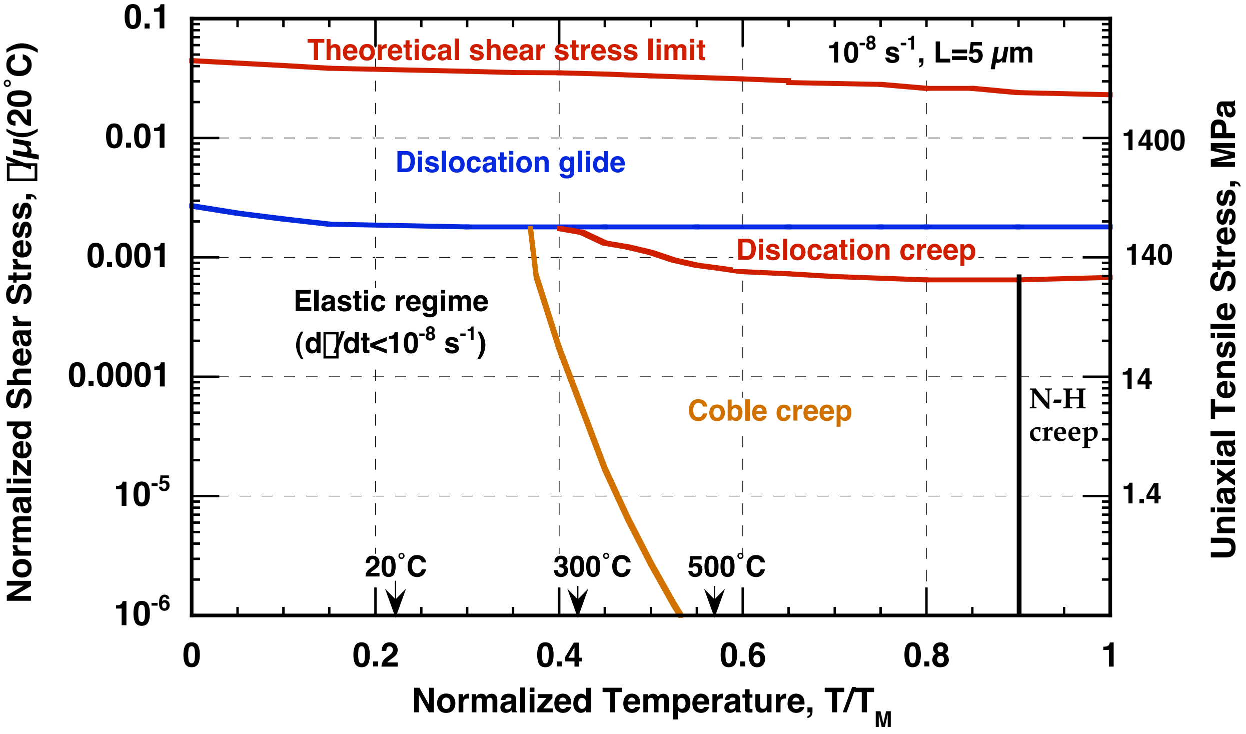

Fig. 8. Deformation map for oxide dispersion strengthened copper (GlidCop Al25) at a plastic strain rate of 10^{-8} s^{-1}. The map was constructed assuming $\square_0$=80 MPa, H_0=1.0 eV, V=200 b^3, $\square_1$=0 and $\square_2$=15 MPa.

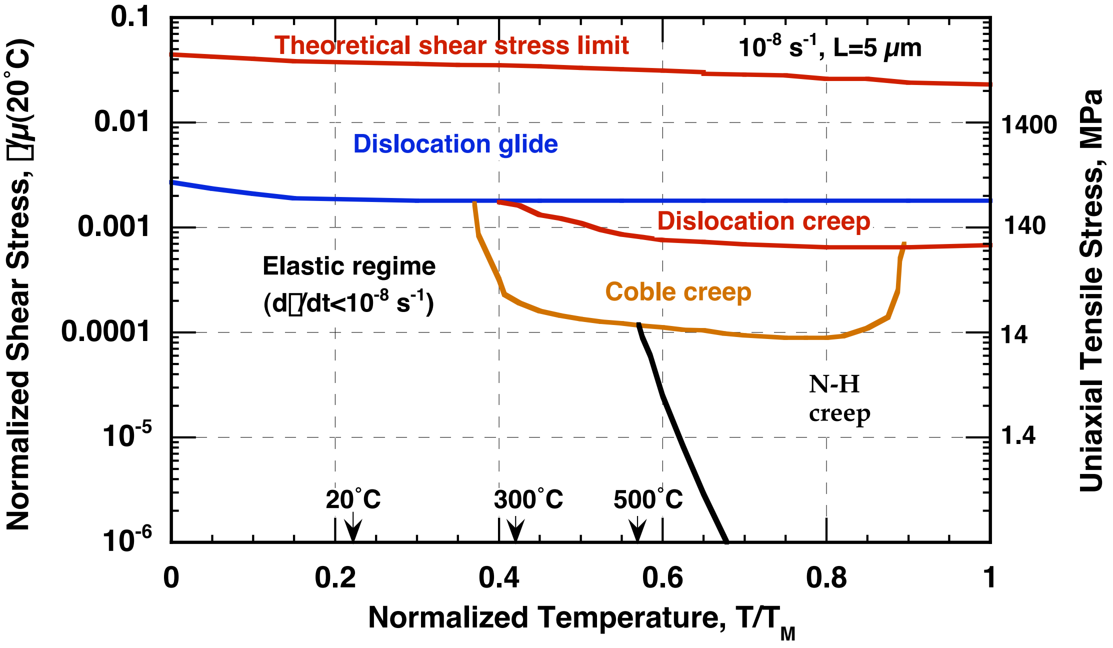

Fig. 9. Deformation map for oxide dispersion strengthened copper (GlidCop Al25) at a plastic strain rate of 10^{-8} s^{-1}. The map was constructed assuming □$_1$ = 10(1-T/T$_M$) MPa and □$_2$=15 MPa.

The deformation map for high-strength CuNiBe at a strain rate of 10^{-8} s^{-1} is summarized in Fig. 10, based on a grain size of 30 μm, a precipitate friction stress of □$_2$=35 MPa and a grain boundary friction stress of □$_1$=0. Dislocation (power law) creep is calculated to be the controlling plastic deformation mechanism in CuNiBe at temperatures from ~180˚C to ~400˚C at this strain rate. Coble creep is calculated to become the controlling plastic deformation process in this alloy at moderate stresses and elevated temperatures (T>400˚C). An examination of the fracture surfaces of CuNiBe specimens tensile tested at 20 to 500˚C has found a transition to ductile intergranular fracture at temperatures above 400˚C [119,123], in qualitative agreement with the calculated transition to Coble creep in this temperature range.

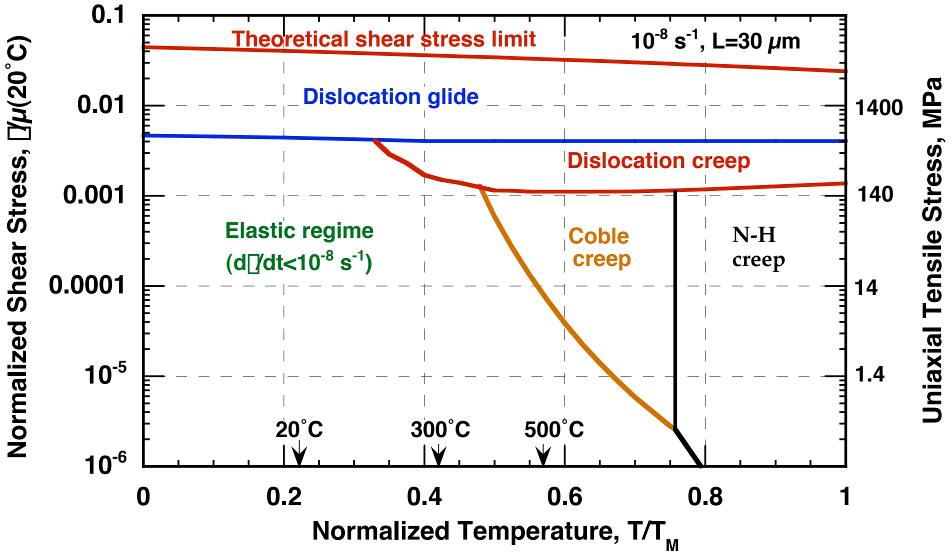

Fig. 10. Deformation map for precipitation-strengthened CuNiBe (Brush-Wellman Hycon 3HP) at a plastic strain rate of 10^{-8} s^{-1}. The map was constructed assuming □$_0$=180 MPa, H_0=0.8 eV, V=150 b^3, □$_1$=0 and □$_2$=35 MPa.

Figure 11 shows the calculated deformation map for Type 316 austenitic stainless steel at a strain rate of 10^{-8} s^{-1}. The assumed value for the grain boundary friction stress was $\square_i$=0 and the value of the solute and precipitate friction stress was taken to be $\square_2$=15 MPa. A grain size of 50 μm was used for the calculation. A very limited twinning regime occurs at temperatures near absolute zero. Dislocation glide is the dominant deformation mechanism from low temperatures up to ~550˚C. Dislocation creep is the dominant creep mechanism for temperatures between ~550 and ~900˚C (0.7 T_M). A limited Coble creep regime occurs at temperatures above 900˚C, and Nabarro-Herring creep is the dominant deformation mechanism at temperatures above ~1050˚C. Due to the absence of Coble and Nabarro-Herring creep at intermediate temperatures, stainless steel retains relatively high strength up to ~650˚C even for strain rates of ~10^{-10} s^{-1}.

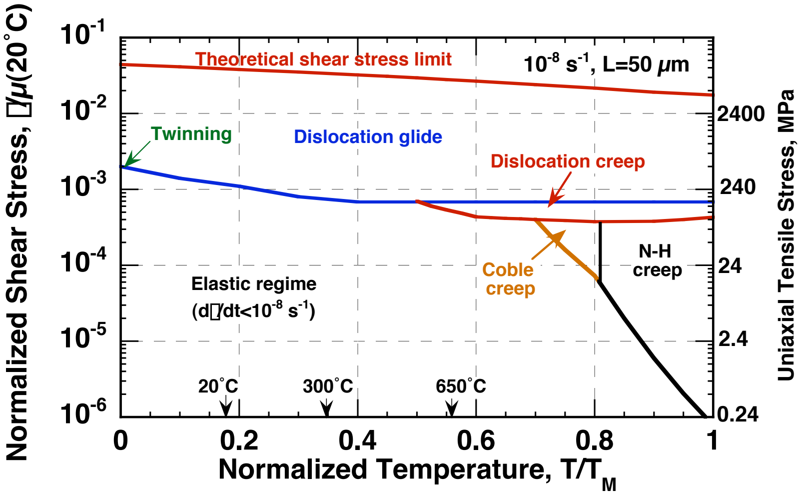

Fig. 11. Deformation map for Type 316 austenitic stainless steel at a plastic strain rate of 10^{-8} s^{-1}. The map was constructed assuming $\square_0$=60 MPa, H_0=1.6 eV, V=150 b^3, $\square_i$=0 and $\square_2$=15 MPa.

5.2. Irradiated deformation maps.

Irradiation causes several modifications to the unirradiated deformation behavior of metals and alloys. The main modifications can be classified as *radiation hardening*, *radiation-enhanced softening*, *irradiation creep*, and *high temperature He embrittlement*. Of these phenomena, only irradiation creep and high temperature He embrittlement represent new deformation mechanisms (as discussed later, some aspects of He embrittlement are similar to diffusional creep, but the stress dependence and activation energies may be different). The primary impact of radiation hardening and radiation-enhanced softening is a modification of the dislocation glide flow stress ($\square_0$) and dislocation creep frictional stress ($\square_2$).

As summarized in sections 2 and 3, increased resistance to dislocation glide (*radiation hardening*) typically occurs for irradiation temperatures below ~0.3 T_M due to the formation of a high density of defect clusters. This defect cluster hardening predominantly contributes to athermal stress term ($\square_0$) in equations 4a-4c. Radiation hardening can also modify the dislocation friction stress ($\square_2$) for dislocation (power law) creep, although the dislocation barriers produced by irradiation at intermediate elevated temperatures (0.3-0.6 T_M, where dislocation creep is significant) are generally of secondary importance compared to the unirradiated solute and precipitate friction stress. Since in most cases radiation hardening is associated with defect clusters with short range stress fields, we will assume quadratic superposition of the radiation hardening and unirradiated dislocation glide obstacle strengths: $\square_0=(\square_0^2(\text{unirr})+\square_0^2(\text{irr}))^{1/2}$, where $\square_0$(unirr) and $\square_0$(irr) are the dislocation glide athermal stresses associated with the obstacles in the unirradiated material and the radiation-produced defect clusters, respectively. One of the consequences of radiation hardening is that the requirement of higher stresses to activate dislocation glide (due to pinning of dislocations by radiation-induced defect clusters) can result in an expansion of the extent of the low-temperature twinning and intermediate-temperature dislocation creep regimes.

The phenomenon of dislocation channeling that is frequently observed in radiation hardened metals and alloys (cf. sections 2 and 3) can be regarded as a manifestation of dislocation glide, as opposed to a new deformation mechanism. Although the consequences of the localized deformation that occur with dislocation channeling can be profound, the fundamental mechanism is still associated with dislocation interaction with matrix obstacles. It should be noted that the strain rate dependence of radiation hardening is often different compared to that for thermally-produced obstacles [1,26,30,66,124-126]. Therefore, the value of σ_0 and σ_2 at the appropriate strain rate should be used for the deformation map analysis. At intermediate temperatures, the phenomenon of void channel fracture has occasionally been observed [84]. This can also be considered to be a modification of dislocation glide deformation with localized flow.

At temperatures above ~0.5 T_M, *radiation-enhanced softening* is often observed in structural alloys (producing a decrease in σ_0 and σ_2) [13,28,29,78,127-129]. This softening can be included as a modification of the dislocation glide flow stress (σ_0) and dislocation creep frictional stress (σ_2).

The constitutive equation for the strain rate dependence of *irradiation creep* is given by

$$\dot{\varepsilon}_7 = 3.06(B_0 + D\dot{S})\sigma P \qquad (8)$$

where P is the displacement rate (dpa/s) and B_0 is the creep compliance (~10^{-6} MPa^{-1} dpa^{-1} at intermediate temperatures of ~0.3-0.6 T_M for FCC alloys, and ~0.5×10^{-6} MPa^{-1} dpa^{-1} for BCC alloys) [71,72,130]. There is evidence that B_o increases at lower temperatures, which has been attributed to an extended transient dose regime due to the difference in mobility of vacancy and interstitial point defects at low temperatures [15,72,131]. This accelerated transient low temperature creep regime was ignored for the present analysis. Similarly, the potentially enhanced irradiation creep rate associated with formation of He bubbles at temperatures near 0.4 T_M [132] has been not included. At very low temperatures (below room temperature), irradiation creep is controlled by the interstitial diffusivity and the value of B_0 becomes very small. The creep-swelling coupling coefficient D has a value of ~0.006/MPa for both austenitic and ferritic steels [72]. The void swelling rate $\dot{S}$ in the void swelling regime (~0.3 to 0.6 T_M) has typical steady-state values of 0.5-1%/dpa for FCC alloys and ~0.05%/dpa for BCC alloys, although a recent reanalysis of experimental data suggests that steady state swelling rates for ferritic/martensitic steels may be as high as 0.25 to 0.5%/dpa [72]. The void swelling rate at doses below the transition to steady state swelling is typically ~0.01-0.05%/dpa. The temperature dependence of swelling at low and high temperatures can be described by approximate analytical expressions [133]. At low doses and strain rates, irradiation creep is a particularly important deformation mechanism for low to intermediate temperatures. At high doses, stress-assisted swelling may become the dominant deformation mode in FCC metals at intermediate temperatures (0.3-0.6 T_M) particularly if the transition to steady-state swelling occurs. However, in this case the material would likely be unacceptable for engineering structures due to the high volumetric swelling that would be introduced (swelling levels above 5% typically cannot be accommodated in the engineering design of structures). The projected impact of the creep-swelling mechanism is lower (but still important) in ferritic-martensitic steels and vanadium alloys due to their lower swelling rates compared to austenitic steels.

High temperature helium embrittlement is due to the migration of transmutation-produced helium to grain boundaries, producing helium-vacancy cavities that cause preferential deformation along grain boundaries [16,73,134]. The diffusion and nucleation of helium-vacancy cavities at grain boundaries is strongly enhanced by applied stress [134,135]. Since this phenomenon involves defect migration to grain boundaries, some aspects of high temperature He embrittlement are analogous to Coble and Nararro-Herring diffusional creep. It is well established that the stress dependence as well as the physical mechanisms that control the He embrittlement creep *rupture* temperature dependence are significantly different from diffusional and power-law creep [16,17,134,136]. However, existing experimental data generally do not show a significant effect of helium on the creep *rate* at temperatures near 0.5 T_M [71,136-138], and there are no known theoretical models that predict an effect of He on steady state creep. Unfortunately, much of the available experimental data on He embrittlement effects have been obtained at relatively high stresses and strain rates (tensile tests), which minimizes the influence of helium on deformation mechanisms. Two competing effects of helium on the steady state creep rate can be envisioned. First, the presence of helium-filled cavities in the matrix can increase the value of the solute and precipitate friction stress (σ_2) for dislocation power law creep. Conversely, helium migration to grain boundaries could significantly reduce the coble creep parameters for the grain boundary frictional stress (σ_1) and grain boundary diffusivity due to grain boundary cavity formation, causing grain boundary deformation and fracture to occur at very low stresses. Further work is needed to assess the importance of these competing mechanisms on the controlling deformation behavior of irradiated materials. In the present study, He embrittlement effects are not included in the deformation maps. Simplified models for the effect of He on rupture time and rupture strain (fracture) are available [134], and will be briefly summarized in section 6.

The calculated deformation map at a strain rate of 10^{-8} s^{-1} for Type 316 stainless steel irradiated to a relatively low dose of 1 dpa at a dose rate of 10^{-6} dpa/s is given in Fig. 12. A grain size of 50 μm was used for the calculation. The assumed value for the grain boundary friction stress was $\square_1=0$ and the value of the solute and precipitate friction stress was taken to be $\square_2=15$ MPa (same values as for Fig. 11). There is some evidence that irradiation-induced defects may decrease the steady state creep rate of stainless steel at elevated temperatures (~650˚C) [136], possibly due to increasing the frictional stress $\square_2$. This possibility needs further investigation. The dislocation glide obstacle stress ($\square_0$) was fitted to temperature-dependent experimental radiation hardening data for stainless steel irradiated to ~1 dpa [77]. The main effect of irradiation at these conditions is to increase the flow stress for dislocation glide. This causes twinning to be the dominant deformation mode up to room temperature, and the dislocation creep regime is extended to lower temperature compared to the unirradiated case (cf. Fig. 11 and Fig. 12). The calculated deformation map for irradiated stainless steel is in agreement with experimental observations which have reported twinning following deformation near room temperature [65-68,139].

Irradiation creep is not predicted to be a significant deformation mechanism for the conditions used in the Fig. 12 calculation. On the other hand, irradiation creep is predicted to be significant at lower plastic strain rates (below 10^{-9} s^{-1}). Figure 13 shows the calculated deformation map at a strain rate of 10^{-10} s^{-1} (0.3%/year) for Type 316 stainless steel irradiated to 1 dpa at a dose rate of 10^{-6} dpa/s. All of the parameters except strain rate were identical for the calculations used to construct Figs. 12 and 13. A swelling rate of 0.05%/dpa was assumed for the temperature range 0.4-0.55 T_M (400-625˚C), and the swelling rate was assumed to decrease to zero at high and lower temperatures using a temperature-dependent relation outlined by Garner and Wolfer [133]. Two distinct irradiation creep regimes are discernable, corresponding to the two terms in Eqn. 8. At very low temperatures where vacancies are immobile (<300 K for stainless steel), irradiation creep becomes negligible due to low self-interstitial atom (SIA) mobility. An SIA migration energy of 24 kJ/mol (0.25 eV) was assumed for the calculation.

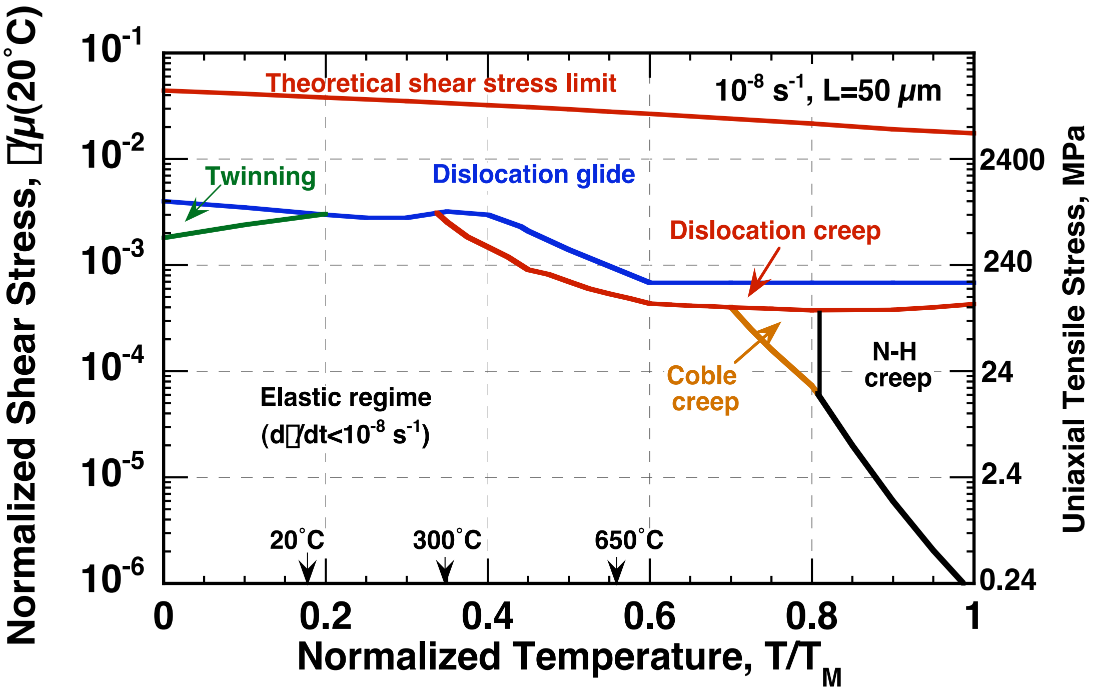

Fig. 12. Deformation map for Type 316 austenitic stainless steel irradiated to 1 dpa at 10^{-6} dpa/s for a plastic strain rate of 10^{-8} s^{-1}. The map was constructed assuming $\square_0=240$ MPa, $H_0=1.0$ eV, V=120 b^3, $\square_1=0$ and $\square_2=15$ MPa.

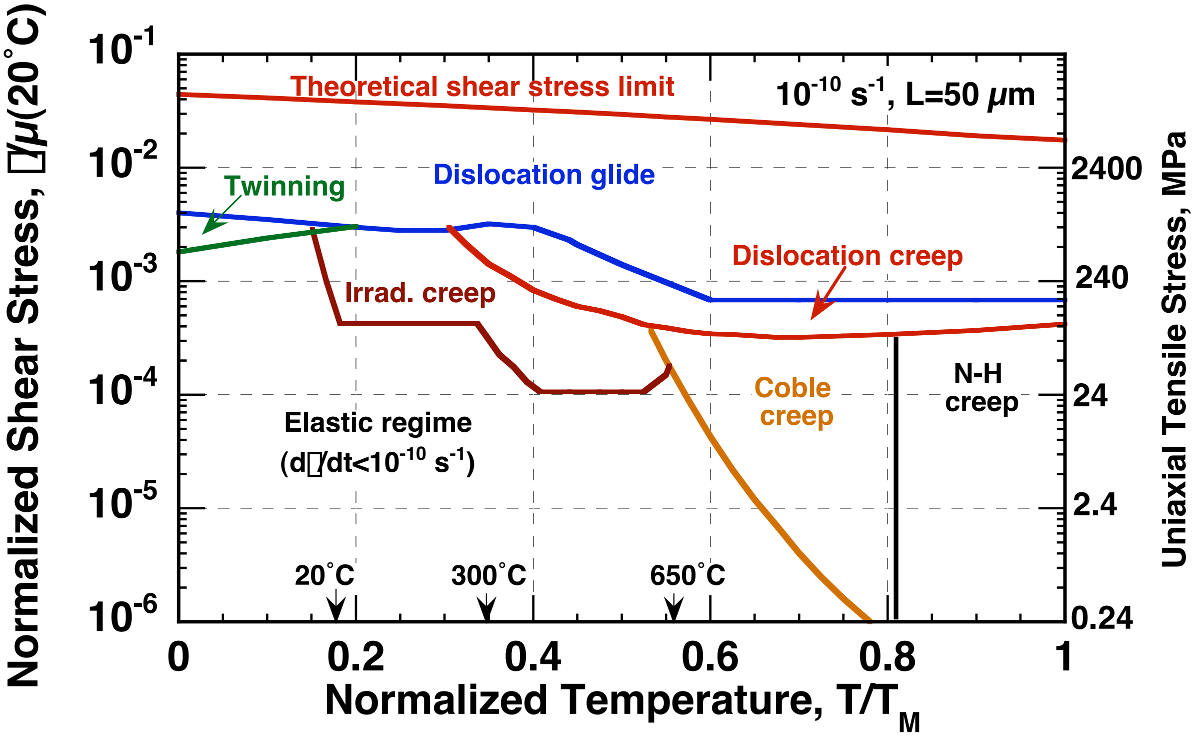

Fig. 13. Deformation map for Type 316 austenitic stainless steel irradiated to 1 dpa for a plastic strain rate of 10^{-10} s^{-1}. The map was constructed assuming $\square_0$=240 MPa, H_0=1.0 eV, V=120 b^3, $\square_1$=0 and $\square_2$=15 MPa.

The main effect of the lower strain rate is that irradiation creep becomes the dominant deformation mode for temperatures up to ~600˚C. At higher temperatures, an expanded Coble creep regime controls the deformation behavior. The appropriate value for the grain boundary frictional stress ($\square_1$) of irradiated stainless steel at high temperatures is uncertain. Due to accumulation of helium bubbles at grain boundaries, the grain boundary frictional stress should be significantly smaller than for unirradiated stainless steel. A value of $\square_1$=0 was used for Fig. 13 (same as for Figs. 11, 12).

6. Fracture mechanisms in unirradiated and irradiated metals

As with deformation maps, Ashby-type *fracture* maps are useful for analyzing mechanical behavior in materials. The methodology for determining the boundary lines between the various fracture mechanisms is to compute or empirically determine the conditions which produce equivalent rupture times for the competing processes. Constraint, notch acuity and strain rate effects are all important factors which must be considered in the construction of fracture maps. However, unlike deformation maps, the constitutive equations for fracture are not well established for many of the fracture mechanisms. Therefore, most of the existing fracture maps [140-143] are empirical in nature. A preliminary Ashby fracture mechanism map for neutron irradiated austenitic stainless steel was previously reported by Grossbeck et al. [144]. Some of the relevant constitutive equations for fracture are summarized elsewhere [143,145].

At least seven different fracture mechanisms can be envisioned, several of which may be significantly altered by irradiation. The fracture mechanisms include 1,2) brittle transgranular cleavage or brittle intergranular fracture for $\square>\square_{crit}(\dot{\square})$, depending on the relative fracture strength of the grain boundary and matrix. Three subset fracture mechanisms were identified by Gandhi and Ashby [141] for this condition, depending on whether critical-sized pre-existing flaws or cracks were present (Type 1), slip or twin-nucleated cracking occurred (Type 2), or brittle failure was initiated following some general plastic deformation (Type 3). It is well established that radiation hardening promotes cleavage fracture in BCC metals and alloys. It is also possible that radiation induced solute segregation to grain boundaries could modify the grain boundary fracture strength. It has been suggested that localized flow associated with dislocation channeling in irradiated and deformed materials may create high stresses at grain boundaries which could initiate brittle fracture [38]. 3,4) Ductile intergranular or transgranular fracture (microvoid growth and coalescence) typically occurs at high stresses and low to medium temperatures. Processes such as shear fracture (void sheeting) are a specialized subset of this fracture mechanism. Second phase particles are often the initiation sites for ductile fracture due to localized enhanced stress. Radiation induced solute segregation, radiation induced precipitation, and radiation hardening can affect this fracture process. 5) Transgranular creep fracture typically occurs at elevated temperatures and intermediate stresses. 6) Intergranular creep fracture occurs at elevated temperatures and low stresses. This mechanism generally becomes increasing important with increasing creep lifetimes. Helium grain boundary embrittlement is a very important fracture mechanism in irradiated materials for temperatures above ~0.5 T_M. It is discussed in more detail in the following paragraph. 7) If void nucleation is suppressed during deformation, ductile rupture due to unstable necking is a viable fracture mechanism (although generally not observed). The controversial phenomenon of low temperature He-enhanced embrittlement, which has been reported to occur in ferritic-martensitic steels, needs further validation to determine if it is a new radiation-induced fracture mechanism that is different from normal matrix hardening effects.

Three mechanistic regimes for creep rupture lifetimes due to He embrittlement effects were identified by Trinkaus [134]: Gas-creep driven growth (bubble coalescence) dominates at high He production rates, moderate temperatures, and high stresses, and the kinetics are controlled by the He diffusivity which is equal to the vacancy diffusivity in this regime. Creep constrained growth dominates at low stresses over a broad range of He production rates (high bubble densities on differently oriented grain boundaries causing inhomogeneous creep). Finally, diffusion-controlled growth dominates at low He production rates, high temperatures, and intermediate stresses, and the kinetics are controlled by He bubble dissociation. For conditions appropriate for fusion reactor first wall and blanket structural materials, the time to rupture for He embrittlement is usually controlled by creep constrained cavity growth rather than by gas driven bubble growth.

7. Conclusions

Pronounced matrix hardening is produced by low-temperature ($<0.3T_M$) irradiation of FCC and BCC metals. This hardening causes an increase in the ductile to brittle transition temperature and a decrease in the fracture toughness of BCC metals, even at temperatures above the DBTT. The fracture toughness of FCC metals is also typically degraded by low-temperature irradiation, although several examples exist where fracture toughness degradation did not occur in radiation hardened FCC alloys (e.g., CuCrZr and 316 stainless steel irradiated at 50-100°C, at least for doses of 0.3-3 dpa where concomitant substantial loss of tensile uniform elongation occurs). Evidence obtained from several studies suggests that the amount of radiation hardening may be higher in fine-grained materials compared to coarse-grained or single crystal materials. Further work is needed to determine the physical phenomena responsible for this apparent "radiation-modified Hall-Petch" effect.

Radiation-induced tensile "embrittlement" (loss of uniform elongation following low temperature irradiation) is not a reliable indicator of fracture toughness embrittlement. Numerous discrepancies exist in both FCC and BCC alloys where high tensile toughness occurs in materials with low fracture toughness and vice versa.

Ashby deformation maps are a useful framework for categorizing the effects of irradiation on the mechanical deformation of FCC and BCC metals. At low irradiation temperatures, radiation hardening produces an increase in the stress required to induce dislocation glide. Under these irradiation conditions, the plastic instability associated with dislocation channeling can be recognized to be a special case of ordinary dislocation glide, the unique feature being that the irradiation-produced microstructural obstacles to dislocation glide are heterogeneously eliminated during the deformation process. The second major feature of irradiation is to introduce an irradiation creep regime in the deformation maps at low strain rates. Irradiation creep is typically the dominant deformation process at moderate stresses up to ~0.5 T_M in both FCC and BCC metals for typical reactor displacement rates of ~10^{-6} dpa/s. Further work is needed to determine whether cavitation processes associated with high temperature He embrittlement introduce any new deformation mechanisms.

Acknowledgements

This research was sponsored by the Office of Fusion Energy Sciences, U.S. Department of Energy under contract DE-AC05-00OR22725 with UT-Battelle, LLC and by grant number DE-FG03-94ER54275 with the University of California-Santa Barbara.

References

[1] T.J. Koppenaal and R.J. Arsenault, Neutron-irradiation-strengthening in fcc single crystals, Metall. Reviews 16 (1971) 175-196.
[2] M.S. Wechsler, Dislocation channeling in irradiated and quenched metals, in R.E. Reed-Hill (ed.) The Inhomogeneity of Plastic Deformation, Am. Society for Metals, Metals Park, OH, 1972, pp. 19-54.
[3] M.J. Makin, Radiation damage in face centered cubic metals and alloys, in W.F. Sheely (ed.) Radiation Effects (Metallurgical Society Conf. Vol. 37), Gordon and Breach, New York, 1967, pp. 627-669.
[4] J. Diehl and G.P. Seidel, Effect of alloying and cold work on the neutron irradiation hardening of metals, in Radiation Damage in Reactor Materials vol. I, IAEA, Vienna, 1969, pp. 187-214.
[5] A.K. Seeger, On the theory of radiation damage and radiation hardening, in 2nd UN Conf. on Peaceful Uses of Atomic Energy vol. 6, United Nations, New York, 1958, pp. 250-273.
[6] A.L. Bement, Jr., Fundamental materials problems in nuclear reactors, in W.C. Leslie (ed.) 2nd Int. Conf. on Strength of Metals and Alloys vol. II, Am. Society for Metals, Metals Park, OH, 1970, pp. 693-728.
[7] J. Diehl and W. Schilling, Hardening of face-centered cubic metals due to reactor irradiation, in 3rd Intern. Conf. on Peaceful Uses of Atomic Energy vol. 9, United Nations, New York, 1965, pp. 72-77.
[8] T.H. Blewitt, R.R. Coltman, R.E. Jamison and J.K. Redman, (Radiation hardening of copper single crystals), J. Nucl. Mater. 2 (1960) 277-298.
[9] M.A. Adams and P.R.B. Higgins, The hardening of copper by neutron irradiation, Philos. Mag. 4 (1959) 777-780.
[10] G.R. Odette and G.E. Lucas, Analysis of cleavage fracture potential of martensitic stainless steel fusion structures, J. Nucl. Mater. 117 (1983) 264-275.
[11] R.L. Klueh and D.J. Alexander, Embrittlement of Cr-Mo steels after low fluence irradiation in HFIR, J. Nucl. Mater. 218 (1995) 151-160.
[12] G.R. Odette, E. Donahue, G.E. Lucas and J.W. Sheckerd, The effects of constraint, loading rate and irradiation on the toughness-temperature behavior of a V-4Cr-4Ti alloy, in R.K. Nanstad et al. (eds.), 18th Int. Symp. on Effects of Radiation on Materials, ASTM STP 1325, American Society for Testing and Materials, West Conshohocken, PA, 1999, pp. 1089-1108.
[13] S.J. Zinkle et al., Research and development on vanadium alloys for fusion applications, J. Nucl. Mater. 258-263 (1998) 205-214.
[14] F.A. Garner and D.S. Gelles, Irradiation creep mechanisms: an experimental perspective, J. Nucl. Mater. 159 (1988) 286-309.
[15] M.L. Grossbeck, L.T. Gibson, S. Jitsukawa, L.K. Mansur and L.J. Turner, Irradiation creep at temperatures of 400°C and below for application to near-term fusion devices, in R.K. Nanstad et al. (eds.), 18th Int. Symp. on Effects of Radiation on Materials, ASTM STP 1325, American Society for Testing and Materials, West Conshohocken, PA, 1999, pp. 725-741.
[16] H. Ullmaier, The influence of helium on the bulk properties of fusion reactor structural materials, Nuclear Fusion 24 (1984) 1039-1083.
[17] H. Schroeder and H. Ullmaier, Helium and hydrogen effects on the embrittlement of iron- and nickel-based alloys, J. Nucl. Mater. 179-181 (1991) 118-124.
[18] M.F. Ashby, A first report on deformation-mechanism maps, Acta Metall. 20 (1972) 887-897.
[19] A.S. Kruglov, V.N. Bykov, I. El-Shanshuri and K. Gaber, Effect of neutron irradiation on the yield point of solid copper-based solutions, Sov. Atomic Energy 26 (1969) 582-584.
[20] I.A. El-Shanshoury, The effect of alloying on the neutron-irradiation hardening of copper, J. Nucl. Mater. 45 (1972) 245-257.

[21] H.G. Mohamed, A.M. Hammad and F.H. Hammad, Hardening of copper by solid solution and neutron irradiation, Trans. Indian Inst. Metals 35 (1982) 258-262.
[22] W. Vandermeulen, V. Massaut, J. Van der Velde and W. Hendrix, The effect of irradiation at 150 and 300°C on the tensile properties of Cu and CuCrZr, in 14th Symp. on Fusion Technology, Pergamon Press, New York, 1986, pp. 1031-1035.
[23] H.L. Heinisch, Effects of the neutron spectrum on mechanical property changes in low dose irradiations, J. Nucl. Mater. 155-157 (1988) 121-129.
[24] S.A. Fabritsiev et al., The Effect of Neutron Spectrum on the Mechanical and Physical Properties of Pure Copper and Copper Alloys, J. Nucl. Mater. 233-237 (1996) 526-533.
[25] B.N. Singh, D.J. Edwards and P. Toft, Effects of neutron irradiation on mechanical properties and microstructures of dispersion and precipitation hardened copper alloys, J. Nucl. Mater. 238 (1996) 244-259.
[26] S.J. Zinkle and L.T. Gibson, Electrical conductivity and tensile properties of copper and oxide dispersion strengthened copper alloys following HFIR irradiation to 13 dpa at 200 and 400°C, in Fusion Materials Semiann. Prog Rep. for period ending Dec. 31 1999, DOE/ER-0313/27, Oak Ridge National Lab, 1999, pp. 163-174.
[27] J.C. Wilson, Hardening of copper by solid solution and neutron irradiation, in 2nd UN International Conference on Peaceful Uses of Atomic Energy vol. 5: Properties of Reactor Materials, United Nations, New York, 1958, pp. 431-445.
[28] G.E. Lucas, The evolution of mechanical property changes in irradiated austenitic stainless steel, J. Nucl. Mater. 206 (1993) 287-305.
[29] J.P. Robertson, R.L. Klueh, K. Shiba and A.F. Rowcliffe, Radiation hardening and deformation behavior of irradiated ferritic-martensitic Cr-steels, in Fusion Materials Semiann. Prog. Report for period ending Dec. 31 1997, DOE/ER-0313/23, Oak Ridge National Lab, 1997, pp. 179-187.
[30] S.J. Zinkle, L.L. Snead, A.F. Rowcliffe, D.J. Alexander and L.T. Gibson, Effect of irradiation temperature and strain rate on the mechanical properties of V-4Cr-4Ti irradiated to low doses in fission reactors, in Fusion Materials Semiann. Prog. Report for period ending June 30 1998, DOE/ER-0313/24, Oak Ridge National Lab, 1998, pp. 33-40.
[31] U.F. Kocks, The theory of an obstacle-controlled yield strength-report after an international workshop, Mater. Sci. Eng. 27 (1977) 291-298.
[32] S.J. Zinkle, Fundamental radiation effects parameters in metals and ceramics, Radiation Effects and Defects in Solids 148 (1999) 447-477.
[33] S. Kojima, S.J. Zinkle and H.L. Heinisch, Radiation hardening in neutron-irradiated polycrystalline copper: barrier strength of defect clusters, J. Nucl. Mater. 179-181 (1991) 982-985.
[34] Y. Dai and M. Victoria, Defect cluster structure and tensile properties of copper single crystals irradiated with 600 MeV protons, in I.M. Robertson et al. (eds.), Microstructure Evolution During Irradiation, MRS Symposium Proceedings vol. 439, Materials Research Society, Pittsburgh, 1997, pp. 319-324.
[35] S.J. Zinkle and R.L. Sindelar, Defect microstructures in neutron-irradiated copper and stainless steel, J. Nucl. Mater. 155-157 (1988) 1196-1200.
[36] P.M. Rice and S.J. Zinkle, Temperature dependence of radiation damage microstructure in V-4Cr-4Ti neutron irradiated to low dose, J. Nucl. Mater. 258-263 (1998) 1414-1419.
[37] B.N. Singh and S.J. Zinkle, Defect accumulation in pure fcc metals in the transient regime: a review, J. Nucl. Mater. 206 (1993) 212-229.
[38] M. Victoria et al., The microstructure and associated tensile properties of irradiated fcc and bcc metals, J. Nucl. Mater. 276 (2000) 114-122.
[39] A.J.E. Foreman and M.J. Makin, Dislocation movement through random arrays of obstacles, Philos. Mag. 14 (1966) 911-924.
[40] G.R. Odette, G.E. Lucas, G. Tedeski and B.D. Wirth, Development of superposition rules for hardening in alloys containing multiple defect populations, in Fusion Materials Semiann. Prog Rep. for period ending Dec. 31 1998, DOE/ER-0313/25, Oak Ridge National Lab, 1998, pp. 221-226.
[41] U.F. Kocks, The relation between polycrystal deformation and single-crystal deformation, Metall. Trans. 1 (1970) 1121-1143.
[42] M.J. Makin and S.A. Manthorpe, Hardening of copper irradiated at -195°C, Acta Metall. 9 (1961) 886-888.

[43] S. Kojima, S.J. Zinkle and H.L. Heinisch, Grain size effect on radiation hardening in neutron-irradiated polycrystalline copper, in Fusion Reactor Materials Semiannual Progress Report for Period ending March 31, 1989, DOE/ER-0313/6, 1989, pp. 43-49.

[44] M.S. Wechsler, in The Interaction of Radiation with Solids, North-Holland, Amsterdam, 1964, pp. 246-.

[45] G.P. Seidel, Phys. Stat. Sol. 25 (1968) 175.

[46] M.J. Makin and J.V. Sharp, A model of "lattice" hardening in irradiated copper crystals with the external characteristics of "source" hardening, Phys. Stat. Sol. 9 (1965) 109-118.

[47] B.N. Singh, A.J.E. Foreman and H. Trinkaus, Radiation hardening revisited: role of intracascade clustering, J. Nucl. Mater. 249 (1997) 103-115.

[48] N. Baluc, C. Bailat, Y. Dai, M.I. Luppo, R. Schaublin and M. Victoria, A comparison of the microstructure and tensile behaviour of irradiated fcc and bcc metals, in S.J. Zinkle et al. (eds.), Microstructural Processes During Irradiation, MRS Symposium Proceedings vol. 540, Materials Research Society, Warrendale, PA, 1999, pp. 539-548.

[49] J.L. Brimhall and B. Mastel, Deformation structure in neutron-irradiated copper-aluminum alloy, Appl. Phys. Lett. 9 (1966) 127-128.

[50] J.V. Sharp, Deformation of neutron-irradiated copper single crystals, Philos. Mag. 16 (1967) 77-96.

[51] J.V. Sharp, Correlation between cleared channels and surface slip steps in neutron irradiated copper crystals, Radiat. Eff. 14 (1972) 71-75.

[52] L.M. Howe, Irradiation hardening and annealing in copper at high neutron fluences, Radiat. Eff. 23 (1974) 181-195.

[53] A. Okada, K. Kanao, T. Yoshiie and S. Kojima, Transition of deformation structures in Ni and Au by D-T neutron irradiation, Mater. Trans. JIM 30 (1989) 265-272.

[54] A. Luft, Microstructural processes of plastic instabilities in strengthened metals, Progress in Materials Science 35 (1991) 97-204.

[55] R.J. Arsenault and J. Bressers, A comparison of the effect of neutron irradiation on high purity vanadium and vanadium oxygen alloys, Metall. Trans. 8A (1977) 925-931.

[56] I.G. Greenfield and H.G.F. Wilsdorf, Effect of neutron irradiation on the plastic deformation of copper single crystals, J. Appl. Phys. 32 (1961) 827-839.

[57] U. Essmann and A. Seeger, Verfestigungsverhalten neutronenbestrahlter Metall - II: Temperaturwechselversuche und Gleitlinienbeobachtungen an Kupfereinkristallen, Phys. Stat. Sol. 4 (1964) 177-197.

[58] J.L. Brimhall, The effect of neutron irradiation on slip lines in molybdenum, Trans. Metall. Soc. AIME 233 (1965) 1737.

[59] B. Mastel, H.E. Kissinger, J.J. Laidler and T.K. Bierlein, Dislocation channeling in neutron-irradiated molybdenum, J. Appl. Phys. 34 (1963) 3637.

[60] R.P. Tucker, S.M. Ohr and M.S. Wechsler, Radiation hardening and transmission electron microscopy in niobium, in Radiation Damage in Reactor Materials vol. I, IAEA, Vienna, 1969, pp. 215-233.

[61] R.P. Tucker, M.S. Wechsler and S.M. Ohr, Dislocation channeling in neutron-irradiated niobium, J. Appl. Phys. 40 (1969) 400.

[62] F.A. Smidt, Jr., Dislocation channeling in irradiated metals, Naval Research Lab, Washington DC Report NRL-7078, 1970.

[63] K. Noda, H. Saka, K. Shiraishi, H. Yoshida and T. Imura, In-situ studies of dynamic formation of dislocation channels in neutron-irradiated Ni by HVEM, in Proc. 5th Intern. Conf. on High Voltage Electron Microscopy, Kyoto, Japanese Soc. of Electron Microscopy, Tokyo, 1977, pp. 403-406.

[64] E. Johnson and P.B. Hirsch, In situ straining in the HVEM of neutron-irradiated copper crystals, Philos. Mag. A 43 (1981) 157-170.

[65] E.H. Lee, T.S. Byun, J.D. Hunn, M.H. Yoo, K. Farrell and L.K. Mansur, On the origin of deformation microstructures in austenitic stainless steel: Part I–Microstructures, Acta Mater. 49 (2001) 3269-3276.

[66] N. Hashimoto, S.J. Zinkle, A.F. Rowcliffe, J.P. Robertson and S. Jitsukawa, Deformation mechanisms in 316 stainless steel irradiated at 60°C and 330°C, J. Nucl. Mater. 283-287 (2000) 528-534.

[67] J.L. Brimhall, J.I. Cole, J.S. Vetrano and S.M. Bruemmer, Temperature and strain-rate effects on deformation mechanisms in irradiated stainless steel, in I.M. Robertson et al. (eds.), Microstructure of Irradiated Materials, MRS Symposium Proceedings vol. 373, Materials Research Society, Pittsburgh, 1995, pp. 177-182.

[68] S.M. Bruemmer, J.I. Cole, R.D. Carter and G.S. Was, Defect microstructures and deformation mechanisms in irradiated austenitic stainless steels, in I.M. Robertson et al. (eds.), Microstructure Evolution During Irradiation, MRS Symposium Proceedings vol. 439, Materials Research Society, Pittsburgh, 1997, pp. 437-444.

[69] K. Farrell, T.S. Byun and N. Hashimoto, Mapping flow localization processes in deformation of irradiated reactor structural alloys, Oak Ridge National Lab, Oak Ridge, TN Report ORNL/TM-2002/66, 2002.

[70] S.J. Zinkle, T.S. Byun, K. Farrell and N. Hashimoto, Review of Experimental Studies of Deformation Mechanisms in Irradiated Metals, 2nd IEA Fusion Materials Workshop on Modeling and Experimental Validation, Les Diablerets, Switzerland, Sept. 30-Oct. 4, 2002; to be submitted to J. Nucl. Mater. (2003).

[71] M.L. Grossbeck, K. Ehrlich and C. Wassilew, An assessment of the tensile, irradiation creep, creep rupture, and fatigue behavior in austenitic stainless steels with emphasis on spectral effects, J. Nucl. Mater. 174 (1990) 264-281.

[72] F.A. Garner, M.B. Toloczko and B.H. Sencer, Comparison of swelling and irradiation creep behavior of fcc-austenitic and bcc-ferritic/martensitic alloys at high neutron exposure, Journal of Nuclear Materials 276 (2000) 123-142.

[73] H. Trinkaus and H. Ullmaier, High temperature embrittlement of metals due to helium: is the lifetime dominated by cavity growth or crack growth?, J. Nucl. Mater. 212-215 (1994) 303-309.

[74] G.J.C. Carpenter and R.B. Nicholson, High-temperature embrittlement of metals by rare gas bubbles, in Radiation Damage in Reactor Materials vol. II, IAEA, Vienna, 1969, pp. 383-400.

[75] S.J. Zinkle, A brief review of radiation-induced cavity swelling and hardening in copper and copper alloys, in R.E. Stoller, A.S. Kumar and D.S. Gelles (eds.), 15th Int. Symp. on Effects of Radiation on Materials, ASTM STP 1125, American Society for Testing and Materials, Philadelphia, 1992, pp. 813-834.

[76] S.J. Zinkle and N.M. Ghoniem, Operating temperature windows for fusion reactor structural materials, Fusion Eng. Design 49-50 (2000) 709-717.

[77] J.P. Robertson, I. Ioka, A.F. Rowcliffe, M.L. Grossbeck and S. Jitsukawa, Temperature dependence of the deformation behavior of type 316 stainless steel after low temperature neutron irradiation, in R.K. Nanstad et al. (eds.), 18th Int. Symp. on Effects of Radiation on Materials, ASTM STP 1325, American Society for Testing and Materials, West Conshohocken, PA, 1999, pp. 671-688.

[78] S.J. Zinkle and S.A. Fabritsiev, Copper Alloys for High Heat Flux Structure Applications, Atomic and Plasma-Material Interaction Data for Fusion (supplement to Nuclear Fusion) 5 (1994) 163-192.

[79] D.J. Edwards, S.J. Zinkle, S.A. Fabritsiev and A.S. Pokrovsky, Round robin comparison of tensile results on GlidCop Al25, in Fusion Materials Semiannual Progress Report for Period ending June 30, 1998, DOE/ER-0313/24, Oak Ridge National Lab, 1998, pp. 193-199.

[80] E.V. van Osch, M.G. Horsten and M.I. de Vries, Irradiation testing of 316L(N)-IG austenitic stainless steel for ITER, J. Nucl. Mater. 258-263 (1998) 301-307.

[81] J.E. Pawel, A.F. Rowcliffe, G.E. Lucas and S.J. Zinkle, Irradiation performance of stainless steels for ITER application, J. Nucl. Mater. 239 (1996) 126-131.

[82] M.G. Horsten and M.I. de Vries, Irradiation hardening and loss of ductility of type 316L(N) stainless steel plate material due to neutron irradiation, in D.S. Gelles et al. (eds.), 17th Int. Symp. on Effects of Radiation on Materials, ASTM STP 1270, American Society for Testing and Materials, West Conshohocken, PA, 1996, pp. 919-932.

[83] S.J. Zinkle, P.J. Maziasz and R.E. Stoller, Dose dependence of the microstructural evolution in neutron-irradiated austenitic stainless steel, J. Nucl. Mater. 206 (1993) 266-286.

[84] R.L. Fish, J.L. Straalsund, C.W. Hunter and J.J. Holmes, Swelling and tensile property evaluation of high-fluence EBR-II thimbles, in J. Moteff (ed.) Effects of radiation on substructure and mechanical properties of metals and alloys, ASTM STP 529, American Society for Testing and Materials, Philadelphia, 1973, pp. 149-164.

[85] S. Tähtinen, M. Pyykkönen, P. Karjalainen-Roikonen, B.N. Singh and P. Toft, Effect of neutron irradiation on fracture toughness behavior of copper alloys, J. Nucl. Mater. 258-263 (1998) 1010-1014.

[86] S. Tähtinen, M. Pyykkönen, B.N. Singh and P. Toft, Effect of neutron irradiation on tensile and fracture toughness properties of copper alloys and their joints with stainless steel, in M.L. Hamilton et al. (eds.), 19th Int. Symp. on Effects of Radiation on Materials, ASTM STP 1366, American Society for Testing and Materials, West Conshohocken, 2000, pp. 1243-1259.

[87] D.J. Alexander, J.E. Pawel, M.L. Grossbeck, A.F. Rowcliffe and K. Shiba, Fracture toughness of irradiated candidate materials for ITER first wall/blanket structures, in D.S. Gelles et al. (eds.), 17th Int. Symp. on Effects of Radiation on Materials, ASTM STP 1270, American Society for Testing and Materials, West Conshohocken, PA, 1996, pp. 945-970.

[88] A.F. Rowcliffe et al., Fracture toughness and tensile behavior of ferritic-martensitic steels irradiated at low temperatures, J. Nucl. Mater. 258-263 (1998) 1275-1279.

[89] L.L. Snead, S.J. Zinkle, D.J. Alexander, A.F. Rowcliffe, J.P. Robertson and W.S. Eatherly, Temperature dependence of the tensile and impact properties of V-4Cr-4Ti irradiated to low neutron doses, in Fusion Materials Semiann. Prog. Report for period ending Dec. 31 1997, DOE/ER-0313/23, Oak Ridge National Lab, 1997, pp. 81-98.

[90] F.R.N. Nabarro and H.L. de Villiers, The Physics of Creep, Taylor and Francis, London, 1995.

[91] S.M. Ohr, R.P. Tucker and M.S. Wechsler, Radiation hardening in bcc metals niobium and iron, Trans. JIM 9 Supplement (Proc. ICSMA-1) (1968) 187-192.

[92] S. Yoshida, M. Kiritani, Y. Deguchi and N. Kamigaki, Hardening and recovery of quenched gold, Trans. JIM 9 Supplement (Proc. ICSMA-1) (1968) 83 [93] J.W. Christian and S. Mahajan, Deformation twinning, Progress in Materials Science 39 (1995) 1-158.

[94] O.D. Sherby and A.K. Miller, Combining phenomenology and physics in describing the high temperature mechanical behavior of crystalline solids, J. Eng. Mater. and Technol. 101 (1979) 387-395.

[95] K.C. Russell and F.H. Froes, Dispersoid formation and stability in alloys, Journal of Metals (March, 1988) 29-35.

[96] B. Burton, The influence of alumina dispersions on the diffusion creep behaviour of polycrystalline copper, Met. Sci. J. 5 (1971) 11-14.

[97] J. Rösler and E. Artz, A new model-based creep equation for dispersion strengthened materials, Acta Metall. Mater. 38 (1990) 671-683.

[98] M.W. Guinan and D.J. Steinberg, Pressure and temperature derivatives of the isotropic polycrystalline shear modulus for 65 elements, J. Phys. Chem. Solids 35 (1974) 1501-1512.

[99] D.B. Butrymowicz, J.R. Manning and M.E. Read, Diffusion in Copper and Copper Alloys, J. Phys. Chem. Ref. Data 2 (1973) 643-656.

[100] H.E. Schaefer, Positron annihilation spectroscopy of defects in metals, in P.G. Coleman, S.C. Sharma and L.M. Diana (eds.), Positron Annihilation, North-Holland, New York, 1982, pp. 369-380.

[101] J.P. Hammond, et al., Dynamic and Static Measurements of Elastic Constants with Data on 2-1/4Cr-1Mo Steel, Types 304 and 316 Stainless Steels, and Alloy 800H, Oak Ridge National Laboratory, Oak Ridge, TN Report ORNL-5442, 1979.

[102] W.A. Simpson, Room temperature elastic properties of V-5Cr-5Ti, in Fusion Materials Semiannual Progress Report for Period ending March 31, 1994, DOE/ER-0313/16, Oak Ridge National Lab, 1994, pp. 258-259.

[103] R.J. Farraro and R.B. McLellan, High temperature elastic properties of polycrystalline niobium, tantalum and vanadium, Metall. Trans. 10A (1979) 1699-1702.

[104] H. Schultz, Defect parameters of bcc metals: group-specific trends, Mater. Sci. Eng. A141 (1991) 149-167.

[105] K. Shiba, A. Hishinuma, A. Tohyama and K. Masamura, Properties of Low Activation Ferritic Steel F82H IEA Heat - Interim Report of IEA Round-Robin Tests (1), Japan Atomic Energy Research Institute Report JAERI-Tech 97-038, 1997.

[106] P.C.J. Gallagher, The influence of alloying, temperature, and related effects on the stacking fault energy, Metall. Trans. 1 (1970) 2429-2461.

[107] R.M. Latanision and A.W. Ruff, Jr., The temperature dependence of stacking fault energy in Fe-Cr-Ni alloys, Metall. Trans. 2 (1971) 505-509.

[108] M.S. Duesbury and V. Vitek, Plastic anisotropy in BCC transition metals, Acta Mater. 46 (1998) 1481-1492.

[109] R.S. Mishra, H. Jones and G.W. Greenwood, On the threshold stress for diffusional creep in pure metals, Philos. Mag. A 60 (1989) 581-590.

[110] G. Martin and B. Perrailllon, Measurements of grain boundary diffusion, in R.W. Balluffi (ed.) Grain-boundary structure and kinetics, American Society for Metals, Materials Park, OH, 1980, pp. 239-295.

[111] R.E. Gold, D.L. Harrod, R.L. Ammon, R.W. Buckman, Jr. and R.C. Svedberg, Technical assessment of vanadium-base alloys for fusion reactor applications, Vols. 1 & 2, Westinghouse Electric Corporation, Pittsburgh Report COO-4540-1, 1978.

[112] H.M. Chung, B.A. Loomis and D.L. Smith, Creep properties of vanadium-base alloys, J. Nucl. Mater. 212-215 (1994) 772-777.

[113] K. Natesan, W.K. Soppett and D.L. Rink, Uniaxial creep behavior of V-4Cr-4Ti alloy, in Fusion Materials Semiann. Prog. Report for period ending June 30 2000, DOE/ER-0313/28, Oak Ridge National Lab, 2000, pp. 39-47.

[114] K. Natesan, W.K. Soppett and D.L. Rink, Uniaxial creep behavior of V-4Cr-4Ti alloy, J. Nucl. Mater. Proc. ICFRM10 (2002) in press.

[115] R.J. Kurtz and M.L. Hamilton, Biaxial thermal creep of V-4Cr-4Ti at 700˚C and 800˚C, in Fusion Materials Semiann. Prog. Report for period ending June 30 1999, DOE/ER-0313/26, Oak Ridge National Lab, 1999, pp. 3-10.

[116] M.L. Grossbeck, R.J. Kurtz, L.T. Gibson and M.J. Gardner, Investigation of the effect of a low-oxygen lithium environment on the creep of the V-4Cr-4Ti alloy, in Fusion Materials Semiann. Prog. Report for period ending June 30 2002, DOE/ER-0313/32, Oak Ridge National Lab, 2002, pp. 6-11.

[117] S. Ukai, T. Nishida, T. Okuda and T. Yoshitake, R&D of oxide dispersion strengthened ferritic/martensitic steels for LMFBR, J. Nucl. Mater. 258-263 (1998) 1745-1749.

[118] R.L. Klueh et al., Tensile and creep properties of an oxide dispersion-strengthened ferritic steel, J. Nucl. Mater. 307-311 (2002) 773-777.

[119] S.J. Zinkle and W.S. Eatherly, Effects of test temperature and strain rate on the tensile properties of high-strength, high-conductivity copper alloys, in Fusion Materials Semiannual Progress Report for Period ending Dec. 31, 1996, DOE/ER-0313/21, Oak Ridge National Lab, 1996, pp. 165-174.

[120] D.J. Edwards, Temperature and strain rate effects in high strength, high conductivity copper alloys tested in air, in Fusion Materials Semiannual Progress Report for Period ending Dec. 31, 1997, DOE/ER-0313/23, Oak Ridge National Lab, 1997, pp. 213-222.

[121] S.J. Zinkle, Tensile properties of high-strength, high-conductivity copper alloys at high temperatures, in Fusion Materials Semiannual Progress Report for Period ending June 30, 2000, DOE/ER-0313/28, Oak Ridge National Lab, 2000, pp. 171-175.

[122] J. Groza, Heat-resistant dispersion-strengthened copper alloys, J. Mater. Eng. and Performance 1 (1992) 113-121.

[123] S.J. Zinkle and W.S. Eatherly, Tensile and Electrical Properties of Unirradiated and Irradiated Hycon 3HP CuNiBe, in Fusion Materials Semiannual Progress Report for Period ending June 30, 1996, DOE/ER-0313/20, Oak Ridge National Lab, 1996, pp. 207-216.

[124] S.J. Zinkle, L.L. Snead, J.P. Robertson and A.F. Rowcliffe, Strain rate dependence of the tensile properties of V-(4-5%)Cr-(4-5%)Ti irradiated in EBR-II and HFBR, in Fusion Materials Semiann. Prog Rep. for period ending Dec. 31 1997, DOE/ER-0313/23, Oak Ridge National Lab, 1997, pp. 77-80.

[125] N. Hashimoto, S.J. Zinkle, R.L. Klueh, A.F. Rowcliffe and K. Shiba, Deformation mechanisms in ferritic/martensitic steels irradiated in HFIR, in G.E. Lucas et al. (eds.), Microstructural Processes During Irradiation-2000, MRS Symposium Proceedings vol. 650, Materials Research Society, Warrendale, PA, 2001, pp. R1.10.11-R11.10.16.

[126] A.F. Rowcliffe, S.J. Zinkle and D.T. Hoelzer, Effect of strain rate on the tensile properties of unirradiated and irradiated V-4Cr-4Ti, J. Nucl. Mater. 283-287 (2000) 508-512.

[127] P. Fenici, D.J. Boerman, G.P. Tartaglia and J.D. Elen, Effect of fast-neutron irradiation on tensile properties of precipitation-hardened Cu-Cr-Zr alloy, J. Nucl. Mater. 212-215 (1994) 399-403.

[128] A.F. Rowcliffe, S.J. Zinkle, J.F. Stubbins, D.J. Edwards and D.J. Alexander, Austenitic Stainless Steels and High Strength Copper Alloys for Fusion Components, J. Nucl. Mater. 258-263 (1998) 183-192.

[129] S.J. Zinkle, J.P. Robertson and R.L. Klueh, Thermophysical and mechanical properties of Fe-(8-9%)Cr reduced activation steels, in Fusion Materials Semiann. Prog. Report for period ending June 30 1998, DOE/ER-0313/24, Oak Ridge National Lab, 1998, pp. 135-143.

[130] K. Ehrlich, Deformation behavior of austenitic stainless steels after and during neutron irradiation, J. Nucl. Mater. 133&134 (1985) 119-126.

[131] R.E. Stoller, M.L. Grossbeck and L.K. Mansur, A theoretical model of accelerated irradiation creep at low temperatures by transient interstitial absorption, in R.E. Stoller, A.S. Kumar and D.S. Gelles (eds.), 15th Int. Symp. on Effects of Radiation on Materials, ASTM STP 1125, American Society for Testing and Materials, Philadelphia, 1992, pp. 517-529.

[132] F.A. Garner, M.B. Toloczko and M.L. Grossbeck, The dependence of irradiation creep in austenitic alloys on displacement rate and helium to dpa ratio, J. Nucl. Mater. 258-263 (1998) 1718-1724.

[133] F.A. Garner and W.G. Wolfer, Factors which determine the swelling behavior of austenitic stainless steels, J. Nucl. Mater. 122&123 (1984) 201-206.

[134] H. Trinkaus, Modeling of helium effects in metals: High temperature embrittlement, J. Nucl. Mater. 133&134 (1985) 105-112.

[135] D.N. Braski, H. Schroeder and H. Ullmaier, The effect of tensile stress on the growth of helium bubbles in an austenitic stainless steel, J. Nucl. Mater. 83 (1979) 265-277.

[136] D.R. Harries, Neutron irradiation-induced embrittlement in type 316 and other austenitic steels and alloys, J. Nucl. Mater. 82 (1979) 2-21.

[137] N. Yamamoto, Y. Murase, J. Nagakawa and K. Shiba, Creep behavior of reduced activation martensitic steel F82H injected with a large amount of helium, J. Nucl. Mater. 307-311 (2002) 217-221.

[138] H. Schroeder, W. Kesternich and H. Ullmaier, Helium effects on the creep and fatigue resistance of austenitic stainless steels at high temperatures, Nucl. Eng. Des./Fusion 2 (1985) 65-95.

[139] R.D. Carter, M. Atzmon, G.S. Was and S.M. Bruemmer, Deformation mechanisms in a proton-irradiated austenitic stainless steel, in I.M. Robertson et al. (eds.), Microstructure of Irradiated Materials, MRS Symposium Proceedings vol. 373, Materials Research Society, Pittsburgh, 1995, pp. 171-176.

[140] M.F. Ashby, C. Gandhi and D.M.R. Taplin, Fracture-mechanism maps and their construction for FCC metals and alloys, Acta Metallurgica 27 (1979) 699-729.

[141] C. Gandhi and M.F. Ashby, Fracture-mechanism maps for materials which cleave: FCC, BCC and HCP metals and ceramics, Acta Metall. 27 (1979) 1565-1602.

[142] R.J. Fields, T. Weerasooriya and M.F. Ashby, Fracture-mechanisms in pure iron, two austenitic steels, and one ferritic steel, Metall. Trans. A 11 (1980) 333-347.

[143] G.D. Quinn, Fracture-mechanism maps for advanced structural ceramics. Part 1. Methodology and hot-pressed silicon nitride results, J. Mater. Sci. 25 (1990) 4361-4376.

[144] M.L. Grossbeck, J.O. Stiegler and J.J. Holmes, Effects of irradiation on the fracture behavior of austenitic stainless steels, in M.L. Bleiberg and J.W. Bennett (eds.), Radiation effects in breeder reactor structural materials, TMS-AIME, New York, 1977, pp. 95-116.

[145] D. Teirlinck, F. Zok, J.D. Embury and M.F. Ashby, Fracture-mechanism maps in stress space, Acta Metall. 36 (1988) 1213-1228.

ATOMIC-LEVEL INTERACTION OF AN EDGE DISLOCATION WITH LOCALIZED OBSTACLES IN FCC AND BCC METALS - Yu. N. Osetsky (Oak Ridge National Laboratory) and D. J. Bacon (Department of Engineering, The University of Liverpool, UK)

SUMMARY

Interaction between a moving dislocation and localized obstacles determines microstructure-induced hardening. The mechanisms and parameters of such interactions are necessary inputs to large scale dislocation dynamics modelling. We have developed a model to investigate these characteristics at the atomic level for dislocation-obstacle interactions under both static (T=0K) and dynamic (T>0K) conditions. We present results on hardening due to pinning of edge dislocations at obstacles such as voids, coherent precipitates and stacking fault tetrahedra in bcc-iron and fcc-copper at temperatures from 0 to 600K. It is demonstrated that atomic-scale simulation is required to determine the effects of stress, strain rate and temperature and that such effects cannot always be rationalized within continuum theory.

PROGRESS AND STATUS

Introduction

Materials subjected to different treatments may suffer degradation of mechanical properties, e.g. hardening, loss of ductility and plastic instability. In many cases, for example under irradiation, the main reason is formation of localised obstacles to dislocation motion. The typical radiation defects affecting mechanical properties are defect clusters of both vacancy and interstitial types and secondary phase precipitates. Three-dimensional dislocation dynamics (3DDD), as a part of multiscale materials modelling approach, can be used to predict mechanical properties on the basis of the microstructure present but suffers from lack of understanding of short-range interactions between moving dislocations and obstacles, which makes 3DDD approximate in some cases. This gap can be filled using atomic modelling techniques at large enough scale to overlap with the continuum approach, and hence provide mutual validation and parameterization of the mechanisms considered. Another essential advantage of the atomic modelling is the possibility for direct study of thermal effects, which is impossible by other techniques. Recent achievements in atomic-scale modelling of dislocation dynamics [1-5] have demonstrated the importance of this approach. In this paper we review new modelling where a variety of obstacles, such as vacancy voids, stacking fault tetrahedra (SFTs) and coherent precipitates, to the glide of edge dislocations was studied in Cu and Fe over a range of temperatures. We focus mainly on mechanisms of dislocation-obstacle interaction, differences observed for different metals and temperature effects.

Model

The model for simulating the dynamics of the edge dislocation is described in detail in [4]. It is based on the approach of Baskes and Daw [1] using a periodic array of dislocations. An advantage of the model described in [4] is that is allows the stress-strain curve to be obtained under both statics (T=0) and dynamics (T>0) conditions. The results discussed here were obtained from bcc-Fe and fcc-Cu model crystals. Edge dislocations ½<111><112> (Fe) and ½<110><112> (Cu) were simulated in crystallites having from ~2,000,000 to ~8,000,000 mobile atoms over the temperature range from 0 to 600K. Voids or coherent copper-precipitates in Fe and voids or SFTs in Cu were created in the vicinity of the previously relaxed dislocation, the crystal was relaxed again and then loaded by applying strain or stress. Two approaches were used. Static modelling provides information on equilibrium structure under a given strain, which can be compared directly with continuum modelling of dislocation line shape for example. Dynamic modelling by molecular dynamics (MD) allows temperature effects as well as kinetic properties of moving dislocations to be investigated. The stress-strain curve can be obtained with both approaches and its dependence on strain rate studied in dynamics.

Results

Voids and copper precipitates in iron

An example of stress-strain curves obtained for an initially straight edge dislocation overcoming a periodic row of voids (diameter D, spacing L) in Fe at T=0K is presented in Fig. 1. According to [4] the total process of dislocation-void interaction can be divided into four stages of dislocation motion, first before it meets the void, second as it enters the void, third as it glides over the void surface and fourth after it breaks away. These stages can be seen clearly in Fig. 1 for all the voids. The maximum stress for each void size gives the corresponding critical resolved shear stress (CRSS) at which the dislocation breaks away and, provided the strain is increasing, gives further plastic deformation in the fourth stage. Data on CRSS obtained for D=0.7-5nm and L=41-82nm versus harmonic mean $(D^{-1}+L^{-1})^{-1}$ are presented in Fig. 2 (empty circles) together with the results of continuum dislocation dynamics modelling for voids and Orowan particles from [6,7]. It can be seen that atomic scale modelling data are qualitatively similar to the result for voids in the continuum treatment, suggesting that the dependence :

$$\tau_{\text{Void}} = \frac{Gb}{2\pi L}\left[\left(D^{-1}+L^{-1}\right)^{-1}+1.52\right] \qquad (1)$$

can be used for estimation of CRSS in higher level continuum modelling of void strengthening.

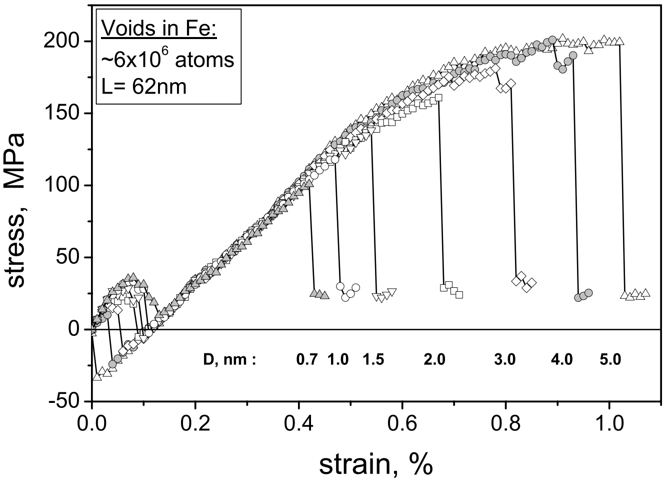

Figure 1. Stress-strain curves obtained for dislocation-void interaction by static modelling in Fe. The number of mobile atoms in the simulated crystal, void spacing, L, and void diameter, D, are indicated.

However, the mechanism of dislocation-void interaction observed by atomic modelling in Fe has some differences from that expected from continuum modelling in [7]. The main difference is that at atomic level this interaction is accompanied by dislocation climb, to an extent that depends on the void size (see e.g. [5]). As a result of this climb, the effective size of a void decreases and it becomes a weaker obstacle for the following dislocation.

MD modelling has demonstrated that stress-strain curves are strongly temperature dependent and the CRSS decreases as T rises. An example of CRSS temperature dependence for the 2nm void is presented in Fig. 3 by open circles. One can see that at T=600K the CRSS drops to 60% of its zero temperature value.

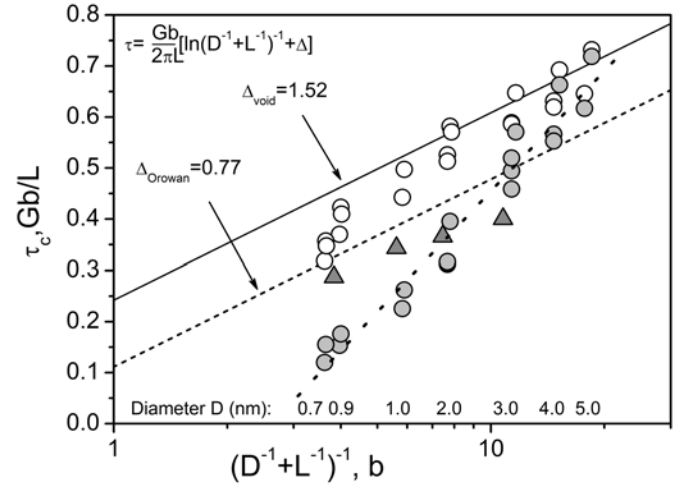

Figure 2. Critical resolved shear stress obtained for different defects as function of harmonic mean of obstacle size D and spacing L. G is the shear modulus and b is the magnitude of the Burgers vector. Open circles – voids in Fe, dark circles – Cu-precipitates in Fe, triangles – voids in Cu. Dashed and solid lines are results obtained in [6,7] by continuum modelling of an edge dislocation passing through a row of Orowan particles and voids respectively, dotted line is interpolation of precipitate results by the dependence $Gb/1.3L[\ln(D^{-1}+L^{-1})^{-1}-0.44]$.

The above data were obtained at strain rate $\dot{\varepsilon}=5\text{x}10^6\text{s}^{-1}$ at which, for the model size used, the dislocation moves with the steady state velocity $V_d \approx 15$m/s, which is a rather low velocity for atomic scale modelling. It was found that the stress at which the dislocation cuts the void depends on its velocity. As an example, consider the following data for the same 2nm void in a crystal under different $\dot{\varepsilon}$. At zero temperature the CRSS was found to be 207MPa and it drops to 179MPa at 100K. However, if simulation at T=100K is made at constant applied stress equal to 100MPa, at which $V_d \approx 900$m/s, the dislocation cuts the void. Notice, this kinetic effect depends on temperature and crystal size, e.g. higher stress should be applied at high temperature but lower stress is sufficient for the dislocation to cut the void in a larger crystal (i.e. lower dislocation density). This effect could be explained in terms of kinetic energy associated with a moving dislocation. More detailed discussion and explanation of kinetic effects can be found in [8]. We also note here that a fast dislocation climbs more than a slow one.

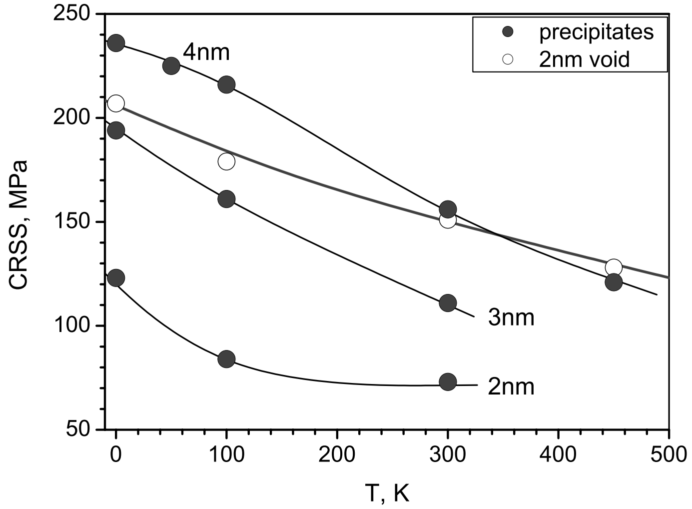

Figure 3. Temperature dependence of the CRSS due to coherent Cu-precipitates of different size and 2nm voids in Fe at applied strain rate $5\text{x}10^6\text{s}^{-1}$.

Copper-precipitates

Results for the CRSS at zero temperature due to a periodic row of coherent spherical Cu precipitates in Fe are presented in Fig. 2 by dark circles. The dependence of the CRSS on $\ln(D^{-1}+L^{-1})^{-1}$ can be approximated by a linear function (indicated by dotted line) with a slope significantly steeper than that for voids, i.e. ~1/1.3 compared with $1/2\pi$. However, the mechanism of dislocation-precipitate interaction depends on precipitate size. Thus small precipitates, D<3nm, suffer simple shear, whereas in the case of large precipitates partial transformation towards the more stable fcc structure inside precipitates and dislocation climb are observed.

It is common to attempt to describe precipitate hardening on the basis of the constant line tension approximation. For this the critical angle, φ, between dislocation segments as they break away from a precipitate are required, e.g. it is estimated from the Cu-Fe modulus difference in [9]. It is obtained accurately in our modelling and is >0 for $D \leq 3$nm and equal to zero for larger precipitates. This angle was used to estimate the corresponding stress in the line-tension treatment, and gave values up to twice the true value estimated in atomic-scale modelling (see [5]). In other words, in order to give correct stresses, the line-tension model has to use incorrect angles.

The temperature dependence of the CRSS due to Cu precipitates in Fe under a constant applied strain rate of $5 \times 10^6 s^{-1}$ is presented in Fig. 3 by full circles. The dependence is strong relative to that of voids. Thus, a row of 2nm voids is weaker at T=0K than 4nm precipitates, they have similar strength at T=300K and at higher temperature the voids are stronger obstacles. Another effect observed for precipitates is an increase of dislocation climb: the higher the temperature the more vacancies are left inside a precipitate.

Voids and SFTs in copper

Examples of stress-strain curves for dislocation-void interaction at T=0K in copper are presented in Fig. 4. It can be seen that the dependences are qualitatively different from those obtained for Fe (see Fig. 1). The explanation lies in the difference of the dislocation core structure in the two metals, for unlike that in Fe, the dislocation in Cu is dissociated into two Shockley partials linked by a stacking fault ribbon of width ≈13a for the edge dislocation. As a result each partial dislocation interacts with an obstacle individually. The first stress peak at yield in Fig. 4 for voids of each size corresponds to the stress when the leading partial breaks away, whereas the second peak is related to the same process for the trailing dislocation. The corresponding partial dislocation line shapes for D=2nm are presented in Fig. 5. It is interesting to note that the relative height of the two stress peaks in Fig. 4 depends on void size. Thus, when the dislocation cuts small voids the stress at the first peak is lower than that at the second, whereas for the

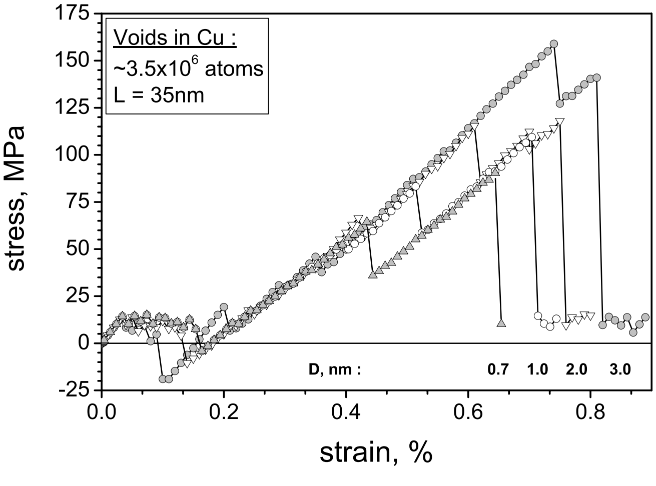

Figure 4. Stress-strain dependence for dislocation-void interaction in Cu at T=0K.

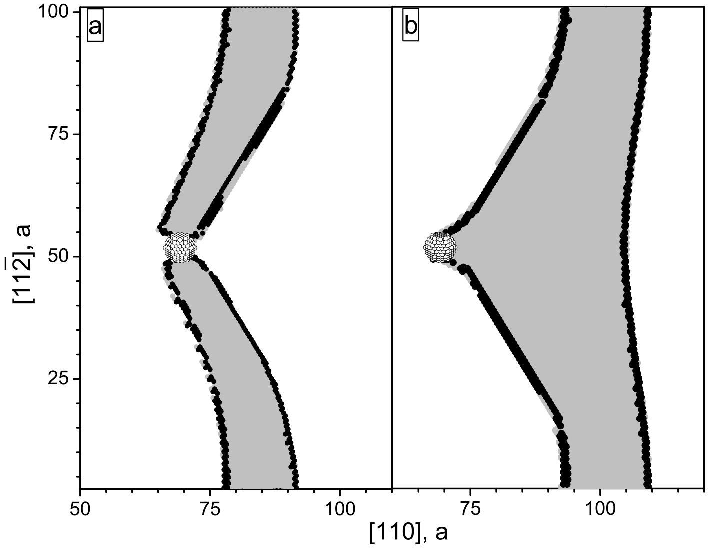

Figure 5. Critical shape of partial dislocations interacting with a 2nm void in Cu at T=0K: (a) leading partial at shear stress 115MPa; (b) trailing partial at 118MPa. The core region of partials is shown by black symbols, the stacking fault is grey and the void surface atoms are indicated by hollow spheres.

largest void studied (D=3nm) the leading partial breaks away at maximum stress. This size-dependent effect is presumably related to the pulling force the leading partial can provide for the trailing one if the area of the stacking fault increases significantly at such a high stress. The assistance of the leading partial may also explain the overall weaker strengthening due to voids in Cu in comparison with Fe, as seen in Fig. 2. Another feature of the dislocation-void interaction mechanism in Cu is the absence of climb and defect absorption, for only pure shear of voids has been found in all the cases studied.

Temperature effects have been studied in dynamic modelling of interaction of a gliding dislocation with 2nm (369 vacancies) and 3nm (1205 vacancies) voids and 2.5nm (45 vacancies) and 3.0nm (78 vacancies) SFTs in Cu. A significant drop in CRSS occurs when temperature is increased from 0 to 100K. Further increase of temperature gives only a weak additional decrease of CRSS, as shown by the data in Fig. 6. Note that the 2.5nm SFT demonstrates very similar strengthening to that of a 2nm void, despite the fact that it contains only 45 vacancies against 369 in the void. Moreover, the 2.5 nm SFT is a stronger obstacle than the 3.0nm one. A detailed analysis of dislocation-SFT interaction sheds light on this paradox. The data presented in Fig. 6 were obtained when the dislocation glide plain cuts an SFT through the centre of mass. In this geometry the glide plane is closer to the parallel face for a smaller SFT than a larger one. By varying the position of the glide plane, we have found that maximum strengthening occurs when a dislocation glide plain coincides with the stacking fault of one of the faces.

The larger the distance between the face and the glide plane, the lower the CRSS. Moreover, when the larger SFT (3nm) is cut though the centre of mass at all temperatures above T=10K it recovers its regular structure via a thermally-activated propagation of a jog on the stair-rod partial dislocations of its edges. This recovery does not occur for the smaller SFT whose regular structure remained disturbed after being cut by the dislocation. Similar damage of a small SFT by a dissociated dislocation at T=0K was observed earlier [10].

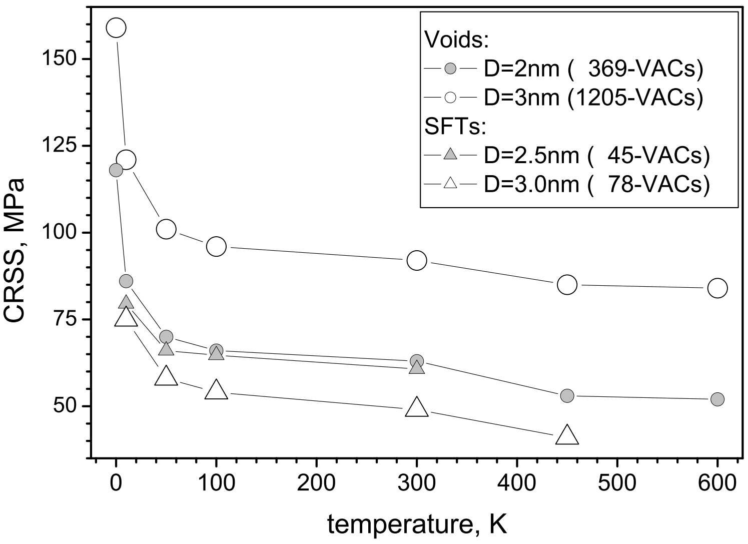

Figure 6. Temperature dependence of the CRSS of voids and SFTs in Cu obtained by molecular dynamics modelling at strain rate $5x10^6 s^{-1}$. Void diameter, SFT size and the corresponding number of vacancies is indicated.

Summary

Atomic-scale modelling with a choice of static (T=0K) and dynamic (T>0K) conditions, together with different types of crystal loading, i.e. applied strain increment or strain rate or applied stress, allows a wide range of features of dislocation-obstacle interactions to be studied. Static modelling reveals many general features which can be treated and understood within continuum dislocation theory. An example is presented in Fig. 2 where stress values for voids and precipitates in Fe are close to the linear dependence of CRSS on logarithm of harmonic mean of obstacle size and spacing found earlier in simulations based on elasticity theory [6,7]. The data for voids in Cu can be described as a linear dependence in principle, but due to the dissociated character of the dislocation the mechanism is more complicated and void-size dependent: strengthening by small voids is controlled by breakaway of the trailing partial whereas that of large voids is controlled by the leading partial. Dissociation also reduces the total strength of these obstacles. Static modelling can also provide information on dislocation line shape in equilibrium at different stress levels (see e.g. [5]), and this can be used for fitting parameters required in continuum dislocation dynamics models. One of the conclusions on dislocation line shape revealed here and in [5] is that the simple constant line tension model widely used in estimations of CRSS (e.g. for hardening due to Cu precipitates in Fe [9]) provides an incorrect relationship between applied stress and line shape.

Atomic-scale details of dislocation-obstacle interactions depend strongly on dislocation core structure, as demonstrated here by comparison of Fe and Cu. The low stacking fault energy in Cu causes wide separation of the partial dislocations and leads to absence of dislocation climb in interactions with obstacles of vacancy type. The perfect edge dislocation in Fe, in contrast, may climb and absorb defects in all the cases considered.

The dynamic simulations demonstrate a strong temperature effect in the stress-strain characteristics for all the obstacles studied. The nature of this is not yet fully understood. Based on the results presented, we can conclude that the temperature enhancement mechanisms may be different for different obstacles, e.g. stronger for coherent precipitates than voids in Fe (see Fig. 3), and for different metals, e.g. the temperature dependence of the CRSS for voids is different in Fe and Cu (see Figs. 3 and 6).

Kinetic effects in dislocation-obstacle interactions have been observed in all the cases treated and this seems to be important for explanation of plastic instability and creation of cleared channels in irradiated metals [11]. In fact, we have demonstrated that a dislocation moving at high speed can cut and breakaway from an obstacle at a stress significantly lower than the CRSS. Moreover, the change in structure of the obstacle due to the fast dislocation is more significant. More studies are necessary to understand these effects and to reveal mechanisms suitable for incorporation in higher level dislocation dynamics applications.

ACKNOWLEDGMENT

Support in the United Kingdom provided by a grant from the UK Engineering and Physical Science Research Council and a JREI grant of the Higher Education Funding Council for England.

REFERENCES

[1] M.I.Baskes and M.S.Daw, Proceedings of Fourth Int. Conf. On the Effects of Hydrogen on the Behaviour of Materials (Jackson Lake Lodge, Moran, WY) eds. N.Moody and A.Thompson, The Minerals, Metals and Materials Society, Warrendale, PA, 1989.

[2] D.Rodney and G.Martin, Dislocation pinning by glissile interstitial loops in nickel crystal: A molecular dynamics study. Phys.Rev.B, 2000; 61: 8714.

[3] D.Rodney, G.Martin and Y.Brechet, Irradiation hardening by interstitial loops : atomistic study and micromechanical model. Materials Science and Engineering. 2001; A309-310: 198-202.

[4] Yu.N.Osetsky and D.J.Bacon, An atomic-level model for studying the dynamics of edge dislocations in metals. Modelling Simul. Mater. Sci. Eng., 2002; 11: 427.

[5] Yu.N.Osetsky, D.J.Bacon and V.Mohles, Atomic modelling of strengthening mechanisms due to voids and copper precipitates in alpha-iron. Philos. Mag.A, 2003; in press.

[6] D.J.Bacon, U.F.Kocks and R.O.Scattergood, The effect of dislocation self-interaction on the Orowan stress, Philos. Mag., 1973; 28: 1241.

[7] R.O.Scattergood and D.J.Bacon, The strengthening effects of voids. Acta Metall., 1982;30: 1665.

[8] E.Bitzek, D.Weygang and P.Gumbsch, Atomistic and DD studies of inertial effects on the dynamics of dislocations. These proceedings pg.

[9] K.C.Russell and L.M.Brown, A dispersed strengthening model based on a differing elastic moduli applied to the iron-copper system, Acta. Metall., 1972; 20: 969.

[10] Yu.N.Osetsky, D.J.Bacon, B.N.Singh and B.Wirth, Atomistic study of interaction, accumulation and annihilation of cascade induced defect clusters, J.Nucl.Mater., 2002; 307-311.

[11] M. Victoria, N. Baluc, C. Bailat, Y. Dai, M. I. Luppo, R. Schaublin and B. N. Singh, The microstructure and associated tensile properties of irradiated fcc and bcc metals, J.Nucl.Mater., 2000; 276:114.

A KINETIC MONTE CARLO MODEL FOR HELIUM DIFFUSION AND CLUSTERING IN FUSION ENVIRONMENTS

-- B. D. Wirth (University of California, Berkeley) and E. M. Bringa (Lawrence Livermore National Laboratory)

ABSTRACT

Structural materials in fusion reactors will operate in harsh radiation conditions including high displacement rates from 14 MeV neutrons with accompanying high levels of hydrogen and helium production and will experience severe property degradation. Predicting their in-service performance requires a detailed understanding of the mechanisms of defect accumulation and microstructure evolution. Here, we describe a kinetic Monte Carlo (KMC) model to simulate the migration and clustering of transmutant helium gas atoms and ultimately determine the role of He in mediating the long term aging of primary defects (vacancies, self-interstitial atoms and their clusters) produced in displacement cascades.

The KMC model is based on modifications to a code that has been successfully used to study copper-vacancy clustering in Fe-Cu alloys. Since He can occupy either interstitial or substitutional sites within the bcc Fe lattice, this model involves the addition of an octahedral site sub-lattice [(0.5,0,0) and (0.5,0.5,0) sites] and is sufficient to describe He migration. As an interstitial, He diffuses between octahedral sites through unstable tetrahedral site saddle points and as a substitutional atom, He migrates via a vacancy exchange mechanism. For substitutional He jumping into a nearest neighbor vacancy, the He atom migrates along trajectories very close to the <111> direction, with an activation energy of 0.12 eV. Notably, our atomistic molecular statics simulations reveal that the He atom can jump into a second nearest neighbor vacancy position along a trajectory close to the <100> directions, with an activation energy of 0.66 eV.

The KMC results illustrate the mechanisms responsible for the formation of vacancy-He clusters, the rather large three-dimensional mobility of small vacancy-He clusters and the role of cluster coalescence events in assisting He cluster nucleation. Future work will clarify the mobility of vacancy-He cluster complexes and extend the simulation durations to predict He bubble nucleation.

Reference

Accepted for publication in Physica Scripta.

SUPPRESSION OF HELIUM BUBBLE GROWTH IN FRICTION STIR WELDING OF IRRADIATED MATERIALS – Zhili Feng and Stan A. David (Oak Ridge National Laboratory)

OBJECTIVE

To conduct preliminary assessment on the potential benefits of friction stir welding process in welding repair of irradiate materials.

SUMMARY

Computational simulations were conducted to investigate the helium bubble growth during friction stir welding of irradiated stainless steel. The helium bubble evolution model by Kawano et al was incorporated into the finite element based welding temperature and stress computational model to obtain the temporal and spatial distribution of the helium bubbles in the heat-affected zone of a weld. The predicted maximum helium bubble location in a gas tungsten arc weld correlated very well with the actual helium induced cracking site. The compressive thermal stress, coupled with the lower temperature, of the friction stir welding process inhibits the helium bubble growth. The calculations show that, even without fine-tuning the FSW process parameters, the maximum helium bubble size in a friction stir weld is only about 27% of a gas tungsten arc weld of comparable size. This preliminary study suggests that friction stir welding is advantageous in circumventing the helium induced cracking for welding of irradiated materials.

PROGRESS AND STATUS

Introduction

Fusion welding of irradiated materials has been difficult. Depending on the level of irradiation, welding can result in cracking in the heat-affected zone (HAZ) of the weld region [1]. The cracking is attributed to the entrapped helium in the post-irradiated material [2,3]. The helium bubbles nucleate, grow and coalesce rapidly at grain boundaries under the high temperature and tensile stresses in welding. Intergranular brittle rupture occurs as the cohesive strength of the grain boundary (weakened by helium bubbles) can no longer bear the tensile stress caused by the cooling contraction of the weld. In principle, the formation of He bubble and the He induced cracking can be inhibited or eliminated by minimizing the exposure to tensile stresses at elevated temperatures [4]. However, eliminating the tensile stress in a fusion welding process is very challenging in practice, if impossible.

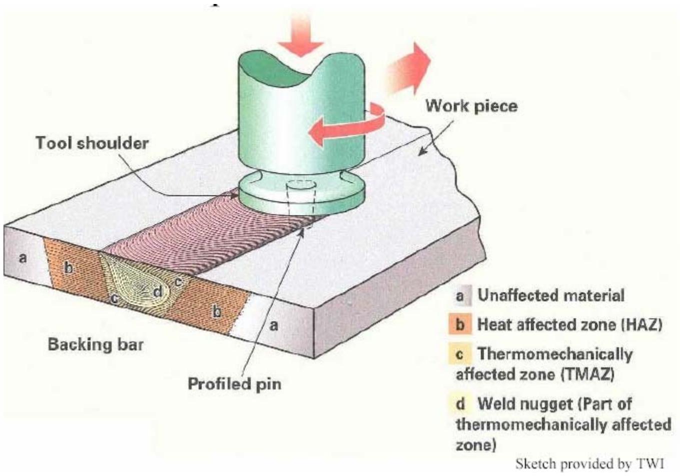

Sketch provided by TWI

Figure 1 Schematics of Friction Stir Welding Process

Friction stir welding (FSW) is a new, innovative solid-state joining process developed in the 1990s [5]. As shown in Figure 1, the process utilizes a rotating tool to generate heat to soften the material which is then mechanically stirred and consolidated to form the metallurgical bond. To date, the FSW has been successfully used for high-strength aluminum alloys that are considered non-weldable with fusion welding processes because of solidification related defects. Although many challenging technical issues still remain, friction stir welding of high-melting temperature materials such as stainless steels and Ti alloys has demonstrated feasible [6].

Approach

Experimentally making friction stir weld on irradiated materials is very costly and time-consuming. As a feasibility study, we utilized the advanced welding simulation models to investigate the formation of He bubble during friction stir welding. For comparison, we also analyzed the formation of He bubble in gas tungsten arc welding (GTAW) process reported from the literature [7].

Materials and Welding Conditions

The materials, specimen geometry, and welding conditions for the GTAW process followed those of the experimental weldability study by Asano et al [7]. The irradiated SS 304 stainless steel plate was autogenously welded at a heat input level of 7.1kJ/cm. The plate was 8-mm thick, 30-mm wide, and 60-mm long. The weld appearance is shown in Figure 2. The He-induced cracks are also apparent in the figure. The cracks are predominately around the bottom of the weld.

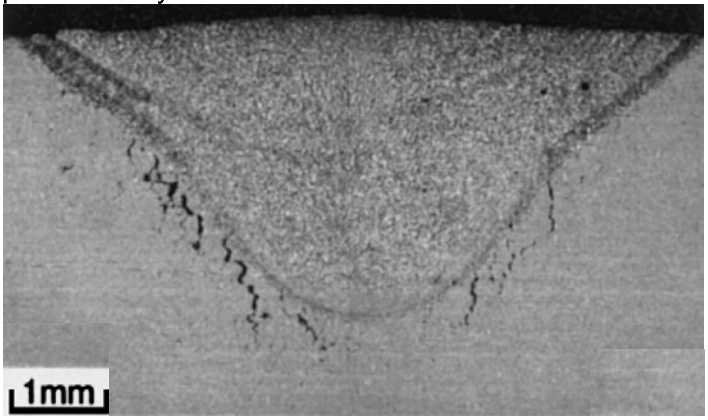

Figure 2 Appearance of helium-induced cracks from Asano's study [7].

For the friction stir weld, the process conditions were selected such that the anticipated weld depth and width would be similar to those of the GTA weld by Asano et al. Key process parameters were ¾" shoulder diameter, 530 rpm rotational speed, and 3 in/min welding travel speed.

Asano reported an initial He concentration of 8.3 appm, but did not report the He bubble size in their test. In this work, the initial He concentration was increased to 100 appm, such that the predicted helium bubble growth could be verified against Hashimoto's work [8].

Modeling of Temperature and Thermal Stress in Welding

The weld plate was modeled as a two-dimensional cross-section model. The generalized plain strain formulations were used to deal with the out-of-plane bending due to the thermal expansion. The welding was modeled as a transient non-linear thermo-mechanical deformation process, with temperature dependent material properties. The effects of solidification on the thermal stress field at elevated temperatures were considered following the approach developed previously [9]. This type of model has been widely used for simulating the temperature and stress evolutions associated with long and straight weld.

For the GTAW process, the welding heat input took the ellipsoidal form.

$$q = \frac{6\sqrt{3}\eta EI}{\pi\sqrt{\pi}abc} e^{\left[-3\left(\frac{x^2}{a^2}+\frac{y^2}{b^2}+\frac{z^2}{c^2}\right)\right]} \tag{1}$$

where E and I are the welding voltage and current respectively. The arc efficiency, η, is assumed to be 70% for the GTA welding process. The parameters a, b, and c are related to characteristics of the welding arc. In this equation, the origin of the coordinate system is located at the center of the welding arc.

For the FSW process, the heat generation was assumed to be from the surface friction between the tool shoulder and material, and took the following form:

$$q = \frac{3\eta T\omega}{2\pi R^3} r \tag{2}$$

where r is the radial distance from the center of the tool, T the torque, ω the rotational speed, R the radius of the tool shoulder.

Modeling of Helium Bubble Evolution

Although more elaborate models available (such as these by Hashimoto et al [8]), we choose to implement the one by Kawano et al [10] for its simplicity in this preliminary phase of study. Kawano's equations are an extension of the work by Grossback et al [3]. We numerically integrated the set of differential equations by Kawano over the entire welding thermal and stress cycle at every integration point of the finite element model, to obtain the temporal and spatial distribution of the helium bubble.

The helium bubble outside the fusion zone was simulated according to Kawano's equations. On the other hand, the helium bubble inside the molten weld pool involves different mechanisms. For example, helium bubble would escape from the weld pool as a result of molten metal flow and transport. Therefore, the helium bubble inside the fusion zone was artificially assumed to be completely escaped, thereby having zero radius and density.

Results

Helium Bubble in GTA weld

Figure 3 shows the predicted distribution of helium bubble size (radius). Outside the fusion zone, significant helium bubble growth only occurs in a narrow band of about 1-mm wide adjacent to the fusion line where the peak temperature reaches the melting point of the material. The bubble grows negligibly if the peak temperature is below 1000K. Within this band, the helium bubble is considerably smaller near the surface of the plate, suggesting the important influence of the stress state. Finally, the predicted maximum helium bubble locations are in very good agreement with the observed cracking sites, indicating the validity of the model.

The predicted final maximum helium bubble radius is about 252 nm. Quantitatively, this prediction is about an order of magnitude smaller than these with simplified stress assumptions [3]. But it agrees with these using more realistic welding temperature and stress conditions [8] and experimental observations of welds made with similar welding conditions and helium concentrations.

Helium Bubble in Friction Stir Weld

Figure 4 show the predicted distribution of final helium bubble radius in the friction stir weld. For reference, the geometry of the FSW tool is superimposed onto the FSW case, and the weld bond region is also highlighted. The result of the GTAW is also plotted next to the FSW which provides direct visual comparisons of the weld shape and he bubble distribution.

As shown in Figure 4, the friction stir weld has similar depth to that of the GTA weld, but is wider near the plate surface due to the heating of the tool shoulder. The growth of the helium bubble is substantially suppressed – the maximum bubble radius of the FSW case is about 69 nm, which is only 27% of the maximum bubble radius in the GTAW case. Analyses of the simulation data suggested that this is primarily due to fact that the hot stirred region subjects to a compressive hydraulic pressure from the tool shoulder.

It should be noted that the selected FSW conditions was based on the previous experience in making friction stir weld in stainless steels. They could be improved to further lower the temperature during the process, and the tool geometry could be refined to maximize the benefits of the compressive stress.

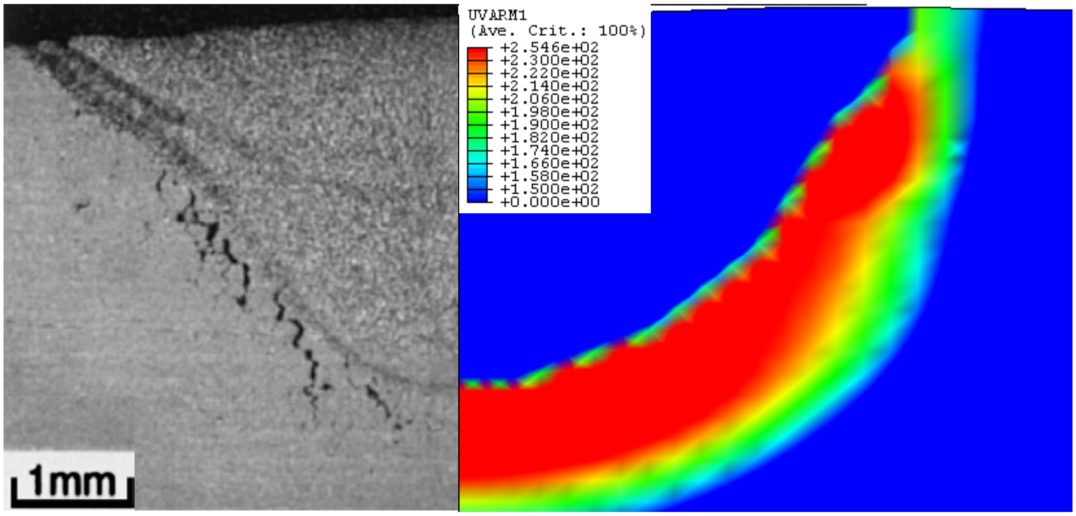

Figure 3 Predicted helium bubble radius in relation to the observed weld shape and location of He induced cracks. He bubble radius in nm.

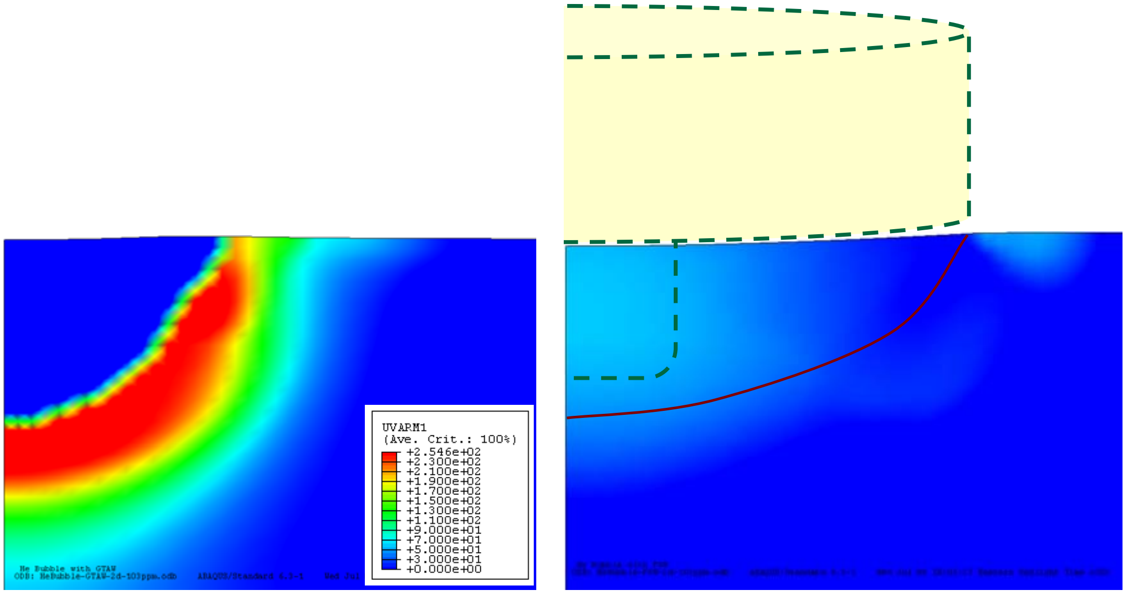

Figure 4 Comparison of helium bubble radius in FSW against GTAW. The GTA weld is on the left, whereas the friction stir weld is on the right.

References

1 Maloney, J.P., Baker, D, Kennedy, W.R., Day, W.A., McClain, J.B., Fraser, W.G, McKenney, D.H, Huxford, H.R., Meyer, C.A., Kehr, K.E., Mittelberg, R.F., and Walls, J.E., 1969, "Repair of a Nuclear Reactor Vessel," AEC R&D Report, Savannah River Laboratory, DP-1199.

2 Kanne Jr., W.R., 1988, "Remote reactor repair: GTA weld cracking caused by entrapped helium," *Welding Journal*, **67**, pp. 33-39.

3 Lin, H.T, Grossbeck, M.L. and Chin, B.A., 1990, "Cavity microstructure and kinetics during gas tungsten welding of helium-containing stainless steel," *Metall. Trans*. **21A**, pp. 2585-2596.

4 Kanne Jr., W.R., Chandler, G.T., Nelson, D.Z. and Franko-Ferreira, E.A., 1995, "Welding irradiated stainless steel," *J. Nuclear Materials*, **225**, pp. 69-75.

5 Thomas, W.M., Nicholas, E.D., Needham, J.C., Murch, M.G., Temple-Smith, P. and Dawes, C.J. 'Improvements relating to friction stir welding', European Patent Specification 0615480 B1, 1991.

6 Gould, J.E., Lienert, T.J. and Feng, Z., 1998, "Recent developments in friction stir welding," SAE Technical Paper Series 981875.

7 Asano, K., Nishimura, S., Saito, Y., Sakamoto, H., Yamada, Y., Kota, T. and Hashimoto, T., 1999, "Weldability of neutron irradiated austenitic stainless steels," *J. Nuclear Materials*, **264** pp 1-9.

8 Hashimoto, T. and Mochizuki, M., 1999, "Modeling of helium bubble formation during welding of irradiated stainless steels," *Proc. 19th Int. Sym. Effects of Radiation on Materials*, ASTM STP 1366. Hamilton M.L. et al. eds. ASTM.

9 Feng, Z. 1994, "A computational analysis of thermal and mechanical conditions for weld metal solidification-cracking," *Welding in the World,* **33**(5) pp. 340-347.

10 Kawano, S., Sumiya, R. and Fukuya, K, 1998, "Simulation of helium bubble behavior in neutron-irradiated stainless steel during welding," *J. Nuclear Materials*, **258-263** pp. 2008-2012.

10. DOSIMETRY, DAMAGE PARAMETERS, AND ACTIVATION CALCULATIONS

No contributions.

11. MATERIALS ENGINEERING AND DESIGN REQUIREMENTS

No contributions.

12. IRRADIATION FACILITIES AND TEST MATRICES

No contributions.

PLANNING OF THE US-JAPAN JP-26 EXPERIMENT FOR IRRADIATION IN THE HFIR - R. E. Stoller (Oak Ridge National Laboratory) and H. Tanigawa (Japan Atomic Energy Research Institute, Tokai, Japan)

OBJECTIVE

This work is being carried out under Annex I of the Collaboration on Fusion Materials between the US DOE and the Japan Atomic Energy Research Institute. The JP-26 experiment is one component of the Phase-IV experiments with the goal of elucidating the effects of helium in candidate engineering and model alloys, and verifying the irradiation response of alloy F82H.

SUMMARY

The experimental matrix for JP-26 was finalized and final design of the irradiation vehicle was completed. Components needed to build the irradiation vehicle are being machined and will be delivered to ORNL by late August. Most of the necessary specimens have been fabricated and final delivery to ORNL is expected by late August. Assembly of the experiment is expected to take place in early September so that the irradiation can begin by mid September.

PROGRESS AND STATUS

Introduction

This experiment is being carried out within the framework of the US DOE-JAERI Collaboration on Fusion Materials, Annex I, which is in its fourth phase. The goals of the experiment include the investigation of the effects of helium on microstructural evolution, the impact of helium on fracture properties, and the development of engineering data on the fusion candidate alloy F82H. A more detailed description of the experiment will be provided in a subsequent report. The goal of this report is to provide a summary of the final design of the JP-26 capsule and the specimens contained in its 17 subcapsules.

Overall Description of JP-26 Capsule

The final design of the JP-26 capsule includes 17 subcapsules designed to accommodate 6 types of specimens and irradiate them at 3 temperatures, 300, 400, and 500°C. The specimen types are a small bendbar (deformation-fracture minibeam, DFMB), a sheet tensile specimen (SS-J3), a subsized pre-crack Charpy V-notch specimen (0.5-1/3-PCCVN), transmission electron microscopy disks (TEM), atom probe specimens (APFIM), and small multi-purpose coupons (MMPC) that have the same overall dimensions as the APFIM specimens. The specimen count at each temperature and the overall specimen dimensions are listed in Table 1. Figure 1 provides a description of the APFIM specimens that are being included in the JP-26 experiment. The pre-slit "tuning forks" are designed to simply handling and sorting, while permitting the two specimens to be made with a single cut following irradiation.

The physical stack up and the capacities of the 17 subcapsules contained in the JP-26 capsule are shown in Table 2. The higher temperature subcapsules are located nearer the vertical centerline where the gamma heating rate is highest. The neutron flux is also higher in this region, will lead to higher irradiation doses for the specimens exposed at the higher temperatures. The relative atomic displacement rate varies from 1.0 at the centerline to about 0.4 at the top or bottom of the capsule. A complete breakdown of the materials and specimens at each temperature is listed in Tables 3 to 5.

Table 1. -- JP26: Total specimen count by type and temperature:

specimen type	irradiation temperature (°C)	specimen count	specimen dimensions (mm)
DFMB	300	64	9.19x1.67x1.67
	400	0	
	500	0	
SS-J3	300	48	16x4x0.76
	400	40	
	500	40	
0.5-1/3 PCCVN	300	16	3.3x1.65x18
	400	16	
	500	16	
TEM	300	100	⌀3x0.25
	400	100	
	500	100	
APFIM or MMPC	300	48	16x1.25x0.5
	400	40	
	500	40	

Figure 1. – APFIM specimen geometry

- two pair (4) of the ‘tuning fork’ specimens is required for each material
- 1.25mm x 1.0mm x 16mm space is required in each corner of SS-J3 holder

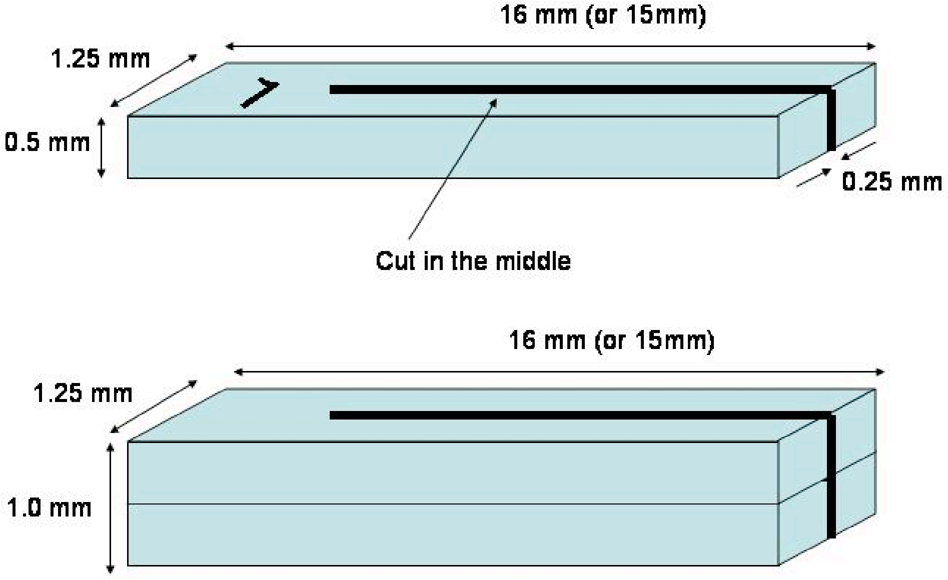

Table 2. - JP26 final capsule layout

subcapsule number	subcapsule type	specimen count	temperature
top of capsule			
1	TEM	100	400
2	SS-J3 + APFIM	8	300
		8	
3	SS-J3 + APFIM	16	400
		16	
4	0.5-1/3 PCCVN	16	300
5	SS-J3 + APFIM	16	300
		16	
6	SS-J3 + APFIM	16	400
		16	
7	SS-J3 + APFIM	16	500
		16	
8	0.5-1/3 PCCVN	16	500
9	SS-J3 + APFIM	8	500
		8	
10	TEM	100	500
11	SS-J3 + APFIM	16	500
		16	
12	0.5-1/3 PCCVN	16	400
13	SS-J3 + APFIM	8	400
		8	
14	DFMB	64	300
15	SS-J3 + APFIM	16	300
		16	
16	SS-J3 + APFIM	8	300
		8	
17	TEM	100	300
bottom of capsule			

ACKNOWLEDGMENT

This experiment is being designed by a multi-institutional team from JAERI, ORNL, PNNL, and the University of California, Santa Barbara.

TABLE 3

JP-26	Tensile									Toughness						Bend bar			TEM						APFIM			MMPC		
	SS-J3			SS-J3 with hole			SS-J3 with notch			0.5-1/3PCCVN			DFMB			DFMB						Ni/Al plated								
	48.0			48.0			48.0			98.0			24.5			24.5			2.0			2.0			9.2			9.2		
300 C. 10 dpa	Share	JP	US	Share	JP	US	Share	JP	US	Share	JP	US	Share	JP	US	Share	JP	US	Share	JP	US	Share	JP	US	Share	JP	US	Share	JP	US
F82H IEA	6									8			16								3			5	2					
F82H TIG WJ																														
F82H TIG WB																														
F82H+1.4%Ni	4									8			16								2				2					
F82H+1.4%Ni60	4																								2					
F82H mod1-A		2																												
F82H mod1-B		2																												
F82H mod1-C		2																												
F82H mod2		2																												
F82H mod3	4			2			2						16			16			2					6						10
JNC-ODS		2																		5						2				
JAERI ODS1		2																		5						2				
JAERI ODS2		2																		5						2				
JAERI ODS3		2																		5						2				
9Cr-2WVTa			2																											
Kobelco 12Cr ODS			2																		3			5			2			
Inco MA957 (Fr)			2																		2			2			2			8
Plansee PM2000			2																		2			2			2			
Eurofer97			2																		2			6						
U14YWT850																					2			3			2			
U14YWT1150																					5						2			
U14YW1150																					5						2			
O14YWT850																					5						2			
U14WT1000																					4						2			
US MA957																					2			2						
Fe																					6									
Fe-2Ni																					2									
Fe-3.5Ni																					2									
Fe-20%CW																					2									
Fe-2Ni+20%CW																					2									
Fe-3.5Ni+20%CW																					8									
F82H-mod.3+20%CW																					8									
sum	18	16	10	2	0	0	2	0	0	16	0	0	48	0	0	16	0	0	2	20	67	0	0	31	6	8	16	0	0	18

TABLE 4

JP-26	Tensile									Toughness						Bend bar			TEM						APFIM			MMPC		
	SS-J3			SS-J3 with hole			SS-J3 with notch			0.5-1/3PCCVN			DFMB			DFMB						Ni/Al plated								
	48.0			48.0			48.0			98.0			24.5			24.5			2.0			2.0			9.2			9.2		
400 C, 10 dpa	Share	JP	US	Share	JP	US	Share	JP	US	Share	JP	US	Share	JP	US	Share	JP	US	Share	JP	US	Share	JP	US	Share	JP	US	Share	JP	US
F82H IEA	5									8											3			5	2					2
F82H TIG WJ																														
F82H TIG WB																														
F82H+1.4%Ni	4									8											2				2					
F82H+1.4%Ni60	4																								2					
F82H mod1-A		2																												
F82H mod1-B		2																												
F82H mod1-C		2																												
F82H mod2		3																												
F82H mod3	4			2			2												2					6						6
JNC-ODS																				5						2				
JAERI ODS1																				5										
JAERI ODS2																				5						2				
JAERI ODS3																				5										
9Cr-2WVTa			2																											
Kobelco 12Cr ODS(12YWT)			2																		3			5			2			
Inco MA957 (Fr)			2																		2			2			2			6
Plansee PM2000 (EuroODS)			2																		2			2			2			
Eurofer97			2																		2			6						
U14YWT850																					2			3			2			
U14YWT1150																					5						2			
U14YW1150																					5						2			
O14YWT850																					5						2			
U14WT1000																					4						2			
US MA957																					2			2			2			
Fe																					6									
Fe-2Ni																					2									
Fe-3.5Ni																					2									
Fe-20%CW																					2									
Fe-2Ni+20%CW																					2									
Fe-3.5Ni+20%CW																					8									
F82H-mod.3+20%CW																					8									
sum	17	9	10	2	0	0	2	0	0	16	0	0	0	0	0	0	0	0	2	20	67	0	0	31	4	4	18	0	0	14

TABLE 5

JP-26	Tensile									Toughness						Bend bar			TEM						APFIM			MMPC		
	SS-J3			SS-J3 with hole			SS-J3 with notch			0.5-1/3PCCVN			DFMB			DFMB						Ni/Al plated								
	48.0			48.0			48.0			98.0			24.5			24.5			2.0			2.0			9.2			9.2		
500 C,10 dpa	Share	JP	US	Share	JP	US	Share	JP	US	Share	JP	US	Share	JP	US	Share	JP	US	Share	JP	US	Share	JP	US	Share	JP	US	Share	JP	US
F82H IEA	7									8											3			5	2					
F82H TIG WJ																														
F82H TIG WB																														
F82H+1.4%Ni	4									8											2				2					
F82H+1.4%Ni60	4																								2					
F82H mod1-A		2																												
F82H mod1-B		2																												
F82H mod1-C		2																												
F82H mod2		3																												
F82H mod3	6																		2					6						6
JNC-ODS																				5						2				
JAERI ODS1																				5										
JAERI ODS2																				5						2				
JAERI ODS3																				5										
9Cr-2WVTa			2																											
Kobelco 12Cr ODS(12YWT)			2																		3			5			2			
Inco MA957 (Fr)			2																		2			2			2			6
Plansee PM2000 (EuroODS)			2																		2			2			2			
Eurofer97			2																		2			6						
U14YWT850																					2			3			2			
U14YWT1150																					5						2			
U14YW1150																					5						2			
O14YWT850																					5						2			
U14WT1000																					4						2			
US MA957																					2			2			2			
Fe																					6									
Fe-2Ni																					2									
Fe-3.5Ni																					2									
Fe-20%CW																					2									
Fe-2Ni+20%CW																					2									
Fe-3.5Ni+20%CW																					8									
F82H-mod.3+20%CW																					8									
sum	21	9	10	0	0	0	0	0	0	16	0	0	0	0	0	0	0	0	2	20	67	0	0	31	6	4	18	0	0	12